

**UCSF**

**UC San Francisco Electronic Theses and Dissertations**

**Title**

Deciphering Host Immune Responses to SARS-CoV-2 Infection

**Permalink**

<https://escholarship.org/uc/item/35n8d0bc>

**Author**

Chen, Irene

**Publication Date**

2023

Peer reviewed|Thesis/dissertation

Deciphering Host Immune Responses to SARS-CoV-2 Infection

by  
Irene Chen

DISSERTATION  
Submitted in partial satisfaction of the requirements for degree of  
DOCTOR OF PHILOSOPHY

in

Biomedical Sciences

in the

GRADUATE DIVISION  
of the  
UNIVERSITY OF CALIFORNIA, SAN FRANCISCO

Approved:

DocuSigned by:

*Barbara Panning*

Barbara Panning

B18F20197C95417...

Chair

DocuSigned by:

*K. Mark Ansel*

K. Mark Ansel

DocuSigned by:

*Warner C. Greene*

Warner C. Greene

DocuSigned by:

*Melanie Ott*

Melanie Ott

000388F2B1EE40C...

Committee Members

Copyright 2023

By

Irene Chen

## **Dedication**

This dissertation is dedicated to my parents, Su-Yi Hsu and Brian Chen, whose respect for academic pursuit, love for curiosity, and guidance in all aspects of life are the reasons why I am here.

## Acknowledgements

The work presented here and beyond, during my time at UCSF, was only made possible with the support, encouragement, and laughter provided by a short list of wonderful people below.

First and foremost, I would like to thank my advisor, Dr. Melanie Ott, for her guidance during the last four years. She has taught me the aspects of doing great science: tenacity, optimism, curiosity, rigor, and resilience. I am still in awe of her brilliance, ability make sense of data that makes no sense, and, most impressively, ability to operate at 110% on five hours of sleep. I am so lucky to call her my mentor and “adoptive mom.” I will be forever grateful for opportunities she has given and pushed me to take to become the scientist I am today.

I am incredibly fortunate to have collaborated with Dr. Danica Fujimori on my thesis work. Her patience and intellect was so refreshing in the midst of a sea of frustrating pandemic-related collaborations. I am thankful for her continued mentorship even after the conclusion of our project and I continue to secretly hope we can work together in the future.

I would like to thank my qualifying and thesis committee members, Drs. Barbara Panning, Mark Ansel, and Warner Greene, for being sounding boards when I felt I had made no progress in my work. They always asked the right questions to improve the scientific rigor and scope of my work. I would like to thank Dr. Nadia Roan, who served on my qualifying committee, for valuable questions and feedback early on in my

graduate work. I would like to thank Dr. Stephen Floor for mentoring me during my first rotation and his continued advice on anything on my mind. I would like to thank my rotation advisor, Dr. Kole Roybal, for giving me the opportunity to work on CAR-T cells and extremely “animated” expressions when I brought him exciting data. I am grateful for Dr. Rushika Peera, who served as my faculty advisor, for always providing a rational listening ear and guidance as I navigated through UCSF. The UCSF Biomedical Sciences graduate program is one of the best programs in the world under the stewardship of Drs. Mark Ansel and Anita Sil. Of course, Demian Sainz, the man behind the curtain, making sure the treacherous path to a PhD was as smooth as can be. I thank the National Institutes of Health for supporting and funding my research.

I am forever indebted to the many mentors who gave me their time and helped me get to where I am today. Dr. Shu-Ou Shan, who took a chance on a 9<sup>th</sup> grader and gave me my first ever research opportunity. Sowmya Chandrasekar and Peera Jarupornpan, who took on the challenge of initiating me in the art of pipetting, gel pouring, and protein purification. Dr. Clodagh O’Shea, who ignited my interest in virology and continues to advise me on my career. Horng Ou for being the most generous and patient scientific mentor that I’m lucky to call close friend. Bill Partlo Shigeki Miyake-Stoner, Marco Bürger, and Witek Kwiatkowski for tolerating my incessant questions and their guidance of a burgeoning viral biochemist. Dr. Gyula Timinszky and Giuliana Möller for the invitation to enter the world of DNA damage and ADP ribosylation, topics I would eventually revisit at UCSF. Dr. Chie-Pein Chen for the opportunity to delve into oocyte and reproductive biology. Dr. Ciara Metcalfe, Jane Guan, and Wei Zhou for the invaluable industry experience at Genentech.

I am so fortunate to have found a wonderful lab to conduct my research. I have appreciated the close friendship, listening ears, and advice of Mir Khalid, Jennifer Hayashi, Parinaz Fozouni, Jesse Chen, Sarah McMahon, Takako Tabata, Francisco Zapatero-Belinchon, Taha Taha, Frank Soveg, Krystal Fontaine, Renu Kumar, and Chia-Lin Tsou. Many members of the Ott lab through the years have been wonderful sources of humor and camaraderie for which I am grateful: Rahul Suryawanshi, Kristoffer Leon, Ansumana Hull, Albert Vallejo-Gracia, Danielle Lyons, Ibraheem Ali, Camille Simoneau, Bharath Sreekumar, Carley Gray, Karsten Krey, Jeffery Shu, Stephanie Stephens, Nathan Meyers, Ursula Schulze-Gahmen, Lauren Weiser, Tessa Divita, Mauricio Montano, Zichong Li, Yusuke Matsui, Kathrin Roesch, Sakshi Tomar, Gili Aviv, Lauren Weiser, Maria McCavitt-Malvido, Ludivine Grzelak, Alia Aguilar, and Veronica Fonseca. Many were the best bench mates, collaborators, mentors, and confidants throughout the years. I also have appreciated the assistance and friendship of the Doudna lab and others on the fifth floor: Abdullah Syed, I-Li Tan, Karen Zhu, Alison Ciling, Wayne Ngo, and Joe Hiatt.

I am indebted to James Longbotham for being the most seamlessly supportive, generous, and critical collaborator. Working with the Fujimori lab has been nothing short of wonderful. The SIRT5 collaboration has been equally lovely; I am grateful for the patience and advice of Marius Walter. Through this work I have found another mentor, Dr. Eric Verdin, who is as into F1 as I am and my “adoptive father.”

I would like to thank my motley crew of UCSF classmates-turned into forever friends-who I have been privileged to embark on this journey with: Austin Hsu, David Shin,

Jiapei Chen, Tyler Fair, Kevin Wilkins, Kyle Kisor, Jenny Umhoefer, Karen Chan, Donovan Trinidad, and Naznin Jahan. My long-time confidants for their unending support: Rosalind Bump, Sophia Liu, Anna Miyajima, Jenny Zeng, Rachael Thorley, Nathan Hall-Snyder, Michael Hall-Snyder, Rachel Fenichel, Gregory Hall, Sasha Zbrozek, Stella Wang, Katie Kahle, Cepideh Razavi, and Sara Vo. Shenanigans and adventures with all of you rejuvenated and reinvigorated my time outside of lab.

Lastly, and most importantly, I would like to thank my family for their continued support through the thick and thin. To mom and dad, thank you for your practical wisdom, compassion, and always asking “are you going to graduate now?” to keep me on my toes. To grandma and grandpa, thank you for the support in my pursuit of higher education even without fully comprehending my work. To my aunts, uncles, and cousins for the support and laughter throughout the years.



## **Contributions**

This dissertation encompasses a couple different projects where I critically contributed in inception and execution since the outbreak of the COVID-19 pandemic. Chapter I represents a literature review where I am grateful for editorial contributions from Melanie Ott. Chapter II represents my main thesis project which I led with the indispensable contribution from James Longbotham, Sarah McMahon, Rahul Suryawanshi, Mir Khalid, Danica Fujimori, and Melanie Ott. Chapter III represents work I co-led with Rahul Suryawanshi with indispensable contribution from Tongcui Ma, Renuka Kumar, Charles Chiu, Nadia Roan, and Melanie Ott. Chapter IV represents work led by Marius Walter and Eric Verdin where I designed and performed critical biosafety level 3 experiments to tease out the proviral function of SIRT5. The chapters described in this work are reproduced from these publications:

### **Chapter I**

Chen IP and Ott M. (2022). Viral Hijacking of BET Proteins. *Viruses* 14. 10.3390/v14102274. <https://doi.org/10.3390/v14102274>

### **Chapter II**

Chen IP\*, Longbotham JE\*, McMahon S, Suryawanshi RK, Khalid MM, Taha TY, Tabata T, Hayashi JM, Soveg FW, Carlson-Stevermer J, Gupta M, Zhang MY, Lam VL, Li Y, Yu Z, Titus EW, Diallo A, Oki J, Holden K, Krogan N, Fujimori D Galonić, Ott M. (2022). Viral E Protein Neutralizes BET Protein-Mediated Post-Entry Antagonism of SARS-CoV-2. *Cell Rep.*, 111088. <https://doi.org/10.1016/j.celrep.2022.111088>.

### **Chapter III**

Suryawanshi RK\*, Chen IP\*, Ma T\*, Syed AM, Brazer N, Saldhi P, Simoneau CR, Ciling A, Khalid MM, Sreekumar B, Chen PY, Kumar GR, Montano M, Gascon R, Tsou CL, Garcia-Knight MA, Sotomayor-Gonzalez A, Servellita V, Gliwa A, Nguyen J, Silva I, Milbes B, Kojima N, Hess V, Shacreaw M, Lopez L, Brobeck M, Turner F, Soveg FW, George AF, Fang X, Maishan M, Matthay M, Morris MK, Wadford D, Hanson C, Greene WC, Andino R, Spraggon L, Roan NR, Chiu CY, Doudna JA, Ott M. (2022). Limited cross-variant immunity from SARS-CoV-2 Omicron without vaccination. *Nature* 607, 351–355. <https://doi.org/10.1038/s41586-022-04865-0>.

### **Chapter IV**

Walter M, Chen IP, Vallejo-Gracia A, Kim I-J, Bielska O, Lam VL, Hayashi JM, Cruz A, Shah S, Soveg FW, Gross JD, Krogan JN, Jerome KR, Schilling B, Ott M, Verdin E. SIRT5 is a proviral factor that interacts with SARS-CoV-2 Nsp14 protein. *PLoS Pathog.* 18, e1010811. <https://doi.org/10.1371/journal.ppat.1010811>.

A virus is “simply a piece of bad news wrapped up in protein.”

Jean and Peter Medawar, 1977

## **Deciphering Host Immune Responses to SARS-CoV-2 Infection**

Irene Chen

### **Abstract**

The ongoing coronavirus disease 2019 (COVID-19) pandemic, caused by the severe acute respiratory syndrome coronavirus 2 (SARS-CoV-2), continues to cause significant morbidity and mortality worldwide. Although most infections are mild and the majority of patients recover, some experience severe and often fatal systemic inflammation, cytokine storm, and acute respiratory distress syndrome. The innate immune system of the human body is the first line of defense against SARS-CoV-2, sensing the virus through pattern recognition receptors and activating inflammatory cascades that promote viral clearance. Simultaneously, the virus has evolved numerous strategies to escape detection and surveillance of the immune system for successful replication. An improved understanding of host immunity and viral evasion strategies will help identify therapeutic targets to mitigate disease and improve patient outcome. Here, we report two cellular epigenetic proteins, BRD4 and SIRT5, as anti- and proviral binding partners of SARS-CoV-2 envelope (E) and non-structural protein Nsp14, respectively. We identify bromodomain and extra-terminal (BET) proteins as critical antiviral factors as genetic or chemical inactivation of BRD4 exacerbates viral infection in cells and enhanced mortality in mice. BET inactivation suppresses interferon production induced by SARS-CoV-2, a process phenocopied by the “histone mimetic” E protein, supporting a model where the E protein evolved to antagonize the innate immune system via BET protein inhibition. Conversely, genetic or chemical inactivation of SIRT5 reduces SARS-CoV-2 replication in cells. While SIRT5 interacts with Nsp14 through its catalytic domain, Nsp14 does not appear to be directly

deacylated by SIRT5. Depletion of SIRT5 results in higher basal levels of innate immunity and a stronger antiviral response during infection, indicating SIRT5 is a proviral factor necessary for efficient viral replication. Lastly, we compared the humoral immune responses elicited by SARS-CoV-2 variants, WA1, Delta, and Omicron. We show that without vaccination, infection with Omicron induces a limited humoral immune response in mice and humans. In contrast to WA1 and Delta, Omicron replicates at low levels in the lungs and brains of infected mice, leading to mild disease with reduced expression of proinflammatory cytokines, diminished activation of lung-resident T cells, and limited cross-variant immunity against non-Omicron variants in unvaccinated individuals. Collectively, these findings advance our understanding on the various host-pathogen interactions that need to be considered in designing novel SARS-CoV-2 therapeutics.

## Table of Contents

<b>Chapter I: Introduction – Viral hijacking of BET proteins</b>	<b>1</b>
Abstract	2
Introduction	3
Domain Architecture of BET Proteins	3
Overlapping and Distinct Function of BET Proteins	4
Current BET Inhibitors Target All Family Members	7
The Role of BET Proteins in the Viral Life Cycle	8
Figures	21
Tables	23
References	25
<b>Chapter II: Viral E protein neutralizes BET protein-mediated post-entry antagonism of SARS-CoV-2</b>	<b>46</b>
Abstract	48
Introduction	49
Results	52
Discussion	61
Material and Methods	69
Figures	80
Tables	94
References	98
<b>Chapter 3: Limited cross-variant immunity from SARS-CoV-2 Omicron without vaccination</b>	<b>107</b>
Abstract	110

Introduction	111
Results	112
Discussion	117
Material and Methods	118
Figures	130
Tables	148
References	151
<b>Chapter 4: SIRT5 is a proviral factor that interacts with SARS-CoV-2</b>	
<b>Nsp14 protein</b>	155
Abstract	156
Author Summary	157
Introduction	158
Results	161
Discussion	177
Material and Methods	182
Figures	200
Tables	219
References	225
<b>Chapter 5: Conclusions and Outlook</b>	235
References	237

## List of Figures

Figure 1.1. BET protein family members.	21
Figure 1.2. Steps in a generic viral life cycle where BET proteins are involved.	22
Figure 2.1. BRD2, BRD3, and BRD4 differentially affect SARS-CoV-2 infection.	80
Figure 2.2. Loss of BET proteins reduces interferon and proinflammatory cytokine expression.	82
Figure 2.3. SARS-CoV-2 E protein interacts with BET proteins at the nuclear periphery.	84
Figure 2.4. Acetylated SARS-CoV-2 E peptide predominantly binds the second bromodomain of BRD4.	86
Figure 2.5. BET inhibitors enhance SARS-CoV-2 infection in K18-hACE2 mice.	88
Figure S2.1. BET proteins are positive regulators of ACE2 expression.	89
Figure S2.2. Acetylated E peptide occupies similar binding sites to known acetylated lysine binding sites of BRD4 BD2.	90
Figure S2.3. SARS-CoV-2 infection of K18-hACE2 mice results in dysregulated immune responses.	92
Figure 3.1. Robust infection of K18-hACE2 mice with Delta and ancestral variant, but not Omicron.	130
Figure 3.2. Robust viral replication of WA1 and Delta, but not Omicron, in mice and human airway cells.	131
Figure 3.3. Ancestral and variant of concern SARS-CoV-2 elicit immune responses in lungs of mice.	133
Figure 3.4. Cross-variant neutralization of SARS-CoV-2 isolates by sera from infected mice.	135



Figure 3.5. Cross-variant neutralization of SARS-CoV-2 isolates by human sera.	137
Figure S3.1. Physical conditions of the infection mice at 5 dpi.	138
Figure S3.2. Lower viral replication of Omicron in mice and human cells.	140
Figure S3.3. Differential expression of proinflammatory markers in lungs of infected mice.	142
Figure S3.3. Cross-variant neutralization of SARS-CoV-2 isolates by human sera.	143
Figure S3.5. Sera neutralizing titer assays of from SARS-CoV-2-infected mice.	144
Figure S3.6. Sera neutralizing titer assays of individuals infected with Omicron.	145
Figure S3.7. Sera neutralizing titer assays from individuals infected with Delta.	146
Figure S3.8. Sera neutralizing titer assays from individuals.	147
Figure 4.1. SARS-CoV-2 Nsp14 interacts with human SIRT5.	200
Figure 4.2. SIRT5 catalytic activity is necessary to interact with Nsp14.	202
Figure 4.3. SARS-CoV-2 Nsp14 interacts with human SIRT1.	204
Figure 4.4. SIRT5 is a proviral factor.	206
Figure 4.5. SIRT5 proviral activity is partially independent from the interaction with Nsp14.	208
Figure 4.6. SIRT5-KO cells mount a stronger innate immune response.	209
Figure 4.7. SIRT5-KO cells express a higher basal level of viral restriction factors.	211
Figure 4.8. SIRT5 proviral activity is independent of the MAVS signaling pathway.	213
Figure S4.1. Characterization of inhibitors.	215
Figure S4.2. Levels of viral restriction factors.	216



## List of Tables

Table 1.1. BET protein interactions with viruses.	23
Table S2.1. sgRNA sequences for RNP editing.	94
Table S2.2. Genotyping primers.	95
Table S2.3. qPCR primers.	96
Table S2.4. SARS-CoV-2 E peptides.	97
Table S3.1. Clinical data of patients.	148
Table S3.2. List of qPCR primers for mouse studies.	149
Table S3.3. List of CyTOF-staining antibodies for mouse studies.	150
Table S4.1. CRISPR gRNAs (knockout in A549-ACE2).	219
Table S4.2. CRISPR genotyping primers (SIRT1-SIRT5 Knockout in A549-ACE2).	220
Table S4.3. CRISPRi gRNAs (knockdown in HEK293T).	221
Table S4.4. qPCR primers.	222
Table S4.5. Antibodies.	223
Table S4.6. Small molecule inhibitors and activators.	224

# Chapter I

## Introduction

### Viral Hijacking of BET Proteins

Irene P. Chen<sup>1,2</sup> and Melanie Ott<sup>1,2,3,\*</sup>

#### Affiliations

<sup>1</sup>Gladstone Institutes, San Francisco, CA, 94158, USA

<sup>2</sup>Department of Medicine, University of California, San Francisco, San Francisco, CA, 94143, USA

<sup>3</sup>Chan Zuckerberg Biohub, San Francisco, CA, 94158, USA

\*Corresponding author: Melanie Ott, [melanie.ott@gladstone.ucsf.edu](mailto:melanie.ott@gladstone.ucsf.edu)

#### Keywords

Coronavirus, Flavivirus, Papillomavirus, Polyomavirus, Retrovirus, Herpesvirus, BET proteins, BET inhibitors, RVX-208, JQ1, BRD4, host-pathogen interactions

## **ABSTRACT**

Proteins of the bromodomain and extraterminal domain (BET) family mediate critical host functions such as cell proliferation, transcriptional regulation, and the innate immune response, which makes them preferred targets for viruses. These multidomain proteins are best known as transcriptional effectors able to read acetylated histone and non-histone proteins through their tandem bromodomains. They also contain other short motif-binding domains such as the extraterminal domain, which recognizes transcriptional regulatory proteins. Here, we describe how different viruses have evolved to hijack or disrupt host BET protein function through direct interactions with BET family members to support their own propagation. The network of virus-BET interactions emerges as highly intricate, which may complicate the use of small-molecule BET inhibitors—currently in clinical development for the treatment of cancer and cardiovascular diseases—to treat viral infections.

## 1. Introduction

The bromodomain and extraterminal domain (BET) proteins, consisting of BRD2, BRD3, BRD4, and BRDT, are characterized by their ability to bind acetylated lysines. BRD2, BRD3, and BRD4 are expressed ubiquitously and will be the focus of this review, while BRDT expression is restricted to the male germline. BET proteins are major transcriptional regulators and when dysregulated, are implicated in cancer as well as autoimmune, cardiovascular, and metabolic diseases <sup>1</sup>. Consequently, there is intense focus on finding selective and potent BET inhibitors to restore normal gene regulation for the treatment of these conditions.

In recent years, an increasing number of viruses have been found to directly engage with BET proteins for their survival. The wide variety of fundamental roles BET proteins play in cells, combined with their shared multifunctional domains, make them natural targets of viruses. Below, we describe general functions of each BET protein and summarize how different viruses directly hijack or subvert BET proteins for their own benefit.

## 2. Domain Architecture of BET Proteins

The functions of BET proteins have been widely associated with their conserved domains reflected in their name: bromodomains (**BDs**) and extraterminal (**ET**) domain (Figure 1.1). BET proteins have two tandem, N-terminal BDs (BD1 and BD2) that engage peptides containing acetylated lysine residues optimally spaced by two amino acids (Kac-XX-Kac) <sup>2-4</sup>. Through their BDs, BET proteins act as transcriptional regulators by interacting with acetylated histones, transcription factors, and viral

proteins <sup>2,3,5</sup>. The extraterminal domain mediates protein-protein interactions and recognizes a short peptide motif, “KIKL,” conserved across many different transcriptional regulators, including catalytic subunits of chromatin remodeling complexes <sup>6</sup>. Other smaller domains identified within BET proteins include a basic interacting domain (BID), phosphorylation-dependent interacting domain (PDID), and N- and C-terminal serine-rich domains that can be phosphorylated (NPS and CPS) and mediate more protein-protein interactions and auto-regulation of function (Figure 1.1) <sup>7-11</sup>. BET proteins can also form hetero- or homodimers within the family through a shared motif B that is required for BET protein association to chromatin <sup>12</sup>.

### **3. Overlapping and Distinct Functions of BET proteins**

While BET proteins share many conserved protein domains and often interact with the same proteins, they can perform unique functions (as reviewed in <sup>13</sup>), in part because of a wide range of binding affinities for the same targets. Lower sequence conservation outside the BD and ET domains may also enable distinct functions and interactions for each BET family member. The functions mentioned below pertain to BET protein-mediated processes that viruses directly exploit as opposed to immunomodulatory functions that BET proteins transcriptionally control during disease as previously reviewed by others (reviewed in <sup>14</sup>).

#### **3.1. BRD2**

BRD2 was originally identified as a mitogen-stimulated nuclear kinase <sup>15</sup>. Upon serum stimulation, it binds the promoters of cell cycle genes and regulates E2F2-dependent genes required for the G1/S transition of the cell cycle <sup>16,17</sup>. BRD2, along with BRD3,

has intrinsic histone chaperone activity that allows RNA Polymerase II (Pol II) to process through hyperacetylated nucleosomes <sup>18</sup>.

BRD2 also regulates transcription by serving as a scaffold for proteins to associate with chromatin. It has been found in association with five major chromatin-related complexes: 1) Pol II, the core promoter, and TATA binding factor (TBP)-associated factors (TAFs), 2) activated transcription factors E2F and DP-1, 3) Mediator complex subunits, 4) histone modification enzymes (HDAC11 and CBP/p300), and 5) SWI/SNF remodeling complex subunits <sup>19</sup>. Depending on its chromatin-binding partners, BRD2 either activates transcription (when associated with Mediator complex and TAFs) or represses it (when associated with HDAC11 and the SWI/SNF chromatin-remodeling complexes). Beyond this, BRD2 can influence transcription by regulating higher-order chromatin architecture. BRD2 is recruited to heterochromatin boundaries and protects euchromatic histone modifications, thus strengthening boundaries and limiting the spread of heterochromatin <sup>20</sup>. It also colocalizes with chromatin architecture/insulator protein CCCTC-binding factor (CTCF) to form transcriptional boundaries and restrict aberrant expression of genes flanking such boundaries <sup>21</sup>.

### **3.2. BRD3**

BRD3, like other BET proteins, is able to bind acetylated histones and transcription factors to regulate transcription. It shares many functions with BRD2, such as regulating cyclin D1 expression and facilitating the elongation of transcripts by Pol II through hyperacetylated nucleosomes <sup>18,22,23</sup>. In concert with BRD2, it binds directly to the transcription factor GATA1 to synergistically regulate GATA1-mediated erythroid



gene expression<sup>24</sup>. Additionally, BRD3 is able to interact with RNA and transcription factors to form phase-separated condensates on enhancers as a transcriptional regulatory strategy<sup>25</sup>.

### **3.3. BRD4**

BRD4 is the best characterized member of the family and has prominent roles in cell proliferation and transcription. It is one of the few nuclear factors retained in the nucleus, bound exclusively to chromosomes, during the M phase, when most factors are dissociated in response to global arrest of transcription. As a mitotic bookmark, BRD4 marks the transcription start sites (TSSs) of many genes programmed to express during or immediately after mitosis, and promotes transition into S phase<sup>26,27</sup>. Beyond its role in cell proliferation, it is able to initiate transcription elongation by recruiting positive transcription elongation factor (P-TEFb) through a P-TEFb interacting domain (PID) found in the long isoform of BRD4 (BRD4L). The binding of BRD4L to active P-TEFb prevents P-TEFb's interaction with inhibitory factors and facilitates Pol II pause release<sup>28,29</sup>. BRD4 can also recruit transcription factors to promoters, interact with catalytic enzymes of the NuRD and SWI/SNF chromatin remodelers, and with lysine methyltransferases, to loosen and compact chromatin for controlling transcription<sup>9,14,30,31</sup>. BRD4 also has atypical kinase activity that allows it to phosphorylate Pol II CTD and facilitate transcription elongation independently of P-TEFb<sup>29,32</sup>. Additionally, BRD4 has intrinsic histone acetyltransferase (HAT) activity where it mediates chromatin decompaction by acetylating and evicting nucleosomes of target genes, thus activating their transcription<sup>32</sup>. Post translational modifications on BRD4, such as phosphorylation of NPS by CK2, methylation of BD1 by SETD6,

proline hydroxylation by PDH2, and ubiquitination by SPOP, modulate BRD4's function in chromatin localization, transcription factor recruitment, protein stability, and transcriptional activation <sup>10,13,33–35</sup>.

On the other hand, the short isoform of BRD4 (BRD4S) lacks PID and intrinsic HAT activity, but shares the same BD and ET domains as BRD4L. A unique aspect of BRD4S is that it plays an active role in repairing DNA double-strand breaks (DSBs) marked by hyperacetylation of histone H4 and phosphorylation of H2AX. BRD4S is typically recruited to DSBs, where it forms DNA repair complexes by recruiting repair proteins <sup>36,37</sup>. Additionally, BRD4S can act as a chromatin insulator regulating responses to DNA damage <sup>38</sup>. In this role, BRD4S inhibits the DNA damage response (DDR) by recruiting the condensin II chromatin remodeling complex to acetylated histones via its BDs to limit chromatin accessibility to repair proteins.

#### **4. Current BET Inhibitors Target All Family Members**

Because BET proteins play many vital functions, their dysregulation underlies many diseases. One way to restore normal cellular function is to disrupt BET proteins' ability to alter gene expression in diseased cells. All current BET inhibitors are small molecules that compete for binding of BDs to their natural ligand, acetyllysines (more extensively reviewed in <sup>39</sup>). Most inhibitors, such as JQ1, IBET-151 and OTX015, non-covalently bind BDs of all BET proteins as they are highly conserved <sup>40–42</sup>. Small differences in amino acids, polarity, and hydrophobicity in BD binding pockets have allowed the recent development of BD1- and BD2-specific inhibitors (Olinone and GSK-778 for BD1; Apabetalone [RVX-208] and ABBV-744 for BD2), but they still target

all BET proteins indiscriminately<sup>4,40,43–49</sup>. Proteolytic targeting chimeric (PROTAC) compounds (dBET6 and ARV-825) that induce BET protein degradation are also being investigated<sup>50–52</sup>. Most BET inhibitors are currently being tested for various cancer and cardiovascular diseases, with growing potential for applications in viral diseases.

## **5. The Role of BET Proteins in the Viral Life Cycle**

This review focuses on direct interactions between viral proteins or genome with members of the BET family during different steps of the viral life cycle (Figure 1.2).

### **5.1. Coordinators of Viral Genome Integration**

A hallmark of retroviral replication is the integration into the host genome. Interestingly, the site of retroviral integration is not at all random; most retroviruses are guided to certain regions of the host genome by its integrase (IN) protein via interactions with specific host proteins. Murine leukemia virus (MLV), a gammaretrovirus, preferentially integrates near transcription start sites (TSSs), CpG islands, and DNase I-hypersensitive sites, which correlate with BET protein-chromatin binding sites, and are best predicted by BRD2 distribution<sup>53–56</sup>. MLV integration site selection is guided by interactions between its IN and the ET domains of BET proteins<sup>54,55</sup>. When cells were infected with MLV in the presence of the BET inhibitors, the number of integrated MLV copies significantly decreased and integration was redirected away from TSSs<sup>54,55</sup>. Conversely, overexpression of the BRD2 ET domain increased the number of integrated MLV genomes<sup>54</sup>. Moreover, the ET domains of BRD2 and BRD4 bind the INs of other gammaretroviruses (but not alpha-, beta-, and delta-retroviruses, or lentiviruses), including porcine endogenous retrovirus-A/C (PERV A/C), feline

leukemia virus (FeLV), and avian Reticulo-Endotheliosis Virus (REV) in a similar manner, suggesting that gammaretroviruses have evolved a common association with BET proteins to select their integration sites<sup>54,57,58</sup>.

## **5.2. Drivers of Viral Genome Persistence**

Unlike many viruses that cause the lysis of the infected host cells, papillomaviruses (PVs) and herpesviruses persist at relatively low copy numbers without destroying their host cells. Both PVs and herpesviruses maintain their DNA genomes as episomes tethered to chromatin via BET proteins. This allows their viral genomes to be partitioned along with the host chromosomes into daughter cells during mitosis, a process termed mitotic segregation.

PV episomes tether to host chromosomes via the interaction between its E2 protein and the C-terminus of chromatin-associated BRD4 to ensure that its genome is retained in the nucleus and partitioned into daughter cells<sup>9,59-61</sup>. In fact, the E2:BRD4 complexes are visible as distinct dots on the mitotic chromosome after successful infection<sup>62-64</sup>. The overexpression of just the BRD4 C-terminus dominantly prevents E2 from binding chromosomes and causes the loss of PV genomes in cells<sup>64-66</sup>. While E2s of all PVs interact with BRD4, not all E2 proteins are readily observed to bind mitotic chromosomes because of differences in their affinity for BRD4<sup>67,68</sup>. E2 proteins from BPV, HPV, and cottontail rabbit PV (CRPV) bind tightly to BRD4 whereas alpha- and beta-PVs bind only weakly<sup>62,64,67,69,70</sup>. This suggests that not all PVs maintain their genomes through a BRD4-dependent mechanism.

Similar to PV's E2, the LANA protein of Kaposi's sarcoma associated herpesvirus (KSHV) likely maintains KSHV's episome through BRD2 and BRD4. LANA contacts the ET domains of BET proteins<sup>6,71</sup>. Typically, BRD2 is associated with euchromatin, but it relocates to heterochromatic regions in the presence of LANA and colocalizes with LANA in infected mitotic and interphase cells<sup>72,73</sup>. Given the role of BRD2 in maintaining transcriptional boundaries and spreading histone acetylation, the LANA:BRD2 complex is proposed to maintain viral genome persistence by mediating local euchromatin formation around the episome, thus tethering it to heterochromatin<sup>20</sup>. BRD2 also stabilizes and possibly maintains mitotic segregation of another herpesvirus, Epstein-Barr virus (EBV)<sup>74</sup>. Reliance on BET proteins to maintain viral genomes is further found in the unrelated raccoon polyomavirus (RacPyV), where treating infected cells with JQ1 reduces viral genome copies<sup>75</sup>. Overall, many DNA viruses take advantage of the fact that BET proteins stably bind chromatin to persist in host cells long-term.

### **5.3. Organizers of Viral Genome Replication**

BET proteins facilitate the replication of oncogenic DNA viruses such as polyomavirus, human papillomaviruses (HPV), and EBV. Merkel Cell polyomavirus (MCPyV) recruits BRD4 via its large T (LT) antigen, a protein that binds to the viral origin of replication (Ori) and functions as a helicase for unwinding viral DNA for replication<sup>76</sup>. Normally diffused in the nucleus, BRD4 forms distinct nuclear foci in the presence of both Ori and LT, suggesting Ori traffics the viral replication complex to specific nuclear locations<sup>77</sup>. The interaction is mediated by the ET domain of BRD4 and results in BRD4-mediated recruitment of cellular replication complex C (RFC), essential for DNA

replication, to LT/Ori foci. Viral DNA replication is reduced upon BRD4 knockdown, but rescued in a dose-dependent manner upon BRD4 reconstitution <sup>77</sup>. Treating infected cells with JQ1 increased viral DNA replication but not viral transcription, most likely because it released chromatin-bound BRD4 and allowed the assembly of more MCPyV LT/Ori replication complexes <sup>77</sup>. The genome replication of a related polyomavirus, John Cunningham polyomavirus (JCPyV) is similarly reduced in the presence of JQ1 <sup>78</sup>.

BRD4 is similarly involved in two different steps of the PV genome replication process. HPVs activate DDR and position DDR factors, such as DNA polymerase  $\delta$ , on the HPV genome for replication <sup>59,68,79</sup>. Given that BRD4 acts as an important scaffolding protein in DDR, it is speculated to be involved in recruiting the replication machinery to the HPV genome <sup>80,81</sup>. Additionally, BRD4 is recruited to active HPV replication origin foci, along with HPV's E2 protein and cellular RFC and DNA polymerase <sup>82</sup>. The E2:BRD4 interaction is dependent on phosphorylation status of both E2 and NPS and PDID in the C terminus of BRD4 <sup>9,10,83</sup>. Mutagenesis disrupting the E2:BRD4 interaction abolishes the formation of HPV replication complexes and impairs viral DNA replication <sup>84</sup>. The addition of JQ1 also enhances HPV genome replication and is thought to function in a manner similar to its effect on MCPyV <sup>82</sup>. In contrast, BET inhibitors block EBV DNA replication initiation by preventing BET proteins from localizing at the lytic origins of replication (OriLyt) <sup>85</sup>.

## 5.4. Accomplices in Viral Transcription

As BET proteins are well-known cellular transcriptional regulators, it is not surprising that viruses subvert their function for transcribing their own genome. PVs, EBV, hepatitis B virus (HBV), herpes simplex virus (HSV), and JCPyV rely on BRD4:P-TEFb for viral transcription, whereas human cytomegalovirus (HCMV) and retroviruses compete with BRD4 for binding to P-TEFb.

### 5.4.1. Recruitment of the BRD4:P-TEFb Complex

The E2 protein of PVs can both activate and repress viral transcription, depending on where it binds in relation to promoter elements <sup>65,86–89</sup>. In both cases, it depends on BRD4: disrupting E2:BRD4 with a dominant-negative BRD4 C-terminal peptide blocks the transactivation function of many PV E2 proteins; conversely, BRD4 knockdown reduces E2's ability to repress genes that regulate the transition between lytic and latent infection <sup>67,90–92</sup>. Additionally, Epstein-Barr nuclear antigen 1 (EBNA1) interacts with the C-terminal domain of BRD4, and this interaction is important for EBNA1-mediated viral transcription from the family of repeats (FR) enhancer elements in the EBV genome <sup>74</sup>. Inhibiting BRD4 with JQ1 prevented the expression of viral immediate-early and late viral proteins during EBV reactivation <sup>85</sup>.

Furthermore, different P-TEFb-containing complexes, including BRD4 or superelongation complex (SEC), have been reported to bind the genome of HBV <sup>93</sup>. JQ1 treatment enhances BRD4 occupancy on the viral genome and induces HBV transcription, suggesting that BRD4 does not rely on BDs to regulate viral transcription <sup>93</sup>. JQ1 most likely releases chromatin-bound BRD4 to allow the recruitment of

BRD4:P-TEFb to the viral genome, a novel mechanism in which HBV hijacks host P-TEFb complexes for its own transcription. This effect has important clinical implications, as BET inhibitors used to treat infections or other conditions could inadvertently reactivate latent HBV.

BET inhibitors are also investigated as a means to dysregulate HSV gene expression (further reviewed in <sup>94</sup>). BET inhibitors increase viral transcripts levels, protein production, and infectious virion production, resulting in HSV reactivation in sensory ganglia explants and mouse models by increasing the recruitment of BRD4:P-TEFb to its viral promoters <sup>95,96</sup>. Unexpectedly, RVX-208, a BD2-specific inhibitor, had no effect on HSV replication suggesting BET inhibitor-mediated HSV reaction is primarily through BD1 <sup>95</sup>.

JCPyV also relies on BRD4 to regulate viral transcription. The genome of JCPyV is divided into two transcriptional regions, early and late, by a noncoding regulatory region (NCRR) that contain many transcription factor binding sites, including an NF- $\kappa$ B binding site. BRD4 activates early JCPyV transcription through its involvement with recruiting NF- $\kappa$ B to the nucleus and its ability to coactivate viral gene transcription by binding to acetylated NF- $\kappa$ B P65 and recruiting P-TEFb <sup>7,78</sup>. JCPyV viral transcription is enhanced by ectopic expression of BRD4 and reduced upon BET inhibition with JQ1<sup>78</sup>.



#### 5.4.2. Competitive Binding to P-TEFb

Although no direct interaction between HCMV and BET proteins has been demonstrated, BRD4 is inextricably linked to HCMV latency and reactivation<sup>97,98</sup>. BRD4 colocalizes on the viral genome with HCMV's immediate-early 2 protein (IE2) to initiate viral transcription<sup>98</sup>. BRD4's ability to bind P-TEFb sequesters the transcriptional activator complex away from HCMV promoters and enforces latency. In the presence of BET inhibitors, P-TEFb is released from BRD4 and recruited to viral promoters by the SEC to induce viral gene expression<sup>97</sup>. Interestingly, BET inhibitor-mediated HCMV reactivation selectively induces expression of a limited subset of viral proteins that can trigger cytotoxic cell killing of latently infected cells without inducing viral DNA replication<sup>97</sup>. Thus, BET inhibitors have been proposed as a strategy to purge the latent HCMV reservoir.

Retroviruses such as human T-lymphotropic virus type 1 (HTLV-1) and human immunodeficiency virus type 1 (HIV-1) encode viral proteins that directly bind P-TEFb to sequester it for viral transcription. The Tax protein of HTLV-1 competes with BRD4L for binding the cyclin T1 subunit of P-TEFb<sup>99</sup>. Similar to BRD4L overexpression, Tax overexpression increases Pol II CTD phosphorylation, indicating that Tax is a positive regulator of P-TEFb. When BRD4L is overexpressed, Tax is no longer able to transactivate the LTR promoter<sup>99</sup>. Similarly, the Tat protein of HIV-1 recruits P-TEFb to stimulate viral transcription elongation at HIV-1 promoters<sup>28,100–104</sup>. Both Tax and Tat competitively bind P-TEFb as a mechanism to decrease the number of BRD4:P-TEFb complexes and redirect the host transcriptional machinery to viral genes. Interestingly, BRD4L can also activate P-TEFb to positively regulate basal HIV-1 transcription in a

Tat-independent manner <sup>105</sup>. The release of P-TEFb bound to BRD4L explains how BET inhibitors are able to reactivate HIV-1 from latency <sup>106</sup>.

On the other hand, BRD4S is a Tat-independent repressor of HIV-1 transcription [91]. BRD4S recruits BRG1, the catalytic subunit of the repressive BAF chromatin remodeling complex, to the LTR to repress HIV-1 transcription [88]. Specific knockdown of BRD4S alone can reactivate HIV-1 [88]. Strikingly, BRD4S and BRG1 share extensive overlap in chromatin occupancies genome-wide, notably enriched at class I (LINEs, SINEs, and LTRs) and II (DNA) transposon sequences [88]. The fact that BRD4S:BRG1 is enriched at endogenous LTR-containing sequences evolutionarily related to HIV-1 suggests that endogenous retroviral sequences share a common mechanism in recruiting the repressive function of this complex.

### **5.5. Unwilling Disruptors of Host Transcription**

During infection, the cellular transcriptome is dramatically reprogrammed. Cells are not only inundated with viral transcripts, but also shifting from maintaining homeostatic processes to producing antiviral and inflammatory mediators or shutting off cellular transcription to control viral infection. Inevitably, viruses have evolved to manipulate the host transcriptome to create a cell state that favors viral replication and spread.

The strategy employed by yellow fever virus (YFV) and SARS-CoV-2 to modulate host transcription is histone mimicry. Both YFV capsid and SARS-CoV-2 envelope (E) proteins contain a histone H4- or H3-like motif, respectively, with two lysine residues that can interact with BDs of BET protein when acetylated <sup>107–109</sup>. Interestingly, the

loss of YVF capsid:BRD4 interaction results in lower YFV infectivity and viral spread, suggesting the interaction optimizes the cell state for virion assembly and cell-to-cell spread <sup>107</sup>. The SARS-CoV-2 E:BRD4 interaction disrupts the function of BRD4 as a critical epigenetic regulator of innate immune genes <sup>108</sup>. E protein sequesters BRD4 and suppresses the expression of BRD4-regulated innate immune genes. The therapeutic use of BET inhibitors during infection further enhances viral replication and infectious particle production <sup>108</sup>. Additionally, the ET domain of BRD4 is predicted to bind a “K-X-K-X” motif in E protein in a BD-independent manner <sup>109</sup>. Other viruses known to manipulate the host’s transcription to their advantage include gammaherpesvirus 68 (MHV-68), whose orf73 interacts with the ET domains of BET proteins to activate cell cycle genes cyclin D2, D1 and E, and PV, whose E2 protein’s interaction with BRD4 regulates matrix metalloproteinase-9 (MMP-9) and c-Fos gene expression to create a cell state that is more favorable to PV-induced carcinogenesis<sup>59,110,111</sup>.

## 6. Conclusion

The shared domains of BET proteins with defined interaction motifs allow viruses to easily engage with multiple members of the family, effectively targeting specific functions of individual BET proteins at the same time. Several major modes of engagement across different viruses emerge: 1) YFV and SARS-CoV-2 proteins have acetylated lysine residues that mimic acetylated histones to dissociate BET proteins via BDs from chromatin. 2) Herpesvirus and polyomavirus engage ET domains for viral genome maintenance and MLV for integration site selection. 3) Many viruses exploit BRD4's ability to recruit the transcription complex P-TEFb not only for their own transcription, but also to modulate the host transcriptome and create a cell state favorable for infection and spread (Figure 1.2).

There is growing interest in using BET inhibitors as therapeutics for viral infection. They have been best studied in the context of HIV-1 eradication, where they act as latency reversing agents (LRAs) (further reviewed in <sup>112</sup>). The first BET inhibitor, JQ1, was a promising LRA *in vitro* and *ex vivo*, but is not a clinical candidate due to unfavorable pharmacokinetic properties <sup>106,113–115</sup>. Newer inhibitors, such as RXV-208, PF-1, and OTX-015, that demonstrate similar LRA potency in addition to having favorable oral bioavailability, fewer side effects, and synergistic effects with other LRAs, have yet to be evaluated *in vivo* <sup>116–119</sup>. BET inhibitors are also possible LRAs for latent HCMV and HSV infections and can limit growth of PV-, HCMV-, EBV-, and MCPyV-associated malignancies and diseases <sup>64,77,85,94,95,120</sup>. A caveat is that the use of BET inhibitors for non-viral indications in patients who harbor latent viruses

(herpesviruses, HBV, or retroviruses) could result in viral reactivation and undesirable outcomes.

The intricacies of BET proteins' functions in host transcriptional processes further complicate the use of pan-BET inhibitors. For example, BRD2 is a positive transcriptional regulator of SARS-CoV-2's entry receptor, angiotensin converting enzyme 2 (ACE2). When given prophylactically, BET inhibitors can reduce ACE2 expression to limit viral infection <sup>108,109,121–125</sup>. But the time point of application is critical as viral infection in cell lines and mortality of infected mice are exacerbated when BET inhibitors are given at the time of infection, due to their immuno-suppressive effects <sup>108</sup>. However, later in infection, the immuno-suppressive effect of BET inhibitors may be desirable as it could block cytokine production associated with COVID-19 cardiac dysfunction <sup>122</sup>. Currently, RVX-208 is under clinical investigation for COVID-19 (clinicaltrials.gov, NCT04894266). A very detailed clinical treatment protocol is needed to avoid negative effects of the drugs and take full advantage of the opportunities offered by BET inhibitors. Selective BET inhibitors may alleviate the issue as BRD2 is primarily involved in ACE2 downregulation, a function that could be selectively targeted.

Another solution may be offered by compounds that selectively target one bromodomain over the other. For example, BD2-specific inhibition preferentially blocks enhancer-driven, stimulus-mediated induction of gene expression programs without affecting pre-existing transcriptional programs, an advantage for diseases like COVID-19, where inflammatory or pro-fibrotic signaling are activated *de novo* <sup>47</sup>. By contrast,

pan- or BD1-specific inhibitors are more effective in disease states where extensive alteration of cellular programming occurs, such as cell proliferation and survival in cancer<sup>47,126</sup>. Furthermore, investigations into selectively targeting the phosphorylation sites of BRD4 offer a unique opportunity to specifically inhibit transcriptional programs mediated by PDID and NPS, such as BRD4:HPV E2, without disrupting broad chromatin-binding activity of BRD4<sup>127,128</sup>. The differential actions of specific domains in BET proteins may prove to be pivotal for better refinement of inhibitors and their therapeutic applications in viral diseases.

Despite growing interest and an impressive list of reports detailing virus-BET interactions, many open questions remain. For example, since viral proteins often only engage with a particular domain of a BET protein, can other domains normally engage with regular partners and still fulfill their functions? While many viral proteins are able to interact with more than one BET protein, most studies primarily focus on BRD4 as it is best understood. What consequences of the same interaction with BRD2 or BRD3 are we then overlooking? Despite these unknowns, our current understanding of virus-BET protein interactions underscore the importance of BET proteins in viral infection. Continued scrutiny of the BET proteins will yield a better understanding of the impact of viruses on their hosts and vice versa. It will also reveal the full picture of pro- and anti-viral functions of BET proteins and allow effective application of BET inhibitors to fight viral infections.

## **ACKNOWLEDGEMENTS**

We thank John Carroll for graphics, Françoise Chanut for editorial assistance, and Veronica Fonseca for administrative support. This work was supported by the National Institute of Allergy and Infectious Diseases: F31 AI164671-01 to I.P.C. and 5R01AI083139-07 to M.O.

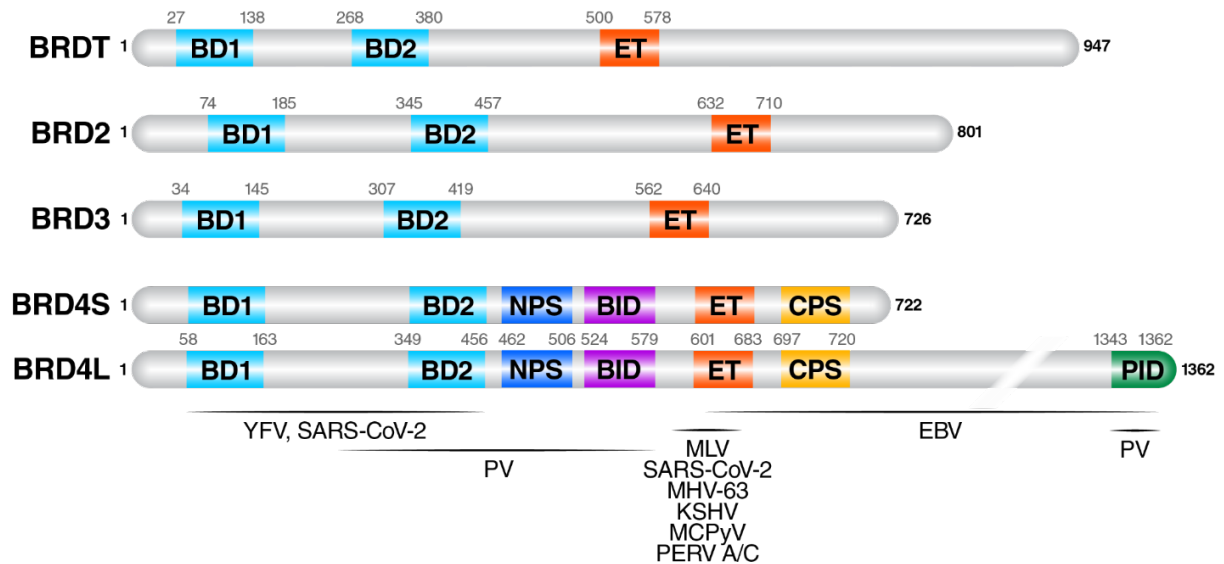


**Figure 1.1. BET protein family members.**

BRDT, BRD2, BRD3, and BRD4 are the four mammalian members of this family. The main functional domains and their amino acid positions are indicated: BD1 (bromodomain 1), BD2 (bromodomain 2), ET (extraterminal domain), PID (P-TEFb interacting domain), BID (basic residue-enriched domain), NPS (N-terminal phosphorylation site), and CPS (C-terminal phosphorylation site). Horizontal lines span the regions of BRD4 that directly interact with the viruses described in this review; note however that other BET proteins can also interact with viruses. See Table 1.1 for more information.



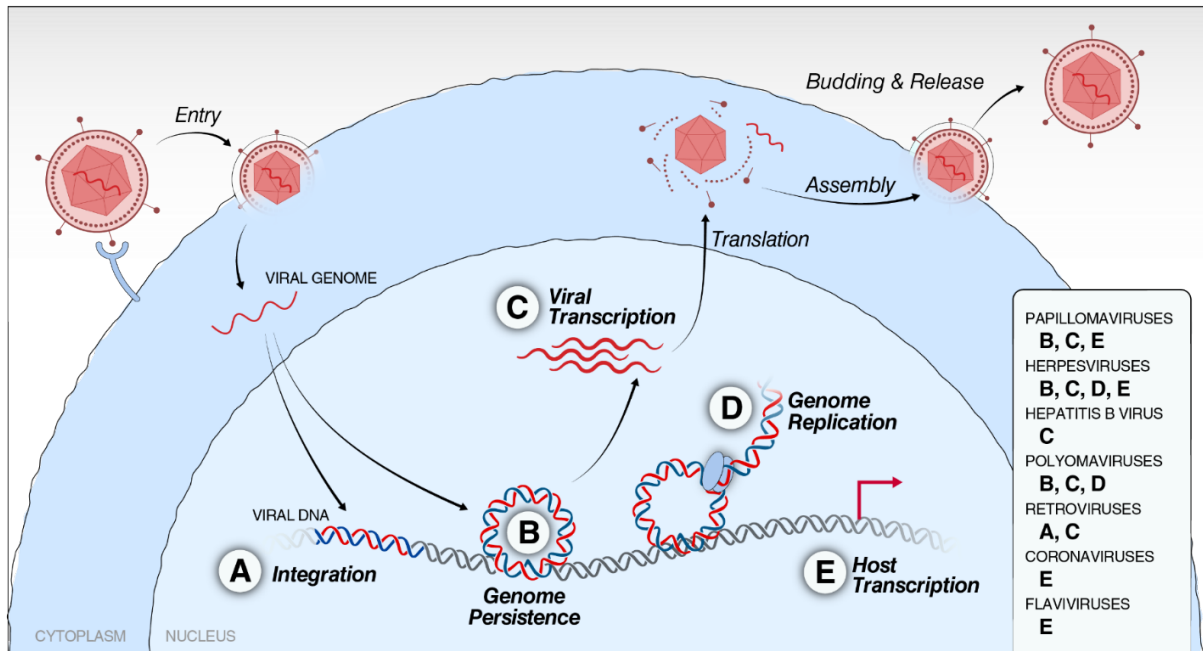


**Figure 1.2. Steps in a generic viral life cycle where BET proteins are involved.**

Many viruses interact with BET family members to mediate viral processes (A-D) and disrupt cellular transcription for their own benefit (E). A) Integration site selection of MLV, a gammaretrovirus, is facilitated by an interaction between its viral IN protein and BET proteins, leading to integration into genomic regions associated with BET proteins. B) PV, herpesviruses, and polyomaviruses take advantage of the association of BET proteins to host chromosomes to maintain their viral genomes in infected cells. C) Certain herpesviruses (EBV and HSV), PV, HBV, and polyomaviruses recruit the BRD4:P-TEFb complex to facilitate viral transcription, while retroviruses encode viral proteins that directly bind the PID of BRD4 to redirect host transcriptional machinery to the viral genes. D) Herpesviruses and polyomaviruses recruit BRD4 along with other host replication machinery, such as RFC or DNA polymerase  $\delta$ , facilitate genome replication at their replication foci. E) PV, Herpesviruses, SARS-CoV-2, and flaviviruses interact with BET proteins to disrupt homeostatic gene transcriptional programs controlled by BET proteins during infection to generate a cell state more favorable to viral replication and virus-induced carcinogenesis.

**Table 1.1. BET protein interactions with viruses.** Parentheses indicate punitive interaction domains. \* indicates viral genome regions. \*\* indicates indirect interaction, but competition for binding to P-TEFb.

Virus	Viral Protein/Genome	BET Protein	BET Domain	Functions	References
MLV	IN	BRD2, BRD3, BRD4	ET	Integration site selection	54–56
PERV A/C	IN	BRD2, BRD3, BRD4	ET	Integration cofactor	57
Papillomaviruses (HPV, CRPV, BPV)	E2	BRD4	C-terminus, NPS, BID	E2 stability, E2-mediated viral and host transcription, tethering viral genome to host chromatin	9,59,63–66
KSHV	LANA	BRD2, BRD3, BRD4	ET	Tethering viral genome to host chromatin, LANA-mediated viral and host transcription	6,71,129
MHV-68	orf73	BRD2, BRD3, BRD4	ET	Tethering viral genome to chromatin, orf73-mediated host transcription	111
EBV	EBNA1 OriLyt*	BRD2, BRD3, BRD4	(C-terminus)	EBNA1-mediated viral transcription, tethering viral genome to host chromatin	74,85
HCMV	HCMV promoters*	BRD4	PID	Competence for P-TEFb	97,98
MCPyV	LT	BRD4	ET	Viral genome replication	77
JCPyV	NCRR*	BRD4	(BDs, PID)	Viral transcription and genome replication	78
RacPyV	RacPyV genome*	BRD4	(BDs, PID)	Viral transcription and genome replication, tether genome to host chromatin	75
HBV	HBV genome*	BRD4	BD-independent	Viral transcription	93
HTLV-1	Tax**	BRD4	PID	Competence for P-TEFb	57,99
HIV	Tat** LTR*	BRD4	PID BDs	Competence for P-TEFb Tat-mediated transcription, enforce viral latency	103,105,106,130,131
YFV	Capsid	BRD2,	BDs	Host transcription	107

<b>Virus</b>	<b>Viral Protein/Genome</b>	<b>BET Protein</b>	<b>BET Domain</b>	<b>Functions</b>	<b>References</b>
		BRD3, BRD4			
SARS-CoV-2	E	BRD2, BRD4	BDs, ET	Host transcription	108,109

## REFERENCES

1. Kulikowski, E., Rakai, B.D., and Wong, N.C.W. (2021). Inhibitors of bromodomain and extra-terminal proteins for treating multiple human diseases. *Med. Res. Rev.* *41*, 223–245.
2. Patel, K., Solomon, P.D., Walshe, J.L., Ford, D.J., Wilkinson-White, L., Payne, R.J., Low, J.K.K., and Mackay, J.P. (2021). BET-Family Bromodomains Can Recognize Diacetylated Sequences from Transcription Factors Using a Conserved Mechanism. *Biochemistry* *60*, 648–662.
3. Lambert, J.-P., Picaud, S., Fujisawa, T., Hou, H., Savitsky, P., Uusküla-Reimand, L., Gupta, G.D., Abdouni, H., Lin, Z.-Y., Tucholska, M., et al. (2019). Interactome Rewiring Following Pharmacological Targeting of BET Bromodomains. *Mol. Cell* *73*, 621–638.e17.
4. Dhalluin, C., Carlson, J.E., Zeng, L., He, C., Aggarwal, A.K., and Zhou, M.M. (1999). Structure and ligand of a histone acetyltransferase bromodomain. *Nature* *399*, 491–496.
5. Josling, G.A., Selvarajah, S.A., Petter, M., and Duffy, M.F. (2012). The role of bromodomain proteins in regulating gene expression. *Genes* *3*, 320–343.
6. Wai, D.C.C., Szyszka, T.N., Campbell, A.E., Kwong, C., Wilkinson-White, L.E., Silva, A.P.G., Low, J.K.K., Kwan, A.H., Gamsjaeger, R., Chalmers, J.D., et al. (2018). The BRD3 ET domain recognizes a short peptide motif through a mechanism that is conserved across chromatin remodelers and transcriptional regulators. *J. Biol. Chem.* *293*, 7160–7175.

7. Schröder, S., Cho, S., Zeng, L., Zhang, Q., Kaehlcke, K., Mak, L., Lau, J., Bisgrove, D., Schnölzer, M., Verdin, E., et al. (2012). Two-pronged binding with bromodomain-containing protein 4 liberates positive transcription elongation factor b from inactive ribonucleoprotein complexes. *J. Biol. Chem.* *287*, 1090–1099.
8. Sawa, C., Nedeá, E., Krogan, N., Wada, T., Handa, H., Greenblatt, J., and Buratowski, S. (2004). Bromodomain factor 1 (Bdf1) is phosphorylated by protein kinase CK2. *Mol. Cell. Biol.* *24*, 4734–4742.
9. Wu, S.-Y., Nin, D.S., Lee, A.-Y., Simanski, S., Kodadek, T., and Chiang, C.-M. (2016). BRD4 Phosphorylation Regulates HPV E2-Mediated Viral Transcription, Origin Replication, and Cellular MMP-9 Expression. *Cell Rep.* *16*, 1733–1748.
10. Wu, S.-Y., Lee, A.-Y., Lai, H.-T., Zhang, H., and Chiang, C.-M. (2013). Phospho switch triggers Brd4 chromatin binding and activator recruitment for gene-specific targeting. *Mol. Cell* *49*, 843–857.
11. Malvezzi, F., Stubbs, C.J., Jowitt, T.A., Dale, I.L., Guo, X., DeGnore, J.P., Degliesposti, G., Skehel, J.M., Bannister, A.J., and McAlister, M.S. (2021). Phosphorylation-dependent BRD4 dimerization and implications for therapeutic inhibition of BET family proteins. *Commun Biol* *4*, 1273.
12. Garcia-Gutierrez, P., Mundi, M., and Garcia-Dominguez, M. (2012). Association of bromodomain BET proteins with chromatin requires dimerization through the conserved motif B. *J. Cell Sci.* *125*, 3671–3680.
13. Cheung, K.L., Kim, C., and Zhou, M.-M. (2021). The Functions of BET Proteins

- in Gene Transcription of Biology and Diseases. *Front Mol Biosci* 8, 728777.
14. Wang, N., Wu, R., Tang, D., and Kang, R. (2021). The BET family in immunity and disease. *Signal Transduct Target Ther* 6, 23.
  15. Denis, G.V., and Green, M.R. (1996). A novel, mitogen-activated nuclear kinase is related to a *Drosophila* developmental regulator. *Genes Dev.* 10, 261–271.
  16. Denis, G.V., Vaziri, C., Guo, N., and Faller, D.V. (2000). RING3 kinase transactivates promoters of cell cycle regulatory genes through E2F. *Cell Growth Differ.* 11, 417–424.
  17. Xu, L., Chen, Y., Mayakonda, A., Koh, L., Chong, Y.K., Buckley, D.L., Sandanaraj, E., Lim, S.W., Lin, R.Y.-T., Ke, X.-Y., et al. (2018). Targetable BET proteins- and E2F1-dependent transcriptional program maintains the malignancy of glioblastoma. *Proc. Natl. Acad. Sci. U. S. A.* 115, E5086–E5095.
  18. LeRoy, G., Rickards, B., and Flint, S.J. (2008). The double bromodomain proteins Brd2 and Brd3 couple histone acetylation to transcription. *Mol. Cell* 30, 51–60.
  19. Denis, G.V., McComb, M.E., Faller, D.V., Sinha, A., Romesser, P.B., and Costello, C.E. (2006). Identification of transcription complexes that contain the double bromodomain protein Brd2 and chromatin remodeling machines. *J. Proteome Res.* 5, 502–511.
  20. Wang, J., Tadeo, X., Hou, H., Tu, P.G., Thompson, J., Yates, J.R., 3rd, and Jia, S. (2013). Epe1 recruits BET family bromodomain protein Bdf2 to establish heterochromatin boundaries. *Genes Dev.* 27, 1886–1902.

21. Hsu, S.C., Gilgenast, T.G., Bartman, C.R., Edwards, C.R., Stonestrom, A.J., Huang, P., Emerson, D.J., Evans, P., Werner, M.T., Keller, C.A., et al. (2017). The BET Protein BRD2 Cooperates with CTCF to Enforce Transcriptional and Architectural Boundaries. *Mol. Cell* 66, 102–116.e7.
22. Lamonica, J.M., Deng, W., Kadauke, S., Campbell, A.E., Gamsjaeger, R., Wang, H., Cheng, Y., Billin, A.N., Hardison, R.C., Mackay, J.P., et al. (2011). Bromodomain protein Brd3 associates with acetylated GATA1 to promote its chromatin occupancy at erythroid target genes. *Proc. Natl. Acad. Sci. U. S. A.* 108, E159–E168.
23. Gamsjaeger, R., Webb, S.R., Lamonica, J.M., Billin, A., Blobel, G.A., and Mackay, J.P. (2011). Structural basis and specificity of acetylated transcription factor GATA1 recognition by BET family bromodomain protein Brd3. *Mol. Cell Biol.* 31, 2632–2640.
24. Stonestrom, A.J., Hsu, S.C., Jahn, K.S., Huang, P., Keller, C.A., Giardine, B.M., Kadauke, S., Campbell, A.E., Evans, P., Hardison, R.C., et al. (2015). Functions of BET proteins in erythroid gene expression. *Blood* 125, 2825–2834.
25. Daneshvar, K., Ardehali, M.B., Klein, I.A., Hsieh, F.-K., Kratkiewicz, A.J., Mahpour, A., Cancelliere, S.O.L., Zhou, C., Cook, B.M., Li, W., et al. (2020). lncRNA DIGIT and BRD3 protein form phase-separated condensates to regulate endoderm differentiation. *Nat. Cell Biol.* 22, 1211–1222.
26. Zhao, R., Nakamura, T., Fu, Y., Lazar, Z., and Spector, D.L. (2011). Gene bookmarking accelerates the kinetics of post-mitotic transcriptional re-activation.

Nat. Cell Biol. *13*, 1295–1304.

27. Dey, A., Ellenberg, J., Farina, A., Coleman, A.E., Maruyama, T., Sciortino, S., Lippincott-Schwartz, J., and Ozato, K. (2000). A bromodomain protein, MCAP, associates with mitotic chromosomes and affects G(2)-to-M transition. *Mol. Cell Biol.* *20*, 6537–6549.
28. Jang, M.K., Mochizuki, K., Zhou, M., Jeong, H.-S., Brady, J.N., and Ozato, K. (2005). The bromodomain protein Brd4 is a positive regulatory component of P-TEFb and stimulates RNA polymerase II-dependent transcription. *Mol. Cell* *19*, 523–534.
29. Devaiah, B.N., Lewis, B.A., Cherman, N., Hewitt, M.C., Albrecht, B.K., Robey, P.G., Ozato, K., Sims, R.J., 3rd, and Singer, D.S. (2012). BRD4 is an atypical kinase that phosphorylates serine2 of the RNA polymerase II carboxy-terminal domain. *Proc. Natl. Acad. Sci. U. S. A.* *109*, 6927–6932.
30. Rahman, S., Sowa, M.E., Ottinger, M., Smith, J.A., Shi, Y., Harper, J.W., and Howley, P.M. (2011). The Brd4 extraterminal domain confers transcription activation independent of pTEFb by recruiting multiple proteins, including NSD3. *Mol. Cell Biol.* *31*, 2641–2652.
31. Sakamaki, J.-I., Wilkinson, S., Hahn, M., Tasdemir, N., O'Prey, J., Clark, W., Hedley, A., Nixon, C., Long, J.S., New, M., et al. (2017). Bromodomain Protein BRD4 Is a Transcriptional Repressor of Autophagy and Lysosomal Function. *Mol. Cell* *66*, 517–532.e9.
32. Devaiah, B.N., Case-Borden, C., Gegonne, A., Hsu, C.H., Chen, Q., Meerzaman,



- D., Dey, A., Ozato, K., and Singer, D.S. (2016). BRD4 is a histone acetyltransferase that evicts nucleosomes from chromatin. *Nat. Struct. Mol. Biol.* *23*, 540–548.
33. Vershinin, Z., Feldman, M., Werner, T., Weil, L.E., Kublanovsky, M., Abaev-Schneiderman, E., Sklarz, M., Lam, E.Y.N., Alasad, K., Picaud, S., et al. (2021). BRD4 methylation by the methyltransferase SETD6 regulates selective transcription to control mRNA translation. *Sci Adv* *7*. 10.1126/sciadv.abf5374.
34. Erber, L., Luo, A., and Chen, Y. (2019). Targeted and Interactome Proteomics Revealed the Role of PHD2 in Regulating BRD4 Proline Hydroxylation. *Mol. Cell. Proteomics* *18*, 1772–1781.
35. Jin, X., Yan, Y., Wang, D., Ding, D., Ma, T., Ye, Z., Jimenez, R., Wang, L., Wu, H., and Huang, H. (2018). DUB3 Promotes BET Inhibitor Resistance and Cancer Progression by Deubiquitinating BRD4. *Mol. Cell* *71*, 592–605.e4.
36. Li, X., Baek, G., Ramanand, S.G., Sharp, A., Gao, Y., Yuan, W., Welti, J., Rodrigues, D.N., Dolling, D., Figueiredo, I., et al. (2018). BRD4 Promotes DNA Repair and Mediates the Formation of TMPRSS2-ERG Gene Rearrangements in Prostate Cancer. *Cell Rep.* *22*, 796–808.
37. Stanlie, A., Yousif, A.S., Akiyama, H., Honjo, T., and Begum, N.A. (2014). Chromatin reader Brd4 functions in Ig class switching as a repair complex adaptor of nonhomologous end-joining. *Mol. Cell* *55*, 97–110.
38. Floyd, S.R., Pacold, M.E., Huang, Q., Clarke, S.M., Lam, F.C., Cannell, I.G., Bryson, B.D., Rameseder, J., Lee, M.J., Blake, E.J., et al. (2013). The

- bromodomain protein Brd4 insulates chromatin from DNA damage signalling. *Nature* *498*, 246–250.
39. Tang, P., Zhang, J., Liu, J., Chiang, C.-M., and Ouyang, L. (2021). Targeting Bromodomain and Extraterminal Proteins for Drug Discovery: From Current Progress to Technological Development. *J. Med. Chem.* *64*, 2419–2435.
  40. Filippakopoulos, P., Qi, J., Picaud, S., Shen, Y., Smith, W.B., Fedorov, O., Morse, E.M., Keates, T., Hickman, T.T., Felletar, I., et al. (2010). Selective inhibition of BET bromodomains. *Nature* *468*, 1067–1073.
  41. Boi, M., Gaudio, E., Bonetti, P., Kwee, I., Bernasconi, E., Tarantelli, C., Rinaldi, A., Testoni, M., Cascione, L., Ponzoni, M., et al. (2015). The BET Bromodomain Inhibitor OTX015 Affects Pathogenetic Pathways in Preclinical B-cell Tumor Models and Synergizes with Targeted Drugs. *Clinical Cancer Research* *21*, 1628–1638. 10.1158/1078-0432.ccr-14-1561.
  42. Baldan, F., Allegri, L., Lazarevic, M., Catia, M., Milosevic, M., Damante, G., and Milasin, J. (2019). Biological and molecular effects of bromodomain and extra-terminal (BET) inhibitors JQ1, IBET-151, and IBET-762 in OSCC cells. *J. Oral Pathol. Med.* *48*, 214–221.
  43. Zeng, L., and Zhou, M.M. (2002). Bromodomain: an acetyl-lysine binding domain. *FEBS Lett.* *513*, 124–128.
  44. Meslamani, J., Smith, S.G., Sanchez, R., and Zhou, M.-M. (2016). Structural features and inhibitors of bromodomains. *Drug Discov. Today Technol.* *19*, 3–15.
  45. Rodríguez, Y., Gerona-Navarro, G., Osman, R., and Zhou, M.-M. (2020). In silico

design and molecular basis for the selectivity of Olinone toward the first over the second bromodomain of BRD4. *Proteins* 88, 414–430.

46. Gacias, M., Gerona-Navarro, G., Plotnikov, A.N., Zhang, G., Zeng, L., Kaur, J., Moy, G., Rusinova, E., Rodriguez, Y., Matikainen, B., et al. (2014). Selective chemical modulation of gene transcription favors oligodendrocyte lineage progression. *Chem. Biol.* 21, 841–854.
47. Gilan, O., Rioja, I., Knezevic, K., Bell, M.J., Yeung, M.M., Harker, N.R., Lam, E.Y.N., Chung, C.-W., Bamborough, P., Petretich, M., et al. (2020). Selective targeting of BD1 and BD2 of the BET proteins in cancer and immunoinflammation. *Science* 368, 387–394.
48. Lin, X., Huang, X., Bellin, R., Faivre, E., Hessler, P., Lam, L., Bui, M.H., Wilcox, D., Uziel, T., Ferguson, D.C., et al. (2018). Abstract 800: ABBV-744, a first-in-class and highly selective inhibitor of the second bromodomain of BET family proteins, displays robust activities in preclinical models of acute myelogenous leukemia. *Cancer Res.* 78, 800–800.
49. McLure, K.G., Gesner, E.M., Tsujikawa, L., Kharenko, O.A., Attwell, S., Campeau, E., Wasiak, S., Stein, A., White, A., Fontano, E., et al. (2013). RVX-208, an inducer of ApoA-I in humans, is a BET bromodomain antagonist. *PLoS One* 8, e83190.
50. Lu, J., Qian, Y., Altieri, M., Dong, H., Wang, J., Raina, K., Hines, J., Winkler, J.D., Crew, A.P., Coleman, K., et al. (2015). Hijacking the E3 Ubiquitin Ligase Cereblon to Efficiently Target BRD4. *Chem. Biol.* 22, 755–763.

51. Winter, G.E., Mayer, A., Buckley, D.L., Erb, M.A., Roderick, J.E., Vittori, S., Reyes, J.M., di Iulio, J., Souza, A., Ott, C.J., et al. (2017). BET Bromodomain Proteins Function as Master Transcription Elongation Factors Independent of CDK9 Recruitment. *Mol. Cell* *67*, 5–18.e19.
52. Zhou, B., Hu, J., Xu, F., Chen, Z., Bai, L., Fernandez-Salas, E., Lin, M., Liu, L., Yang, C.-Y., Zhao, Y., et al. (2018). Discovery of a Small-Molecule Degradator of Bromodomain and Extra-Terminal (BET) Proteins with Picomolar Cellular Potencies and Capable of Achieving Tumor Regression. *Journal of Medicinal Chemistry* *61*, 462–481. 10.1021/acs.jmedchem.6b01816.
53. Wu, X., Li, Y., Crise, B., and Burgess, S.M. (2003). Transcription start regions in the human genome are favored targets for MLV integration. *Science* *300*, 1749–1751.
54. Gupta, S.S., Maetzig, T., Maertens, G.N., Sharif, A., Rothe, M., Weidner-Glunde, M., Galla, M., Schambach, A., Cherepanov, P., and Schulz, T.F. (2013). Bromo- and extraterminal domain chromatin regulators serve as cofactors for murine leukemia virus integration. *J. Virol.* *87*, 12721–12736.
55. De Rijck, J., de Kogel, C., Demeulemeester, J., Vets, S., El Ashkar, S., Malani, N., Bushman, F.D., Landuyt, B., Husson, S.J., Busschots, K., et al. (2013). The BET family of proteins targets moloney murine leukemia virus integration near transcription start sites. *Cell Rep.* *5*, 886–894.
56. Sharma, A., Larue, R.C., Plumb, M.R., Malani, N., Male, F., Slaughter, A., Kessler, J.J., Shkriabai, N., Coward, E., Aiyer, S.S., et al. (2013). BET proteins promote

- efficient murine leukemia virus integration at transcription start sites. *Proc. Natl. Acad. Sci. U. S. A.* *110*, 12036–12041.
57. Gallay, K., Blot, G., Chahpazoff, M., Yajjou-Hamalian, H., Confort, M.-P., De Boissésou, C., Leroux, A., Luengo, C., Fiorini, F., Lavigne, M., et al. (2019). In vitro, in cellulo and structural characterizations of the interaction between the integrase of Porcine Endogenous Retrovirus A/C and proteins of the BET family. *Virology* *532*, 69–81.
58. Serrao, E., Ballandras-Colas, A., Cherepanov, P., Maertens, G.N., and Engelman, A.N. (2015). Key determinants of target DNA recognition by retroviral intasomes. *Retrovirology* *12*, 39.
59. Iftner, T., Haedicke-Jarboui, J., Wu, S.-Y., and Chiang, C.-M. (2017). Involvement of Brd4 in different steps of the papillomavirus life cycle. *Virus Res.* *231*, 76–82.
60. Abbate, E.A., Voitenleitner, C., and Botchan, M.R. (2006). Structure of the papillomavirus DNA-tethering complex E2:Brd4 and a peptide that ablates HPV chromosomal association. *Mol. Cell* *24*, 877–889.
61. Muller, M., Jacob, Y., Jones, L., Weiss, A., Brino, L., Chantier, T., Lotteau, V., Favre, M., and Demeret, C. (2012). Large scale genotype comparison of human papillomavirus E2-host interaction networks provides new insights for e2 molecular functions. *PLoS Pathog.* *8*, e1002761.
62. Oliveira, J.G., Colf, L.A., and McBride, A.A. (2006). Variations in the association of papillomavirus E2 proteins with mitotic chromosomes. *Proc. Natl. Acad. Sci. U. S. A.* *103*, 1047–1052.

63. Baxter, M.K., McPhillips, M.G., Ozato, K., and McBride, A.A. (2005). The mitotic chromosome binding activity of the papillomavirus E2 protein correlates with interaction with the cellular chromosomal protein, Brd4. *J. Virol.* *79*, 4806–4818.
64. Morse, M.A., Balogh, K.K., Brendle, S.A., Campbell, C.A., Chen, M.X., Furze, R.C., Harada, I.L., Holyer, I.D., Kumar, U., Lee, K., et al. (2018). BET bromodomain inhibitors show anti-papillomavirus activity in vitro and block CRPV wart growth in vivo. *Antiviral Res.* *154*, 158–165.
65. Ilves, I., Mäemets, K., Silla, T., Janikson, K., and Ustav, M. (2006). Brd4 is involved in multiple processes of the bovine papillomavirus type 1 life cycle. *J. Virol.* *80*, 3660–3665.
66. You, J., Schweiger, M.-R., and Howley, P.M. (2005). Inhibition of E2 binding to Brd4 enhances viral genome loss and phenotypic reversion of bovine papillomavirus-transformed cells. *J. Virol.* *79*, 14956–14961.
67. McPhillips, M.G., Oliveira, J.G., Spindler, J.E., Mitra, R., and McBride, A.A. (2006). Brd4 is required for e2-mediated transcriptional activation but not genome partitioning of all papillomaviruses. *J. Virol.* *80*, 9530–9543.
68. McBride, A.A., and Jang, M.K. (2013). Current understanding of the role of the Brd4 protein in the papillomavirus lifecycle. *Viruses* *5*, 1374–1394.
69. Poddar, A., Reed, S.C., McPhillips, M.G., Spindler, J.E., and McBride, A.A. (2009). The human papillomavirus type 8 E2 tethering protein targets the ribosomal DNA loci of host mitotic chromosomes. *J. Virol.* *83*, 640–650.
70. Donaldson, M.M., Boner, W., and Morgan, I.M. (2007). TopBP1 regulates human

- papillomavirus type 16 E2 interaction with chromatin. *J. Virol.* *81*, 4338–4342.
71. You, J., Srinivasan, V., Denis, G.V., Harrington, W.J., Jr, Ballestas, M.E., Kaye, K.M., and Howley, P.M. (2006). Kaposi's sarcoma-associated herpesvirus latency-associated nuclear antigen interacts with bromodomain protein Brd4 on host mitotic chromosomes. *J. Virol.* *80*, 8909–8919.
72. Mattsson, K., Kiss, C., Platt, G.M., Simpson, G.R., Kashuba, E., Klein, G., Schulz, T.F., and Szekely, L. (2002). Latent nuclear antigen of Kaposi's sarcoma herpesvirus/human herpesvirus-8 induces and relocates RING3 to nuclear heterochromatin regions. *J. Gen. Virol.* *83*, 179–188.
73. Szekely, L., Kiss, C., Mattsson, K., Kashuba, E., Pokrovskaja, K., Juhasz, A., Holmvall, P., and Klein, G. (1999). Human herpesvirus-8-encoded LNA-1 accumulates in heterochromatin-associated nuclear bodies. *J. Gen. Virol.* *80* (Pt 11), 2889–2900.
74. Lin, A., Wang, S., Nguyen, T., Shire, K., and Frappier, L. (2008). The EBNA1 protein of Epstein-Barr virus functionally interacts with Brd4. *J. Virol.* *82*, 12009–12019.
75. Church, M.E., Estrada, M., Leutenegger, C.M., Dela Cruz, F.N., Pesavento, P.A., and Woolard, K.D. (2016). BRD4 is associated with raccoon polyomavirus genome and mediates viral gene transcription and maintenance of a stem cell state in neuroglial tumour cells. *J. Gen. Virol.* *97*, 2939–2948.
76. Decaprio J. A., Imperiale M. J., Major E. O. (2013). Polyomaviruses. In *Fields Virology*, Peter M. Howley MD, David M. Knipe PhD, Jeffrey L. Cohen, Blossom

- A. Damania, ed. (WOLTERS KLUWER), pp. 1633–1661.
77. Wang, X., Li, J., Schowalter, R.M., Jiao, J., Buck, C.B., and You, J. (2012). Bromodomain protein Brd4 plays a key role in Merkel cell polyomavirus DNA replication. *PLoS Pathog.* *8*, e1003021.
  78. Wollebo, H.S., Bellizzi, A., Cossari, D.H., Salkind, J., Safak, M., and White, M.K. (2016). The Brd4 acetyllysine-binding protein is involved in activation of polyomavirus JC. *J. Neurovirol.* *22*, 615–625.
  79. Sakakibara, N., Chen, D., and McBride, A.A. (2013). Papillomaviruses use recombination-dependent replication to vegetatively amplify their genomes in differentiated cells. *PLoS Pathog.* *9*, e1003321.
  80. Gillespie, K.A., Mehta, K.P., Laimins, L.A., and Moody, C.A. (2012). Human papillomaviruses recruit cellular DNA repair and homologous recombination factors to viral replication centers. *J. Virol.* *86*, 9520–9526.
  81. Moody, C.A., and Laimins, L.A. (2009). Human papillomaviruses activate the ATM DNA damage pathway for viral genome amplification upon differentiation. *PLoS Pathog.* *5*, e1000605.
  82. Wang, X., Helfer, C.M., Pancholi, N., Bradner, J.E., and You, J. (2013). Recruitment of Brd4 to the human papillomavirus type 16 DNA replication complex is essential for replication of viral DNA. *J. Virol.* *87*, 3871–3884.
  83. DeSmet, M., Jose, L., Isaq, N., and Androphy, E.J. (2019). Phosphorylation of a Conserved Tyrosine in the Papillomavirus E2 Protein Regulates Brd4 Binding and Viral Replication. *J. Virol.* *93*. 10.1128/JVI.01801-18.



84. Sakakibara, N., Chen, D., Jang, M.K., Kang, D.W., Luecke, H.F., Wu, S.-Y., Chiang, C.-M., and McBride, A.A. (2013). Brd4 is displaced from HPV replication factories as they expand and amplify viral DNA. *PLoS Pathog.* *9*, e1003777.
85. Keck, K.M., Moquin, S.A., He, A., Fernandez, S.G., Somberg, J.J., Liu, S.M., Martinez, D.M., and Miranda, J.L. (2017). Bromodomain and extraterminal inhibitors block the Epstein-Barr virus lytic cycle at two distinct steps. *J. Biol. Chem.* *292*, 13284–13295.
86. Chin, M.T., Hirochika, R., Hirochika, H., Broker, T.R., and Chow, L.T. (1988). Regulation of human papillomavirus type 11 enhancer and E6 promoter by activating and repressing proteins from the E2 open reading frame: functional and biochemical studies. *J. Virol.* *62*, 2994–3002.
87. Cripe, T.P., Haugen, T.H., Turk, J.P., Tabatabai, F., Schmid, P.G., 3rd, Dürst, M., Gissmann, L., Roman, A., and Turek, L.P. (1987). Transcriptional regulation of the human papillomavirus-16 E6-E7 promoter by a keratinocyte-dependent enhancer, and by viral E2 trans-activator and repressor gene products: implications for cervical carcinogenesis. *EMBO J.* *6*, 3745–3753.
88. Spalholz, B.A., Yang, Y.C., and Howley, P.M. (1985). Transactivation of a bovine papilloma virus transcriptional regulatory element by the E2 gene product. *Cell* *42*, 183–191.
89. Helfer, C.M., Yan, J., and You, J. (2014). The cellular bromodomain protein Brd4 has multiple functions in E2-mediated papillomavirus transcription activation. *Viruses* *6*, 3228–3249.

90. Sénéchal, H., Poirier, G.G., Coulombe, B., Laimins, L.A., and Archambault, J. (2007). Amino acid substitutions that specifically impair the transcriptional activity of papillomavirus E2 affect binding to the long isoform of Brd4. *Virology* *358*, 10–17. 10.1016/j.virol.2006.08.035.
91. Schweiger, M.-R., You, J., and Howley, P.M. (2006). Bromodomain protein 4 mediates the papillomavirus E2 transcriptional activation function. *J. Virol.* *80*, 4276–4285.
92. Schweiger, M.-R., Ottinger, M., You, J., and Howley, P.M. (2007). Brd4-independent transcriptional repression function of the papillomavirus e2 proteins. *J. Virol.* *81*, 9612–9622.
93. Francisco, J.C., Dai, Q., Luo, Z., Wang, Y., Chong, R.H.-H., Tan, Y.J., Xie, W., Lee, G.-H., and Lin, C. (2017). Transcriptional Elongation Control of Hepatitis B Virus Covalently Closed Circular DNA Transcription by Super Elongation Complex and BRD4. *Mol. Cell. Biol.* *37*. 10.1128/MCB.00040-17.
94. Groves, I.J., Sinclair, J.H., and Wills, M.R. (2020). Bromodomain Inhibitors as Therapeutics for Herpesvirus-Related Disease: All BETs Are Off? *Front. Cell. Infect. Microbiol.* *10*, 329.
95. Ren, K., Zhang, W., Chen, X., Ma, Y., Dai, Y., Fan, Y., Hou, Y., Tan, R.X., and Li, E. (2016). An Epigenetic Compound Library Screen Identifies BET Inhibitors That Promote HSV-1 and -2 Replication by Bridging P-TEFb to Viral Gene Promoters through BRD4. *PLoS Pathog.* *12*, e1005950.
96. Alfonso-Dunn, R., Turner, A.-M.W., Jean Beltran, P.M., Arbuckle, J.H.,

- Budayeva, H.G., Cristea, I.M., and Kristie, T.M. (2017). Transcriptional Elongation of HSV Immediate Early Genes by the Super Elongation Complex Drives Lytic Infection and Reactivation from Latency. *Cell Host Microbe* *21*, 507–517.e5.
97. Groves, I.J., Jackson, S.E., Poole, E.L., Nachshon, A., Rozman, B., Schwartz, M., Prinjha, R.K., Tough, D.F., Sinclair, J.H., and Wills, M.R. (2021). Bromodomain proteins regulate human cytomegalovirus latency and reactivation allowing epigenetic therapeutic intervention. *Proc. Natl. Acad. Sci. U. S. A.* *118*. 10.1073/pnas.2023025118.
98. Kapasi, A.J., and Spector, D.H. (2008). Inhibition of the cyclin-dependent kinases at the beginning of human cytomegalovirus infection specifically alters the levels and localization of the RNA polymerase II carboxyl-terminal domain kinases cdk9 and cdk7 at the viral transcriptosome. *J. Virol.* *82*, 394–407.
99. Zhou, M., Lu, H., Park, H., Wilson-Chiru, J., Linton, R., and Brady, J.N. (2006). Tax interacts with P-TEFb in a novel manner to stimulate human T-lymphotropic virus type 1 transcription. *J. Virol.* *80*, 4781–4791.
100. Yang, Z., Yik, J.H.N., Chen, R., He, N., Jang, M.K., Ozato, K., and Zhou, Q. (2005). Recruitment of P-TEFb for stimulation of transcriptional elongation by the bromodomain protein Brd4. *Mol. Cell* *19*, 535–545.
101. Huo, L., Li, D., Sun, X., Shi, X., Karna, P., Yang, W., Liu, M., Qiao, W., Aneja, R., and Zhou, J. (2011). Regulation of Tat acetylation and transactivation activity by the microtubule-associated deacetylase HDAC6. *J. Biol. Chem.* *286*, 9280–9286.

102. Kiernan, R.E., Vanhulle, C., Schiltz, L., Adam, E., Xiao, H., Maudoux, F., Calomme, C., Burny, A., Nakatani, Y., Jeang, K.-T., et al. (1999). HIV-1 Tat transcriptional activity is regulated by acetylation. *EMBO J.* *18*, 6106–6118.
103. Ott, M., Schnölzer, M., Garnica, J., Fischle, W., Emiliani, S., Rackwitz, H.R., and Verdin, E. (1999). Acetylation of the HIV-1 Tat protein by p300 is important for its transcriptional activity. *Curr. Biol.* *9*, 1489–1492.
104. Pagans, S., Pedal, A., North, B.J., Kaehlcke, K., Marshall, B.L., Dorr, A., Hetzer-Egger, C., Henklein, P., Frye, R., McBurney, M.W., et al. (2005). SIRT1 regulates HIV transcription via Tat deacetylation. *PLoS Biol.* *3*, e41.
105. Bisgrove, D.A., Mahmoudi, T., Henklein, P., and Verdin, E. (2007). Conserved P-TEFb-interacting domain of BRD4 inhibits HIV transcription. *Proc. Natl. Acad. Sci. U. S. A.* *104*, 13690–13695.
106. Boehm, D., Calvanese, V., Dar, R.D., Xing, S., Schroeder, S., Martins, L., Aull, K., Li, P.-C., Planelles, V., Bradner, J.E., et al. (2013). BET bromodomain-targeting compounds reactivate HIV from latency via a Tat-independent mechanism. *Cell Cycle* *12*, 452–462.
107. Mourão, D., Chen, S., Schaefer, U., Bozzacco, L., Carneiro, L.A., Gerber, A., Adura, C., Dill, B.D., Molina, H., Carroll, T., et al. (2020). A histone-like motif in yellow fever virus contributes to viral replication. *bioRxiv*, 2020.05.05.078782. 10.1101/2020.05.05.078782.
108. Chen, I.P., Longbotham, J.E., McMahon, S., Suryawanshi, R.K., Khalid, M.M., Taha, T.Y., Tabata, T., Hayashi, J.M., Soveg, F.W., Carlson-Stevermer, J., et al.

- (2022). Viral E Protein Neutralizes BET Protein-Mediated Post-Entry Antagonism of SARS-CoV-2. *Cell Rep.*, 111088.
109. Vann, K.R., Acharya, A., Jang, S.M., Lachance, C., Zandian, M., Holt, T.A., Smith, A.L., Pandey, K., Durden, D.L., El-Gamal, D., et al. (2022). Binding of the SARS-CoV-2 envelope E protein to human BRD4 is essential for infection. *Structure*. 10.1016/j.str.2022.05.020.
110. de Wilde, J., De-Castro Arce, J., Snijders, P.J.F., Meijer, C.J.L.M., Rösl, F., and Steenbergen, R.D.M. (2008). Alterations in AP-1 and AP-1 regulatory genes during HPV-induced carcinogenesis. *Cell. Oncol.* 30, 77–87.
111. Ottinger, M., Pliquet, D., Christalla, T., Frank, R., Stewart, J.P., and Schulz, T.F. (2009). The interaction of the gammaherpesvirus 68 orf73 protein with cellular BET proteins affects the activation of cell cycle promoters. *J. Virol.* 83, 4423–4434.
112. Boehm, D., Conrad, R.J., and Ott, M. (2013). Bromodomain proteins in HIV infection. *Viruses* 5, 1571–1586.
113. Li, F., MacKenzie, K.R., Jain, P., Santini, C., Young, D.W., and Matzuk, M.M. (2020). Metabolism of JQ1, an inhibitor of bromodomain and extra terminal bromodomain proteins, in human and mouse liver microsomes†. *Biol. Reprod.* 103, 427–436.
114. Zhu, J., Gaiha, G.D., John, S.P., Pertel, T., Chin, C.R., Gao, G., Qu, H., Walker, B.D., Elledge, S.J., and Brass, A.L. (2012). Reactivation of latent HIV-1 by inhibition of BRD4. *Cell Rep.* 2, 807–816.

115. Banerjee, C., Archin, N., Michaels, D., Belkina, A.C., Denis, G.V., Bradner, J., Sebastiani, P., Margolis, D.M., and Montano, M. (2012). BET bromodomain inhibition as a novel strategy for reactivation of HIV-1. *J. Leukoc. Biol.* *92*, 1147–1154.
116. Lu, P., Shen, Y., Yang, H., Wang, Y., Jiang, Z., Yang, X., Zhong, Y., Pan, H., Xu, J., Lu, H., et al. (2017). BET inhibitors RVX-208 and PFI-1 reactivate HIV-1 from latency. *Sci. Rep.* *7*, 16646.
117. Zhang, X.-X., Lin, J., Liang, T.-Z., Duan, H., Tan, X.-H., Xi, B.-M., Li, L., and Liu, S.-W. (2019). The BET bromodomain inhibitor apabetalone induces apoptosis of latent HIV-1 reservoir cells following viral reactivation. *Acta Pharmacol. Sin.* *40*, 98–110.
118. Lu, P., Qu, X., Shen, Y., Jiang, Z., Wang, P., Zeng, H., Ji, H., Deng, J., Yang, X., Li, X., et al. (2016). The BET inhibitor OTX015 reactivates latent HIV-1 through P-TEFb. *Sci. Rep.* *6*, 24100.
119. Zhao, M., De Crignis, E., Rokx, C., Verbon, A., van Gelder, T., Mahmoudi, T., Katsikis, P.D., and Mueller, Y.M. (2019). T cell toxicity of HIV latency reversing agents. *Pharmacol. Res.* *139*, 524–534.
120. Canarte, V., and Munger, K. (2021). BRD4 downregulation inhibits the viability of cervical cancer cells without affecting viral oncoprotein expression. *Current Research in Virological Science* *2*, 100010.
121. Gilham, D., Smith, A.L., Fu, L., Moore, D.Y., Muralidharan, A., Reid, S.P.M., Stotz, S.C., Johansson, J.O., Sweeney, M., Wong, N.C.W., et al. (2021).

- Bromodomain and Extraterminal Protein Inhibitor, Apabetalone (RVX-208), Reduces ACE2 Expression and Attenuates SARS-Cov-2 Infection In Vitro. *Biomedicines* 9. 10.3390/biomedicines9040437.
122. Mills, R.J., Humphrey, S.J., Fortuna, P.R.J., Lor, M., Foster, S.R., Quaife-Ryan, G.A., Johnston, R.L., Dumenil, T., Bishop, C., Rudraraju, R., et al. (2021). BET inhibition blocks inflammation-induced cardiac dysfunction and SARS-CoV-2 infection. *Cell* 184, 2167–2182.e22.
123. Qiao, Y., Wang, X.-M., Mannan, R., Pitchiaya, S., Zhang, Y., Wotring, J.W., Xiao, L., Robinson, D.R., Wu, Y.-M., Tien, J.C.-Y., et al. (2020). Targeting transcriptional regulation of SARS-CoV-2 entry factors ACE2 and TMPRSS2. *Proc. Natl. Acad. Sci. U. S. A.* 10.1073/pnas.2021450118.
124. Samelson, A.J., Tran, Q.D., Robinot, R., Carrau, L., Rezelj, V.V., Kain, A.M., Chen, M., Ramadoss, G.N., Guo, X., Lim, S.A., et al. (2022). BRD2 inhibition blocks SARS-CoV-2 infection by reducing transcription of the host cell receptor ACE2. *Nat. Cell Biol.* 24, 24–34.
125. Acharya, A., Pathania, A.S., Pandey, K., Thurman, M., Vann, K.R., Kutateladze, T.G., Challagundala, K.B., Durden, D.L., and Byraredy, S.N. (2022). PI3K- $\alpha$ /mTOR/BRD4 inhibitor alone or in combination with other anti-virals blocks replication of SARS-CoV-2 and its variants of concern including Delta and Omicron. *Clin. Transl. Med.* 12, e806.
126. Picaud, S., Wells, C., Felletar, I., Brotherton, D., Martin, S., Savitsky, P., Diez-Dacal, B., Philpott, M., Bountra, C., Lingard, H., et al. (2013). RVX-208, an

- inhibitor of BET transcriptional regulators with selectivity for the second bromodomain. *Proceedings of the National Academy of Sciences* *110*, 19754–19759. 10.1073/pnas.1310658110.
127. Cai, D., Lee, A.-Y., Chiang, C.-M., and Kodadek, T. (2011). Peptoid ligands that bind selectively to phosphoproteins. *Bioorg. Med. Chem. Lett.* *21*, 4960–4964.
128. Chiang, C.-M. (2016). Phospho-BRD4: transcription plasticity and drug targeting. *Drug Discov. Today Technol.* *19*, 17–22.
129. Viejo-Borbolla, A., Ottinger, M., Brüning, E., Bürger, A., König, R., Kati, E., Sheldon, J.A., and Schulz, T.F. (2005). Brd2/RING3 interacts with a chromatin-binding domain in the Kaposi's Sarcoma-associated herpesvirus latency-associated nuclear antigen 1 (LANA-1) that is required for multiple functions of LANA-1. *J. Virol.* *79*, 13618–13629.
130. Conrad, R.J., Fozouni, P., Thomas, S., Sy, H., Zhang, Q., Zhou, M.-M., and Ott, M. (2017). The Short Isoform of BRD4 Promotes HIV-1 Latency by Engaging Repressive SWI/SNF Chromatin-Remodeling Complexes. *Mol. Cell* *67*, 1001–1012.e6.
131. Barboric, M., and Peterlin, B.M. (2005). A new paradigm in eukaryotic biology: HIV Tat and the control of transcriptional elongation. *PLoS Biol.* *3*, e76.



## Chapter II

### Viral E Protein Neutralizes BET Protein-Mediated Post-Entry Antagonism of SARS-CoV-2

Irene P. Chen<sup>1,2,3,4,†</sup>, James E. Longbotham<sup>4,5,6,†</sup>, Sarah McMahon<sup>1,2,3,4</sup>, Rahul K. Suryawanshi<sup>1</sup>, Mir M. Khalid<sup>1</sup>, Taha Y. Taha<sup>1</sup>, Takako Tabata<sup>1</sup>, Jennifer M. Hayashi<sup>1</sup>, Frank W. Soveg<sup>1</sup>, Jared Carlson-Stevermer<sup>7</sup>, Meghna Gupta<sup>4,8</sup>, Meng Yao Zhang<sup>4,5,6</sup>, Victor L. Lam<sup>4,5</sup>, Yang Li<sup>4,5</sup>, Zanlin Yu<sup>4,5</sup>, Erron W. Titus<sup>4,5</sup>, Amy Diallo<sup>4,5</sup>, Jennifer Oki<sup>7</sup>, Kevin Holden<sup>7</sup>, QCRG Structural Biology Consortium<sup>4,5</sup>, Nevan Krogan<sup>1,4,5</sup>, Danica Galonić Fujimori<sup>4,5,6,9,\*</sup>, Melanie Ott<sup>1,3,4,10,11,\*</sup>

#### Affiliations

<sup>1</sup>Gladstone Institutes, San Francisco, CA 94158, USA.

<sup>2</sup>Biomedical Sciences Graduate Program, University of California San Francisco; San Francisco, CA 94143, USA.

<sup>3</sup>Department of Medicine, University of California San Francisco; California, USA.

<sup>4</sup>Quantitative Biosciences Institute COVID-19 Research Group (QCRG), University of California San Francisco; San Francisco, CA 94158, USA.

<sup>5</sup>Quantitative Biosciences Institute (QBI), University of California San Francisco; San Francisco, CA 94158, USA.

<sup>6</sup>Department of Cellular and Molecular Pharmacology, University of California San Francisco; San Francisco, CA 94158, USA.

<sup>7</sup>Synthego Corporation, 3696 Haven Avenue, Suite A, Menlo Park, CA 94063, USA.

<sup>8</sup>Department of Biochemistry and Biophysics, University of California San Francisco;  
San Francisco, CA 94158, USA.

<sup>9</sup>Department of Pharmaceutical Chemistry, University of California San Francisco; San  
Francisco, CA 94158, USA.

<sup>10</sup>Chan Zuckerberg Biohub, San Francisco, CA 94158, USA

<sup>11</sup>Lead Contact.

†Equal Contribution.

\*Correspondence: danica.fujimori@ucsf.edu (D.G.F.),  
melanie.ott@gladstone.ucsf.edu (M.O.)

## **ABSTRACT**

Inhibitors of Bromodomain and Extra-terminal domain (BET) proteins are possible anti-SARS-CoV-2 prophylactics as they downregulate angiotensin-converting enzyme 2 (ACE2). Here, we show that BET proteins should not be inactivated therapeutically as they are critical antiviral factors at the post-entry level. Depletion of BRD3 or BRD4 in cells overexpressing ACE2 exacerbate SARS-CoV-2 infection; the same is observed when cells with endogenous ACE2 expression are treated with BET inhibitors during infection, and not before. Viral replication and mortality are also enhanced in BET inhibitor-treated mice overexpressing ACE2. BET inactivation suppresses interferon production induced by SARS-CoV-2, a process phenocopied by the envelope (E) protein previously identified as a possible “histone mimetic.” E protein, in an acetylated form, directly binds the second bromodomain of BRD4. Our data support a model where SARS-CoV-2 E protein evolved to antagonize interferon responses via BET protein inhibition; this neutralization should not be further enhanced with BET inhibitor treatment.

## INTRODUCTION

The bromodomain and extraterminal domain (BET) family of proteins consists of BRD2, BRD3, BRD4, and BRDT, the latter only found in testis. BET proteins characteristically harbor two highly conserved N-terminal bromodomains (BDs [BD1 and BD2]) and an extraterminal (ET) domain. BDs function as *bone fide* reader domains of acetylated lysines in histone and non-histone proteins and are the molecular targets of small-molecule BET inhibitors such as JQ1, while the ET domain has less defined protein binding properties<sup>1-3</sup>. Through their interaction with histones and cellular transcriptional machinery, BET proteins play an instrumental role in many cellular functions, including cell proliferation, chromatin remodeling, and gene expression<sup>4</sup>. BRD4 is the best studied BET protein and exists in different splice isoforms: a so-called long isoform (amino acids [aa] 1-1362, BRD4L), a short isoform (aa 1-720, BRD4S), and an intermediate third isoform (aa 1-794, isoform B) reported only in osteosarcoma cells<sup>5</sup>. BRD4L has an extended C-terminus that recruits the positive transcription elongation factor (PTEF-b) termed the PTEF-b binding domain (PID)<sup>6</sup>. Furthermore, BRD2, BRD3, and BRD4 interact with viral proteins of herpesviruses, flaviviruses, and papillomaviruses and regulate the integration and latent viral infection of retroviruses<sup>7-13</sup>.

The recently emerged SARS-CoV-2 is the causative agent of the on-going coronavirus disease 2019 (COVID-19) pandemic<sup>14</sup>. COVID-19 patients are characterized by impaired type I interferon (IFN-I) responses paired with an overproduction of proinflammatory cytokines<sup>15-17</sup>. A potent coactivator of proinflammatory and antiviral genes is BRD4. In the lung, BRD4 coactivates interferon-stimulated genes (ISGs)

during viral infection by recruiting P-TEFb and activating proinflammatory responses associated with lung fibrosis, chronic obstructive pulmonary disease, and asthma<sup>18,19</sup>. Treatment with BET inhibitors like JQ1 attenuates transcriptional activation of the antiviral response in the context of influenza A infection<sup>20</sup>. In addition, we previously identified BRD4 and BRD2 as high-confidence interactors of the SARS-CoV-2 E protein and described a histone-like motif similar to histone H3 within E protein that may interfere with the canonical histone:BET protein interactions<sup>21</sup>.

The E protein of coronaviruses is a small, but critical membrane protein involved in many steps of the viral life cycle such as virion assembly, budding, and pathogenesis. One of the reported functions of E protein is that of an ion-channeling viroporin that transports positive ions, including calcium, to trigger inflammasome activation<sup>22</sup>. The expression of inflammatory cytokines in animals infected with SARS-CoV (SARS) lacking the ion-channel function of E protein is reduced, suggesting E protein is important for viral pathogenicity<sup>23</sup>. Furthermore, the E proteins of SARS and SARS-CoV-2 have been reported to interact with tight junction proteins, PALS1 and ZO-1, suggesting that E protein may contribute to the damage of epithelial barrier function and more severe respiratory dysfunction<sup>22,24,25</sup>.

Notably, BRD2 functions as a transcriptional regulator of the viral entry receptor angiotensin-converting enzyme 2 (ACE2), where knockout of BRD2 or prophylactic application of BET inhibitors reduces ACE2 expression and *de novo* viral infection<sup>26,27</sup>. To reconcile this proviral function of BRD2 with known antiviral effects of BRD4, we tested the function of all relevant BET proteins during SARS-CoV-2 infection. Inhibition

of BET proteins after viral entry or depletion of BRD3 or BRD4 in cells overexpressing ACE2 significantly enhanced viral replication, indicating a post-entry antiviral function of BET proteins on SARS-CoV-2. This enhancement in viral replication was also observed in infected, BET inhibitor-treated K18-hACE2 mice. The viral E protein in an acetylated form effectively thwarts this antiviral function as it binds to the second bromodomain of BRD4, underscoring the relevance of BET proteins as positive regulators of antiviral gene expression and cautioning against the use of BET inhibitors in an ongoing SARS-CoV-2 infection.

## RESULTS

### **BRD3 and BRD4 Proteins Antagonize SARS-CoV-2 Infection**

To test post-entry functions of all relevant BET proteins, we depleted them in A549 cells overexpressing ACE2 (A549-ACE2). We generated polyclonal knockout (KO) cells of BRD2 and BRD3 and knockdown (KD) cells of BRD4 via nucleofection of CRISPR-Cas9 ribonucleoprotein (RNP) complexes incorporating multiple guide RNAs against each target. As controls, cells were nucleofected with the RNP complex without guide RNAs (RNP only). The depletion of individual BET proteins was validated by western blotting before infection with SARS-CoV-2 (Isolate USA/WA-1/2020) at multiplicities of infection (MOI) of 0.01 and 0.1 (Figure 2.1A). Loss of BRD3 and BRD4 significantly enhanced cell-associated viral RNA titers (9-fold and 17-fold, respectively) and infectious particle production in plaque assays (1.4 log fold increase for BRD4) at MOI of 0.1, while only BRD4 KD significantly enhanced viral replication in cells infected at MOI of 0.01 (Figure 2.1B and 2.1C). BRD2 KO also significantly enhanced viral infection at any MOI, albeit not as much as BRD4 depletion, supporting a model where individual BET proteins play distinct roles in SARS-CoV-2 infection.

In parallel, we generated BET protein KOs and KD in Calu3 cells, airway epithelial cells with sufficient endogenous ACE2 expression to support SARS-CoV-2 infection. The KOs and KD were validated by western blotting for BET protein expression and infected with SARS-CoV-2 (Figure 2.1D). As expected, BRD2 KO decreased ACE2 transcript levels by ~80%, resulting >2 log decrease in viral RNA and >1 log decrease in infectious viral titers (Figure 2.1E, 2.1F, and S2.1A). BRD3 KO also reduced ACE2 expression by ~50% and viral replication about 3-fold (Figure 2.1E and S2.1A). Overall,

BRD4 KD had the least effect on viral RNA expression and in fact increased infectious particle production despite decreasing ACE2 expression (Figure 2.1E, 2.1F, and S2.1A). These results show distinct effects of BET proteins on pre- and post-entry steps of SARS-CoV-2 infection and underscore BRD4's role regulating the antiviral state after viral entry.

Next, we tested the pan-BET inhibitors, JQ1 and dBET6 that disrupt both BD1- and BD2-mediated interactions, in A549-ACE2 and Calu3 cells. Infectious particle production was significantly increased when JQ1 or dBET6 were added at the time of infection (Figure 2.1G). The same was observed with JQ1- and dBET6-treated Calu3 cells which express ACE2 endogenously (Figure 2.1H). The use of the BET inhibitors at these effective concentrations was non-toxic in A549-ACE2 and Calu3 cells (Figure S2.1B and S2.1C). Collectively, these results demonstrate that BRD3 and BRD4 are post-entry antagonists of SARS-CoV-2 viral replication; inactivating them, either genetically or chemically, exacerbates infection.

### **Loss of BET Proteins Reduces Interferon and Proinflammatory Cytokine Expression**

To test whether the loss of BET proteins reduces interferon production during SARS-CoV-2 infection, we infected Calu3 cells and then immediately treated them with either JQ1 or dBET6 for 48 hours, and analyzed mRNA expression of interferon- $\beta$  (*IFNB1*), interferon stimulated gene 15 (*ISG15*) as well as of the proinflammatory cytokine interleukin 6 (*IL6*). We observed robust inductions of all three genes in control (DMSO-treated) cells that correlated with increasing MOI (Figure 2.2A). In contrast, upon JQ1



or dBET6 treatment, the expression of all three genes (*IFNB1*, *ISG15*, and *IL6*) was suppressed.

Next, we used the Calu3 BET KO and KD cells to determine whether the loss of individual BET proteins was sufficient to suppress the induction of these genes. After infection with SARS-CoV-2, the control (RNP only) cells showed a robust induction of *IFNB1*, *ISG15*, and *IL6* at all MOIs (Figure 2.2B). In contrast, depletion of all BET proteins significantly decreased expression of *IFNB1*, *ISG15*, and *IL6* at low MOI infection, phenocopying the effect of JQ1 and dBET6 on infected Calu3 cells (Figure 2.2B). Interestingly, at higher MOI, BET depletion still suppressed *IFNB1* and *IL6* induction but *ISG15* expression was not significantly suppressed in BRD3- and BRD4-depleted cells, implicating other ISGs as possible targets of BET action (Figure 2.2B). Notably, BRD2 KO cells showed the lowest interferon response reflecting their reduced infection due to low ACE2 levels (Figure S2.1A). These results underscore the role of different BET proteins in activating interferon and proinflammatory responses.

### **SARS-CoV-2 E Protein Suppresses Host Antiviral Responses and Localizes to the Nucleus**

The recent SARS-CoV-2 protein:protein interactome identified BRD2 and BRD4 as high confidence interactors with the viral E protein; BRD3 was also detected but just below the MiST scoring threshold (Figure 2.3A)<sup>21</sup>. We therefore tested whether E protein phenocopies the effect of BET inactivation. An E protein expression construct or the empty control vector (EV) was transfected into A549 cells and stimulated with

poly (I:C) to induce interferon production (Figure 2.2C). Expression of E protein, similar to JQ1 and dBET6 treatment alone, dampened poly (I:C)-mediated induction of *IFNB1*, *ISG15*, and *IL6*, supporting the model that E protein evolved to suppress the antiviral response by inhibiting BET proteins.

We previously identified two lysine residues in the C-terminus of SARS-CoV-2 E protein (K53 and K63) that could be acetylated and, in fact, K63 resides in the short motif (aa 60-64) of E protein that mimics the N-terminus of histone H3 (Figure 2.3B)<sup>21</sup>. This motif was conserved in the E proteins of other coronaviruses, supporting a broader model where coronavirus E proteins may neutralize the antiviral response by antagonizing BET proteins. Mechanistically, this may be achieved by inhibiting the interaction of BET proteins with chromatin. To test this model, we performed co-immunoprecipitation studies in HEK293T cells overexpressing tagged forms of E and BET proteins. We found that SARS-CoV-2 E protein (C-Terminal double Streptavidin [Strep]-tagged) interacted with both isoforms of BRD4 (N-terminal FLAG-tagged) and BRD2 (N-terminal green fluorescent protein [GFP]-tagged) (Figure 2.3C, 2.3D, and 2/3F). To determine whether the lysine residues within E protein interacted with BET proteins, we generated double Strep-tagged, acetylation-null point mutants (K53R, K63R, and K53/63R) of E protein. We performed the co-immunoprecipitation studies in HEK293T cells overexpressing BRD2 and the wildtype or mutant E proteins. The K53/63R mutant had decreased binding to BRD2 compared to the wildtype, suggesting that the two lysine residues in E protein are involved in facilitating the interaction with BRD2 and likely other BET proteins (Figure 2.3E and 2.3F). Compared to the double mutant, the K53R and K63R single mutants had similar decrease in

interaction with BRD2 to K53/63R, suggesting that the BDs are able to recognize each lysine residue individually. Additionally, the retained interaction of the double mutant with BRD2 suggests possible other interactions between the E protein and BRD2, independent of bromodomain-mediated recognition of acetylated lysine residues.

Next, we performed cellular fractionation studies in HEK293T cells overexpressing Strep-tagged E protein. E protein was enriched in the nuclear and chromatin fractions (Figure 2.3G). These same fractions also contained the majority of BET proteins (Figure 2.3G). We did not observe a difference in BET protein fractionation between cells expressing E protein or the empty vector, excluding the possibility that E protein grossly mislocalizes BET proteins. This was further confirmed by confocal microscopy, where E protein, a membrane-bound protein, showed a ring-like perinuclear localization that overlapped with staining of the cellular nuclear pore complex (NPC) (Figure 2.3H). Of note, previous reports of E proteins from SARS and MERS-CoV (MERS) imaged in infected cells also showed a perinuclear localization<sup>28,29</sup>. We also confirmed previous reports showing SARS-CoV E protein colocalizing with endoplasmic reticulum-Golgi intermediate complex (ERGIC) (Figure 2.3H)<sup>22</sup>. However, reliable antibodies to detect untagged SARS-CoV-2 E protein during infection are still lacking, thus hampering staining of endogenous E during infection. Overall, our data support a model where the E:BET protein interaction likely occurs on chromatin in the nuclear periphery.

## **Acetylated SARS-CoV-2 E Peptide Predominantly Binds the Second Bromodomain of BRD4**

Next, we tested whether E protein is acetylated in cells in order to act as a histone mimetic and interact with BDs. For this, we immunoprecipitated either wildtype or acetylation-null (K53/63R) Strep-tagged E proteins from transfected HEK293T cells and probed for acetylation with pan-acetyl-lysine antibodies (Figure 2.4A). To better visualize acetylation of E protein, we treated the cells with a cocktail of cellular pan-histone deacetylase (HDAC) inhibitors and observed a signal for wildtype, but not the double arginine mutant, E proteins. This indicates that E protein is reversibly acetylated in cells.

We used nuclear magnetic resonance (NMR) titration experiments to assess binding of acetyl lysine-containing E peptides to recombinant BD1 and BD2 domains of BRD4. The SARS-CoV-2 E protein contains two lysines, K53 and K63, and we used peptides that were acetylated at either position or were non-acetylated. In two-dimensional <sup>1</sup>H-<sup>15</sup>N heteronuclear single quantum coherence (HSQC) spectra of BD2, we saw significant chemical shift perturbations of peaks upon the addition of either E-K53ac or E-K63ac peptides, indicating BD2 is able to bind either acetyl-lysine position (Figure 2.4B, upper panels). BD2 was found to have a higher affinity for the E-K63ac peptide ( $K_d$  value of  $170 \pm 60 \mu\text{M}$ ) than for the E-K53ac peptide ( $K_d$  value of  $610 \pm 160 \mu\text{M}$ ) (Figure S2.2A). The interaction was acetylation-dependent as the addition of non-acetylated E peptide did not elicit changes in chemical shifts in BD2 as observed with the acetylated peptides (Figure 2.4B). In order to determine the peptide binding site, the backbone amides most perturbed upon peptide binding were mapped onto the

surface of BD2. Both peptides were found to occupy a similar binding site to where other acetylated lysine peptides have been shown to bind previously (Figure S2.2B and S2.2C). Unlike with BD2, little to no chemical shift perturbations in HSQC spectra were observed upon addition of the acetylated E peptides to BD1 indicating very weak to no interaction of acetylated E protein with BD1 (Figure 2.4B, lower panels).

We further investigated if acetylated E peptides compete with bromodomain inhibitors for binding. We performed fluorescence polarization-based competition assays with BD2 bound to TAMRA-conjugated JQ1 molecule. The decrease in fluorescence polarization upon increasing the peptide concentration indicates that the JQ1-TAMRA molecule is being competed off by the acetylated E peptides (Figure S2.2D). Next, we assessed whether BD2 could bind acetylation-null peptides where the lysine residues were replaced by arginines (K53R and K63R). Similar to the observed HSQC spectra with a non-acetylated peptide, little to no chemical shift perturbations were observed upon addition of the E-K53R and E-K63R peptides to BD2 indicating very weak to no interaction (Figure 2.4C).

Overall, these data show that the E protein is acetylated and that the interaction of BRD4 with acetylated E peptide predominantly involves the second bromodomain of BRD4. The relevance of the second bromodomain to the antiviral function of BRD4 was further explored in studies with ABBV-744, a BET inhibitor that specifically targets BD2-mediated interactions<sup>30</sup>. In A549-ACE2 cells treated with ABBV-744 at the time of infection, SARS-CoV-2 viral RNA and infectious particle production were significantly increased (3-fold for both) when compared to cells treated with the vehicle

alone, demonstrating that selective inhibition of BD2 alone is sufficient to suppress the antiviral function of BET proteins (Figure 2.4D and 2.4E).

### **BET Inhibitors Enhance SARS-CoV-2 Infection in K18-hACE2 mice**

To test the post-entry effects of BET inhibitors, JQ1 and ABBV-744, *in vivo*, we used K18-hACE2 transgenic mice constitutively expressing the human ACE2 receptor in epithelial tissues from the cytokeratin 18 (K18) promoter<sup>31</sup>. Mice were infected intranasally, and BET inhibitors were administered daily intraperitoneally or orally starting on the day of infection (Figure 2.5A). DMSO at the same concentration as JQ1 and ABBV-744 was used as a control. Based on the *in vitro* observations, we hypothesized that BET inhibitor treatment would similarly result in an increase viral replication in the mice.

As expected, all infected mice exhibited weight loss and change in body temperature as a sign of infection, and no significant differences between the treatment groups were observed (Figure S2.3A and S2.3B). Viral replication in all treatment groups was analyzed at 2 and 4 days post infection. During these time points, we observed increased viral titer in the lungs of JQ1- and ABBV-744-treated mice (Figure 2.5B and 2.5C). Specifically, there was an 18-fold increase in infectious particle production in JQ1-treated mice and a 37-fold increase in ABBV-744-treated mice compared to DMSO at 2 days post infection. Concordantly, there was increased immunohistochemical staining for SARS-CoV-2 nucleocapsid (N) protein in the lungs of JQ1- and ABBV-744-treated mice at 7 days post infection compared to DMSO-treated mice (Figure S2.3C). Similar to the *in vitro* treatment, the JQ1- and ABBV-744-

treated mice experienced significant decreases in the expression of interferons, cytokines, and chemokines, including *ISG15*, *IL6*, *RIG-I*, *IL1a*, *CCL2*, *CXCL9*, and *CXCL10* (Figure S2.3D). The decrease in expression of these host defense genes paired with the subsequent increase in infectious particle production was accompanied by a decrease in immune cell infiltration in the lung at 7 days post infection in the JQ1- and ABBV-744-treated mice compared to DMSO-treated mice (Figure 2.5D). The DMSO treatment showed widespread large inflammatory foci consistent with interstitial pneumonia with perivascular inflammation comprised of lymphocytes, macrophages and neutrophils. These histological changes are attributed to SARS-CoV-2 infection as healthy, uninfected mice did not experience lung inflammation upon identical treatment with DMSO, JQ1, and ABBV-744 (Figure S2.3E).

Overall, 60–80% of animals with BET inhibitor treatment reached a humane endpoint at day 6 post infection whereas 100% of the animals in the DMSO-treated group survived (Figure 2.5E). These data underscore the finding that BET proteins regulate an antiviral state during viral infection that prevents exacerbation of virally induced disease and document the clinical relevance of the second bromodomain of BET proteins, which is targeted by the viral E protein.

## DISCUSSION

We report that BET proteins (BRD4 > BRD3 > BRD2) block SARS-CoV-2 infection at the post-entry level as each of them is necessary for full induction of the type I interferon response and proinflammatory cytokines. Viral replication is exacerbated after chemical or genetic inactivation of BET proteins, underscoring the critical role of this antiviral step in controlling SARS-CoV-2 infection. We further report a so far unknown function of the SARS-CoV-2 E protein in antagonizing interferon and ISG expression. E protein is acetylated in cells and in an acetylated form binds to the second bromodomain of BRD4. Lastly, BET inhibitor treatment increases viral titers in the lungs of SARS-CoV-2 infected mice and results in higher mortality. As the SARS-CoV-2 E protein is functionally similar to BET antagonists in suppressing the interferon response and directly binds one of the two bromodomains, we propose a model where E protein evolved to neutralize the antiviral gene activation mediated by BET proteins to promote efficient SARS-CoV-2 replication, a process further enhanced with BET inhibitor treatment.

Our data highlight the unique and overlapping roles of BET proteins during SARS-CoV-2 infection where individual BET proteins may serve proviral and antiviral roles. Previous reports have demonstrated that prophylactic treatment of cell lines with pan-BET inhibitors decrease ACE2 expression and reduce viral replication<sup>26,27</sup>. Here, we show that BET proteins can promote or block SARS-CoV-2 infection, and this is likely dependent on the specific gene targets with which individual BET proteins interact. Comparing the effects of genetic and chemical neutralization of BET proteins in cells that either endogenously express or overexpress ACE2 allows for more nuanced



parsing of the pre- and post-viral entry roles of BET proteins. With genetic neutralization of BET proteins in cells with endogenous ACE2 expression (Calu3), only the knockout of BRD2 reliably ablates viral replication as ACE2 expression is reduced. On the other hand, genetic neutralization of BET proteins in cells that overexpress ACE2 (A549-ACE2) does not affect the constitutive ACE2 overexpression; the pro-inflammatory role of BRD4 is prominently suppressed and results in an increase in viral replication. The chemical inhibition of BET proteins at the time of infection in either cell line results in enhancement of viral replication similar to the genetic neutralization of BET proteins in A549-ACE2 cells.

Among the BET proteins, BRD2 is the most proviral because it positively regulates the expression of the SARS-CoV-2 entry receptor ACE2. In contrast, BRD4 has the strongest antiviral function due to its co-activator role in the induction of interferon genes. Differences between BRD2 and BRD4 lie in their domain structure; while sharing roughly 70% sequence similarity in their N-terminus including the tandem BDs, the C-terminus of BRD4L contains the PID which enhances the recruitment of P-TEFb to BET target genes<sup>6,30</sup>. Small molecule BET inhibitors reduce the recruitment of BET proteins, along with P-TEFb, to interferon target genes upon interferon- $\beta$  or Toll-like receptor ligand stimulation<sup>32-34</sup>. Furthermore, BRD4 plays a critical role in coordinating both positive and negative regulation of paused RNA polymerase II at the transcription start sites of ISGs by recruiting NELF/DSIF (negative elongation factor/DRB sensitivity-inducing factor) to fine-tune ISG expression<sup>34</sup>. On the other hand, BRD2 functions as a chromatin organizer that assembles enhancer elements<sup>35</sup>. The depletion of BRD2 versus BRD4 results in distinct transcriptional changes, suggesting

non-overlapping roles in function<sup>36</sup>. In contrast, the identification of a conserved motif B in BET proteins that facilitates heterodimerization of proteins within this family may explain partial functional redundancy and shared chromatin occupancy of BRD2 and BRD4<sup>37</sup>. The fact that BRD2 and BRD4 play opposing roles in the regulation of SARS-CoV-2 highlights the complexity of genes regulated by BET proteins and future studies aimed at disentangling these regulatory networks will be of value to the field.

We also show that SARS-CoV-2 E protein predominantly targets the second bromodomain of BRD4. Research has classically focused on histones as BD targets, but BD2 of BRD4 also binds the acetylated cyclin T1 subunit of P-TEFb<sup>38</sup>. Recent studies defining the unique roles of BD1 and BD2 in disease models indicated that inhibiting BD2 preferentially blocks stimulus-mediated induction of gene expression programs without affecting pre-existing transcriptional programs<sup>32</sup>. BD1-specific inhibitors are effective in inhibiting cell proliferation in cancer models, whereas BD2-specific inhibitors had the greatest effect in ameliorating inflammatory and autoimmune diseases<sup>32</sup>. Our finding that SARS-CoV-2 E protein binds BD2 of BRD4 supports the notion that BD2 is important for rapid gene expression, especially in inflammatory disease settings such as COVID-19.

SARS-CoV-2 E protein joins a growing number of viral proteins containing histone-like motifs in their sequences. Histone tails are often mimicked by viruses since many host chromatin factors interact with histones to modulate gene expression<sup>39</sup>. A prominent example of a viral histone mimetic is NSP1 of influenza A H3N2 subtype, which contains a short histone H3-like motif capable of sequestering the transcription

elongation factor, PAF1, to prevent the expression of antiviral genes<sup>40</sup>. Similarly, Human Immunodeficiency Virus (HIV-1) factor Tat is reversibly acetylated at multiple lysines in its basic domain to recruit key host transcriptional regulators in a coordinated manner, enhancing viral transcription<sup>41–44</sup>. A recent study identified the capsid protein of the Yellow Fever Virus as a histone H4 mimetic with acetylated lysine residues that bind BRD4 to interfere with gene regulation<sup>9</sup>. Overall, BRD4 appears to be a hotspot of viral antagonism due to its critical role in positively regulating the antiviral response.

The E proteins of coronaviruses are similar in domain structure: a short, hydrophilic N-terminus, followed by a hydrophobic transmembrane domain, and a subsequent C-terminus that comprises the majority of the protein and contains a PDZ-binding motif (PBM). Among the E proteins of human pathogenetic coronaviruses, those from SARS and SARS-CoV-2 share ~95% sequence similarity along with the histone H3-like motif whereas the MERS E protein shares only ~35% similarity to SARS and SARS-CoV-2 E proteins and does not have the histone-like motif<sup>45</sup>. The histone-like motif of interest is also present in common coronavirus NL63 and bat coronavirus SHC014, suggesting that the function of E:BET proteins could also be conserved in these viruses. Future work should address if E proteins from these coronaviruses are similarly capable of derailing antiviral responses through BRD4 antagonism.

Since the beginning of the pandemic, there has been growing interest in the prophylactic application of BET inhibitors to prevent SARS-CoV-2 infection as they reduce ACE2 expression. All previous studies relied on multi-day pretreatment of cell lines, organoids, and primary cells with BET inhibitors to inhibit infection<sup>26,27,46</sup>. In

contrast, our study focuses on the concurrent administration of BET inhibitors, JQ1 and ABBV-744, at the time of infection. Similar to our observations, Mills et al. found that therapeutic application in K18-hACE2 mice with BET inhibitor, INCB054329, resulted in severe lung pathology and significant viral RNA in the lung. We demonstrate the therapeutic application of the BET inhibitors worsens viral pathogenesis as evidenced by enhanced immune infiltration, marked increase in infectious particle production, and lower probability of survival, underscoring the clinical significance of post entry restriction of SARS-CoV-2 by BET proteins.

Our study sheds light on the antiviral function of BET proteins during SARS-CoV-2 infection, highlighting their contrasting functions at different stages of the viral life cycle. Whether SARS-CoV-2 evolved the anti-BET protein function of the E protein because of the unique influence of BRD2 on ACE2 receptor levels or the necessity for a more surgical inactivation of BET proteins as transcriptional coactivators necessary for antagonizing the virus remains to be determined. Because most BET inhibitors do not distinguish between the different BET proteins and inhibit all of them indiscriminately, our study urges caution with the clinical use, prophylactic or therapeutic, of pan-BET inhibitors in people at risk or afflicted with COVID-19.

### **Limitations of the Study**

This study explores the nuanced role for BET proteins in pre- and post-entry steps of SARS-CoV-2 infection. While we characterize the cellular interaction between SARS-CoV-2 E protein with BRD2 and BRD4 proteins and their effect on the viral life cycle, additional work is necessary to translate this into clinical application. First, while we

focus on K53 and K63 residues in SARS-CoV-2 E protein, a comprehensive analysis of E protein acetylation, ideally in infected cells, is missing and would give better insight into the functional consequences of this modification. Secondly, the nature of the cellular lysine acetyltransferases and deacetylases that modify the E protein are not yet known; this would help to potentially harness available inhibitors for these enzymes for COVID-19 treatment. Lastly, the continued development of more targeted small molecules for each BET protein will allow for specific tuning of cellular signaling pathways to achieve a more desirable therapeutic outcome. For example, a molecule that specifically inhibits BRD2, and not BRD4, could be useful for therapeutic applications in COVID-19 in the future.

## **ACKNOWLEDGEMENTS**

We thank all members of the Ott and Fujimori laboratories for sharing reagents, expertise, and feedback in the preparation of this manuscript. We thank Lauren Weiser and Veronica Fonseca for administrative support, Dr. Francoise Chanut for editorial support, and John Carroll and Sarah Gardner for graphical support. This research is funded by grants from the National Institutes of Health: NCI R01CA250459 and NIAID R01AI137270 to D.G.F.; NIAID R37AI083139 to M.O. I.P.C. was supported by NIH/NIAID (F31 AI164671-01). S.M. was supported by TRDRP (T30DT1006) and the UCSF Discovery Fellowship. M.O. acknowledges support from the Roddenberry Foundation, Pam and Ed Taft, and the Gladstone Institutes. We are grateful for philanthropic support from QCRG philanthropic donors and the James B. Pendleton Charitable Trust. Histology, imaging, and image processing was performed at the Gladstone Institutes' Histology and Light Microscopy Core.

## **Author Contributions**

I.P.C., J.E.L., S.M., D.G.F., and M.O. conceived and designed the study. I.P.C., J.E.L., R.K.S., and M.M.K. performed experiments and data analysis. I.P.C. and R.K.S. designed and conducted the animal study. J.C.-S. and J.O. generated the knockout cell lines. M.Y.Z. contributed to binding studies. S.M., J.M.H., T.Y.T, T.T., and F.W.S. provided experimental support. M.G., M.Y.S., V.L.L., Y.L., Z.Y., E.W.T., A.D., and QCRG SBC provided protein expression support. D.G.F. and M.O. supervised the study design and provided technical guidance. K.H., N.K., D.G.F., and M.O. secured funding. I.P.C., J.E.L., D.G.F., and M.O. wrote the manuscript.

## **Declaration of Interests**

J.C.-S., J.O., and K.H. are employees and shareholders of Synthego Corporation. All authors declare no other competing interests.

## **MATERIAL AND METHODS**

### **RESOURCE AVAILABILITY**

#### **Lead contact**

Further information and requests for resources and reagents should be directed to and will be fulfilled by the Lead Contact, Melanie Ott ([melanie.ott@gladstone.ucsf.edu](mailto:melanie.ott@gladstone.ucsf.edu)).

#### **Materials availability**

This study did not generate new unique reagents.

#### **Data and code availability**

- All data reported in this paper is available from the lead contact upon request.
- This paper does not report original code.
- Any additional information required to reanalyze the data reported in this paper is available from the lead contact upon request.

## **EXPERIMENTAL MODEL AND SUBJECT DETAILS**

### **Mammalian cell lines and culture conditions**

HEK293T and Vero-E6 were obtained from ATCC were cultured in DMEM (Corning) supplemented with 10% fetal bovine serum (FBS) (GeminiBio), 1% glutamine (Corning), and 1% penicillin-streptomycin (Corning) at 37°C, 5% CO<sub>2</sub>.

Calu3 cells were obtained from ATCC and cultured in AdvancedMEM (Gibco) supplemented with 2.5% FBS, 1% GlutaMax, and 1% penicillin-streptomycin at 37°C, 5% CO<sub>2</sub>.



A549 cells stably expressing ACE2 (A549-ACE2) were a gift from O. Schwartz. A549-ACE2 cells were cultured in DMEM supplemented with 10% FBS, blasticidin (20 µg/ml) (Sigma) and maintained at 37°C with 5% CO<sub>2</sub>. Short Terminal Repeat (STR) analysis by the Berkeley Cell Culture Facility on 17 July 2020 authenticates these as A549 cells with 100% probability.

### **Generation of CRISPR A549-ACE2 and Calu3 KO cell lines**

sgRNAs were designed according to Synthego's multi-guide gene knockout. Briefly, three sgRNAs are bioinformatically designed to work in a cooperative manner to generate small fragment deletions in early exons causing knock out. These fragment deletions are larger than standard indels generated from single guides. The genomic repair patterns from a multi-guide approach are highly predictable based on the spacing of and on design constraints that limit off-targets, resulting in a higher probability of protein knockout phenotype.

To induce gene knockout, 10 pmol *Streptococcus Pyogenes* NLS-Sp.Cas9-NLS (SpCas9) nuclease (Aldevron, 9212) was combined with 30 pmol total synthetic sgRNA (10 pmol each sgRNA) (Synthego) to form ribonucleoproteins (RNPs) in 20µL total volume with SE Buffer for Calu-3 and A549-ACE2 cells. The RNP assembly reaction was mixed by pipetting up and down and incubated at room temperature for 10 minutes. Cells were resuspended in transfection buffer according to cell type and added to the preformed RNP solution and gently mixed. Nucleofections were performed on a Lonza nucleofector system (Lonza, AAU-1001) using program CM-130 and CM-120 for Calu-3 and A549-ACE2 cells, respectively. Two days post-

nucleofection, DNA was extracted with DNA QuickExtract (Lucigen, QE09050). Amplicons for indel analysis were generated by PCR using AmpliTaq Gold 360 polymerase (Thermo Fisher Scientific, 4398813). PCR products were cleaned-up and analyzed by Sanger sequencing. Sanger data files and sgRNA target sequences were input into Inference of CRISPR Edits (ICE) analysis ([ice.synthego.com](http://ice.synthego.com)) to determine editing efficiency and to quantify generated indels<sup>47</sup>. A list of sgRNA sequences and genotyping primers can be found in Table S2.1 and 2.2.

## **Mice**

All protocols concerning animal use were approved (AN169239-01B) by the Institutional Animal Care and Use committees at the University of California, San Francisco and Gladstone Institutes and conducted in strict accordance with the National Institutes of Health *Guide for the Care and Use of Laboratory Animals*<sup>48</sup>. Studies were conducted with 6-8 week old male and female K18-hACE2 C57BL/6J mice (strain B6.Cg-Tg(K18-ACE2)2Primn/J) (The Jackson Laboratory, 034860). Mice were housed in a temperature- and humidity-controlled pathogen-free facility with 12-hour light/dark cycle and ad libitum access to water and standard laboratory rodent chow.

## **SARS-CoV-2 culture**

SARS-CoV-2 Isolate USA-WA1/2020 (BEI NR-52281) was used for all infection studies. All live virus experiments were performed in a Biosafety Level 3 laboratory. SARS-CoV-2 stocks were propagated in Vero-E6 cells and their sequence verified by

next-generation sequencing. Viral stock titer was calculated using plaque forming assays.

## **Plasmids**

The plasmids expressing the envelope protein of SARS-CoV-2 were generous gifts from Dr. Nevan Krogan (UCSF, The Gladstone Institutes). The majority of BRD4 plasmids were generous gifts from Dr. Eric Verdin (The Buck Institute for Research on Aging, Novato, CA). GFP-BRD2 was a gift from Kyle Miller (Addgene plasmid # 65376 ; <http://n2t.net/addgene:65376> ; RRID:Addgene\_65376). All plasmids and corresponding sequence information are available upon request.

## **Method Details**

### **Cell Fractionation**

Cell fractionation was performed with the NE-PER Nuclear and Cytoplasmic Extraction Kit (Thermo Fisher Scientific, 78835) with additional modifications to extract the chromatin fraction. Following the extraction of the nuclear fraction per manufacturer's instructions, the resulting pellet was resuspended in NER with MNase (NEB, M0247S), Halt protease inhibitor cocktail (Thermo Fisher Scientific, 1861282), and CaCl<sub>2</sub> (Sigma, C4901). Samples were vortexed on the highest setting and sheared on the Bioruptor (Diagenode) with 10 cycles of 10 seconds on and 10 seconds off on medium setting. The samples were pelleted by centrifugation and the resulting supernatant was the chromatin fraction.

## **Western Blot Analysis**

Cells were lysed in RIPA lysis buffer (50 mM Tris-HCl [pH 8], 150 mM NaCl, 1% NP-40, 0.5% sodium deoxycholate, 0.1% SDS, supplemented with Halt protease inhibitor cocktail) to obtain whole-cell lysates or lysed using the NE-PER nuclear and cytoplasmic extraction kit to obtain cytoplasmic, nuclear, and chromatin fractions. Protein concentrations of cell fractions were determined using a BCA Assay (Thermo Fisher Scientific, 23225), and normalized among samples per experiment before analysis via western blotting using standard techniques. Proteins were visualized by chemiluminescent detection with ECL on ChemiDoc MP (Bio-Rad). Antibodies: BRD2 (Abcam, ab139690), BRD3 (Abcam, ab50818), BRD4 (Abcam, ab128874), LaminB1 (Abcam, ab16048), PARP (Cell Signaling, 9532S), GAPDH (Cell Signaling, 5174S), Strep (Qiagen, 1023944), FLAG (Sigma, F3165), Histone H4 (Cell Signaling, 13919S), pan acetyl lysine (Cell Signaling 9441S; Abcam, ab80178), Rabbit IgG-HRP (Bethyl, A120-201P), and Mouse IgG-HRP (Bethyl, A90-516P).

## **Quantitative Polymerase Chain Reaction**

RNA was extracted from cells or supernatants using RNA STAT-60 (AMSBIO, CS-110) and the Direct-Zol RNA Miniprep Kit (Zymo Research, R2052). RNA from cells or supernatant was reverse-transcribed to cDNA with iScript cDNA Synthesis Kit (Bio-Rad, 1708890). qPCR reaction was performed with cDNA and SYBR Green Master Mix (Thermo Scientific) using the CFX384 Touch Real-Time PCR Detection System (Bio-Rad). See Table S2.3 for primers sequences. E gene standards were used to generate a standard curve for copy number quantification. E gene standard was

generated by PCR using extracted genomic SARS-CoV-2 RNA as template. A single product was confirmed by gel electrophoresis and DNA was quantified by Nanodrop.

### **Immunoprecipitation**

Transfected HEK293T cells were lysed in IP buffer (50mM Tris-HCl, 150mM NaCl, 1mM EDTA, 1% Triton-X, supplemented with Halt protease inhibitor cocktail) and 1mg of lysate was incubated with Strep-Tactin Sepharose resin (Iba Life Science, 2-1201-002) overnight rotating at 4°C. Bound protein was washed five times with IP buffer and eluted with Strep-Tactin elution buffer (Iba Life Sciences, 2-1000-025). Eluted samples were analyzed by western blot.

### **Immunofluorescence Microscopy**

Transfected HEK293T cells were plated onto rat tail collagen (EMS, 72295) coated, 22- by 22-mm no. 1.5 coverslips. Cells were fixed in 4% paraformaldehyde, permeabilized with methanol on ice for 10 minutes, and blocked in 3% bovine serum albumin. Cells were then immunostained with the indicated antibodies: Strep (Qiagen, 1023944), ERGIC-53 (Santa Cruz Biotechnology, sc-365158), Nuclear Pore Complex (Biolegend, 682204), Hoescht 33342 (Invitrogen, H3570), Mouse IgG-AlexaFluor549 (Invitrogen, A11005), and Rabbit IgG-AlexaFluor488 (Invitrogen, A11008). Coverslips were mounted onto glass slides using ProLong Gold Antifade Mountant (Invitrogen, P36934) and analyzed by confocal microscopy (Olympus FV3000RS) using a Olympus UPLAN S-APO 60X OIL OBJ, NA1.35, WD0.15MM objective. The resulting Z-stack was reconstructed and rendered in 3D using Imaris software (Oxford Instruments).

### **Expression and purification of Brd4 bromodomains**

His-SUMO-BD1 (42-168) and BD2 (349-460) constructs were expressed in LOBSTR *E. coli* cells (Kerafast, EC1002). Expression and purification of both constructs followed the same protocol. For NMR studies the His-SUMO-BD constructs were expressed in M9 minimal media containing  $^{15}\text{N}$  ammonium chloride. Cells were induced with 0.1 mM IPTG and grown at 16°C overnight before the pellet was collected. The cells were resuspended in lysis buffer (50 mM Tris, 200 mM NaCl, pH 7.5), lysed by sonication and centrifuged. The supernatant was purified using Ni resin equilibrated in binding buffer (50 mM Tris, 200 mM NaCl, 20 mM imidazole, pH 7.5), washed first with lysis buffer and 30 mM imidazole and then a final wash with lysis buffer and 50 mM imidazole. The protein was eluted from the Ni resin after incubation with SUMO protease Ulp1 in order to remove the His-SUMO tag. The cleaved proteins were then further purified by size-exclusion chromatography using a Hiload 26/60 Superdex 75 gel filtration column (GE, GE28-9893-34) in a buffer of 50 mM sodium phosphate, 100 mM NaCl pH 7.4 buffer before being concentrated and flash-frozen.

### **NMR binding experiments.**

For 2D  $^1\text{H}$ ,  $^{15}\text{N}$  HSQC peptide titration experiments, 50  $\mu\text{M}$   $^{15}\text{N}$ -labeled BD1 or BD2 in 50 mM sodium phosphate, 100 mM NaCl, 5 %  $\text{D}_2\text{O}$ , pH 7.4 buffer was used, and spectra were measured after each addition of E protein peptide. The 2D  $^{15}\text{N}$ -FHSQC spectra for the E protein peptide titration series were recorded on a Bruker 500 MHz AVANCE DRX spectrometer equipped with an actively shielded Z-gradient QCI cryoprobe ( $^{15}\text{N}/^{13}\text{C}/^{31}\text{P}$ ,  $^1\text{H}$ ) using programs from the pulse program library (TopSpin

1.3pI10) at 298 K. Chemical shift perturbations of HSQC peaks, upon addition of E peptide, were calculated with the following equation:

$$\Delta\text{Chemical shift} = \sqrt{\frac{\Delta H^2 + (0.2\Delta N)^2}{2}}$$

Dissociation constants ( $K_d$ ) were determined after the change in chemical shift was plotted against peptide concentration. Data were then fit to the following equation:

$$\Delta\text{Chemical shift} = \text{CSPmax} \left( \frac{([P] + [L] + K_d) - \sqrt{([P] + [L] + K_d)^2 - 4[P][L]}}{2[P]} \right)$$

Where [P] is the concentration of BD2, [L] is the peptide concentration,  $K_d$  is the dissociation constant and CSPmax is the maximum chemical shift perturbation. The majority of residues were assigned after data from BMRB entry 50146 were transferred to our spectra. See Table S2.4 for peptide sequences.

### Fluorescence Polarization Assays

E protein peptide binding to purified Brd4 bromodomains was determined by competition-based fluorescence polarization (FP) using a JQ1-TAMRA molecule. Synthesis of JQ1-TAMRA followed a protocol previously described<sup>49</sup>. For competition-based FP assays, His-SUMO-BD1 and His-SUMO-BD2, at a concentration equal to the  $K_d$  value for JQ1-TAMRA, were incubated with 10 nM of JQ1-TAMRA and different concentrations of unlabeled peptides were used as competitors. See Table S2.4 for peptide sequences.

### Compound Treatments

Compounds, JQ1 (Selleckchem, S7110), dBET6 (Selleckchem, S8762), and ABBV-744 (Selleckchem, S8732), were dissolved in DMSO as per manufacturer's

instructions. Cells were treated at the time of infection for 48 hours with media changes with fresh compound-containing media every 24 hours.

### **Compound Cytotoxicity Measurements**

A549-ACE2 and Calu3 cells were seeded into 96-well plates and treated with identical compound concentrations used in the infection assays for 48 hours, where fresh compound-containing media was added every 24 hours. At the end of 48 hours, cell viability was assayed following the manufacturer's protocol of CellTiter-Glo (Promega, G7571). Luminescence was recorded with an Infinite M Plex plate reader (Tecan) using an integration time of 1 second.

### **Viral Infection Studies**

A549-ACE2 and Calu3 cells were seeded into 12-well plates and rested for at least 24 hours prior to infection. At the time of infection, media containing compound and/or viral inoculum (MOI 0.01 or 0.1) was added on the cells for 24 hours. At 24 hours post infection, fresh compound-containing media or media only was added on the cells. The supernatant and cells were harvested by adding STAT-60 for downstream quantification of genes.

### **Plaque-Forming Assays**

Viral inoculations were harvested from experiments and serially diluted in DMEM (Corning). At the time of infection, the media on Vero-E6 cells were replaced with viral inoculation for one hour. After the one-hour absorption period, 2.5% Avicel (Dupont, RC-591) was layered on the cells and incubated for 72 hours. Then, Avicel was



removed and cells were fixed in 10% formalin for one hour, stained with crystal violet for 10 minutes, and washed multiple times with water. Plaques were counted and averaged from two technical replicates.

### **Preparation of Compounds for Animal Study**

A stock solution of JQ1 (50mg/ml in DMSO) and ABBV-744 (50mg/ml in DMSO) was prepared. JQ1 was then diluted to a working concentration of 5mg/ml in an aqueous carrier ((2-Hydroxypropyl)- $\beta$ -cyclodextrin [Sigma C0926]) using vigorous vortexing. Mice were injected at a dose of 50mg/kg given intraperitoneally once daily. ABBV-744 was diluted to a working concentration of 5mg/ml in an carrier ((V/V): 2% DMSO, 30% PEG-400 [Sigma, 8074850050], 68% Phosal-50PG [MedchemExpress, HY-Y1903]) using vigorous vortexing. Mice were treated at a dose of 20mg/kg given orally once daily.

### **SARS-CoV-2 K18-hACE2 mouse infection model**

A total of 50 animals were used in the study. Forty five animals were anesthetized and intranasally infected with  $5 \times 10^4$  PFU/mL (50 $\mu$ l) of SARS-CoV-2 WA1 strain, five animals were mock infected and used as a control. The infected animals were divided in three groups each of 15 animals. Each group were treated with either JQ1 (50mg/kg) or ABBV-744 (20mg/kg), while DMSO at a vehicle concentration was used as a control. The animals were dosed from day 0 to day 7 post infection. All animals were monitored for their temperature and weight loss on daily basis. At 2 and 4 days post infection five animals from each group were euthanized by cervical dislocation and their lung tissue were homogenized for downstream analysis. Rest of the animals were monitored for

their survival after infection. Lungs tissues from virus and mock infected animals were further processed for histological observations.

### **Histology**

Mouse lung tissues were fixed in 4% paraformaldehyde (Sigma, 47608) for 24 hours, washed three times with phosphate buffer saline, and stored in 70% ethanol. Briefly, tissues were processed and embedded in paraffin, and tissue sections were stained for SARS-CoV-2 Nucleocapsid (Genetex, GTX135357). The sections were then imaged using Leica Aperio ImageScope.

### **Virus neutralization assay**

The serum samples from mice were collected at 7 days post infection. The serum dilutions (50 $\mu$ L) were made to get final dilution as 1:100, 1:200, 1:400, 1:800, 1:1600, 1:3200 in serum-free DMEM. The dilutions were separately added with 50 PFU (50 $\mu$ L) of SARS-CoV-2 WA1 isolate. The mixture was mixed gently, incubated at 37°C for 30 mins, followed by a plaque-forming assay. The virus neutralization efficacy of sera were presented as 50% neutralization titer (NT50) and the average of each variant and compared to others in terms of fold change.

### **QUANTIFICATION AND STATISTICAL ANALYSIS**

The number of experiments and replicates are indicated in individual figure legends. Data were processed and visualized using GraphPad Prism. All quantified data are represented mean  $\pm$  SEM or SD, as indicated, and quantification details are available in figure legends. Western blot band intensities were quantified using ImageJ.

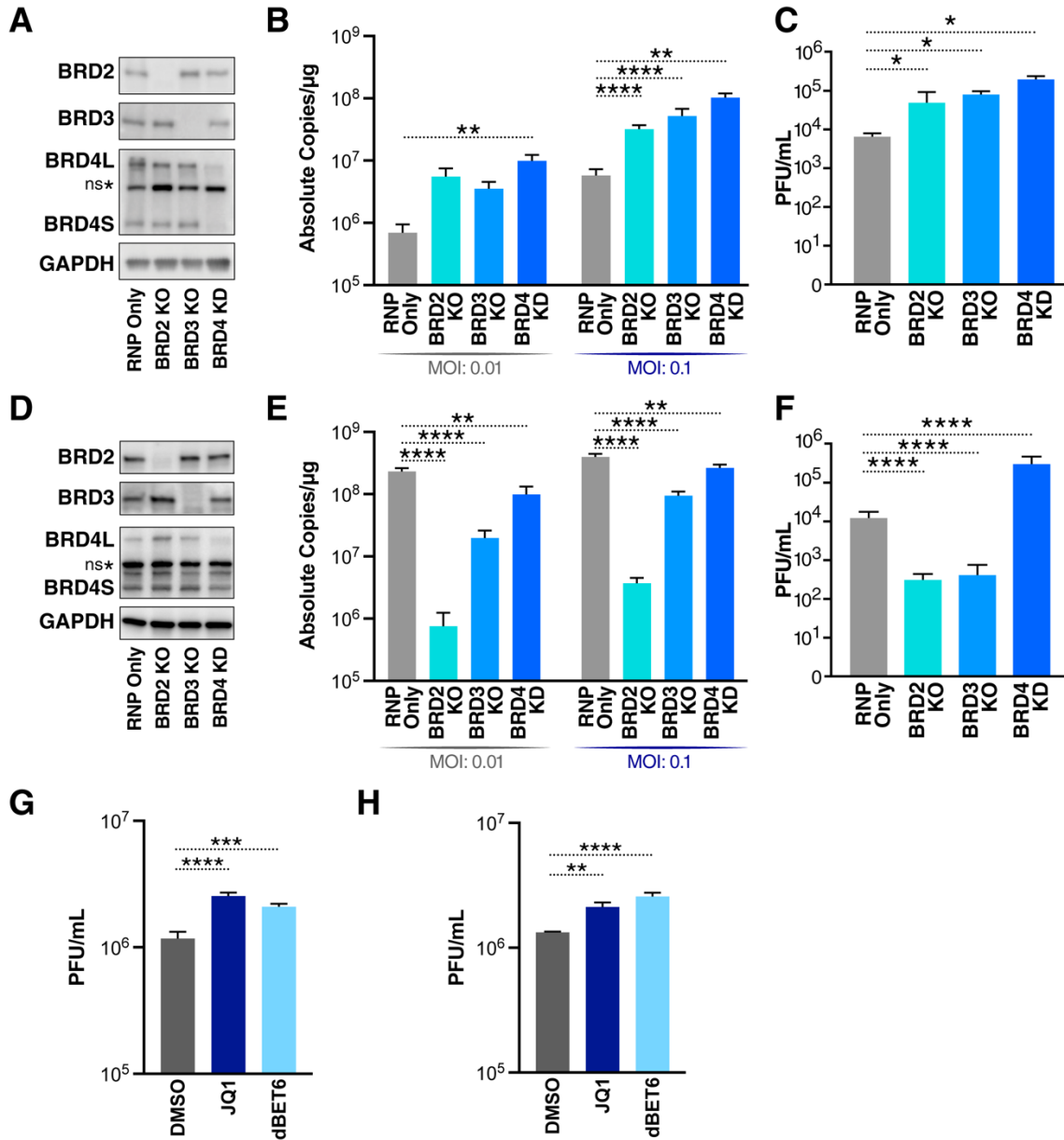


**Figure 2.1. BRD2, BRD3, and BRD4 differentially affect SARS-CoV-2 infection.**

- A. Representative western blots from A549-ACE2 cells with indicated BET protein KO and KD. Lysates were probed for the epitope indicated beside each panel. \*ns denotes a non-specific band.
- B. RT-qPCR of SARS-CoV-2 E RNA isolated 48 hours post infection (h.p.i) from A549-ACE2 cells with indicated BET protein KO or KD infected with SARS-CoV-2 (MOI of 0.01 or 0.1). Data are expressed in absolute copies/ $\mu\text{g}$  based on a standard curve of E gene with known copy number. Average of three independent experiments analyzed in triplicate  $\pm$  SEM are shown and compared to RNP Only samples by ANOVA: \* $p=0.0397$ , \*\* $p=0.0026$ , \*\*\*\* $p<0.0001$ .
- C. Plaque assay titers from supernatant of infected A549-ACE2 cells with indicated BET protein KO and KD at MOI of 0.1. Average of three independent experiments analyzed in duplicate  $\pm$  SEM are shown and compared to RNP Only condition by Student's t-test: \* $p<0.5$ .

- D. Representative western blots from Calu3 cells with indicated BET protein KOs and KD. Lysates were probed for the epitope indicated beside each panel. \*ns denotes a non-specific band.
- E. RT-qPCR of SARS-CoV-2 E RNA isolated 48 h.p.i from Calu3 cells with indicated BET protein KOs or KD infected with SARS-CoV-2 (MOI of 0.01 or 0.1). Data are expressed in absolute copies/ug based on a standard curve of E gene with known copy number. Average of three independent experiments analyzed in triplicate  $\pm$  SEM are shown and compared to RNP Only samples by ANOVA: \*\* $p < 0.005$ , \*\*\*\* $p < 0.0001$ .
- F. Plaque assay titers from supernatant of infected Calu3 cells with indicated BET protein KOs and KD at MOI of 0.1. Average of three independent experiments analyzed in duplicate  $\pm$  SEM are shown and compared to RNP Only condition by Student's t-test: \*\*\*\* $p < 0.0001$ .
- G. Plaque assay titers from supernatant of infected A549-ACE2 cells treated JQ1 (500nM) and dBET6 (500nM) at MOI of 0.1. Average of three independent experiments analyzed in duplicate  $\pm$  SEM are shown and compared to DMSO condition by ANOVA: \*\*\* $p = 0.0005$ , \*\*\*\* $p < 0.0001$ .
- H. Plaque assay titers from supernatant of infected Calu3 cells treated JQ1 (500nM) and dBET6 (500nM) at MOI of 0.1. Average of three independent experiments analyzed in duplicate  $\pm$  SEM are shown and compared to DMSO condition by ANOVA: \*\* $p = 0.0059$ , \*\*\*\* $p < 0.0001$ .

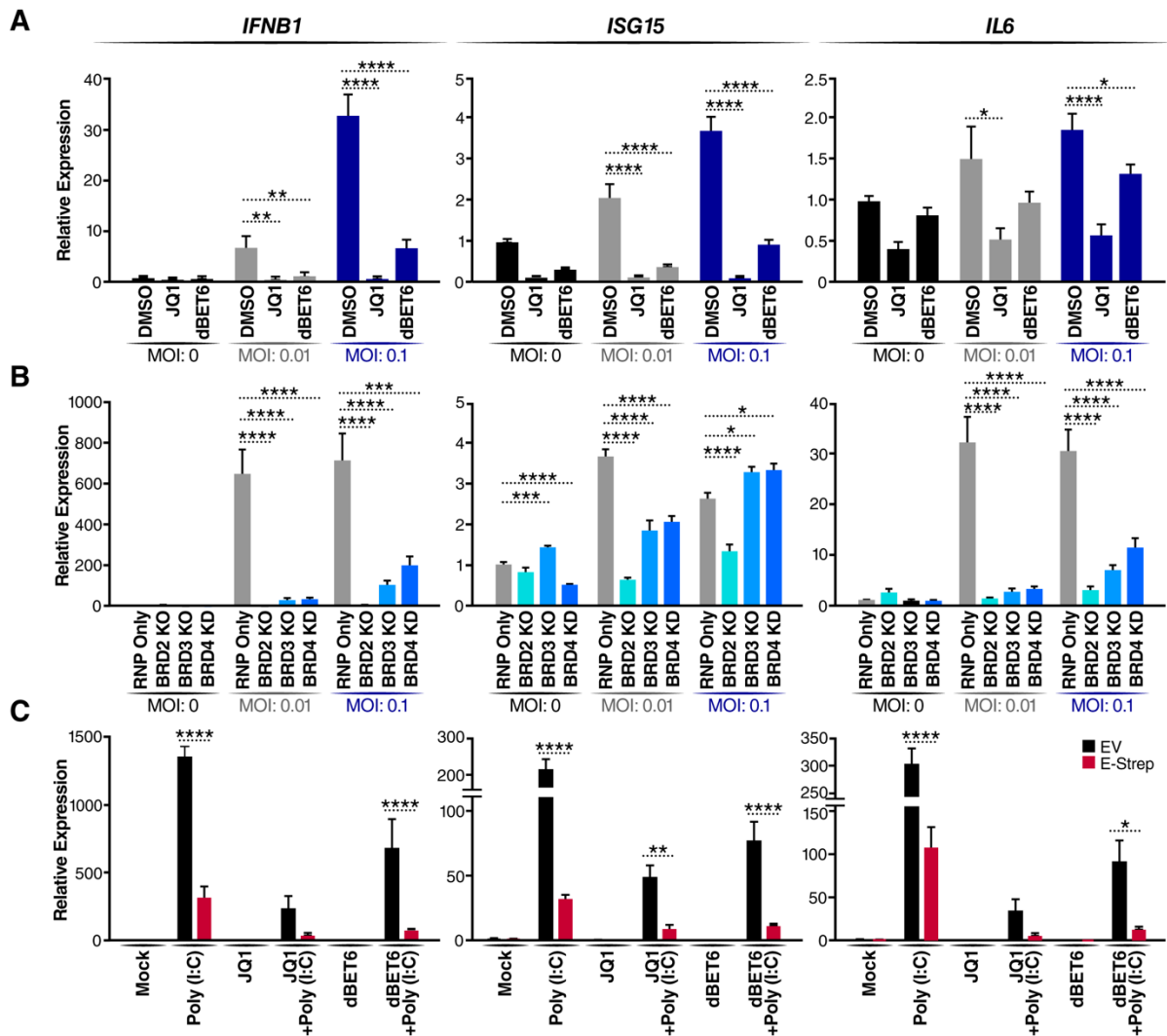


**Figure 2.2. Loss of BET proteins reduces interferon and proinflammatory cytokine expression.**

- A. RT-qPCR of RNA isolated 48 h.p.i. from Calu3 cells infected SARS-CoV-2 (MOI of 0.01 or 0.1) and concurrently treated with JQ1 (500nM) or dBET6 (500nM). Data are expressed relative to DMSO-treated cells for each respective MOI. Average of three independent experiments analyzed in triplicate  $\pm$  SEM are shown and compared to DMSO condition by ANOVA for each MOI: \* $p < 0.05$ , \*\* $p < 0.005$ , \*\*\*\* $p < 0.0001$ .
- B. RT-qPCR of RNA isolated 48 h.p.i. from Calu3 cells with indicated BET protein KOs or KD infected with SARS-CoV-2 (MOI of 0.01 or 0.1). Data are expressed relative to RNP Only cells for each respective MOI. Average of three independent experiments analyzed in triplicate  $\pm$  SEM are shown and compared to RNP Only samples by ANOVA for each MOI: \* $p < 0.05$ , \*\* $p < 0.005$ , \*\*\* $p < 0.001$ , \*\*\*\* $p < 0.0001$ .
- C. RT-qPCR of RNA isolated from A549 cells transfected with empty vector (EV) or SARS-CoV-2 E (E-Strep) plasmid and treated with 10ng/ml Poly (i:C) for 24 hours with and without JQ1 (500nM) or dBET6 (500nM). Mock refers to mock transfection and DMSO treatment to mimic Poly (i:C) transfection and JQ1 or dBET6 treatment. Data are expressed relative to the mock

treated cells. Average of three independent experiments analyzed in triplicate  $\pm$  SEM are shown with ANOVA compared to mock: \* $p=0.0139$ , \*\* $p=0.0097$ , \*\*\* $p<0.0001$ .

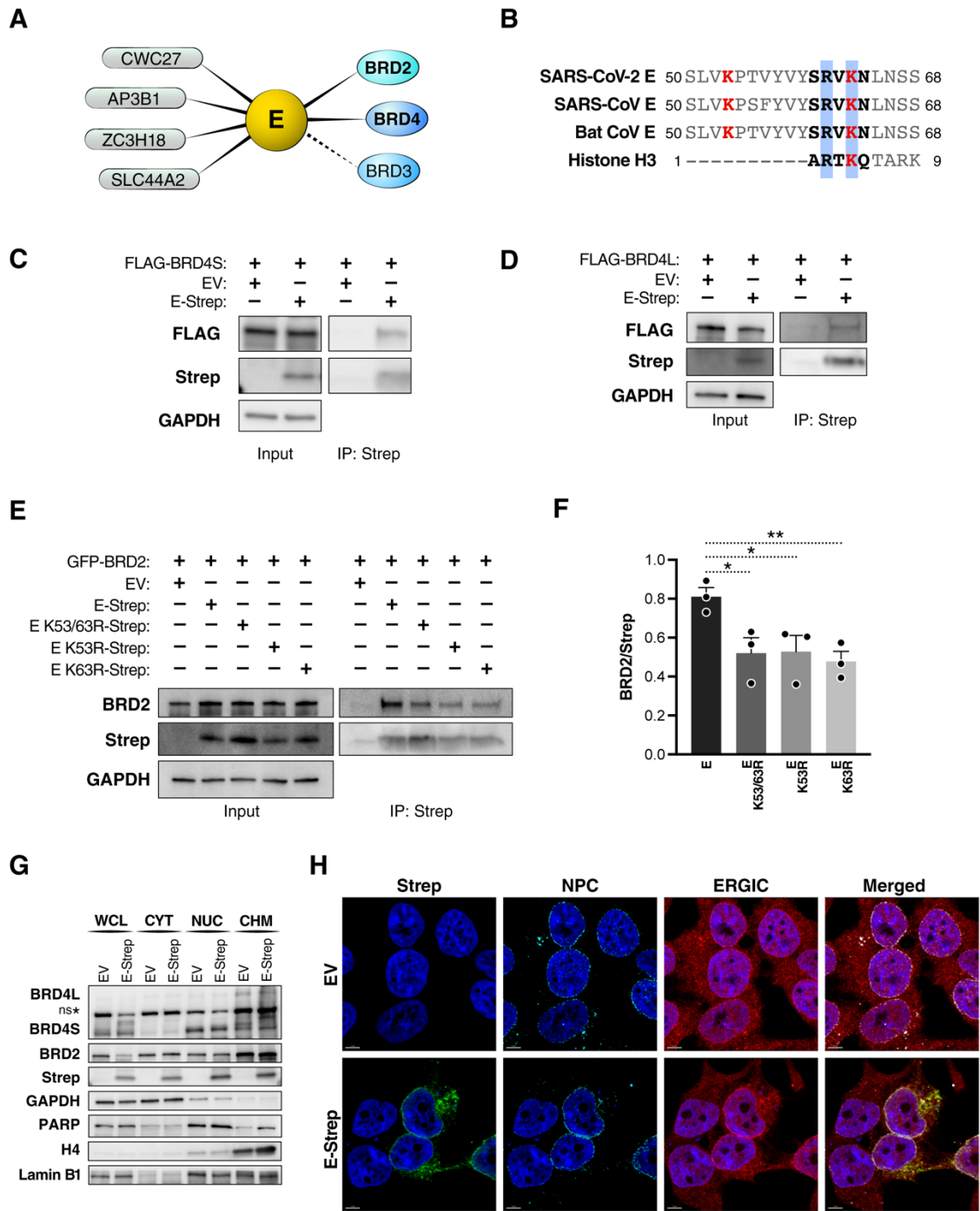


**Figure 2.3. SARS-CoV-2 E protein interacts with BET proteins at the nuclear periphery.**

- A. Host protein interactors, including members of the BET protein family (BRD2, BRD3, BRD4), of the SARS-CoV-2 E protein (Gordon et al., 2020). High confidence interactors above the MiST threshold are shown in solid lines and interactors below the threshold are shown with dashed lines.
- B. The E protein sequences from human and bat (RsHC014) coronaviruses share a histone H3-like motif. Lysine residues at position 53 and 63 are shown in red and the histone H3-like motif is bolded, in black, with RXK motif highlighted in blue. SARS-CoV (YP\_009724392.1), SARS-CoV-2 (NP\_828854.1), Bat CoV (AGZ48809.1), and histone H3 (P68431).

- C. Representative immunoprecipitation of overexpressed Strep-tagged SARS-CoV-2 E (E-Strep) protein with FLAG-tagged BRD4S from co-transfected HEK293T whole-cell lysates, followed by western blotting using FLAG, Strep, and GAPDH antibodies. EV is empty vector control.
- D. Representative immunoprecipitation of overexpressed Strep-tagged SARS-CoV-2 E (E-Strep) protein with FLAG-tagged BRD4L from co-transfected HEK293T whole-cell lysates, followed by western blotting using FLAG, Strep, and GAPDH antibodies. EV is empty vector control.
- E. Representative immunoprecipitation of overexpressed Strep-tagged SARS-CoV-2 E protein constructs with GFP-tagged BRD2 from co-transfected HEK293T whole-cell lysates, followed by western blotting using BRD2, Strep, and GAPDH antibodies. EV is empty vector control.
- F. Densitometry of Figure 2.3E. Average of three independent experiments analyzed in triplicate  $\pm$  SEM are shown and analyzed by Student's t-test: \* $p < 0.05$ , \*\* $p = 0.009$ .
- G. Representative western blotting of whole-cell lysate (WCL), cytoplasmic (CYT), nuclear (NUC), and chromatin (CHM) fractions from HEK293T cells transfected with EV (empty vector) or Strep-tagged SARS-CoV-2 E (Strep-E) with indicated antibodies. \*ns denotes a non-specific band.
- H. Representative confocal microscopy images of HEK293T cells transfected with Strep-tagged SARS-CoV-2 E or control (empty vector). Cells were processed for immunostaining with Strep (SARS-CoV-2 E, green), ERGIC-53 (Endoplasmic reticulum-golgi intermediate compartment, red), NPC (nuclear pore complexes, turquoise), and Hoechst (nuclei, blue). Scale bars, 5 $\mu$ m.



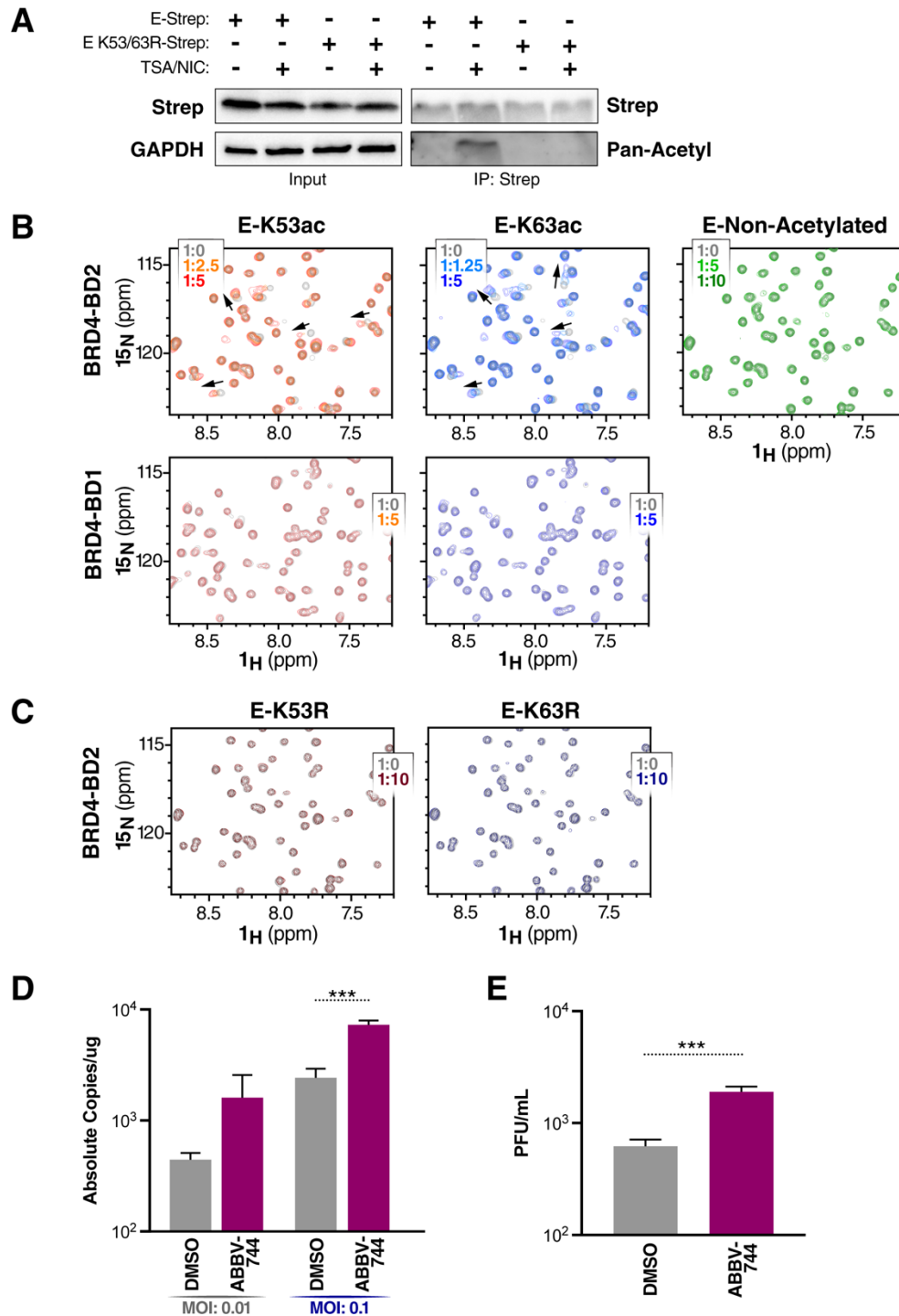


**Figure 2.4. Acetylated SARS-CoV-2 E peptide predominantly binds the second bromodomain of BRD4.**

- A. Representative immunoprecipitation of overexpressed Strep-tagged SARS-CoV-2 E protein constructs (E-Strep and E K53/63R-Strep) from co-transfected HEK293T whole-cell lysates with and without TSA (1 $\mu$ M) and NIC (1mM), followed by western blotting using Strep, pan-acetyl lysine, and GAPDH antibodies.
- B. 2D  $^1\text{H}$   $^{15}\text{N}$  HSQC spectra measured after addition of either E-K53ac (residues 48-58, acetylated), E-K63ac (residues 58-68, acetylated) or Non-

Acetylated (residues 58-70) peptides to  $^{15}\text{N}$  labeled BD1 or BD2. Arrows indicate chemical shift perturbations of peaks. Protein-to-ligand ratio is indicated.

- C. 2D  $^1\text{H}$   $^{15}\text{N}$  HSQC spectra measured after addition of either E-K53R (residues 48-58) and E-K63R (residues 58-68) peptides to  $^{15}\text{N}$  labeled BD2. Protein-to-ligand ratio is indicated.
- D. RT-qPCR of SARS-CoV-2 E RNA isolated 48 h.p.i. from A549-ACE2 cells infected with SARS-CoV-2 (MOI of 0.01 or 0.1) and concurrently treated with BD2-selective inhibitor, ABBV-744 (500nM). Data are expressed in absolute copies/ug based on a standard curve of E gene with known copy number. Average of three independent experiments analyzed in triplicate  $\pm$  SEM are shown and compared to DMSO by Student's t-test:  $***p=0.0004$ .
- E. Plaque assay titers from supernatant of infected A549-ACE2 cells at MOI of 0.1 treated with ABBV-744 (500nM). Average of three independent experiments analyzed in duplicate  $\pm$  SEM are shown and compared to DMSO by Student's t-test:  $***p=0.0001$ .

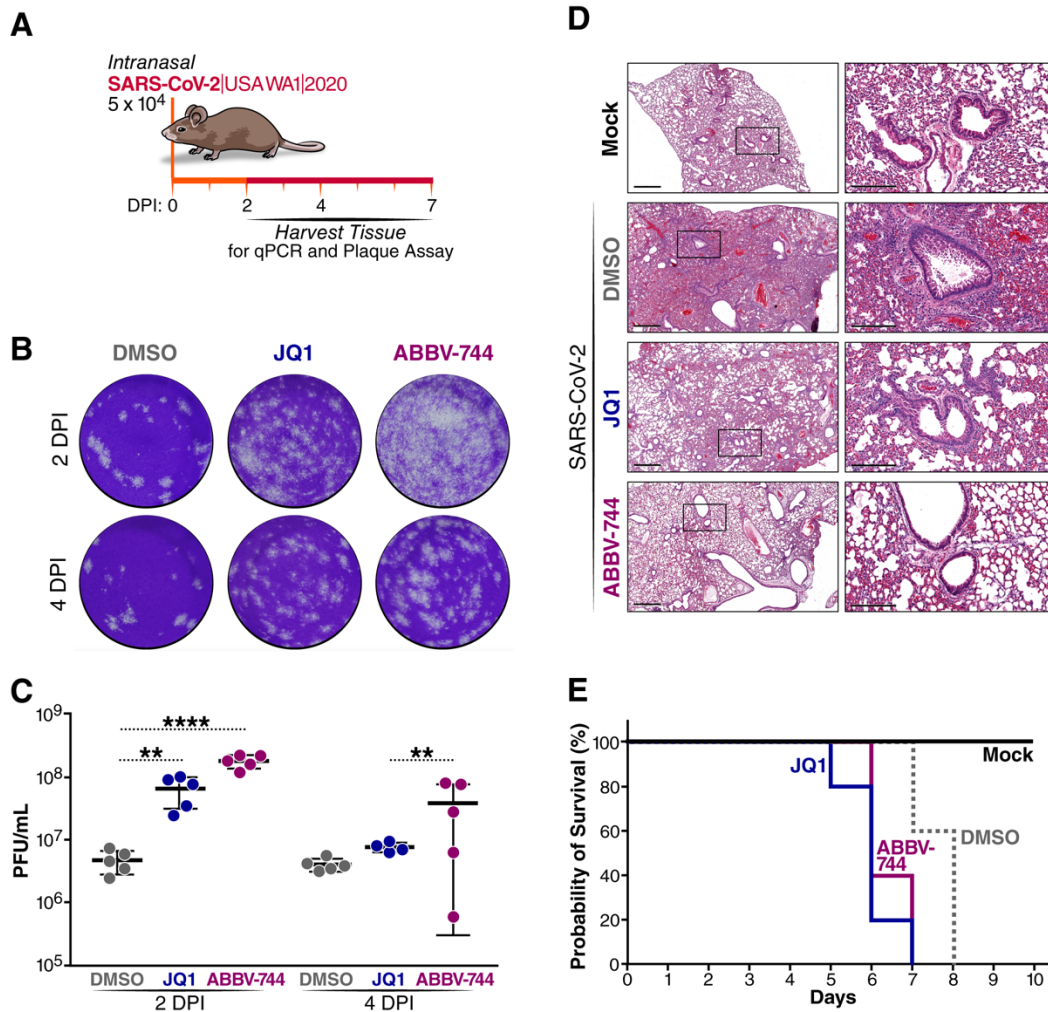


**Figure 2.5. BET inhibitors enhance SARS-CoV-2 infection in K18-hACE2 mice.**

- Schematic of the experiment.
- Representative images of plaque assays at the same dilution from infected mice lungs at 2 and 4 days post infection.
- Plaque assay titers from the lungs of infected mice. Average of 5 mice per group were analyzed, average  $\pm$  SD are shown and compared to DMSO by Student's t-test. 2 dpi: \*\* $p=0.0041$ , \*\*\*\* $p<0.0001$ . 4dpi: \*\* $p=0.0021$ .
- Representative images of H&E staining of lung tissue at 7 days post infection. Box indicates region of inset. Left panels, scale bars, 600 $\mu$ m. Right panels, scale bars, 200 $\mu$ m.
- Survival curve of mock (uninfected) and infected DMSO- (n=15), JQ1- (n=15), and ABBV-744- (n=15) treated mice.

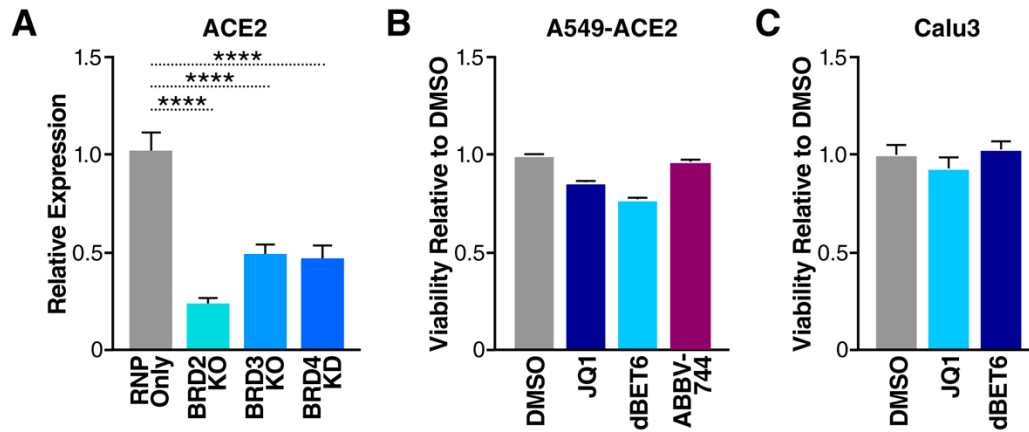


**Figure S2.1. BET proteins are positive regulators of ACE2 expression.**

- A. RT-qPCR of ACE2 RNA isolated from Calu3 cells with indicated BET KOs. Data are expressed relative to RNP Only cells. Average of three independent experiments analyzed in triplicate  $\pm$  SEM are shown and compared to RNP Only samples by ANOVA: \*\*\*\* $p < 0.0001$ .
- B. Viability of A549-ACE2 cells treated with DMSO (vehicle), JQ1 (500nM), dBET6 (500nM), and ABBV-744 (500nM) for 48 hours relative to DMSO.
- C. Viability of Calu3 cells treated with DMSO (vehicle), JQ1 (500nM), and dBET6 (500nM) for 48 hours relative to DMSO.

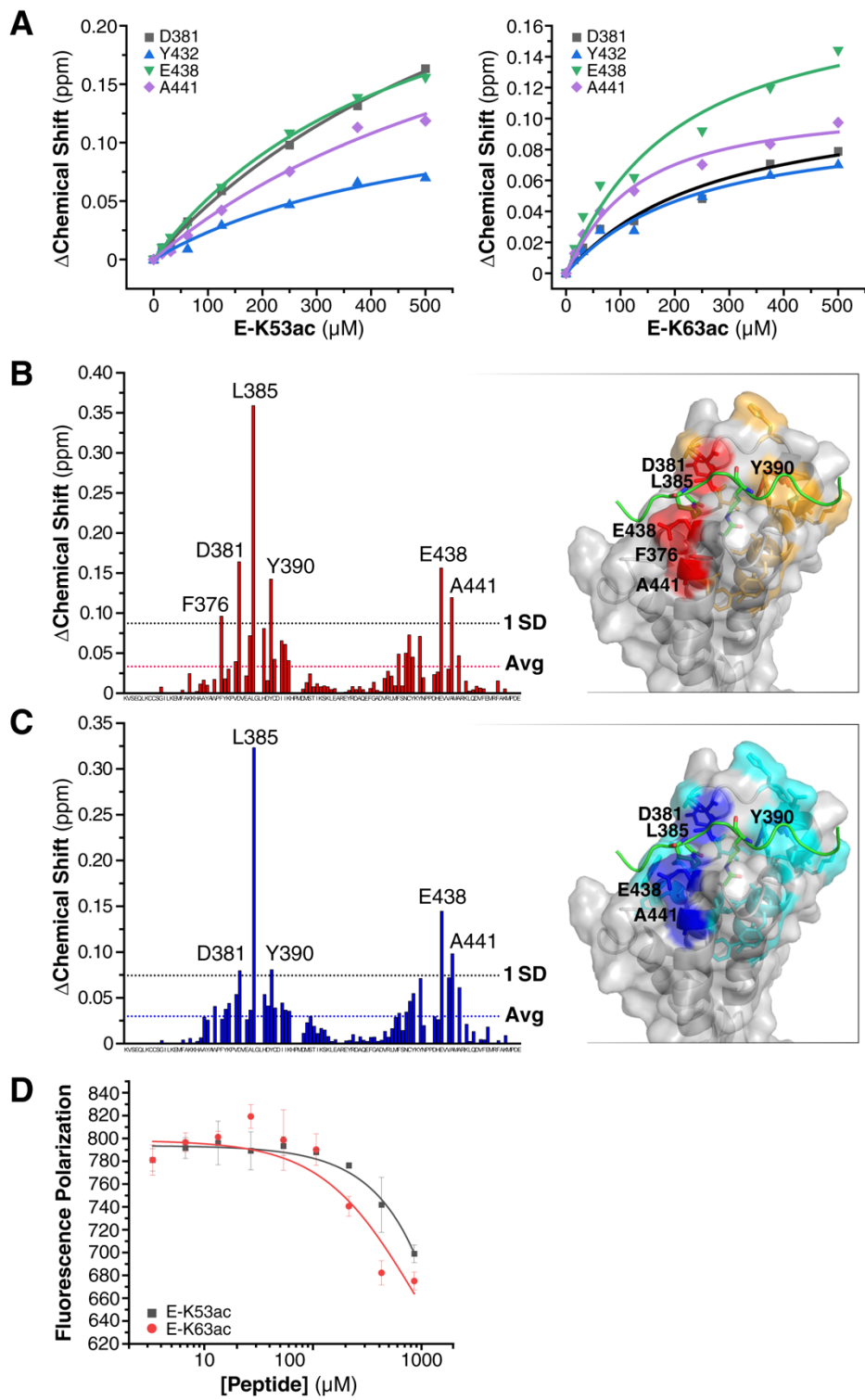


**Figure S2.2. Acetylated E peptide occupies similar binding sites to known acetylated lysine binding sites of BRD4 BD2.**

- A. Binding curve of either E-K53ac or E-K63ac peptides binding to BD2 as measured by change in chemical shift of residue peaks measured in  $^1\text{H}$   $^{15}\text{N}$  HSQC experiments.
- B. Change in chemical shifts in backbone amides of BD2 at a 1:10 molar ratio of protein to E-K53ac (aa 48-58). The right-hand panel shows the structure of BRD4-BD2 in complex with Twist1 K73ac K76ac peptide (PDB ID: 2MJV). Twist1 is in green and acetylated lysine residues are shown. Residues shown in orange are those with a higher-than-average change in chemical shift and those shown in red have shifts larger than 1x SD.
- C. The same as B, but with E-K63ac (aa 58-68) peptide. Residues shown in cyan are those with a higher-than-average change in chemical shift and those shown in blue have shifts larger than 1x SD.
- D. Normalized Fluorescence Polarization (FP) of SUMO-BD2 bound to a JQ1-TAMRA molecule after increasing concentrations of competing peptide E-K53ac (48-58) or E-K63ac (58-68) were added.

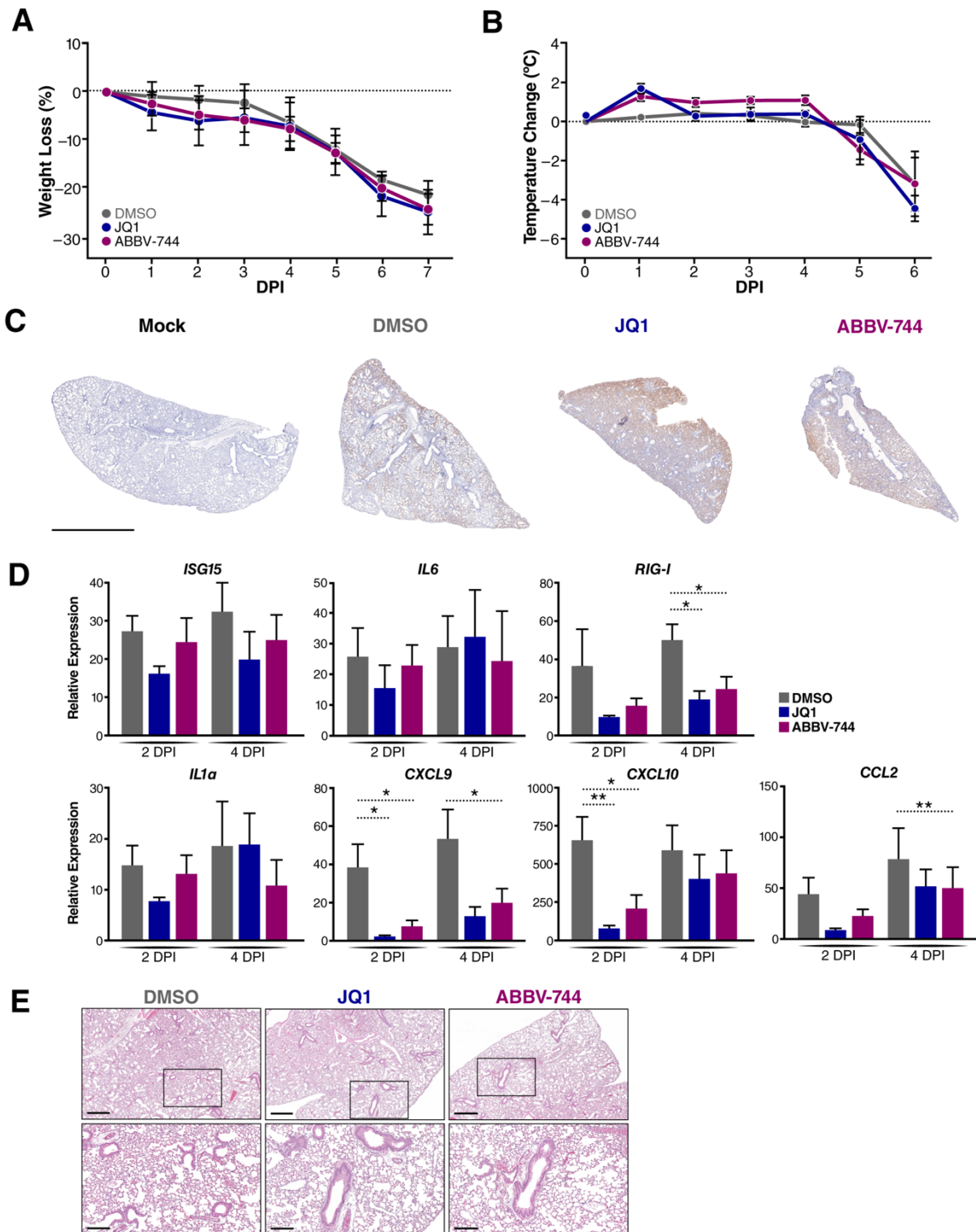


**Figure S2.3. SARS-CoV-2 infection of K18-hACE2 mice results in dysregulated immune responses.**

- A. Changes in weight of SARS-CoV-2 infected mice. n=5 mice per group per time point.
- B. Changes in body temperature of SARS-CoV-2 infected mice. n=5 mice per group per time point.
- C. Representative immunohistochemical staining for SARS-CoV-2 Nucleocapsid in lungs of mice at 7 days post infection. Scale bar, 3mm.

- D. RT-qPCR of RNA isolated 2 and 4 days post infection from lungs of SARS-CoV-2 infected mice treated with DMSO, JQ1, or ABBV-744. Data are expressed relative to uninfected mice for each respective gene. Average of 5 mice in each treatment group per time point analyzed  $\pm$  SEM are shown and compared to DMSO by ANOVA: \*\* $p < 0.005$ , \* $p < 0.05$ .
- E. Representative H&E staining of lungs from healthy, uninfected mice treated with DMSO, JQ1, or ABBV-774. Box indicates region of inset. Top panels, scale bars, 600 $\mu$ m. Bottom panels, scale bars, 200 $\mu$ m.



**Table S2.1. sgRNA sequences for RNP editing.**

Sequences of sgRNA used for generating BET protein KO or KD cells.

<b>Gene</b>	<b>sgRNAs</b>
BRD2	UGAGAGCCCCACAAUGGCUU
	GGU AACUCGUCCUGGCUUUU
	AUCAGUUCGCAUGGCCAUUC
BRD3	AUGUGGUGGUGAAGACGCUC
	UUGCUGGGGUUGGAGACCUC
	GGGGGCGACUGUCGUGGCGG
BRD4	CCUCUUGGGCUUGUUAGGGU
	UCUAGUCCAUCCCCAUUAC
	ACUAGCAUGUCUGCGGAGAG

**Table S2.2. Genotyping primers.**

Genotyping primers used to sequence verify the cas9 editing of BET KO and KD cells.

<b>Gene</b>	<b>Primer F</b>	<b>Primer R</b>	<b>Primer Seq</b>
BRD2	AGCACCTGGATTCA TCAGACT	CCCCATTACACGCAT TCTTG	GATGCACTTTTTCTCA TTTGGACGATATT
BRD3	AGCAAATTCCCAAG GCCAGA	CTTCCTCCTCTGCAGC TGTC	AGCAAATTCCCAAGGC CAGAG
BRD4	CTGACCAGGAGACA TGCAGG	GTGCCCATCTGCTGA CTGAT	CTGACCAGGAGACATG CAGG

**Table S2.3. qPCR primers.**

qPCR primer sequences for gene expression.

<b>Name</b>	<b>Sequence</b>
SARS-CoV-2 E_F	ACAGGTACGTTAATAGTTAATAGCGT
SARS-CoV-2 E_R	ATATTGCAGCAGTACGCACACA
B2M_F	GAGGCTATCCAGCGTACTCCA
B2M_R	CGGCAGGCATACTCATCTTTT
ACE2_F	CGAAGCCGAAGACCTGTTCTA
ACE2_R	GGGCAAGTGTGGACTGTTCC
ISG15_F	CTGTTCTGGCTGACCTTCG
ISG15_R	GGCTTGAGGCCGTACTCC
IFNb_F	CAGGAGAGCAATTTGGAGGA
IFNb_R	CTTTCGAAGCCTTTGCTCTG
IL6_F	AGGAGACTTGCCTGGTGAAA
IL6_R	GCTCTGGCTTGTTCCCTCACT
mISG15_F	GGCCACAGCAACATCTATGA
mISG15_R	CGCAAATGCTTGATCACTGT
mIL6_F	TAGTCCTTCCTACCCCAATTTCC
mIL6_R	TTGGTCCTTAGCCACTCCTTC
mRIG-I_F	CAGACAGATCCGAGACACTA
mRIG-I_R	TGCAAGACCTTTGGCCAGTT
mIL1 $\alpha$ _F	ACTGTTTCTAATGCCTTCCC
mIL1 $\alpha$ _R	ATGGTTTCTTGTGACCCTGA
mCXCL9_F	GCCATGAAGTCCGCTGTTCT
mCXCL9_R	GGGTTCCCTCGAACTCCACACT
mCXCL10_F	GCCGTCATTTTCTGCCTCAT
mCXCL10_R	GCTTCCCTATGGCCCTCATT
mCCL2_F	CTTCTGGGCCTGCTGTTCA
mCCL2_R	CCAGCCTACTCATTGGGATCA

**Table S2.4. SARS-CoV-2 E peptides.**  
Sequences of peptides used in binding studies.

<b>Name</b>	<b>Sequence</b>
E-K53ac (48-58)	NVSLV- <b>K</b> ac-PSFYV
E-K63ac (58-68)	VYSRV- <b>K</b> ac-NLNSS
E-non acetylated (58-70)	VYSRVKLNSSRV
E-K53R (48-58)	NVSLVRPSFYV
E-K63R (58-68)	VYSRVRNLNSS

## REFERENCES

1. Dhalluin, C., Carlson, J.E., Zeng, L., He, C., Aggarwal, A.K., and Zhou, M.M. (1999). Structure and ligand of a histone acetyltransferase bromodomain. *Nature* *399*, 491–496.
2. Filippakopoulos, P., Picaud, S., Mangos, M., Keates, T., Lambert, J.-P., Barsyte-Lovejoy, D., Felletar, I., Volkmer, R., Müller, S., Pawson, T., et al. (2012). Histone recognition and large-scale structural analysis of the human bromodomain family. *Cell* *149*, 214–231.
3. Rahman, S., Sowa, M.E., Ottinger, M., Smith, J.A., Shi, Y., Harper, J.W., and Howley, P.M. (2011). The Brd4 extraterminal domain confers transcription activation independent of pTEFb by recruiting multiple proteins, including NSD3. *Mol. Cell. Biol.* *31*, 2641–2652.
4. Taniguchi, Y. (2016). The Bromodomain and Extra-Terminal Domain (BET) Family: Functional Anatomy of BET Paralogous Proteins. *Int. J. Mol. Sci.* *17*. 10.3390/ijms17111849.
5. Floyd, S.R., Pacold, M.E., Huang, Q., Clarke, S.M., Lam, F.C., Cannell, I.G., Bryson, B.D., Rameseder, J., Lee, M.J., Blake, E.J., et al. (2013). The bromodomain protein Brd4 insulates chromatin from DNA damage signalling. *Nature* *498*, 246–250.
6. Bisgrove, D.A., Mahmoudi, T., Henklein, P., and Verdin, E. (2007). Conserved P-TEFb-interacting domain of BRD4 inhibits HIV transcription. *Proc. Natl. Acad. Sci. U. S. A.* *104*, 13690–13695.

7. Conrad, R.J., Fozouni, P., Thomas, S., Sy, H., Zhang, Q., Zhou, M.-M., and Ott, M. (2017). The Short Isoform of BRD4 Promotes HIV-1 Latency by Engaging Repressive SWI/SNF Chromatin-Remodeling Complexes. *Mol. Cell* 67, 1001–1012.e6.
8. De Rijck, J., de Kogel, C., Demeulemeester, J., Vets, S., El Ashkar, S., Malani, N., Bushman, F.D., Landuyt, B., Husson, S.J., Busschots, K., et al. (2013). The BET family of proteins targets moloney murine leukemia virus integration near transcription start sites. *Cell Rep.* 5, 886–894.
9. Mourão, D., Chen, S., Schaefer, U., Bozzacco, L., Carneiro, L.A., Gerber, A., Adura, C., Dill, B.D., Molina, H., Carroll, T., et al. (2020). A histone-like motif in yellow fever virus contributes to viral replication. *bioRxiv*, 2020.05.05.078782. 10.1101/2020.05.05.078782.
10. Platt, G.M., Simpson, G.R., Mitnacht, S., and Schulz, T.F. (1999). Latent nuclear antigen of Kaposi's sarcoma-associated herpesvirus interacts with RING3, a homolog of the *Drosophila* female sterile homeotic (*fsh*) gene. *J. Virol.* 73, 9789–9795.
11. Sharma, A., Larue, R.C., Plumb, M.R., Malani, N., Male, F., Slaughter, A., Kessler, J.J., Shkriabai, N., Coward, E., Aiyer, S.S., et al. (2013). BET proteins promote efficient murine leukemia virus integration at transcription start sites. *Proc. Natl. Acad. Sci. U. S. A.* 110, 12036–12041.
12. Wu, S.-Y., Lee, A.-Y., Hou, S.Y., Kemper, J.K., Erdjument-Bromage, H., Tempst, P., and Chiang, C.-M. (2006). Brd4 links chromatin targeting to HPV

- transcriptional silencing. *Genes Dev.* *20*, 2383–2396.
13. You, J., Srinivasan, V., Denis, G.V., Harrington, W.J., Jr, Ballestas, M.E., Kaye, K.M., and Howley, P.M. (2006). Kaposi's sarcoma-associated herpesvirus latency-associated nuclear antigen interacts with bromodomain protein Brd4 on host mitotic chromosomes. *J. Virol.* *80*, 8909–8919.
  14. Zhu, N., Zhang, D., Wang, W., Li, X., Yang, B., Song, J., Zhao, X., Huang, B., Shi, W., Lu, R., et al. (2020). A Novel Coronavirus from Patients with Pneumonia in China, 2019. *N. Engl. J. Med.* *382*, 727–733.
  15. Blanco-Melo, D., Nilsson-Payant, B.E., Liu, W.-C., Uhl, S., Hoagland, D., Møller, R., Jordan, T.X., Oishi, K., Panis, M., Sachs, D., et al. (2020). Imbalanced Host Response to SARS-CoV-2 Drives Development of COVID-19. *Cell* *181*, 1036–1045.e9.
  16. Hadjadj, J., Yatim, N., Barnabei, L., Corneau, A., Boussier, J., Smith, N., Péré, H., Charbit, B., Bondet, V., Chenevier-Gobeaux, C., et al. (2020). Impaired type I interferon activity and inflammatory responses in severe COVID-19 patients. *Science* *369*, 718–724.
  17. Jose, R.J., and Manuel, A. (2020). COVID-19 cytokine storm: the interplay between inflammation and coagulation. *The Lancet Respiratory Medicine* *8*, e46–e47.
  18. Hargreaves, D.C., Horng, T., and Medzhitov, R. (2009). Control of inducible gene expression by signal-dependent transcriptional elongation. *Cell* *138*, 129–145.

19. Stratton, M.S., Haldar, S.M., and McKinsey, T.A. (2017). BRD4 inhibition for the treatment of pathological organ fibrosis. *F1000Res.* *6*. 10.12688/f1000research.11339.1.
20. Wienerroither, S., Rauch, I., Rosebrock, F., Jamieson, A.M., Bradner, J., Muhar, M., Zuber, J., Müller, M., and Decker, T. (2014). Regulation of NO synthesis, local inflammation, and innate immunity to pathogens by BET family proteins. *Mol. Cell. Biol.* *34*, 415–427.
21. Gordon, D.E., Jang, G.M., Bouhaddou, M., Xu, J., Obernier, K., White, K.M., O’Meara, M.J., Rezelj, V.V., Guo, J.Z., Swaney, D.L., et al. (2020). A SARS-CoV-2 protein interaction map reveals targets for drug repurposing. *Nature* *583*, 459–468.
22. Schoeman, D., and Fielding, B.C. (2019). Coronavirus envelope protein: current knowledge. *Viol. J.* *16*, 69.
23. Nieto-Torres, J.L., DeDiego, M.L., Verdiá-Báguena, C., Jimenez-Guardeño, J.M., Regla-Nava, J.A., Fernandez-Delgado, R., Castaño-Rodriguez, C., Alcaraz, A., Torres, J., Aguilera, V.M., et al. (2014). Severe acute respiratory syndrome coronavirus envelope protein ion channel activity promotes virus fitness and pathogenesis. *PLoS Pathog.* *10*, e1004077.
24. Shepley-McTaggart, A., Sagum, C.A., Oliva, I., Rybakovsky, E., DiGuilio, K., Liang, J., Bedford, M.T., Cassel, J., Sudol, M., Mullin, J.M., et al. (2021). SARS-CoV-2 Envelope (E) protein interacts with PDZ-domain-2 of host tight junction protein ZO1. *PLoS One* *16*, e0251955.



25. Javorsky, A., Humbert, P.O., and Kvensakul, M. (2021). Structural basis of coronavirus E protein interactions with human PALS1 PDZ domain. *Commun Biol* 4, 724.
26. Mills, R.J., Humphrey, S.J., Fortuna, P.R.J., Lor, M., Foster, S.R., Quaife-Ryan, G.A., Johnston, R.L., Dumenil, T., Bishop, C., Rudraraju, R., et al. (2021). BET inhibition blocks inflammation-induced cardiac dysfunction and SARS-CoV-2 infection. *Cell* 184, 2167–2182.e22.
27. Qiao, Y., Wang, X.-M., Mannan, R., Pitchiaya, S., Zhang, Y., Wotring, J.W., Xiao, L., Robinson, D.R., Wu, Y.-M., Tien, J.C.-Y., et al. (2020). Targeting transcriptional regulation of SARS-CoV-2 entry factors ACE2 and TMPRSS2. *Proc. Natl. Acad. Sci. U. S. A.* 10.1073/pnas.2021450118.
28. Nal, B., Chan, C., Kien, F., Siu, L., Tse, J., Chu, K., Kam, J., Staropoli, I., Crescenzo-Chaigne, B., Escriou, N., et al. (2005). Differential maturation and subcellular localization of severe acute respiratory syndrome coronavirus surface proteins S, M and E. *J. Gen. Virol.* 86, 1423–1434.
29. Nieto-Torres, J.L., Dediego, M.L., Alvarez, E., Jiménez-Guardeño, J.M., Regla-Nava, J.A., Llorente, M., Kremer, L., Shuo, S., and Enjuanes, L. (2011). Subcellular location and topology of severe acute respiratory syndrome coronavirus envelope protein. *Virology* 415, 69–82.
30. Sheppard, G.S., Wang, L., Fidanze, S.D., Hasvold, L.A., Liu, D., Pratt, J.K., Park, C.H., Longenecker, K., Qiu, W., Torrent, M., et al. (2020). Discovery of N-Ethyl-4-[2-(4-fluoro-2,6-dimethyl-phenoxy)-5-(1-hydroxy-1-methyl-ethyl)phenyl]-6-

- methyl-7-oxo-1H-pyrrolo[2,3-c]pyridine-2-carboxamide (ABBV-744), a BET Bromodomain Inhibitor with Selectivity for the Second Bromodomain. *J. Med. Chem.* *63*, 5585–5623.
31. Jia, H.P., Look, D.C., Shi, L., Hickey, M., Pewe, L., Netland, J., Farzan, M., Wohlford-Lenane, C., Perlman, S., and McCray, P.B., Jr (2005). ACE2 receptor expression and severe acute respiratory syndrome coronavirus infection depend on differentiation of human airway epithelia. *J. Virol.* *79*, 14614–14621.
  32. Gilan, O., Rioja, I., Knezevic, K., Bell, M.J., Yeung, M.M., Harker, N.R., Lam, E.Y.N., Chung, C.-W., Bamborough, P., Petretich, M., et al. (2020). Selective targeting of BD1 and BD2 of the BET proteins in cancer and immunoinflammation. *Science* *368*, 387–394.
  33. Malik, N., Vollmer, S., Nanda, S.K., Lopez-Pelaez, M., Prescott, A., Gray, N., and Cohen, P. (2015). Suppression of interferon  $\beta$  gene transcription by inhibitors of bromodomain and extra-terminal (BET) family members. *Biochem. J* *468*, 363–372.
  34. Patel, M.C., Debrosse, M., Smith, M., Dey, A., Huynh, W., Sarai, N., Heightman, T.D., Tamura, T., and Ozato, K. (2013). BRD4 coordinates recruitment of pause release factor P-TEFb and the pausing complex NELF/DSIF to regulate transcription elongation of interferon-stimulated genes. *Mol. Cell. Biol.* *33*, 2497–2507.
  35. Cheung, K.L., Zhang, F., Jaganathan, A., Sharma, R., Zhang, Q., Konuma, T., Shen, T., Lee, J.-Y., Ren, C., Chen, C.-H., et al. (2017). Distinct Roles of Brd2

- and Brd4 in Potentiating the Transcriptional Program for Th17 Cell Differentiation. *Mol. Cell* *65*, 1068–1080.e5.
36. Andrieu, G.P., and Denis, G.V. (2018). BET Proteins Exhibit Transcriptional and Functional Opposition in the Epithelial-to-Mesenchymal Transition. *Mol. Cancer Res.* *16*, 580–586.
  37. Garcia-Gutierrez, P., Mundi, M., and Garcia-Dominguez, M. (2012). Association of bromodomain BET proteins with chromatin requires dimerization through the conserved motif B. *J. Cell Sci.* *125*, 3671–3680.
  38. Schröder, S., Cho, S., Zeng, L., Zhang, Q., Kaehlcke, K., Mak, L., Lau, J., Bisgrove, D., Schnölzer, M., Verdin, E., et al. (2012). Two-pronged binding with bromodomain-containing protein 4 liberates positive transcription elongation factor b from inactive ribonucleoprotein complexes. *J. Biol. Chem.* *287*, 1090–1099.
  39. Schaefer, U., Ho, J.S.Y., Prinjha, R.K., and Tarakhovsky, A. (2013). The “histone mimicry” by pathogens. *Cold Spring Harb. Symp. Quant. Biol.* *78*, 81–90.
  40. Qin, S., Liu, Y., Tempel, W., Eram, M.S., Bian, C., Liu, K., Senisterra, G., Crombet, L., Vedadi, M., and Min, J. (2014). Structural basis for histone mimicry and hijacking of host proteins by influenza virus protein NS1. *Nat. Commun.* *5*, 1–11.
  41. Pagans, S., Pedal, A., North, B.J., Kaehlcke, K., Marshall, B.L., Dorr, A., Hetzer-Egger, C., Henklein, P., Frye, R., McBurney, M.W., et al. (2005). SIRT1 regulates HIV transcription via Tat deacetylation. *PLoS Biol.* *3*, e41.

42. Huo, L., Li, D., Sun, X., Shi, X., Karna, P., Yang, W., Liu, M., Qiao, W., Aneja, R., and Zhou, J. (2011). Regulation of Tat acetylation and transactivation activity by the microtubule-associated deacetylase HDAC6. *J. Biol. Chem.* *286*, 9280–9286.
43. Kiernan, R.E., Vanhulle, C., Schiltz, L., Adam, E., Xiao, H., Maudoux, F., Calomme, C., Burny, A., Nakatani, Y., Jeang, K.-T., et al. (1999). HIV-1 Tat transcriptional activity is regulated by acetylation. *EMBO J.* *18*, 6106–6118.
44. Ott, M., Schnölzer, M., Garnica, J., Fischle, W., Emiliani, S., Rackwitz, H.R., and Verdin, E. (1999). Acetylation of the HIV-1 Tat protein by p300 is important for its transcriptional activity. *Curr. Biol.* *9*, 1489–1492.
45. Schoeman, D., and Fielding, B.C. (2020). Is There a Link Between the Pathogenic Human Coronavirus Envelope Protein and Immunopathology? A Review of the Literature. *Front. Microbiol.* *11*, 2086.
46. Gilham, D., Smith, A.L., Fu, L., Moore, D.Y., Muralidharan, A., Reid, S.P.M., Stotz, S.C., Johansson, J.O., Sweeney, M., Wong, N.C.W., et al. (2021). Bromodomain and Extraterminal Protein Inhibitor, Apabetalone (RVX-208), Reduces ACE2 Expression and Attenuates SARS-Cov-2 Infection In Vitro. *Biomedicines* *9*. 10.3390/biomedicines9040437.
47. Conant, D., Hsiau, T., Rossi, N., Oki, J., Maures, T., Waite, K., Yang, J., Joshi, S., Kelso, R., Holden, K., et al. (2022). Inference of CRISPR Edits from Sanger Trace Data. *CRISPR J* *5*, 123–130.
48. National Research Council (US) Committee for the Update of the Guide for the Care and Use of Laboratory Animals (2011). *Guide for the Care and Use of*

Laboratory Animals (National Academies Press (US)).

49. Olp, M.D., Zhu, N., and Smith, B.C. (2017). Metabolically Derived Lysine Acylations and Neighboring Modifications Tune the Binding of the BET Bromodomains to Histone H4. *Biochemistry* 56, 5485–5495.

## Chapter III

### Limited cross-variant immunity from SARS-CoV-2 Omicron without vaccination

Rahul K. Suryawanshi<sup>1†</sup>, Irene P Chen<sup>1,2,3,4†</sup>, Tongcui Ma<sup>1,16,†</sup>, Abdullah M. Syed<sup>1,8</sup>, Noah Brazer<sup>6</sup>, Prachi Saldhi<sup>6</sup>, Camille R Simoneau<sup>1,3,4</sup>, Alison Ciling<sup>1,8</sup>, Mir M. Khalid<sup>1</sup>, Bharath Sreekumar<sup>1</sup>, Pei-Yi Chen<sup>1</sup>, G. Renuka Kumar<sup>1</sup>, Mauricio Montano<sup>1,17</sup>, Ronne Gascon<sup>1</sup>, Chia-Lin Tsou<sup>1</sup>, Miguel A Garcia-Knight<sup>5</sup>, Alicia Sotomayor-Gonzalez<sup>6</sup>, Venice Servellita<sup>6</sup>, Amelia Gliwa<sup>6</sup>, Jenny Nguyen<sup>6</sup>, Ines Silva<sup>7</sup>, Bilal Milbes<sup>7</sup>, Noah Kojima<sup>7</sup>, Victoria Hess<sup>7</sup>, Maria Shacreaw<sup>7</sup>, Lauren Lopez<sup>7</sup>, Matthew Brobeck<sup>7</sup>, Fred Turner<sup>7</sup>, Frank W Soveg<sup>1</sup>, Ashley F. George<sup>1,14</sup>, Xiaohui Fang<sup>15</sup>, Mazharul Maishan<sup>15</sup>, Michael Matthay<sup>15</sup>, Mary Kate Morris<sup>18</sup>, Debra Wadford<sup>18</sup>, Carl Hanson<sup>18</sup>, Warner C. Greene<sup>1,3,5,17</sup>, Raul Andino<sup>5</sup>, Lee Spraggon<sup>7</sup>, Nadia R. Roan<sup>1,14\*</sup>, Charles Y. Chiu<sup>3,6,8,16,19\*</sup>, Jennifer Doudna<sup>1,8-13\*</sup>, Melanie Ott<sup>1,3,4,19\*</sup>

#### Affiliations

<sup>1</sup>Gladstone Institutes, San Francisco, CA, USA.

<sup>2</sup>Biomedical Sciences Graduate Program, University of California San Francisco, San Francisco, CA, USA.

<sup>3</sup>Department of Medicine, University of California San Francisco, San Francisco, CA, USA

<sup>4</sup>Quantitative Biosciences Institute COVID-19 Research Group, University of California San Francisco; San Francisco, CA, USA.

<sup>5</sup>Department of Microbiology and Immunology, University of California, San Francisco, San Francisco, CA, USA

<sup>6</sup>Department of Laboratory Medicine, University of California, San Francisco, San Francisco, CA 94158, USA

<sup>7</sup>Curative Inc., 430 S Cataract Ave San Dimas, CA, USA

<sup>8</sup>Innovative Genomics Institute, University of California, Berkeley, Berkeley, CA, USA

<sup>9</sup>Department of Molecular and Cell Biology, University of California, Berkeley, CA, USA

<sup>10</sup>Molecular Biophysics and Integrated Bioimaging Division, Lawrence Berkeley National Laboratory, Berkeley, CA, USA

<sup>11</sup>Howard Hughes Medical Institute, University of California, Berkeley, Berkeley, CA, USA

<sup>12</sup>Department of Chemistry, University of California, Berkeley, Berkeley, CA, USA

<sup>13</sup>California Institute for Quantitative Biosciences, University of California, Berkeley, Berkeley

<sup>14</sup>Department of Urology, University of California, San Francisco, San Francisco, United States

<sup>15</sup>Department of Medicine and Department of Anesthesia, Cardiovascular Research Institute, University of California San Francisco, San Francisco, CA, USA.

<sup>16</sup>UCSF-Abbott Viral Diagnostics and Discovery Center, San Francisco, CA, USA

<sup>17</sup>Michael Hulton Center for HIV Cure Research at Gladstone; San Francisco, CA, USA

<sup>18</sup>California Department of Public Health, Richmond, CA 94804, USA

<sup>19</sup>Chan Zuckerberg Biohub, San Francisco, CA 94158, USA.

†Equal contribution

\*Correspondence: melanie.ott@gladstone.ucsf.edu, doudna@berkeley.edu,  
charles.chiu@ucsf.edu, nadia.roan@gladstone.ucsf.edu



## **ABSTRACT**

SARS-CoV-2 Delta and Omicron are globally relevant variants of concern (VOCs). While individuals infected with Delta are at risk to develop severe lung disease, infection with Omicron often causes milder symptoms, especially in vaccinated individuals<sup>1,2</sup>. The question arises whether widespread Omicron infections could lead to future cross-variant protection, accelerating the end of the pandemic. Here we show that without vaccination, infection with Omicron induces a limited humoral immune response in mice and humans. Sera from mice overexpressing the human ACE2 receptor and infected with Omicron neutralize only Omicron, but no other VOCs, whereas broader cross-variant neutralization was observed after WA1 and Delta infections. Unlike WA1 and Delta, Omicron replicates to low levels in the lungs and brains of infected animals, leading to mild disease with reduced pro-inflammatory cytokine expression and diminished activation of lung-resident T cells. Sera from unvaccinated, Omicron-infected individuals show the same limited neutralization of only Omicron itself. In contrast, Omicron breakthrough infections induce overall higher neutralization titers against all VOCs. Our results demonstrate that Omicron infection enhances preexisting immunity elicited by vaccines but, on its own, may not confer broad protection against non-Omicron variants in unvaccinated individuals.

## INTRODUCTION

Since the beginning of the COVID-19 pandemic, multiple waves of infection have occurred from SARS-CoV-2 VOCs that continue to arise and out-compete preceding variants. VOCs with worldwide relevance are Delta (B.1.617.2) and most recently Omicron (BA.1), while Alpha (B.1.1.7), Beta (B.1.351), and Gamma (P.1) variants spread more locally. Compared to ancestral isolate (WA1 or B.1) Omicron is characterized by a large number of unique mutations in spike as well as in other structural proteins, select nonstructural proteins, and accessory open reading frames. Omicron bears over 50 mutations across its genome, including ~37 mutations (28 being unique and nine overlapping with other variants) in the spike glycoprotein, which may contribute to its antigenic differences<sup>3-9</sup>.

The constellation of mutations in the Omicron spike protein has been associated with increased transmission<sup>10</sup>, decreased spike cleavage<sup>11</sup>, and decreased cell-to-cell fusion<sup>11,12</sup>. Importantly, Omicron spike mutations limit efficacies of neutralizing antibodies generated by previous infections, vaccines, and monoclonal antibody treatment<sup>3-9,13</sup>. Indeed, the risk of breakthrough infections and re-infections is increased with Omicron<sup>13-15</sup>. However, disease severity is lower with Omicron than Delta<sup>1,2,13</sup>, and prior infection or vaccination reduces the risk of hospitalization with Omicron<sup>16,17</sup>. Pressing questions are how effective Omicron-induced immunity is, and whether it is cross-protective against other variants.

## RESULTS

### **Robust infection of mice and human airway cells by Delta and the ancestral isolate but not Omicron**

To answer these questions, we studied WA1, Delta, and Omicron infections in mice. Because WA1 and Delta variants cannot infect regular laboratory mice<sup>18</sup>, we used transgenic mice overexpressing human ACE2 (K18-hACE2)<sup>19</sup>. We intranasally infected ( $10^4$  PFU) these mice with the three viral isolates and over 7 days monitored their body temperature and weight, which serves as indicators of disease progression (Figure 3.1a). While Delta- and WA1-infected mice showed progressive hypothermia and severe weight loss during this time, Omicron-infected mice exhibited very mild symptoms with only a small increase in body temperature and no weight loss (Figure 3.1b, c). Five days after infection, the WA1- and Delta-infected mice were hunched or lethargic, but the Omicron-infected mice appeared completely normal (Figure S3.1a). All of the Omicron-infected mice survived the 1-week experiment; yet, 100% of WA1- and 60% of the Delta-infected animals reached the humane end-point during this time (Figure 3.1d). This replicates previous findings from infected individuals, mice, and hamsters that show mild disease with Omicron, but not with Delta and WA1 infections<sup>1,2,20–24</sup>.

To assess viral replication dynamics, we quantified infectious particle production (Figure 3.2a, b), and viral RNA expression (Figure S3.2a, b) in the respiratory tracts and lungs of infected mice over time. Across all time points, high titers of infectious virus were present in upper airways (nasal turbinates and bronchi) and lungs of WA1- and Delta-infected mice, whereas Omicron replication was significantly lower in these

organs, as reported<sup>20-22</sup>. Lung histology showed that Omicron infection resulted in small localized foci of infected cells (marked by nucleocapsid staining, green) (Figure S3.1b, c, d). A similar pattern but enhanced numbers were observed after WA1 infection, and Delta infection showed large patches of infected cells, indicative of enhanced cell-to-cell spread, as reported in human lung organoids and cell lines<sup>11</sup> (Figure S3.1b, c, d). In addition, brain tissue, which is a target for viral replication in K18-hACE2 mice, showed lower Omicron replication 4 and 7 days after infection. Omicron also produced fewer infectious particles in human airway organoids and the human alveolar A549 epithelial cell line overexpressing ACE2 than WA1 and Delta infections (Figure 3.2c, d), which is consistent with our findings in the mice.

### **Inflammatory and T-cell markers differ between variants**

As severe COVID-19 is associated with cytokine storms in conjunction with exhaustion of T cells<sup>25</sup>, we next assessed cytokine expression and T-cell phenotypes in infected mouse lungs. While infection with WA1 and Delta readily induced proinflammatory markers of severe COVID, such as CXCL10 and CCL2<sup>26</sup>, induction by Omicron was significantly reduced early after infection (Figure S3.3a). Induction of interleukin 1 $\alpha$  (IL1 $\alpha$ ) was not significantly different between the three viral isolates, but trended towards lower expression in Omicron-infected animals 2 days post-infection (Figure S3.3a). Although no significant differences between the viral variants were observed in the induction of interferon- $\alpha$  (IFN $\alpha$ ) or relevant downstream induced genes, such as interferon-stimulated gene 15 (ISG15) and 2'-5'-oligoadenylate synthetase 1 (OAS1), we cannot exclude that this is caused by low number of animals at later time points (Figure S3.3a-b).

To determine if the pro-inflammatory response we observed in WA1-infected mice is also associated with T-cell exhaustion in late infection, we generated single-cell suspensions from the lungs of mock- and WA1-infected mice, and performed Cytometry by Time of Flight (CyTOF) mass spectrometry before and after stimulation with overlapping 15-mer peptides spanning the entire spike protein. tSNE visualization of the CyTOF data corresponding to total immune (CD45+) cells from the unstimulated specimens revealed that both CD4+ and CD8+ T cells of infected mice segregate distinctly from their respective counterparts in the mock-infected mice, indicating profound phenotypic changes in pulmonary T cells upon WA1 infection, including upregulation of activation/exhaustion marker programmed cell death 1 (PD1) on T cells from the infected animals (Figure 3.3a).

When similar experiments were performed with infections by WA1, Delta, and Omicron, we found elevated expression of not only PD1 but also cytotoxic T-lymphocyte-associated protein 4 (CTLA4, another activation/exhaustion marker) on pulmonary T cells in all infected animals, although to a significantly lesser extent in the Omicron-infected mice (Figure 3.3b, c). Despite evidence of pulmonary T-cell exhaustion in mice infected with all three isolates, functional SARS-CoV-2-specific T cells were still generated in the lungs, as demonstrated by our identification of IFN $\gamma$ - and TNF $\alpha$ -producing cells specifically in the peptide-stimulated specimens (Figure 3.3d, e, f). These results suggest the diminished pro-inflammatory cytokines and activated/exhausted pulmonary T cells elicited by Omicron associates with diminished Omicron pathogenicity and the 2–3 logs decrease in Omicron replication.

### **Infection with Omicron does not induce cross-variant neutralization**

To determine humoral immune responses induced by infection with the three different isolates, we collected sera from mice at 7 days after infection, and tested their neutralization efficiency against SARS-CoV-2 isolates: WA1, Alpha, Beta, Delta, and Omicron. We determined the plaque-forming units at different serum dilutions and calculated the 50% neutralization titers (NT50) (Figure 3.4). As expected, sera from uninfected mice showed no neutralization across all variants (Figure 3.4a). Sera from WA1-infected mice showed effective neutralization of WA1 and Alpha and, to a lesser extent, Beta and Delta isolates, but no efficacy against Omicron (NT50 6) (Figure 3.4b). In contrast, sera from Delta-infected mice effectively neutralized Delta (NT50 422), WA-1 (NT50 275), Alpha (NT50 356), and to a lesser extent Omicron (NT50 115) and Beta (NT50 62), with the latter significantly decreased, compared to Delta and Alpha (Figure 3.4c). Omicron infection, however, only induced neutralization of Omicron (NT50 113), but no other isolate (NT50 3–7) (Figure 3.4d). This was repeated and confirmed in a second experiment in which, 9 days after infection, all mice infected with Omicron showed significant serum neutralization of Omicron (NT50 92), but no other VOC (NT50 7-16) (Figure 3.4e). These results indicate limited cross-variant neutralization induced by Omicron relative to other isolates, which may be due to its highly mutated spike protein or its lower replicative capacity (Figure 3.2). Notably, Delta and WA1, despite having similar replicative and inflammatory capacities, exhibited different neutralization profiles, underscoring the role of the different spike (and possibly other viral) proteins in eliciting cross-variant neutralization.

These data were confirmed with sera from 10 unvaccinated individuals, who had recovered from Omicron infection (Table S3.1). These sera showed the same limited cross-variant neutralization as observed in mice with effective neutralization of only Omicron itself (NT50 1452) and a ~15-fold decrease in neutralizing titers against non-Omicron isolates (NT50 15–96) (Figure 3.5a). Analysis of sera from 11 matched, unvaccinated individuals with Delta infection showed a similar pattern: highest neutralization of Delta itself (NT50 2811), followed by WA1 (NT50 619) and decreased neutralization of Alpha, Beta and Omicron (NT50 41-62) (Figure 3.5b, Table S3.1). Sera from uninfected, unvaccinated individuals showed no neutralization across all variants as expected (Figure S3.4a).

Notably, sera from vaccinated individuals with confirmed Omicron or Delta breakthrough infections showed high neutralizing titers against all isolates, with highest titers against WA1 (NT50 17994 and 23308) and lowest against Omicron (NT50 1241 and 1692) (Figure S3.5c-d). These values exceeded neutralizing titers induced by the third shot of Pfizer/BioNTech vaccines where titers were, on average, 10 times lower than those observed after breakthrough infections (Figure S3.4b). These results suggest that Omicron and Delta breakthrough infections can boost existing immunity conferred by vaccination, thereby eliciting a form of “hybrid immunity” that is effective against not only itself, but also other SARS-CoV-2 variants.

## **DISCUSSION**

Collectively, our study shows that, while the Omicron variant is immunogenic, infection in unvaccinated individuals may not elicit effective cross-neutralizing antibodies against non-Omicron variants. In vaccinated individuals, however, Omicron infection effectively induces immunity against itself and enhances neutralization of other variants. This, together with our finding that Delta infection also elicits broad cross-variant neutralization in vaccinated individuals, supports the inclusion of Omicron- and Delta-based immunogens in future heterologous or multivalent vaccination strategies for broad protection against variants.



## **MATERIAL AND METHODS**

### **Human lung organoids**

Whole human lung tissue was digested to a single-cell suspension and plated in basement membrane extract as published<sup>27</sup>. Briefly, organoids were maintained in DMEM supplemented with supplemented with 10% (vol/vol) R-spondin1 conditioned medium, 1% B27 (Gibco), 25 ng/mL Noggin (Peprotech), 1.25 mM N-acetylcysteine (Sigma-Aldrich), 10 mM nicotinamide (Sigma-Aldrich), 5 nM Herefulin Beta-1 (Peprotech), and 100  $\mu$ g/mL Primocin (InvivoGen). HAO medium was further supplemented with 5  $\mu$ M Y-27632, 500 nM A83-01, 500 nM SB202190, 25 ng/mL FGF-7, and 100 ng/mL FGF-10 (all from Stem Cell Technologies). HAO medium was replaced every 3-4 days.

A549 cells expressing ACE2 (A549-ACE2) from ATCC and Vero cells expressing TMPRSS2 (Vero-TMPRSS2) were a gift from O. Schwartz and S.P.J. Whelan, respectively. A549-ACE2 and Vero-TMPRSS2 cells were cultured in DMEM supplemented with 10% FBS and blasticidin (20  $\mu$ g/ml) (Sigma) at 37°C and 5% CO<sub>2</sub>. Short terminal repeat analysis by the Berkeley Cell Culture Facility authenticated these as A549 cells with 100% probability.

Vero stably co-expressing human ACE2 and TMPRSS2 cells (gifted from A. Creanga and B. Graham at NIH) were maintained at 37°C and 5% CO<sub>2</sub> in DMEM (Gibco) supplemented with 10% fetal calf serum, 100  $\mu$ g/mL penicillin and streptomycin (Gibco) and 10  $\mu$ g/mL of puromycin (Gibco).

293T cells stably co-expressing ACE2 and TMPRSS2 were generated by sequential transduction of 293T cells with TMPRSS2-encoding (generated using Addgene plasmid #170390, a gift from Nir Hacohen and ACE2-encoding (generated using Addgene plasmid #154981, a gift from Sonja Best) lentiviruses and selection with hygromycin (250  $\mu\text{g}/\text{mL}$ ) and blasticidin (10  $\mu\text{g}/\text{mL}$ ) for 10 days, respectively. ACE2 and TMPRSS2 expression was verified by western blot.

### **SARS-CoV-2 virus culture**

SARS-CoV-2/human/USA/USA-WA1/2020 (WA1) (BEI NR-52281), B.1.1.7 (California Department of Health), B.1.351 (BEI NR-54008), B.1.617.2 (California Department of Health) and B.1.1.529 (California Department of Health, BA.1) were used for animal infection studies or serum virus neutralization. The virus infection experiments were performed in a Biosafety Level 3 laboratory. Working stocks of SARS-CoV-2 were made in Vero-TMPRSS2 cells and were stored at  $-80^{\circ}\text{C}$  until used.

The Omicron variant was isolated from a nasopharyngeal swab sample from a patient hospitalized with COVID-19 at the University of California, San Francisco (UCSF). A 200  $\mu\text{L}$  aliquot of the sample was serially diluted 1:1 with medium (DMEM supplemented with 1x penicillin/streptomycin) in a 96-well plate for five dilutions, in duplicate. Then, 100  $\mu\text{L}$  of freshly trypsinized Vero-hACE2-TMPRSS2 cells, resuspended in infection medium (made as above but with 2x penicillin/streptomycin, 5  $\mu\text{g}/\text{mL}$  amphotericin B [Bioworld] and no puromycin) were added to the nasal sample dilutions at  $2.5 \times 10^5$  cells/mL concentration. Cells were cultured at  $37^{\circ}\text{C}$  and 5%  $\text{CO}_2$  and checked for cytopathic effects (CPEs) from day 2-3. Vero-hACE2-TMPRSS2 cells

formed characteristic syncytia upon infection with SARS-CoV-2, enabling rapid and specific visual evaluation for CPE. Supernatants were harvested on day 3 after inoculation. A 200  $\mu$ l aliquot of P0 was used to infect a confluent T25 flask to generate a P1 culture, harvested after 3 days. Virus stocks were titered by plaque assay, and the sequence was confirmed by nanopore sequencing.

### **K18-hACE2 mouse infection model**

All protocols concerning animal use were approved (AN169239-01C) by the Institutional Animal Care and Use committees at the University of California, San Francisco and Gladstone Institutes and conducted in strict accordance with the National Institutes of Health Guide for the Care and Use of Laboratory Animal<sup>28</sup>. Mice were housed in a temperature (65-75° F) and humidity (40-60%) controlled pathogen-free facility with 12-hour light/dark cycle and ad libitum access to water and standard laboratory rodent chow.

Briefly, the study involved intranasal infection ( $1 \times 10^4$ ) of 6–8-week-old female K18-hACE2 mice with Delta and Omicron, and WA1 served as a control isolate of SARS-CoV-2. A total of 15 animals were infected for each variant. Five mice from each group were euthanized at days 2, 4 and 7 post-infection. The brain, lungs, and upper respiratory tract, including bronchus and nasal turbinates, were processed for further analysis of virus replication.

### **Cellular infection studies**

A549-ACE2 cells were seeded into 12-well plates. Cells were rested for at least 24 hours prior to infection. At the time of infection, medium containing viral inoculum (MOI 0.01 and 0.1) was added on the cells. At 1 h after addition of inoculum, the medium was replaced with fresh medium without viral inoculum. Supernatants were harvested at 24, 48, and 72 h post-infection for further plaque assays.

### **Organoid infection studies**

Organoids were plated on geltrex-coated plates (ThermoFisher, 12760013) with 100,000 cells per well, and infected at an MOI of 1. At 2 h after addition of the inoculum, the supernatant was removed, cells were washed with PBS, and fresh HAO medium was added. Supernatants were harvested for a plaque assay at 24 and 48 h.

### **Virus neutralization assay**

K18-hACE2 mice infected with  $1 \times 10^4$  plaque forming units of WA1, B.1.617.2 and B.1.1.529 (n=5). With the early humane endpoints with WA1 and B.1.617.2, more animals (n=15) were infected for these groups. Serum samples from mice were collected at 7 days post-infection. Mock-infected animals served as controls. Serum dilutions (50  $\mu$ L) were made to get final dilutions of 1:30, 1:90, 1:270, 1:810, 1:2430, and 1:7290 in serum-free DMEM. Dilutions were separately added with 50 PFU (50  $\mu$ L) of SARS-CoV-2 WA1, Alpha, Beta, Delta, and Omicron. The mixture was mixed gently, incubated at 37°C for 30 mins, followed by a plaque assay. Similar assays were performed for serum samples from Omicron-infected ( $5 \times 10^2$ ) mice obtained at 9 dpi, and human serum samples acquired from ongoing clinical trials led by Curative and

UCSF or from hospitalized patients at UCSF (Table S3.1). The virus neutralization efficacy of sera was presented as 50% neutralization titer (NT50) and the average of each variant and compared to others in terms of fold-change. NT50 graphs were generated by MATLAB (Version 9.12). Data analysis was performed by using GraphPad Prism version 9.3.

### **Plaque assays**

Tissue homogenates and cell supernatants were analyzed for viral particle formation for *in vivo* and *in vitro* experiments, respectively. Briefly, Vero-TMPRSS2 were seeded and incubated overnight. Cells were inoculated with 10<sup>-1</sup> to 10<sup>-6</sup> dilutions of the respective homogenates or supernatant in serum-free DMEM. After the 1-h absorption period, the media in the wells were overlaid with 2.5% Avicel (Dupont, RC-591). After 72 h, the overlay was removed, and the cells were fixed in 10% formalin for 1 h and stained with crystal violet for visualization of plaque forming units. Data analysis was performed by using GraphPad Prism version 9.3.

### **Quantitative polymerase chain reaction**

RNA was extracted from cells, supernatants, or tissue homogenates with RNA-STAT-60 (AMSBIO, CS-110) and the Direct-Zol RNA Miniprep Kit (Zymo Research, R2052). RNA was then reverse-transcribed to cDNA with iScript cDNA Synthesis Kit (Bio-Rad, 1708890). qPCR reaction was performed with cDNA and SYBR Green Master Mix (Thermo Scientific) using the CFX384 Touch Real-Time PCR Detection System (Bio-Rad). See Table S3.2 for primers sequences. N gene standards were used to generate a standard curve for copy number quantification. N gene standard was generated by

PCR using extracted genomic SARS-CoV-2 RNA as template. A single product was confirmed by gel electrophoresis, and DNA was quantified by Nanodrop.

### **CyTOF analysis of mouse lung specimens**

The mice used in the CyTOF study were infected with  $5 \times 10^2$  PFU of WA1 and monitored for clinical signs of infection (e.g., body weight and body temperature) starting from day 1 to day 9 post-infection. CyTOF was conducted as described<sup>29</sup>. Single-cell suspensions of lung tissue specimens processed using the GentleMACS system (Miltenyi) were treated with 25  $\mu$ M cisplatin (Sigma) for 60 sec as a viability dye. Cells were then quenched with CyFACS buffer (PBS supplemented with 0.1% BSA and 0.1% sodium azide) and fixed for 10 min with 2% paraformaldehyde (PFA; Electron Microscopy Sciences). Cells were then washed twice with CyFACS and frozen at  $-80^\circ\text{C}$  until CyTOF antibody staining. Prior to antibody staining, specimens were barcoded using the Cell-ID™ 20-Plex PD Barcoding kit (Fluidigm, South San Francisco, CA, USA). Fc blocking was performed by treating the cells with 1.5% mouse and rat sera (both from Thermo Fisher) for 15 min at  $4^\circ\text{C}$ . After washing with CyFACS, cells were stained for 45 min at  $4^\circ\text{C}$  with the cell-surface antibodies listed in Table S3.3. Antibodies were purchased pre-conjugated from Fluidigm or conjugated using the Maxpar® X8 antibody labeling kit (Fluidigm). After staining, cells were washed with CyFACS and fixed overnight at  $4^\circ\text{C}$  in 2% PFA and permeabilized for 30 min with Foxp3 Fix/Permeabilization Buffer (Fisher Scientific). After two washes with Permeabilization Buffer (Fisher Scientific), cells were Fc blocked again for 15 min at  $4^\circ\text{C}$  with mouse and rat sera diluted in Permeabilization Buffer. After washing with Permeabilization Buffer, cells were stained for 45 min at  $4^\circ\text{C}$  with the intracellular

antibodies listed in Table S3.3. The details about the antibody dilutions have been provided in the Table S3.3. Prior to CyTOF analysis, cells were incubated for 20 min with a 1:500 dilution DNA intercalator (Fluidigm), and then washed twice with CyFACS and once with Cell Acquisition Solution (CAS, Fluidigm). Acquisition was performed in the presence of EQ™ Four Element Calibration Beads (Fluidigm) diluted in CAS. Cells were analyzed on a CyTOF 2 instrument (Fluidigm) at the UCSF Parnassus Flow Core. For data analysis, CyTOF datasets were normalized to EQ calibration using CyTOF software (6.7.1014, Fluidigm) and manually gated using the FlowJo software (10.7.2, FlowJo LLC, BD Biosciences). tSNE visualizations of the datasets were performed in Cytobank (9.1, 2022 Cytobank, Inc.), with default settings.

## **Histology**

Mouse lung tissues were fixed in 4% paraformaldehyde (Sigma 47608) for 24 h, washed three times with PBS, and stored in 70% ethanol. Briefly, tissues were processed and embedded in paraffin, and tissue sections were stained for SARS-CoV-2 Nucleocapsid (Genetex, GTX135357). The sections were then imaged using Leica Aperio ImageScope.

## **Human serum samples**

Human serum samples were acquired from two ongoing clinical trials led by Curative and UCSF. The Curative clinical trial protocol was approved by Advarra under Pro00054108 for a study designed to investigate immune escape by SARS-CoV-2 variant (University of California, Los Angeles Protocol Record PTL-2021-0007, ClinicalTrials.gov Identifier NCT05171803). Sample specimens were collected from

adults (18–50 years) who either had been vaccinated for COVID-19 and/or had a history of COVID-19. Sample acquisition involved standard venipuncture procedure to collect a maximum of 15 ml of whole blood, incubation at ambient temperature for 30–60 min to coagulate, centrifugation at 2200–2500 rpm for 15 min at room temperature, and storage on ice until delivered to the laboratory for serum aliquoting and storage at –80 °C until use. A quantitative SARS-CoV-2 IgG ELISA was performed on serum specimens (EuroImmun, Anti-SARS-CoV-2 ELISA (IgG), 2606–9621G, New Jersey). Remnant plasma samples from patients hospitalized with COVID-19 at UCSF were obtained from UCSF Clinical Laboratories daily, based on availability. Remnant samples were aliquoted and biobanked and the retrospective medical chart review for relevant demographic and clinical metadata were performed under a waiver of consent and according to “no subject contact” protocols approved by the UCSF Institutional Review Board (protocol number 10-01116). Plasma samples were also collected through the UMPIRE (UCSF EMPLOYEE and community member Immune REsponse) study (protocol number 20-33083), a longitudinal COVID-19 research study focused on collection of prospective whole-blood and plasma samples from enrolled subjects to evaluating the immune response to vaccination, with and without boosting, and/or vaccine breakthrough infection. The study cohorts included (1) fully vaccinated individuals with either two doses of Emergency Use Authorization (EUA)-authorized mRNA vaccine (Pfizer or Moderna). Consented participants came to a UCSF CTSI Clinical Research Service (CRS) Laboratory where their blood was drawn by nurses and phlebotomists. At each visit, two to four 3-mL EDTA tubes of whole blood were drawn, and one or two EDTA tubes were processed to plasma from each timepoint. Relevant demographic and clinical metadata from UMPIRE participants were obtained



through participant Qualtric surveys performed at enrollment and at each blood draw. Serum samples were heat inactivated at 56°C for 30 mins prior to use in neutralization assays.

For adequate sample selection, the criteria were age, disease severity, and days after infection for serum collection. A Wilcoxon-Mann-Whitney significance test was performed between the unvaccinated + Omicron infected and unvaccinated + Delta infected individuals, which showed no statistical significance in serum collection days after infection ( $p=0.147540$ ), disease severity index ( $p=0.820174$ ) and age of the individuals ( $p=0.591680$ ). A Wilcoxon-Mann-Whitney significance test was also performed between the vaccinated + Omicron infected and vaccinated + Delta infected individuals and showed no significant difference in serum collection days after infection ( $p$ -value: 0.5267) and age of the individuals ( $p=0.065$ ).

## **ACKNOWLEDGEMENTS**

This research is funded by grants from the National Institutes of Health: NIH/NIAID (F31 AI164671-01) to I.P.C., NHLBI U54HL147127 to M.M. A.M.S is supported by Natural Sciences and Engineering Research Council of Canada (NSERC PDF-533021-2019). M.O. and W.C.G also received support from the Roddenberry Foundation, from Pam and Ed Taft and the Gladstone Institutes. M.O. thanks Fast Grants and the Innovative Genomics Institute for support. J.A.D. acknowledges support from the National Institutes of Health (R21AI59666) and support from the Howard Hughes Medical Institute and the Gladstone Institutes. N.R. acknowledges support from the Van Auken Private Foundation, David Henke, and Pamela and Edward Taft; and Awards #2164 and #2208 from Fast Grants, a part of Emergent Ventures at the Mercatus Center, George Mason University. C.Y.C thanks the staff at UCSF Clinical Laboratories and the UCSF Clinical Microbiology Laboratories for help in identifying and aliquoting nasal swab and plasma samples. CYC acknowledges support by the Innovative Genomics Institute at UC Berkeley and UCSF, US Centers for Disease Control and Prevention contract 75D30121C10991, Abbott Laboratories, and the Sandler Program for Breakthrough Biomedical Research at UCSF. We thank Stanley Tamaki and Claudia Bispo for CyTOF assistance at the Parnassus Flow Core, and the lab of Eliver Ghosn for guidance on lung cell processing. We thank the Gladstone Histology Core. The group also acknowledges support from the James B. Pendleton Charitable Trust. The funders had no role in study design, data collection and analysis, decision to publish, or preparation of the manuscript.

## **Data Availability Statement**

The datasets generated during and/or analyzed during the current study are available in the manuscript or in the Extended data set.

## **Author Contributions**

Conceptualization: RKS, IPC, MO

Investigation: RKS, IPC, TM, AMS, CRS, AC, MMK, BS, PC, AG

Anti-sera: NB, PS, AS, VS, AG, JN, IS, BM, NK, VH, MS, LL, MB, FT, FWS, CYC, LS

Omicron virus culture: MAG, MKM, DW, CH, RA

Lung tissue for organoids: XF, MM, MM

BSL3 facility maintenance: MM

Supervision: LS, JAD, NR, CYC, MO

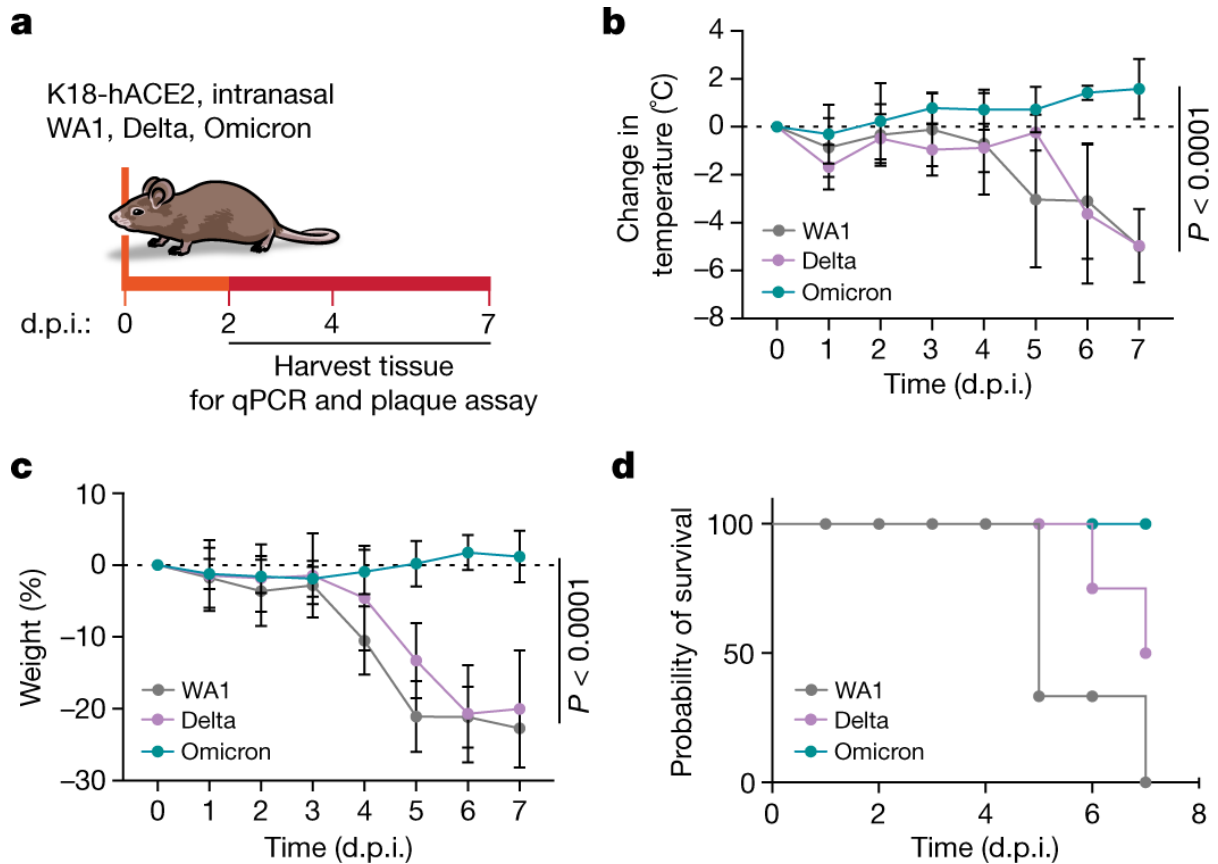
Writing - original draft: RKS, IPC, MO

Writing - reviewing, & editing: RKS, IPC, GRK, WCG, TM, NR, MO

## **Competing Interests**

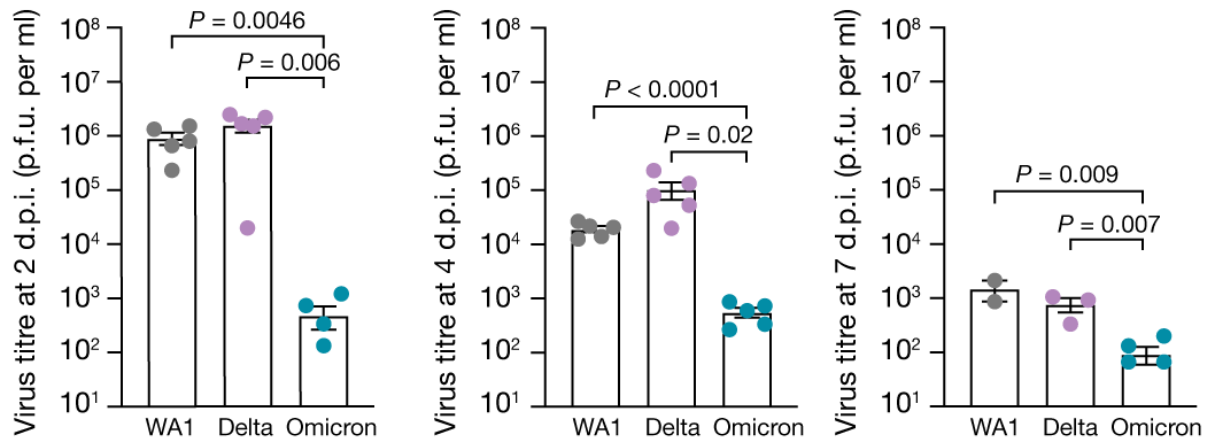
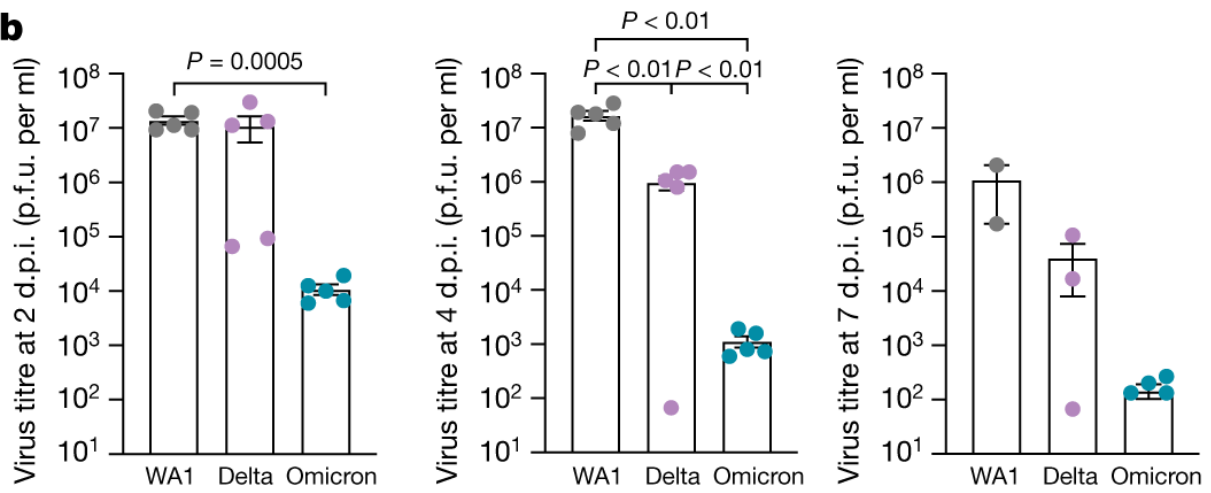
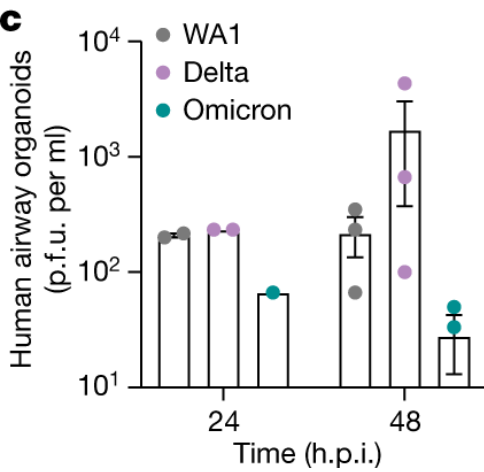
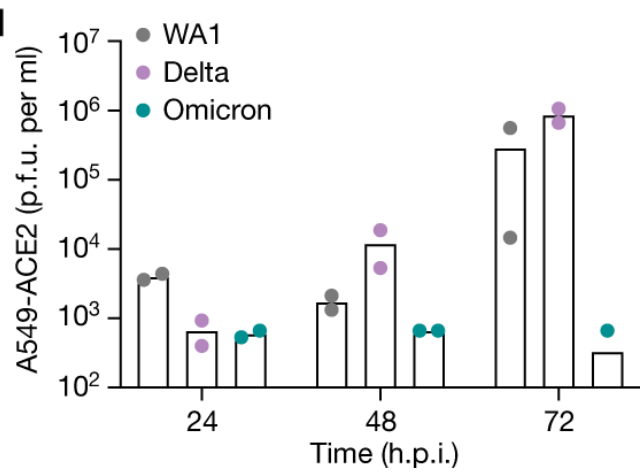
J.A.D. is a cofounder of Caribou Biosciences, Editas Medicine, Scribe Therapeutics, Intellia Therapeutics, and Mammoth Biosciences. J.A.D. is a scientific advisory board member of Vertex, Caribou Biosciences, Intellia Therapeutics, eFFECTOR Therapeutics, Scribe Therapeutics, Mammoth Biosciences, Synthego, Algen Biotechnologies, Felix Biosciences, The Column Group, and Inari. J.A.D. is a director at Johnson & Johnson and Tempus and has research projects sponsored by Biogen, Pfizer, AppleTree Partners, and Roche. C.Y.C. is the director of the UCSF-Abbott Viral Diagnostics and Discovery Study and receives research support from Abbott

Laboratories. C.Y.C. also receives support for SARS-CoV-2 research unrelated to this study from Mammoth Biosciences.



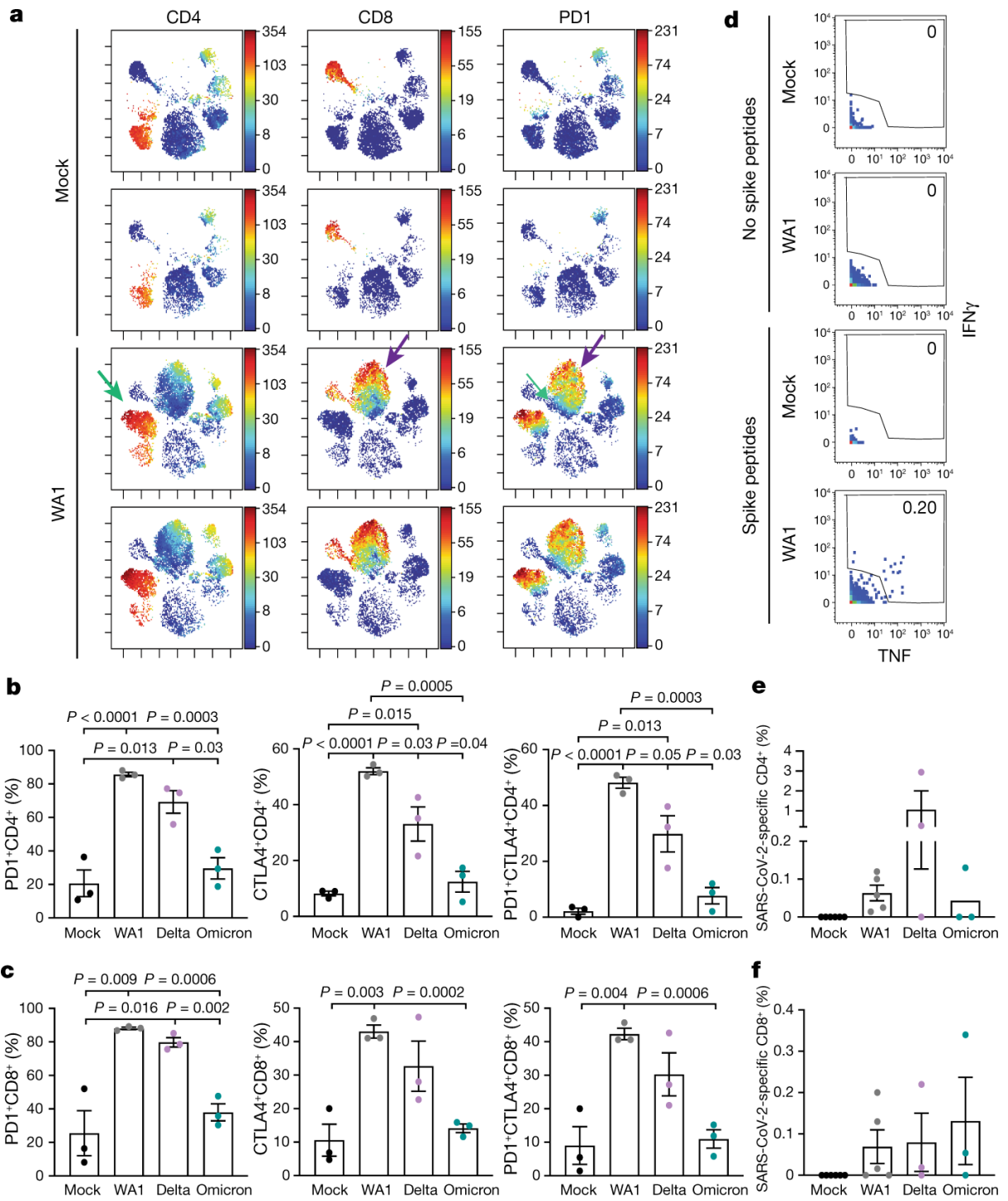
**Figure 3.1. Robust infection of K18-hACE2 mice with Delta and ancestral variant, but not Omicron.**

- Schematic of the experiment. Fifteen mice per group were intranasally infected with  $10^4$  PFU of the indicated variant. Body temperature and weight were monitored daily. At days 2, 4, and 7 post-infection (dpi), the upper respiratory tract and lungs were harvested and processed for downstream analysis.  $n=5$  per group.
- Changes in body temperature of mice infected with WA1 (grey), Delta (purple), and Omicron (teal). Data are shown as the average  $\pm$  SD and analyzed by 2-way ANOVA and adjusted for multiple testing using the Bonferroni test.
- Severe weight loss of WA1- and Delta-infected mice. Data are shown as the average  $\pm$  SD and analyzed by 2-way ANOVA and adjusted for multiple testing using the Bonferroni test.
- Probability of survival of variant-infected mice.

**a****b****c****d**

**Figure 3.2. Robust viral replication of WA1 and Delta, but not Omicron, in mice and human airway cells.**

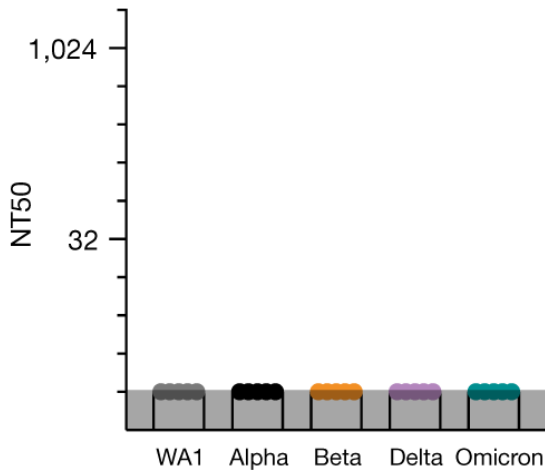
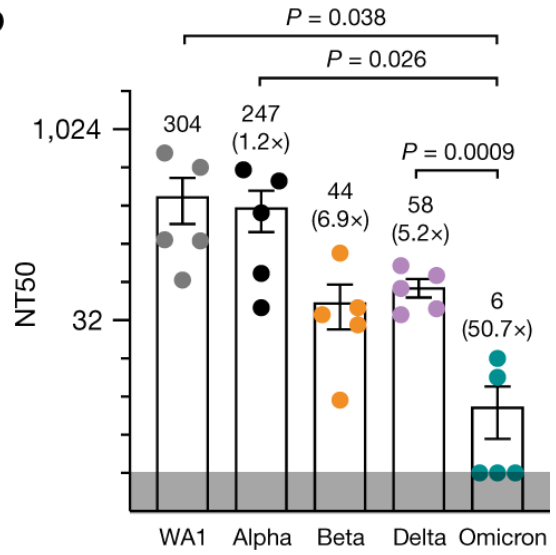
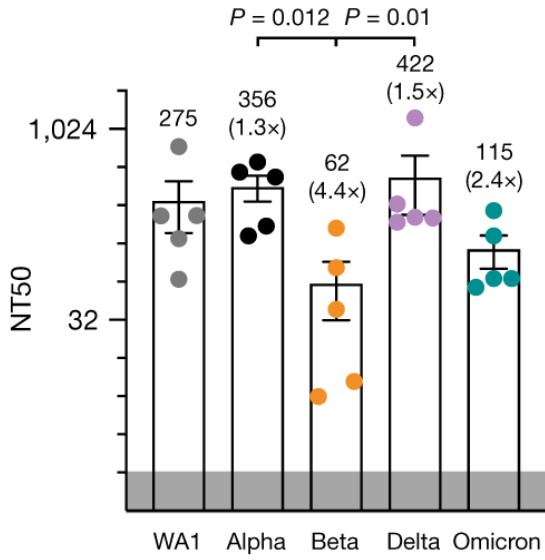
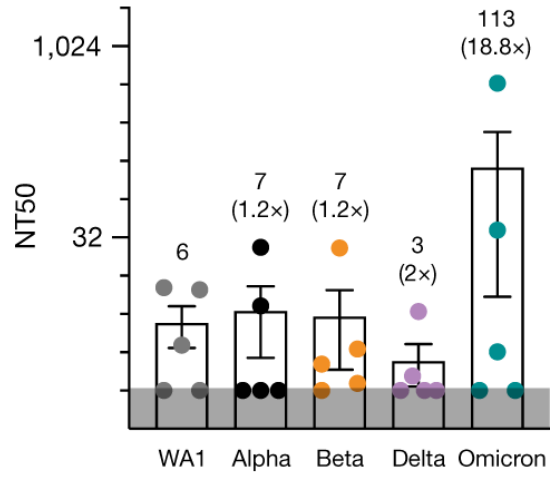
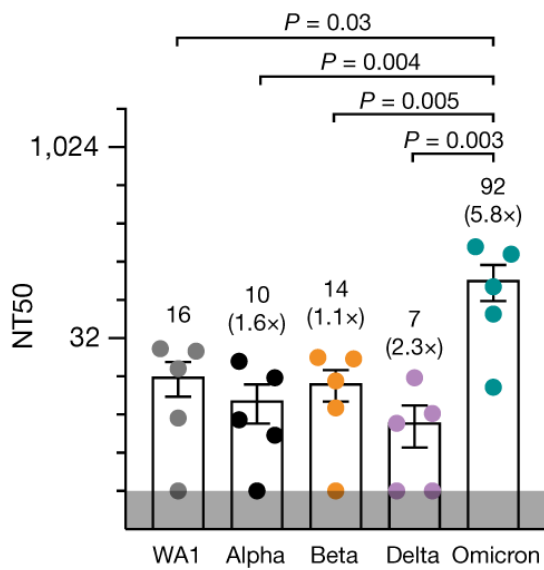
- A. Plaque assay titers from the upper airway (nasal turbinates and bronchus) of WA1- (grey), Delta- (purple), and Omicron- (teal) infected mice at the indicated time points. Data are shown as the average  $\pm$  SEM analyzed by the two-tailed unpaired student's t-test. Each dot represents infectious virus titer in an individual mouse, 2 dpi (n=5), 4 dpi (n=5), and 7 dpi (WA1 infection group n=2, Delta n=2 and Omicron n=5).
- B. Plaque assay titers from the lungs of infected mice at the indicated time points. Data are shown as the average  $\pm$  SEM at each time point and analyzed by the two-tailed unpaired student's t-test. Each dot represents infectious virus titer in individual mice 2 dpi (n=5), 4 dpi (n=5), and 7 dpi (WA1 infection group n=2, Delta n=2 and Omicron n=5).
- C. Plaque assay titers from supernatants of infected human airway organoids (multiplicity of infection [MOI] of 1). Data are shown as the average. Each dot represents independent experiment using human lung airway organoids generated, 24h n=2, 48h n=3 where each dot represents independent experiment using human lung airway organoids.
- D. Plaque assay titers from supernatants of infected A549-ACE2 cells (MOI of 0.1), n= 2 represents infectious virus titer in independent experiment.





**Figure 3.3. Ancestral and variant of concern SARS-CoV-2 elicit immune responses in lungs of mice.**

- A. T cells from lungs of infected mice (n=3) were phenotypically distinct and expressed PD1. Single-cell suspensions of lungs from mock infected (top two rows) and WA1-infected (bottom two rows) K18-hACE2 mice were harvested 9 dpi and analyzed by CyTOF. Shown are tSNE plots gated on total immune cells (CD45+) from the lungs of the mice, colored by expression levels of the antigen listed at the top (red = highest expression, blue = lowest expression). “Islands” of CD4+ and CD8+ T cells unique to the infected mice (identified by the green and purple arrows, respectively, in the third row) express especially high levels of the activation/exhaustion marker PD1, as demonstrated in the right-hand column.
- B. T cells from lungs of infected mice (n=3) expressed elevated levels of the activation/checkpoint antigens PD1 and CTLA4. The proportions of CD4+ T cells expressing PD1, CTLA4, or both PD1 and CTLA4, are indicated. Data are shown as the average  $\pm$  SEM analyzed by the two-tailed unpaired student’s t-test.
- C. T cells from lungs of infected mice (n=3) expressed elevated levels of the activation/checkpoint antigens PD1 and CTLA4. The proportions of CD8+ T cells expressing PD1, CTLA4, or both PD1 and CTLA4, are indicated. Data are shown as the average  $\pm$  SEM analyzed by the two-tailed unpaired student’s t-test.
- D. SARS-CoV-2-specific T cells are elicited in lungs of SARS-CoV-2-infected mice. Representative plots corresponding to pulmonary T cells from uninfected (Mock) and WA1-infected K18-hACE2 mice, stimulated for 6 h with (bottom) or without (top) overlapping SARS-CoV-2 spike peptides. Note SARS-CoV-2-specific T cells (those producing IFN $\gamma$  and/or TNF $\alpha$ ) were only detected in infected mice after peptide stimulation, (n=3).
- E. SARS-CoV-2-specific T cells are elicited in lungs of mice infected with WA1 (n=6), Delta (n=3), and Omicron (n=3). The proportions of CD4+ T cells expressing IFN $\gamma$  and/or TNF $\alpha$  (gated as shown in *panel C*) are indicated. CD4+ T-cell responses trended highest in Delta-infected mice. Data are shown as the average  $\pm$  SEM analyzed by the two-tailed unpaired student’s t-test.
- F. SARS-CoV-2-specific T cells are elicited in lungs of mice infected with WA1 (n=6), Delta (n=3), and Omicron (n=3). The proportions of CD8+ T cells expressing IFN $\gamma$  and/or TNF $\alpha$  (gated as shown in *panel C*) are indicated. CD8+ T-cell responses were highest in Delta- and Omicron-infected mice. Data are shown as the average  $\pm$  SEM analyzed by the two-tailed unpaired student’s t-test.

**a****b****c****d****e**

**Figure 3.4. Cross-variant neutralization of SARS-CoV-2 isolates by sera from infected mice.**

- A-D. K18-hACE2 mice were infected with  $1 \times 10^4$  PFU of WA1, Delta or Omicron. Virus neutralization assay was carried out with sera collected at 7 dpi. Data points in the graph represent individual sera samples showing 50% neutralization titer (NT50) against SARS-CoV-2 isolates. The numbers in parentheses indicate the fold-change in neutralization efficacy or resistance of respective isolates relative to NT50 of ancestral isolate (WA1). The grey band at the bottom of the graph indicates the limit of detection. A-D. Graphs representing NT50 of sera from **A.** naive, **B.** WA1-infected, **C.** Delta-infected, and **D.** Omicron-infected mice against different viral isolates.  $n=5$  mouse in each group.
- E. K18-hACE2 mice were infected with  $5 \times 10^2$  PFU of Omicron,  $n=5$ . Virus neutralization assay was carried out with serum collected at 9 dpi. Data are presented as average  $\pm$  SEM and analyzed by 2-way ANOVA and two-tailed unpaired student's t-test.

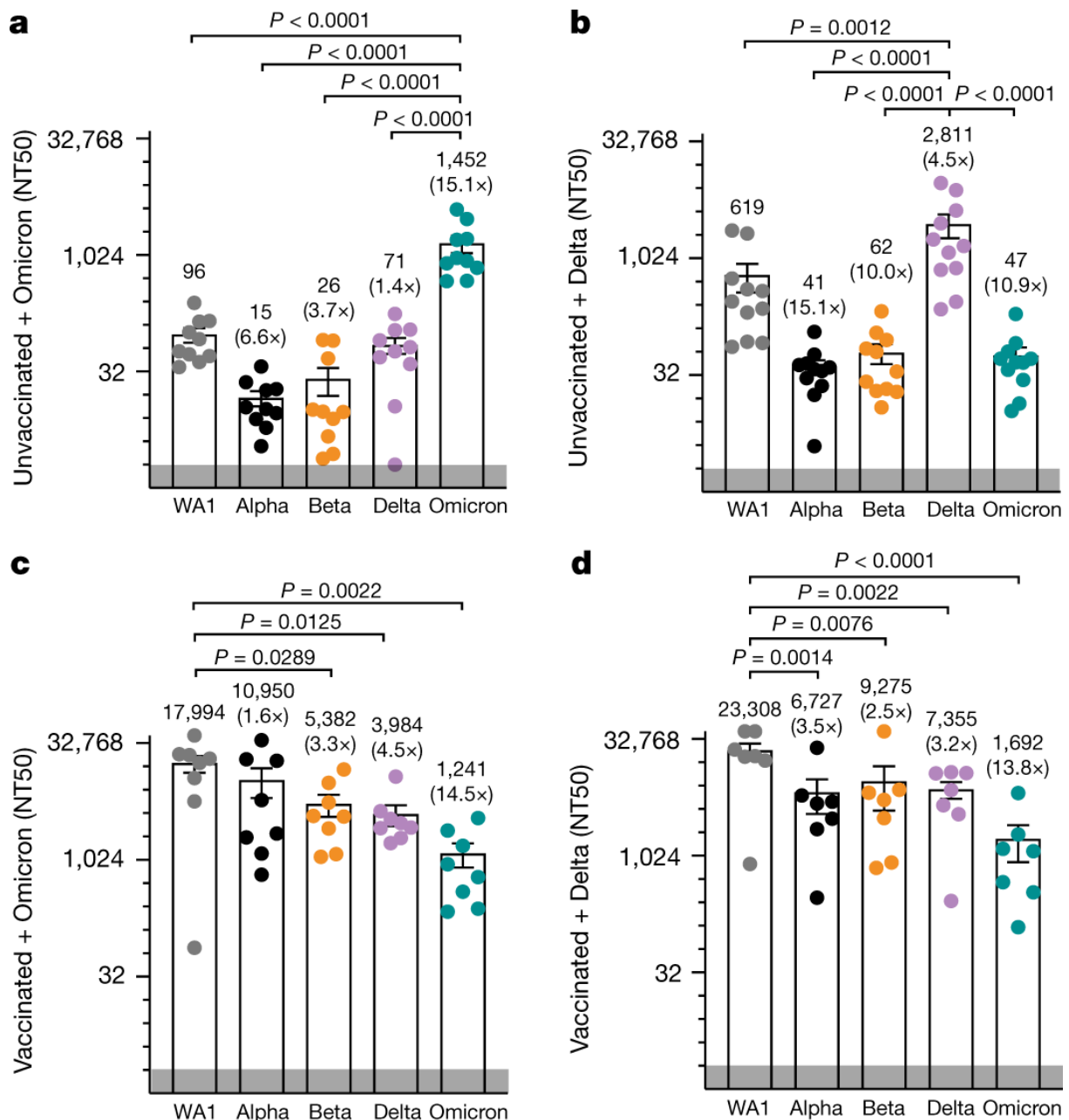


**Figure 3.5. Cross-variant neutralization of SARS-CoV-2 isolates by human sera.**

A-D. Graphs representing NT50 of variants by sera from **A.** Unvaccinated individuals with likely Omicron infection (based on date of collection), n=10, **B.** unvaccinated individuals with likely Delta infection (based on date of collection), n=11, **C.** vaccinated individuals with a confirmed Omicron infection, n=8, and **D.** vaccinated individuals with a Delta infection (based on date of collection). Data points in the graph represent individual serum samples. The grey band at the bottom of the graph indicates the limit of detection. Data are presented in a-d is average  $\pm$  SEM and analyzed by 2-way ANOVA and two-tailed unpaired student's t-test. The details regarding samples (group, age, sex, COVID-19 infection status, vaccination dates, and sample collection dates after infection/symptoms are summarized in Table S3.1).

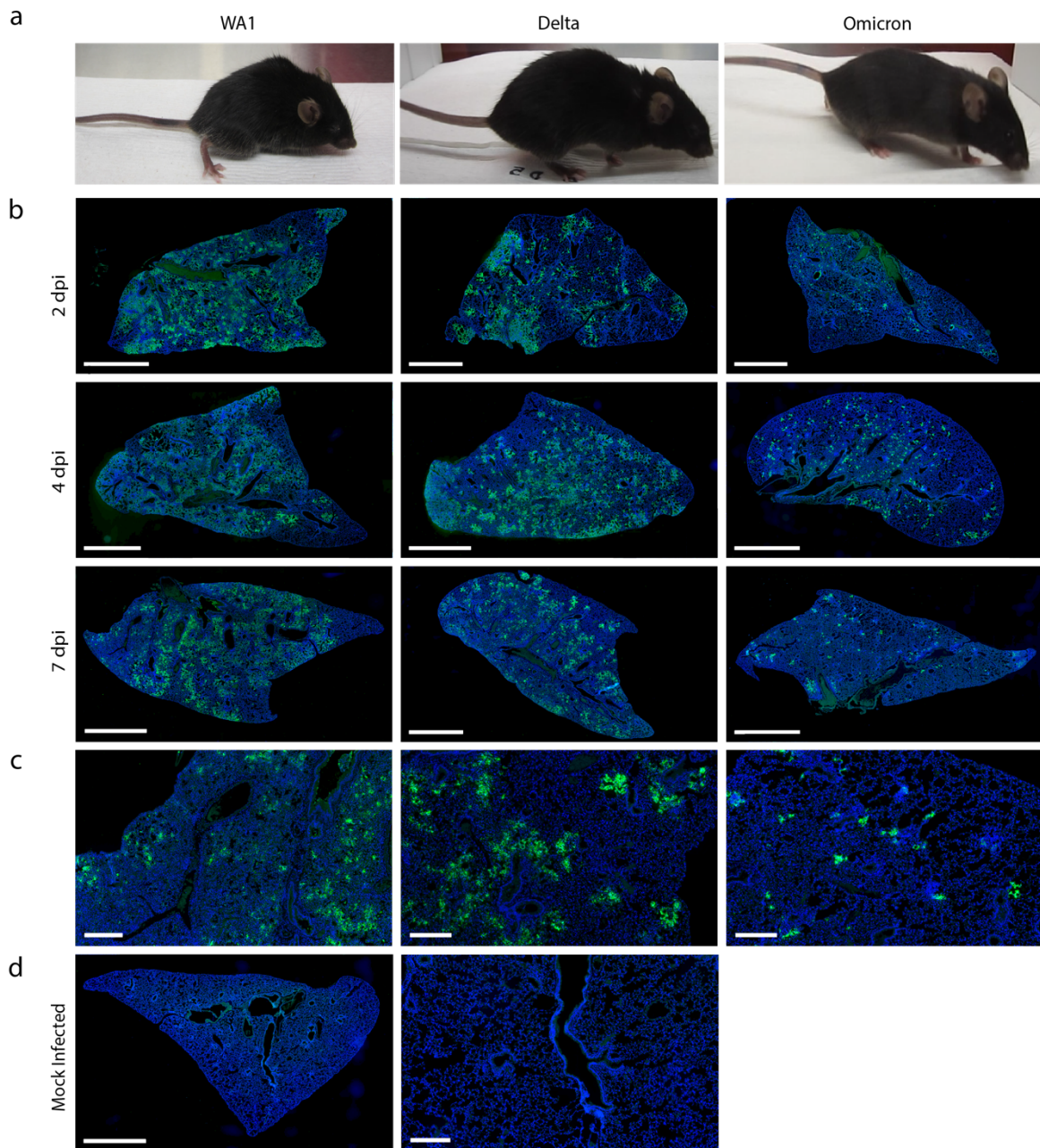


**Figure S3.1. Physical conditions of the infection mice at 5 dpi.**

- Representative images of WA1-, Delta-, and Omicron-infected mice 5 dpi. WA1-infected mice were lethargic and had a hunched posture, ungroomed coat, and squinted eyes. Delta-infected mice are mildly lethargic. Omicron-infected mice appeared normal.
- Representative images of lungs from mice infected with WA1, Delta, or Omicron at 2 dpi (n=5), 4 dpi (n=5), and 7 dpi (WA1 infection group n=2, Delta n=2 and Omicron n=5). SARS-CoV-2 nucleocapsid is stained in green and nucleus is stained in blue. Scale bar, 2 mm.
- Representative images of tissue sections from lung tissue infected with WA1, Delta, or Omicron collected at 7 dpi (WA1 infection group n=2, Delta n=2 and Omicron n=2). SARS-CoV-2 nucleocapsid is stained in green and nuclei are stained in blue. Scale bar, 2 mm.

Omicron n=5). SARS-CoV-2 nucleocapsid is stained in green and nucleus is stained in blue. Scale bar, 300  $\mu$ m.

- D. Representative images of mock infected lungs. SARS-CoV-2 nucleocapsid is stained in green and nucleus is stained in blue. Scale bar, 2 mm (left panel) and 300  $\mu$ m (right panel), n=5 mice.

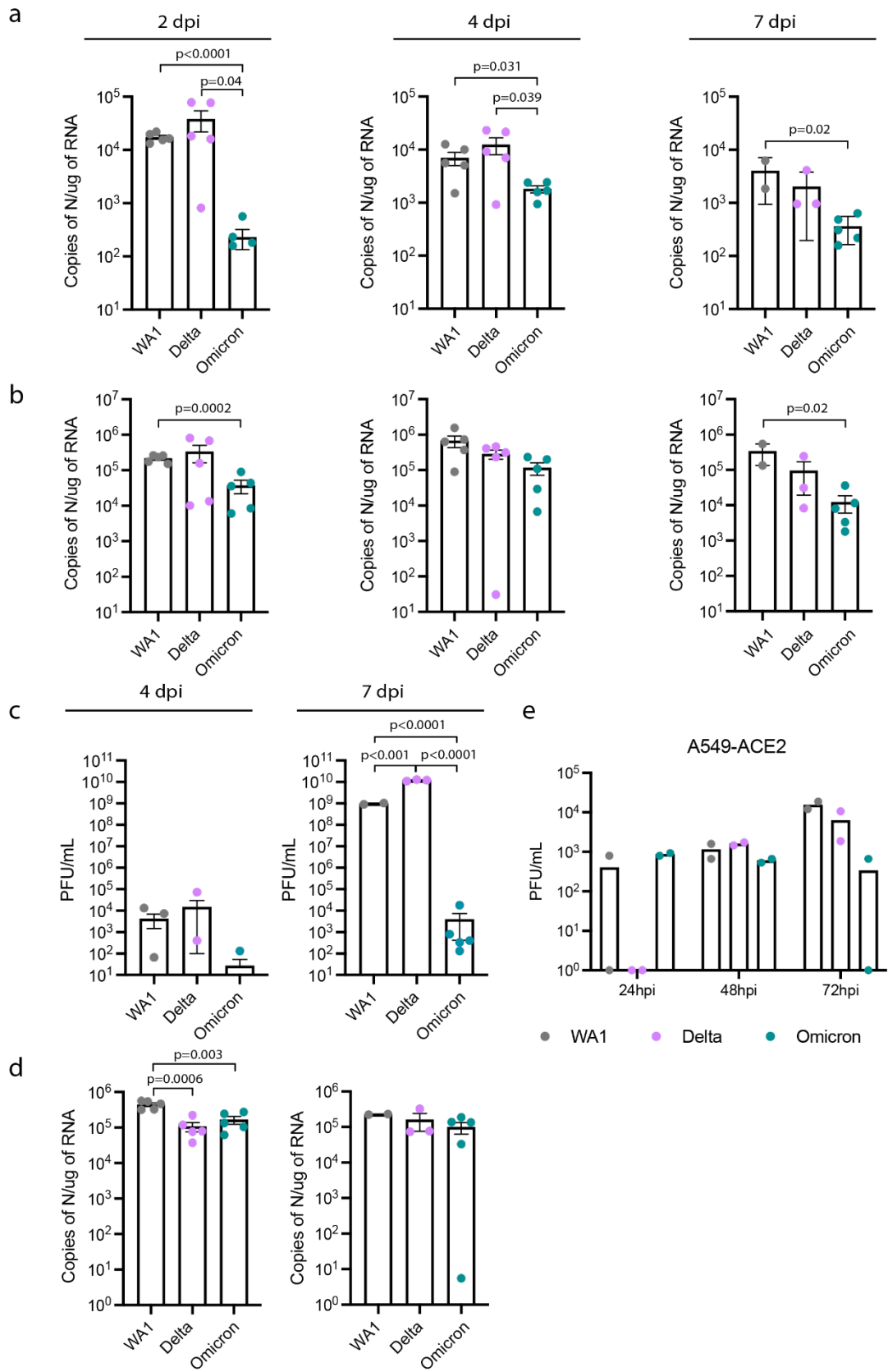


**Figure S3.2. Lower viral replication of Omicron in mice and human cells.**

- A. RT-qPCR of SARS-CoV-2 N RNA isolated from upper respiratory tract (nasal turbinates and bronchus) of WA1-(grey), Delta-(purple), and Omicron-(teal) infected mice at indicated time points. Data are expressed in absolute copies/ $\mu$ g based on a standard curve of N gene with known copy number. Data are shown as an average  $\pm$  SEM at 2 dpi (n=5), 4 dpi (n=5), and 7 dpi (WA1 infection group n=2, Delta n=2 and Omicron n=5) and analyzed by two-tailed unpaired student's t-test.
- B. RT-qPCR of SARS-CoV-2 N RNA isolated from lungs of infected mice at indicated time points. Data are expressed in absolute copies/ $\mu$ g based on a standard curve of N gene with known copy number. Data are shown as an average  $\pm$  SEM at 2 dpi (n=5), 4 dpi (n=5), and 7 dpi (WA1 infection group n=2, Delta n=2 and Omicron n=5) and analyzed by the two-tailed unpaired student's t-test.
- C. Plaque assay titers from the brains of infected mice at indicated time points. Data are shown as an average  $\pm$  SEM at 4 dpi (n=5) and 7 dpi (WA1 infection group n=2, Delta n=2 and Omicron n=5) and analyzed by the two-tailed unpaired student's t-test.
- D. RT-qPCR of SARS-CoV-2 N RNA isolated from brains of infected mice at indicated time points. Data are expressed in absolute copies/ $\mu$ g based on a standard curve of N gene with known copy number. Data are shown as an average  $\pm$  SEM at 4 (n=5) and 7 (n=2–5) dpi and analyzed by the two-tailed unpaired student's t-test.
- E. Plaque assay titers from supernatants of infected A549-ACE2 (MOI of 0.01). Data are shown as average  $\pm$  SEM, n=2.



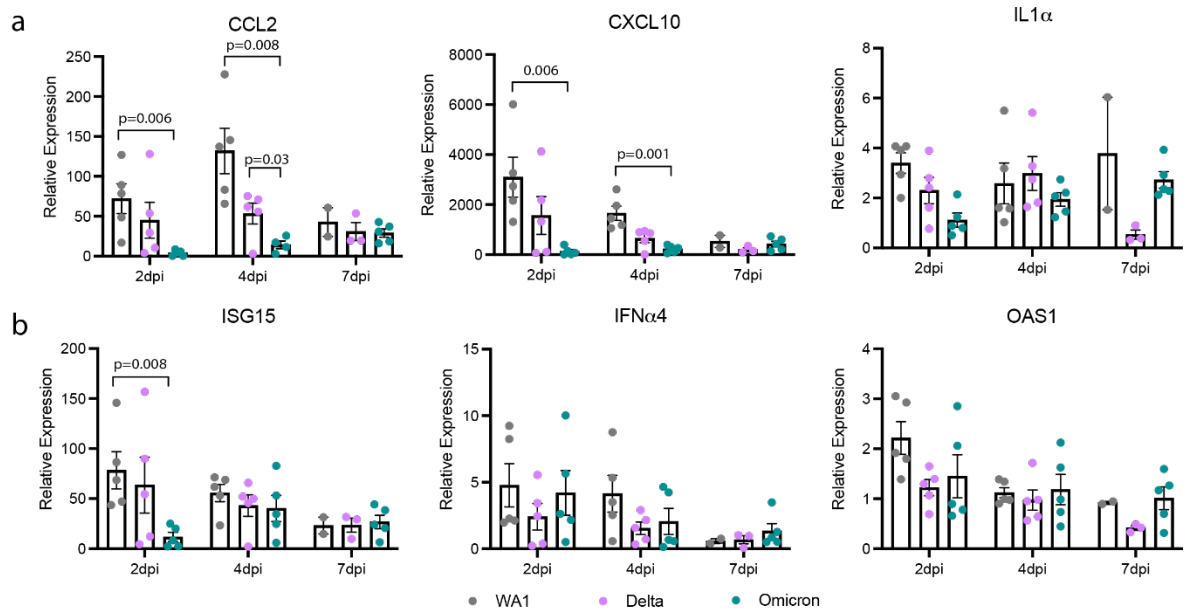


**Figure S3.3. Differential expression of proinflammatory markers in lungs of infected mice.**

- A. RT-qPCR of proinflammatory cytokines and chemokines from RNA isolated from lungs of infected mice at the indicated time points. Data are expressed relative to mock-infected mice. Data are shown as the average  $\pm$  SEM at 2 dpi (n=5), 4 dpi (n=5), and 7 dpi (WA1 infection group n=2, Delta n=2 and Omicron n=5) and analyzed by two-tailed unpaired student's t-test.
- B. RT-qPCR of interferon-stimulated genes from RNA isolated from lungs of infected mice at the indicated time points. Data are expressed relative to mock-infected mice. Data are shown as the average  $\pm$  SEM at 2 dpi (n=5), 4 dpi (n=5), and 7 dpi (WA1 infection group n=2, Delta n=2 and Omicron n=5) and analyzed by the two-tailed unpaired student's t-test.

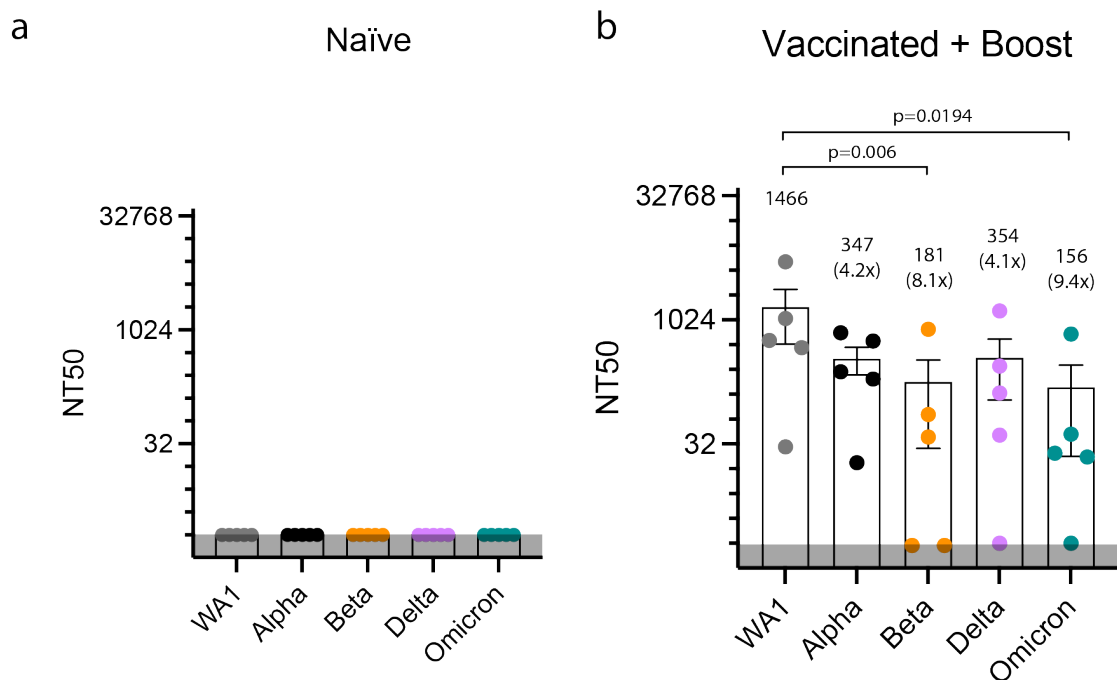


**Figure S3.4. Cross-variant neutralization of SARS-CoV-2 isolates by human sera.**

A-B. Graphs representing NT50 of sera from **A.** naive and **B.** vaccinated and Pfizer-boosted individuals against different viral isolates, n=5 in each group. The average neutralization efficacies of sera from each graph are shown and fold-changes relative to ancestral isolate (WA1) are shown in parentheses. The grey band indicates the limit of detection. Data are shown as the average  $\pm$  SEM and analyzed by 2-way ANOVA and adjusted for multiple testing using the Bonferroni test.

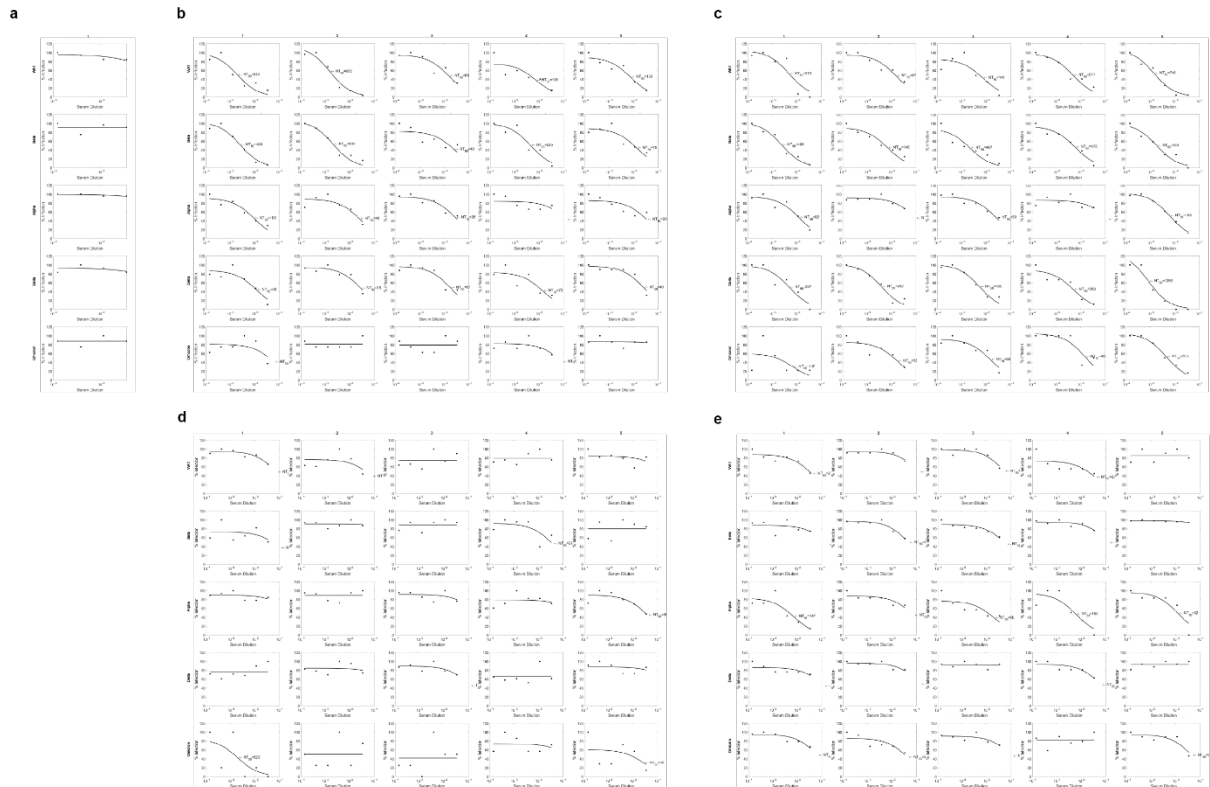


**Figure S3.5. Sera neutralizing titer assays of from SARS-CoV-2-infected mice.**  
 A-E. Neutralization assays of sera from **A.** naive (representative), **B.** WA1-, **C.** Delta-, and **D.** Omicron-infected mice at 7 days post-infection against WA1, Alpha, Beta, Delta, and Omicron isolates. **E.** Neutralization assays of sera from Omicron-infected mice at 9 days post-infection against WA1, Alpha, Beta, Delta, and Omicron isolates.

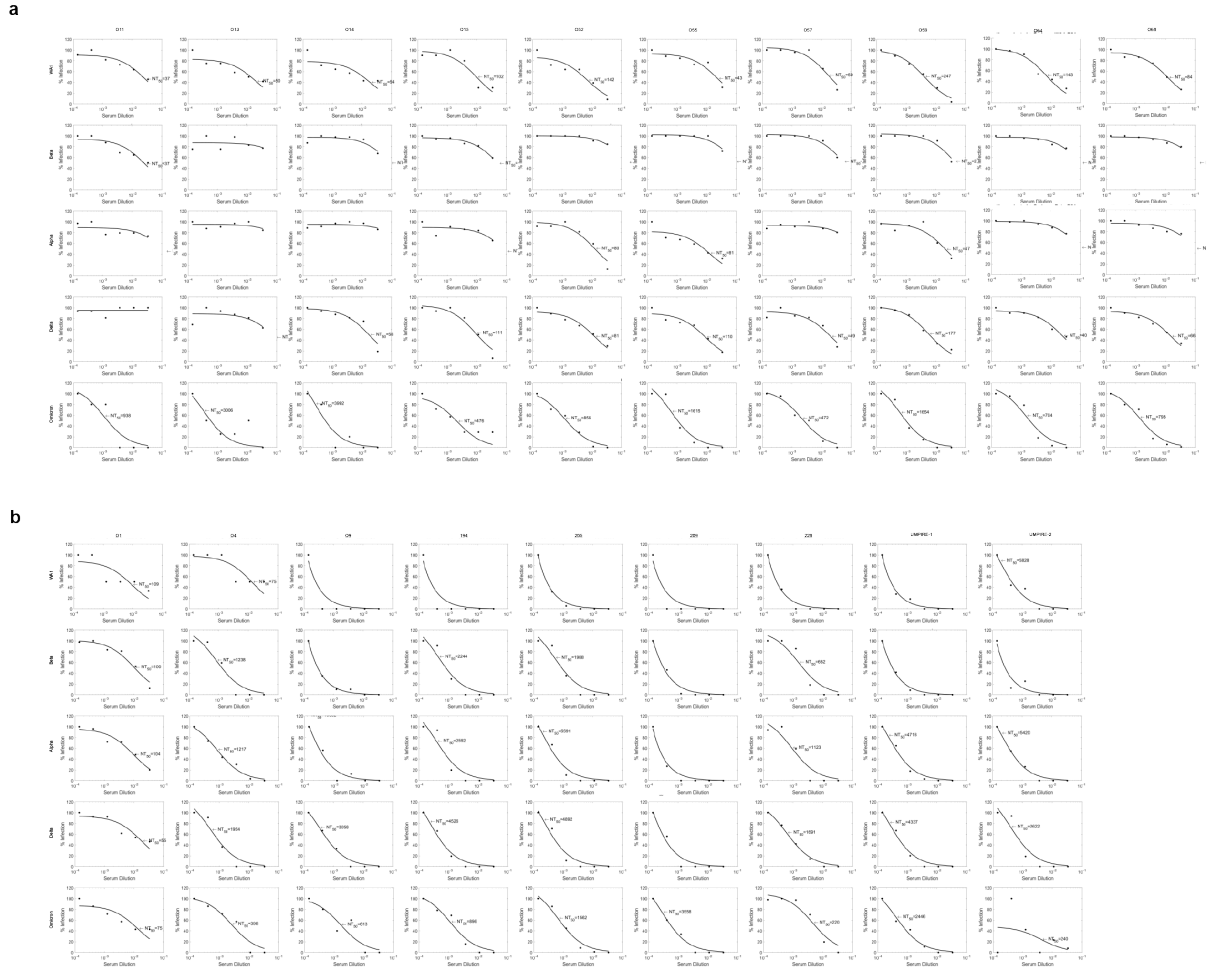


**Figure S3.6. Sera neutralizing titer assays of individuals infected with Omicron.**  
 A-B. Neutralization assays of sera from **A.** unvaccinated and **B.** vaccinated individuals infected with Omicron (likely based on time of collection) against WA1, Alpha, Beta, Delta, and Omicron isolates.

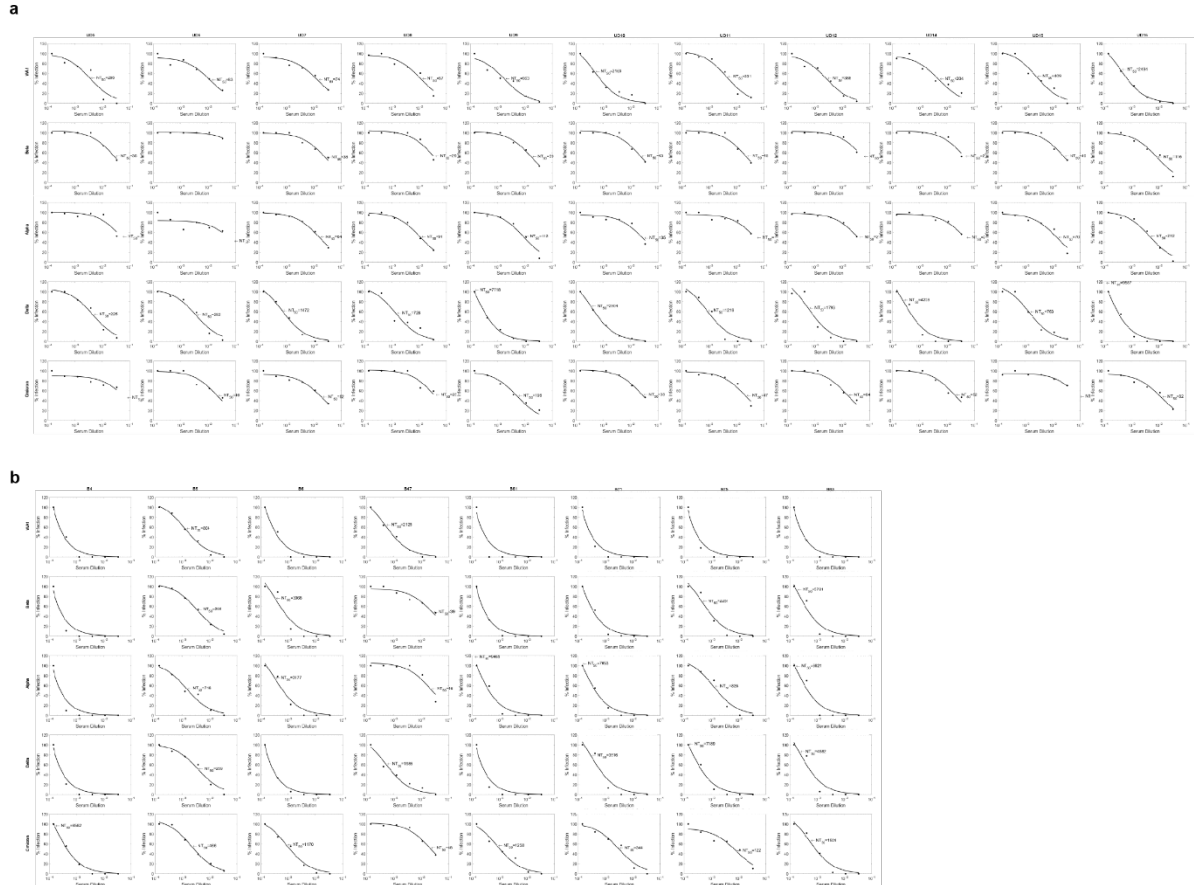
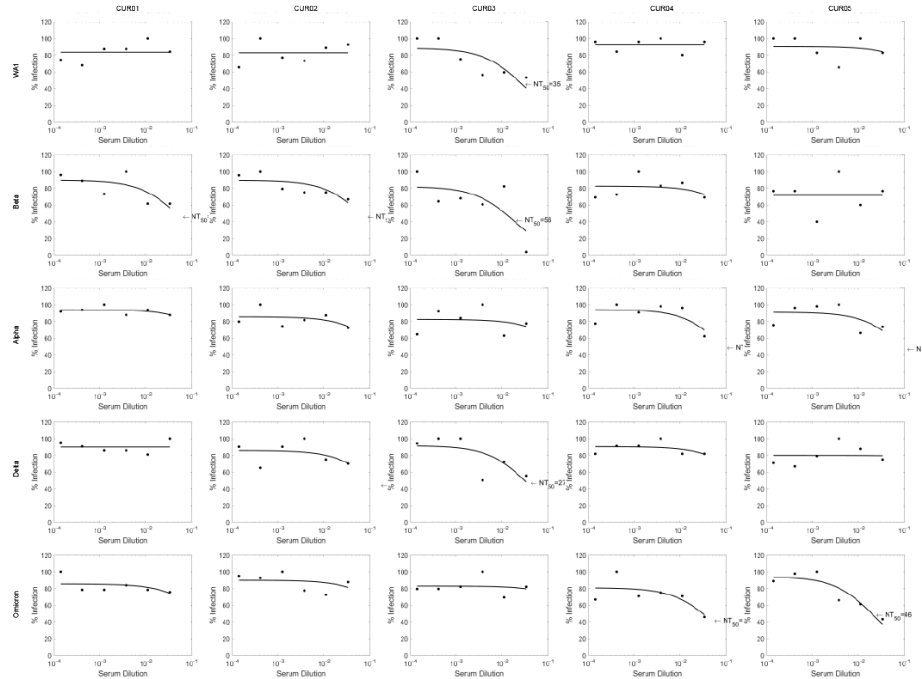


**Figure S3.7. Sera neutralizing titer assays from individuals infected with Delta.**  
 A-B. Neutralization assays of sera from **A.** unvaccinated and **B.** vaccinated individuals infected with Delta (likely based on time of collection) against WA1, Alpha, Beta, Delta, and Omicron isolates.

**a**



**b**

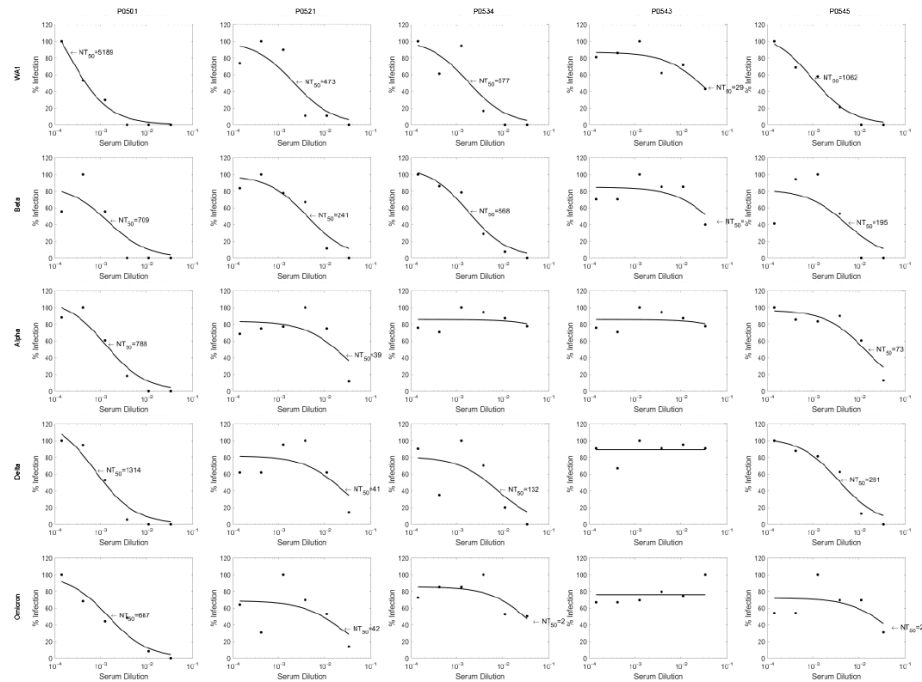


**Figure S3.8. Sera neutralizing titer assays from individuals.**

A-B. Neutralization assays of sera from **A.** naive and **B.** vaccinated and Pfizer boosted individuals against WA1, Alpha, Beta, Delta, and Omicron isolates.

**Table S3.1. Clinical data of patients.**

Clinical data of patients (N=47) included in the study. The human samples were acquired through clinical trials led by Curative Inc. and University of California, San Francisco (UCSF). F= Female, M= Male, N/A- Not applicable, severity index: 1-mild, 2-moderate, 3-severe.

Group	Patient ID	Age	Sex	Vaccine #1 date	Vaccine #1 manuf	Vaccine #2 date	Vaccine #2 manuf	Vaccine #3 date	Vaccine #3 manuf	Collection Date #1	Date COVID positive	Days after infection	Severity index
Native	CUR01	28	F	N/A	N/A	N/A	N/A	N/A	N/A	Not provided	N/A	N/A	N/A
	CUR02	65	M	N/A	N/A	N/A	N/A	N/A	N/A	Not provided	N/A	N/A	N/A
	CUR03	67	M	N/A	N/A	N/A	N/A	N/A	N/A	Not provided	N/A	N/A	N/A
	CUR04	26	F	N/A	N/A	N/A	N/A	N/A	N/A	Not provided	N/A	N/A	N/A
	CUR05	36	F	N/A	N/A	N/A	N/A	N/A	N/A	Not provided	N/A	N/A	N/A
Vaccinated + Boost	P0501	49	F	2/23/2021	Pfizer	3/23/2021	Pfizer	11/17/2021	Pfizer	12/1/2021	N/A	N/A	N/A
	P0521	52	M	2/23/2021	Pfizer	3/22/2021	Pfizer	10/4/2021	Pfizer	10/19/2021	N/A	N/A	N/A
	P0534	52	M	2/23/2021	Pfizer	3/23/2021	Pfizer	9/30/2021	Pfizer	10/15/2021	N/A	N/A	N/A
	P0543	48	M	2/23/2021	Pfizer	3/22/2021	Pfizer	10/8/2021	Pfizer	10/25/2021	N/A	N/A	N/A
	P0545	62	F	2/23/2021	Pfizer	3/22/2021	Pfizer	11/18/2021	Pfizer	12/3/2021	N/A	N/A	N/A
Vaccinated + Delta	B4	47	F	1/15/2021	Moderna	2/12/2021	Moderna	2/12/2021	Moderna	7/23/2021	7/18/2021	16	N/A
	B5	71	M	1/27/2021	Pfizer	2/17/2021	Pfizer	N/A	N/A	7/15/2021	7/14/2021	17	N/A
	B6	68	M	2/10/2021	Pfizer	3/12/2021	Pfizer	N/A	N/A	7/23/2021	7/22/2021	18	N/A
	B47	72	M	2/28/2021	Moderna	7/16/2021	Moderna	9/16/2021	Not provided	10/14/2021	10/10/2021	19	N/A
	B61	71	F	2/23/2021	Moderna	3/23/2021	Moderna	N/A	N/A	7/31/2021	7/31/2021	15	N/A
	B71	69	M	2/11/2021	Pfizer	3/4/2021	Pfizer	N/A	N/A	8/11/2021	8/11/2021	15	N/A
	B75	48	F	3/29/2021	Moderna	4/26/2021	Moderna	9/13/2021	Moderna	10/28/2021	10/30/2021	13	N/A
	B83	78	F	1/23/2021	Moderna	2/20/2021	Moderna	8/27/2021	Moderna	11/21/2021	11/18/2021	15	N/A
Vaccinated + Omicron	O4	28	F	8/22/2021	Pfizer	9/13/2021	Pfizer	Not provided	Not provided	1/5/2022	12/26/2021	11	N/A
	O6	81	F	1/29/2021	Moderna	3/5/2021	Moderna	11/10/2021	Moderna	1/13/2022	12/27/2021	18	N/A
	O7	70	M	3/25/2021	Pfizer	4/15/2021	Pfizer	N/A	N/A	12/28/2021	12/21/2021	8	N/A
	UMPIRE-1	30	M	3/10/2021	Pfizer	4/1/2021	Pfizer	10/7/2021	Pfizer	12/27/2021	12/17/2021	11	N/A
	194	39	F	3/29/2021	Moderna	4/26/2021	Moderna	N/A	N/A	2/10/2022	11/27/2021	75	N/A
	205	28	M	1/8/2021	Pfizer	1/31/2021	Pfizer	12/9/2021	Pfizer	2/15/2022	12/27/2021	48	N/A
	209	53	M	3/4/2021	Pfizer	4/4/2021	Pfizer	12/16/2021	Pfizer	2/8/2022	12/26/2021	44	N/A
228	39	F	4/10/2021	Moderna	5/8/2021	Moderna	12/7/2021	Moderna	1/27/2022	12/28/2021	31	N/A	
Unvaccinated + Omicron	O11	81	F	N/A	N/A	N/A	N/A	N/A	N/A	1/17/2022	12/30/2021	19	2
	O13	61	M	N/A	N/A	N/A	N/A	N/A	N/A	1/17/2022	12/31/2021	18	1
	O14	29	F	N/A	N/A	N/A	N/A	N/A	N/A	1/16/2022	1/6/2022	11	3
	O15	38	M	N/A	N/A	N/A	N/A	N/A	N/A	1/17/2022	1/4/2022	19	0
	O52	65	F	N/A	N/A	N/A	N/A	N/A	N/A	2/8/2022	1/24/2022	17	3
	O55	82	M	N/A	N/A	N/A	N/A	N/A	N/A	2/8/2022	1/19/2022	20	3
	O57	19	M	N/A	N/A	N/A	N/A	N/A	N/A	2/8/2022	1/18/2022	21	3
	O59	51	M	N/A	N/A	N/A	N/A	N/A	N/A	2/3/2022	1/17/2022	20	3
Unvaccinated + Delta	O64	72	F	N/A	N/A	N/A	N/A	N/A	N/A	2/17/2022	1/30/2022	18	1
	O68	21	F	N/A	N/A	N/A	N/A	N/A	N/A	1/30/2022	1/16/2022	14	1
	UD5	81	F	N/A	N/A	N/A	N/A	N/A	N/A	9/10/2021	9/5/2021	11	1
	UD6	81	F	N/A	N/A	N/A	N/A	N/A	N/A	10/27/2021	10/6/2021	21	1
	UD7	31	M	N/A	N/A	N/A	N/A	N/A	N/A	8/6/2021	8/4/2021	16	1
	UD8	100	F	N/A	N/A	N/A	N/A	N/A	N/A	10/6/2021	9/23/2021	16	2
	UD9	59	M	N/A	N/A	N/A	N/A	N/A	N/A	8/20/2021	8/1/2021	41	2
	UD10	25	F	N/A	N/A	N/A	N/A	N/A	N/A	8/13/2021	7/31/2021	15	2
Unvaccinated + Delta	UD11	58	M	N/A	N/A	N/A	N/A	N/A	N/A	8/12/2021	7/6/2021	38	3
	UD12	57	F	N/A	N/A	N/A	N/A	N/A	N/A	8/13/2021	7/20/2021	24	3
	UD14	89	F	N/A	N/A	N/A	N/A	N/A	N/A	9/20/2021	8/31/2021	24	3
	UD15	32	M	N/A	N/A	N/A	N/A	N/A	N/A	10/7/2021	8/31/2021	37	3
	UD16	31	F	N/A	N/A	N/A	N/A	N/A	N/A	11/5/2021	10/12/2021	24	3

**Table S3.2. List of qPCR primers for mouse studies.**

The primers used to analyze cytokine expression in SARS-CoV-2- or mock-infected mice are listed.

<b>Gene</b>	<b>Forward</b>	<b>Reverse</b>
CCL2	CTTCTGGGCCTGCTGTTCA	CCAGCCTACTCATTGGGATCA
CXCL10	GCCGTCATTTTCTGCCTCAT	GCTTCCCTATGGCCCTCATT
IL1 $\alpha$	ACTGTTTCTAATGCCTTCCC	ATGGTTTCTTGTGACCCTGA
ISG15	GGCCACAGCAACATCTATGA	CGCAAATGCTTGATCACTGT
IFN $\alpha$ 4	TCCATCAGCAGCTCAATGAC	AGGAAGAGAGGGCTCTCCAG
OAS1	ATTACCTCCTCCCGACACC	CAAACCTCCACCTCCTGATGC



**Table S3.3. List of CyTOF-staining antibodies for mouse studies.**

The table describes antibody reagents used to analyze the immune response in SARS-CoV-2- or mock-infected mice by CyTOF.

<b>Antibody</b>	<b>Clone</b>	<b>Metal label</b>	<b>Cat#</b>	<b>Vendor</b>
Ly6G/C [Gr1]	RB6-8C5	141Pr	201306	Fluidigm
CD11c	N418	142Nd	201306	Fluidigm
CD69	H1.2F3	145Nd	104502	In-house
CD103	2E7	146Nd	121402	In-house
CD45	30-F11	147Sm	201306	Fluidigm
CD11b [MAC1]	M1/70	148Nd	201306	Fluidigm
CD19	6D5	149Sm	201306	Fluidigm
CD123	5B11	150Nd	106002	In-house
CD25	3C7	151Eu	101902	In-house
CD3e	145-2C11	152Sm	201306	Fluidigm
TER-119	TER119	154Sm	201306	Fluidigm
CXCR4	L276F12	159Tb	146502	In-house
CD62L	MEL-14	160Gd	104402	In-house
CD127	A7R34	161Dy	135029	In-house
CXCR5	L138D7	163Dy	145505	In-house
PD1	RMP1-30	164Dy	109113	In-house
CD8 $\alpha$	53-6.7	168Er	201306	Fluidigm
TCR $\beta$	H57-597	169Tm	201306	Fluidigm
NK1.1	PK136	170Er	201306	Fluidigm
CD44	IM7	171Yb	201306	Fluidigm
CD4	RM4-5	172Yb	201306	Fluidigm
CD304	3E12	173Yb	145202	In-house
B220	RA3-6B2	176Yb	201306	Fluidigm
IL-5 <sup>#</sup>	TRFK5	143Nd	201310	Fluidigm
IL-2 <sup>#</sup>	JES6-5H4	144Nd	201310	Fluidigm
IL-21 <sup>#</sup>	149204	155Gd	MAB594	In-house
Foxp3 <sup>#</sup>	3G3	156Gd	MA5-16222	In-house
CTLA4 <sup>#</sup>	UC10-4B9	157Gd	106302	In-house
IL-10 <sup>#</sup>	JES5-16E3	158Gd	201310	Fluidigm
TNF $\alpha$ <sup>#</sup>	MP6-XT22	162Dy	201310	Fluidigm
IFN $\gamma$ <sup>#</sup>	XMG1.2	165Ho	201310	Fluidigm
IL-4 <sup>#</sup>	11B11	166Er	201310	Fluidigm
IL-6 <sup>#</sup>	MP5-20F3	167Er	201310	Fluidigm
IL-17A <sup>#</sup>	TC11-18H10.1	174Yb	201310	Fluidigm
IFN $\alpha$ <sup>#</sup>	F18	175Lu	NB100-64387	In-house

<sup>#</sup>Intracellular antibodies

## REFERENCES

1. Sigal, A. Milder disease with Omicron: is it the virus or the pre-existing immunity? *Nat. Rev. Immunol.* **22**, 69–71 (2022).
2. Wolter, N. *et al.* Early assessment of the clinical severity of the SARS-CoV-2 omicron variant in South Africa: a data linkage study. *Lancet* **399**, 437–446 (2022).
3. Dejnirattisai, W. *et al.* SARS-CoV-2 Omicron-B.1.1.529 leads to widespread escape from neutralizing antibody responses. *Cell* (2022) doi:10.1016/j.cell.2021.12.046.
4. Syed, A. M. *et al.* Omicron mutations enhance infectivity and reduce antibody neutralization of SARS-CoV-2 virus-like particles. *medRxiv* (2022) doi:10.1101/2021.12.20.21268048.
5. Mannar, D. *et al.* SARS-CoV-2 Omicron variant: Antibody evasion and cryo-EM structure of spike protein-ACE2 complex. *Science* eabn7760 (2022).
6. Cao, Y. *et al.* Omicron escapes the majority of existing SARS-CoV-2 neutralizing antibodies. *Nature* (2021) doi:10.1038/s41586-021-04385-3.
7. VanBlargan, L. A. *et al.* An infectious SARS-CoV-2 B.1.1.529 Omicron virus escapes neutralization by therapeutic monoclonal antibodies. *Nat. Med.* (2022) doi:10.1038/s41591-021-01678-y.
8. Hoffmann, M. *et al.* The Omicron variant is highly resistant against antibody-mediated neutralization: Implications for control of the COVID-19 pandemic. *Cell* **185**, 447–456.e11 (2022).
9. Planas, D. *et al.* Considerable escape of SARS-CoV-2 Omicron to antibody neutralization. *Nature* (2021) doi:10.1038/s41586-021-04389-z.

10. Espenhain, L. *et al.* Epidemiological characterisation of the first 785 SARS-CoV-2 Omicron variant cases in Denmark, December 2021. *Euro Surveill.* **26**, (2021).
11. Meng, B. *et al.* SARS-CoV-2 Omicron spike mediated immune escape, infectivity and cell-cell fusion. *bioRxiv* 2021.12.17.473248 (2021) doi:10.1101/2021.12.17.473248.
12. Sato, K. *et al.* Attenuated fusogenicity and pathogenicity of SARS-CoV-2 Omicron variant. *Research Square* (2022) doi:10.21203/rs.3.rs-1207670/v1.
13. Dejnirattisai, W. *et al.* Reduced neutralisation of SARS-CoV-2 omicron B.1.1.529 variant by post-immunisation serum. *Lancet* (2021) doi:10.1016/S0140-6736(21)02844-0.
14. Pulliam, J. R. C. *et al.* Increased risk of SARS-CoV-2 reinfection associated with emergence of the Omicron variant in South Africa. *MedRxiv* (2021).
15. Miyamoto, S. *et al.* Vaccination-infection interval determines cross-neutralization potency to SARS-CoV-2 Omicron after breakthrough infection by other variants. *bioRxiv* (2022) doi:10.1101/2021.12.28.21268481.
16. Report 50 - Hospitalisation risk for Omicron cases in England. *Imperial College London* <https://www.imperial.ac.uk/mrc-global-infectious-disease-analysis/covid-19/report-50-severity-omicron/>.
17. England, P. H. SARS-CoV-2 variants of concern and variants under investigation in England. *technical briefing 12* (2021).
18. Shuai, H. *et al.* Emerging SARS-CoV-2 variants expand species tropism to murines. *EBioMedicine* **73**, 103643 (2021).
19. Winkler, E. S. *et al.* SARS-CoV-2 infection of human ACE2-transgenic mice causes severe lung inflammation and impaired function. *Nat. Immunol.* **21**, 1327–

- 1335 (2020).
20. Bentley, E. G. *et al.* SARS-CoV-2 Omicron-B.1.1.529 Variant leads to less severe disease than Pango B and Delta variants strains in a mouse model of severe COVID-19. *bioRxiv* 2021.12.26.474085 (2021) doi:10.1101/2021.12.26.474085.
  21. Halfmann, P. J. *et al.* SARS-CoV-2 Omicron virus causes attenuated disease in mice and hamsters. *Nature* (2022) doi:10.1038/s41586-022-04441-6.
  22. Shuai, H. *et al.* Attenuated replication and pathogenicity of SARS-CoV-2 B.1.1.529 Omicron. *Nature* (2022) doi:10.1038/s41586-022-04442-5.
  23. McMahan, K. *et al.* Reduced Pathogenicity of the SARS-CoV-2 Omicron Variant in Hamsters. *bioRxiv* 2022.01.02.474743 (2022) doi:10.1101/2022.01.02.474743.
  24. Abdelnabi, R. *et al.* The omicron (B.1.1.529) SARS-CoV-2 variant of concern does not readily infect Syrian hamsters. *Antiviral Res.* **198**, 105253 (2022).
  25. Le Bert, N. *et al.* SARS-CoV-2-specific T cell immunity in cases of COVID-19 and SARS, and uninfected controls. *Nature* **584**, 457–462 (2020).
  26. Coperchini, F., Chiovato, L., Croce, L., Magri, F. & Rotondi, M. The cytokine storm in COVID-19: An overview of the involvement of the chemokine/chemokine-receptor system. *Cytokine Growth Factor Rev.* **53**, 25–32 (2020).
  27. Sachs, N. *et al.* Long-term expanding human airway organoids for disease modeling. *EMBO J.* **38**, (2019).
  28. National Research Council, Division on Earth and Life Studies, Institute for Laboratory Animal Research & Committee for the Update of the Guide for the Care and Use of Laboratory Animals. *Guide for the Care and Use of Laboratory Animals: Eighth Edition.* (National Academies Press, 2011).
  29. Neidleman, J. *et al.* mRNA vaccine-induced T cells respond identically to SARS-

CoV-2 variants of concern but differ in longevity and homing properties depending on prior infection status. *Elife* **10**, (2021).

## Chapter IV

### **SIRT5 is a proviral factor that interacts with SARS-CoV-2 Nsp14 protein**

Marius Walter<sup>1,8\*</sup>, Irene P Chen<sup>2,3</sup>, Albert Vallejo-Gracia<sup>2,3</sup>, Ik-Jung Kim<sup>1</sup>, Olga Bielska<sup>1</sup>, Victor L Lam<sup>3</sup>, Jennifer M Hayashi<sup>2,3</sup>, Andrew Cruz<sup>1</sup>, Samah Shah<sup>1</sup>, Frank W Soveg<sup>2,3</sup>, John D Gross<sup>3,4</sup>, Nevan J Krogan<sup>2,3,4,5</sup>, Keith R Jerome<sup>6,7</sup>, Birgit Schilling<sup>1</sup>, Melanie Ott<sup>2,3</sup>, Eric Verdin<sup>1\*</sup>.

#### **Affiliations**

<sup>1</sup> Buck Institute for Research on Aging, Novato, CA, USA.

<sup>2</sup> Gladstone Institutes, San Francisco, CA, USA.

<sup>3</sup> University of California San Francisco, San Francisco, CA, USA.

<sup>4</sup> Quantitative Biosciences Institute (QBI), University of California San Francisco, San Francisco, CA, USA.

<sup>5</sup> QBI COVID-19 Research Group (QCRG), San Francisco, CA, United States.

<sup>6</sup> Vaccine and Infectious Disease Division, Fred Hutch Cancer Center, Seattle, WA, USA.

<sup>7</sup> Department of Laboratory Medicine, University of Washington, Seattle, WA, USA.

<sup>8</sup> Current address: Vaccine and Infectious Disease Division, Fred Hutch Cancer Center, Seattle, WA, USA.

\*Correspondence to [mwalter2@fredhutch.org](mailto:mwalter2@fredhutch.org), [everdine@buckinstitute.org](mailto:everdine@buckinstitute.org)

## **ABSTRACT**

SARS-CoV-2 non-structural protein Nsp14 is a highly conserved enzyme necessary for viral replication. Nsp14 forms a stable complex with non-structural protein Nsp10 and exhibits exoribonuclease and N7-methyltransferase activities. Protein-interactome studies identified human sirtuin 5 (SIRT5) as a putative binding partner of Nsp14. SIRT5 is an NAD-dependent protein deacylase critical for cellular metabolism that removes succinyl and malonyl groups from lysine residues. Here we investigated the nature of this interaction and the role of SIRT5 during SARS-CoV-2 infection. We showed that SIRT5 interacts with Nsp14, but not with Nsp10, suggesting that SIRT5 and Nsp10 are parts of separate complexes. We found that SIRT5 catalytic domain is necessary for the interaction with Nsp14, but that Nsp14 does not appear to be directly deacylated by SIRT5. Furthermore, knock-out of SIRT5 or treatment with specific SIRT5 inhibitors reduced SARS-CoV-2 viral levels in cell-culture experiments. SIRT5 knock-out cells expressed higher basal levels of innate immunity markers and mounted a stronger antiviral response, independently of the Mitochondrial Antiviral Signaling Protein MAVS. Our results indicate that SIRT5 is a proviral factor necessary for efficient viral replication, which opens novel avenues for therapeutic interventions.

## **AUTHOR SUMMARY**

SARS-CoV-2 is a pathogen of global concern. After cellular entry, SARS-CoV-2 hijacks the cellular machinery, and the viral proteins physically interact with hundreds of human proteins. Here we described the interaction between SARS-CoV-2 protein Nsp14, a key enzyme necessary for viral replication, and human sirtuin 5 (SIRT5), a protein deacylase that removes succinyl and malonyl groups from lysine residues. We showed that SIRT5 strongly interacts with Nsp14 and that SIRT5 catalytic domain is necessary for the interaction, despite Nsp14 not being directly deacylated by SIRT5. Furthermore, we found that knocking out or inhibiting SIRT5 reduced SARS-CoV-2 viral levels in cell-culture experiments, and that SIRT5 knock-out cells mounted a stronger antiviral response. Altogether, our result indicates that SIRT5 is a proviral factor necessary for efficient viral replication. SIRT5 is a critical metabolic enzyme that regulates several important metabolic processes, but its role during disease and infection is currently unknown. Our work suggests that SIRT5, and potentially other sirtuins, could act as a bridge between cellular metabolism and the innate responses against viral infections.



## INTRODUCTION

Severe acute respiratory syndrome coronavirus 2 (SARS-CoV-2) is a pathogen of global concern that needs no further introduction. After cellular entry, SARS-CoV-2 hijacks the cellular machinery, and the viral proteins physically interact with hundreds of human proteins<sup>1-4</sup>. In most cases, however, the exact nature of the interactions and their functions and relevance during viral infection remain unknown.

SARS-CoV-2 encodes two large open reading frames, ORF1a and ORF1b, that are processed into 16 non-structural proteins after proteolytic cleavage by viral proteases. The 16 non-structural proteins, Nsp1 to Nsp16, are involved in every aspect of viral replication and are highly conserved in coronaviruses. Coronavirus Nsp14 protein is part of the replication-transcription complex and has two conserved domains with distinct functions. The N-terminal domain acts as a 3' to 5' exoribonuclease (ExoN), and the C-terminal domain displays RNA cap guanine N7-methyltransferase (MTase) activity (Figure 4.1A)<sup>5-8</sup>. The N-terminal ExoN domain provides proofreading activity during RNA replication, allowing the removal of mismatched nucleotides introduced by the viral RNA polymerase<sup>9-11</sup>. This proofreading activity ensures a high level of fidelity during RNA replication and is unique among RNA viruses<sup>12,13</sup>. Coronaviruses and related viruses in the order nidovirales have some of the largest genomes (26–32 kb) among known RNA viruses<sup>14</sup>, and the acquisition of ExoN activity is thought to have allowed nidoviruses to evolve these large genomes<sup>9,15</sup>. The C-terminal MTase domain of Nsp14 is an S-adenosyl methionine (SAM)-dependent methyltransferase critical for viral RNA capping that methylates the 5' guanine of the Gppp-RNA cap at the N7 position<sup>6,7</sup>. The 5' cap is important for viral mRNA stability and translation and for

escaping host innate antiviral responses. Importantly, Nsp14 forms a stable complex with the non-structural protein Nsp10, a small zinc-binding co-factor with no reported enzymatic activity on its own <sup>7,10</sup>. Nsp10 binds and stabilizes the N-terminal ExoN domain of Nsp14 and is necessary for ExoN activity, but not for MTase activity. Interestingly, mutations that abolish ExoN activity cause a lethal phenotype in SARS-CoV-2 and MERS-CoV, but not in SARS-CoV or other coronaviruses <sup>16</sup>, suggesting that ExoN has additional functions beyond its proofreading activity. Indeed, Nsp14 triggers translational shutdown, participates in evasion of innate immunity, activates proinflammatory signals, and mediates viral recombination <sup>17-20</sup>.

Large-scale protein-protein interaction analyses of SARS-CoV-2 and human proteins revealed putative interacting partners for all of the SARS-CoV-2 proteins. Several independent studies, from us and others, suggested that SARS-CoV-2 Nsp14 protein interacts with human sirtuin 5 (SIRT5) <sup>1-4</sup>. Sirtuins are a family of conserved protein deacylases and mono-ADP-ribosyltransferases found in organisms ranging from bacteria to humans. Sirtuins use nicotinamide adenine dinucleotide (NAD) as a co-substrate and are important regulators of cellular metabolism and aging <sup>21,22</sup>. Most sirtuins act as NAD-dependent protein deacetylases, removing acetyl groups from lysine residues and, as such, tightly connect post-translational protein regulation with cellular metabolism. The seven mammalian sirtuins (SIRT1-7) are found in different cellular compartments. They deacylate histones and transcriptional regulators in the nucleus and also specific proteins in the cytoplasm and mitochondria. Sirtuins are crucial regulators of cellular metabolism and energy homeostasis and have emerged as key regulators of aging and age-related diseases.

SIRT5 is unique among the seven mammalian sirtuins. It is only a weak protein deacetylase, but it efficiently removes longer-chain acyl groups from proteins, such as succinyl, malonyl or glutaryl groups <sup>23,24</sup>. By preferentially catalyzing the removal of these negatively charged acidic modifications, SIRT5 functions as the main cellular desuccinylase, demalonylase, and deglutarylase <sup>24–26</sup>. SIRT5 is predominantly found in the mitochondria, but also exerts regulatory activity in the cytoplasm. It is involved in several important metabolic processes, such as glycolysis, fatty acid oxidation and ketone body production <sup>27</sup>. Despite elevated succinylation or malonylation levels in several tissues, no obvious phenotype or abnormalities are observed in *Sirt5* knockout mice under basal conditions <sup>28</sup>. The roles of SIRT5 in disease, infection, and aging, are unclear.

Here we investigated the role of SIRT5 during infection with SARS-CoV-2. We showed that SIRT5 interacts with Nsp14, but not with its cofactor Nsp10, and that SIRT5 catalytic activity is necessary for the interaction. Furthermore, knock-out or inhibition of SIRT5 reduced viral levels in cell-culture experiments, revealing that SIRT5 is a proviral factor necessary for efficient viral replication.

## RESULTS

### SARS-CoV-2 Nsp14 interacts with human SIRT5

Protein-protein interaction mass-spectrometry studies suggested that SARS-CoV-2 Nsp14 binds to SIRT5<sup>1-4</sup>. We first sought to confirm and characterize the nature of this interaction. We used a mammalian expression vector developed by Gordon et al. that contains Nsp14 with a 2xStrep affinity tag (Nsp14-strep) that can be used for affinity purification<sup>1</sup>. Plasmids expressing Nsp14-strep or a GFP control were transfected into HEK-293T cells for 48 hours, and tagged proteins were purified by affinity purification using magnetic beads. Using western blots, we found that SIRT5 was specifically co-purifying with Nsp14, confirming published mass spectrometry results (Figure 4.1B). Immunofluorescence in human alveolar basal epithelial A549 cells transfected with Nsp14 expression plasmid further showed that Nsp14 and SIRT5 co-localized into the same cellular compartments, with a predominantly cytoplasmic and peri-nuclear localization (Figure 4.1C).

We next used Cellular Thermal Shift Assay (CETSA) to quantify the changes in the thermal stability of Nsp14 and SIRT5 in intact cells. The thermal stability of proteins changes upon ligand binding, and CETSA can be used to record the strength of the interaction in the physiological context. HEK-293T cells were transfected with plasmids expressing Nsp14 and SIRT5, either alone or in combination, and the shift in thermal stability was assessed by western blot (Figure 4.1D). We observed an important increase in the stability of both proteins when they were co-transfected together. Nsp14, in particular, was poorly expressed and barely detectable when transfected alone, but a strong signal appeared in the presence of SIRT5. Overall, these initial

observations showed that SIRT5 and Nsp14 were interacting in human cells and that SIRT5 strongly stabilized Nsp14 expression.

Nsp14 forms a stable complex with the small viral protein Nsp10<sup>7,10</sup>. We thus tested whether SIRT5 also interacted with Nsp10, or whether they were parts of independent complexes. To eliminate endogenous expression of SIRT5, we generated a *SIRT5* knockdown cell line (*SIRT5*-KD), using CRISPR interference in HEK-293T cells<sup>29</sup>. Several guide RNAs were tested, and one was selected for the rest of the study. SIRT5 was undetectable in this cell line (Figure 4.1E). Expression plasmids for SIRT5, Nsp14-strep and Nsp10 with a Flag tag (Nsp10-Flag) were transfected alone or in combination for 48 hours in *SIRT5*-KD cells. Proteins were then co-purified either by strep affinity purification (Strep-AP) or Flag immunoprecipitation (Flag-IP) (Figure 4.1F). Strep-AP confirmed that both SIRT5 and Nsp10 interacted with Nsp14. By contrast, pulling down Nsp10 by Flag-IP showed that only Nsp14 co-purified with Nsp10. This indicates that Nsp10 and SIRT5 do not interact. Besides, the SIRT5 signal after Strep-AP appeared to be lower in the presence of Nsp10, and we hypothesized that Nsp10 and SIRT5 compete for Nsp14 binding. To test this hypothesis, Nsp14, SIRT5, and an increasing quantity of Nsp10 plasmids were co-transfected in *SIRT5*-KD cells. SIRT5 binding was lost with high concentrations of Nsp10 (Figure 4.1G). Thus, SIRT5 and Nsp10 competitively bind Nsp14, and Nsp14/SIRT5 and Nsp14/Nsp10 likely form independent complexes.

### **SIRT5 catalytic activity is necessary for the interaction with Nsp14**

SIRT5 is the main cellular desuccinylase, demalonylase, and deglutarylase, and a weak deacetylase<sup>24–26</sup>. SIRT5 can physically bind to some of its enzymatic targets, such as Mitochondrial Antiviral Signaling Protein MAVS<sup>30</sup>, mitochondrial serine hydroxymethyltransferase SHMT2<sup>31</sup>, or pyruvate kinase PKM2<sup>32</sup>. In these examples, SIRT5 both desuccinylates and binds the target protein as determined by co-immunoprecipitation. We thus hypothesized that SIRT5 could enzymatically modify Nsp14 and remove a putative succinyl, malonyl or glutaryl group.

To test this hypothesis, we determined if SIRT5 catalytic mutants bind Nsp14. Based on the structure of the SIRT5 catalytic domain and the homology with other sirtuins, we used or generated several expression constructs with mutations in conserved residues: H158 is catalytically required to abstract a proton from NAD, Q140 and I142 are involved in NAD binding, and Y102 and T105 interact with the extended acidic chains of succinyl or malonyl groups (Figure 4.2A). H158, Q140 and I142 are universally conserved in sirtuins, but Y102 and T105 are specific to SIRT5 and mediate the specificity to longer-chain acidic groups<sup>23,33</sup>. Mutation of these residues is known (for H158Y, Y102F and R105M) or predicted (for Q140A and I142A, based on homology with other sirtuins) to abolish SIRT5 desuccinylation activity. After transfection of Nsp14-strep and SIRT5 mutants in *SIRT5*-KD cells, the binding of SIRT5 to Nsp14 was lost or severely reduced in most mutants (Figure 4.2B). In particular, SIRT5 binding completely disappeared in H158Y and Q140A mutants, and only remained in significant amounts with the Y102F mutation. This result shows that an intact SIRT5 catalytic domain is necessary for the interaction with Nsp14. Of note,

treatment of HEK293T cells with the proteasome inhibitor MG-132 did not affect the stability of the overexpressed catalytic mutants, which suggested that the different proteins could fold properly (Figure S4.1A).

To further establish that the catalytic activity of SIRT5 is necessary for the interaction with Nsp14, we used a recently described, potent and specific SIRT5 inhibitor (Sirt5-i)<sup>34</sup>. This inhibitor has a published IC<sub>50</sub> of 0.11 μM, and we measured an IC<sub>50</sub> of 0.44 μM in desuccinylation assays *in vitro* (Figure S4.1B). *SIRT5*-KD cells were transfected with Nsp14 and SIRT5 and incubated with increasing concentrations of Sirt5-i. The binding of SIRT5 was lost at high concentrations of Sirt5-i, with the interaction almost absent at 25 and 100 μM (Figure 4.2C). This observation again suggested that the SIRT5 catalytic activity was necessary for the interaction. Notably, until now, Sirt5-i had not been characterized in cell culture. This experiment suggested that Sirt5-i could be efficiently used in cells, with a putative IC<sub>50</sub> of approximately 10 μM. Next, we tested whether the interaction depended on cellular NAD levels. NAD is a necessary co-substrate, and SIRT5 activity is highly correlated with cellular NAD levels. In cells, most NAD is synthesized through the NAD salvage pathway<sup>35</sup>. Treating cells with the NAMPT inhibitor FK866 blocks the rate-limiting step in the pathway and rapidly depletes NAD levels, and supplementing cells with the NAD precursor nicotinamide mononucleotide (NMN) rescues the depletion<sup>36</sup> (Figure S4.1C). *SIRT5*-KD cells were transfected for 24 hours with Nsp14 and SIRT5 and for an additional 24 hours with FK866 and/or NMN (Figure 4.2D). SIRT5 binding was highly reduced in the presence of FK866 (low NAD levels), but the binding was rescued in presence of NMN, and

appeared slightly stronger when cells were treated with NMN alone (high NAD levels). This finding indicated that the interaction of Nsp14 and SIRT5 positively correlated with cellular NAD levels. Altogether, by directly inhibiting SIRT5 or modulating the level of its co-substrate NAD, these experiments confirmed that SIRT5 catalytic activity was necessary for the interaction with Nsp14.

Finally, we determined if Nsp14 was directly modified by SIRT5 and if we could detect changes in the levels of acetylation, succinylation or malonylation. *SIRT5*-KD cells were transfected with SIRT5, Nsp14 and/or a GFP expression control. After affinity purification, pan-acetylation/succinylation/malonylation antibodies were used to detect changes in the levels of different lysine modifications (Figure 4.2E). Independent of the presence of SIRT5, we detected no measurable changes in acetylation, succinylation or malonylation, either among input or purified proteins. Weak bands were observed for purified GFP and Nsp14, but the intensity of the signal was not affected by the presence or absence of SIRT5, suggesting that it is not specific. Pan-modification antibodies are often not very sensitive, and we tested whether we could detect changes in lysine modifications by mass spectrometry. Nsp14-strep was transfected in *SIRT5*-KD cells, purified by affinity purification, and analyzed by mass spectrometry. The experiment was done with and without SIRT5 co-transfection, in three biological replicates each. In both conditions, Nsp14 had high coverage (65% coverage in presence of SIRT5, 88% without SIRT5), and we confirmed the interaction of Nsp14 with the two human proteins GLA and IMDH2 as reported <sup>1</sup>. However, despite 94% of lysine residues being covered (28 out of 30) and high quality of the data, we found no acetylated, succinylated, malonylated or glutarylated sites. We



detected a previously characterized phosphorylation site at serine 56<sup>37</sup> and a nitrosylation site on tyrosine 351. Since SIRT5 is the only known cellular desuccinylase, demalonylase, and deglutarylase, we had hoped that analyzing Nsp14 post-translational modifications in the presence or absence of SIRT5 would reveal changes in the level of these acylations marks. On the contrary, the absence of detectable acetylation, succinylation, malonylation and glutarylation suggested that Nsp14 was not directly modified by SIRT5. This series of experiments revealed that, even though SIRT5 catalytic activity is necessary for the interaction with Nsp14, Nsp14 did not appear to be a direct target of SIRT5.

### **Nsp14 also interacts with SIRT1**

The seven human sirtuins share conserved domains, and we tested whether Nsp14 also interacts with the other sirtuins. We found that Nsp14 interacted with SIRT1, but not with SIRT2, 3, 6 or 7 (Figure 4.3A). We could not investigate the interaction with SIRT4 because we lacked a specific antibody. The signal from SIRT1 was specific but appeared weaker than with SIRT5, which might explain why it was not detected by mass spectrometry<sup>1</sup>. Interestingly, and as we observed with SIRT5, mutating SIRT1 catalytic domain or treating cells with the SIRT1 inhibitor Ex-527 eliminated the interaction (Figure 4.3B, C). This finding suggested again that SIRT1 catalytic activity is necessary for the interaction with Nsp14. By contrast, treating cells with the specific SIRT1 activator SRT1720 or the non-specific activator Resveratrol had no measurable effect on Nsp14 binding (Figure 4.3D, E). Both activators were toxic to cells at high concentrations, and the apparent decrease in binding after affinity purification correlated with reduced levels of Nsp14 and SIRT5 in input lanes.

To uncover a putative molecular function of the Nsp14-SIRT5 interaction, Nsp14 and SIRT5 were expressed in *E. coli* and purified. Unfortunately, and even though the complex could be readily observed in mammalian cells, we could not reconstitute it *in vitro* with purified proteins, either by column chromatography or gel electrophoresis. This was the case when the two proteins were expressed separately and purified, or when co-expressed in *E. coli*. This observation suggests that the *in vitro* conditions that we used were inadequate and that additional parameters in mammalian cells were likely missing, such as other protein cofactors, post-translational modifications, or specific buffer conditions. Even though the complex could not be observed *in vitro*, we determined if the enzymatic activities of SIRT5 or Nsp14 were perturbed when in presence of each other. We measured the desuccinylation activity of SIRT5 alone or when incubated with increasing concentrations of Nsp14, using an *in vitro* desuccinylation assay. We detected no changes in desuccinylation activity in presence of Nsp14, whereas adding known inhibitors, such as nicotinamide or the specific SIRT5 inhibitor Sirt5-i, completely inhibited the activity (Figure 4.3F). Similarly, we used a methyltransferase assay to characterize the MTase activity of Nsp14 in presence of SIRT5. This assay measures the conversion of the methyl donor S-adenosyl methionine (SAM) into S-adenosyl homocysteine and can be used to measure the activity of any SAM-dependent methyltransferase. Nsp14 methylates the mRNA cap and Nsp14 was incubated with an unmethylated GpppG cap-analog, in presence of SAM, NAD and increasing concentrations of SIRT5 (Figure 4.3G). The Nsp14/Nsp10 complex and Nsp14 alone had similar activities, as predicted. We detected a small 10% increase of methyltransferase activity with excess SIRT5, but

this increase persisted in presence of the SIRT5 inhibitor Sirt5-i. Since we showed above that Sirt5-i disrupted the interaction (Figure 4.3G), this small increase might not be specific. Besides, Nsp14 ExoN activity depends on Nsp10, and Nsp14 has no ExoN activity by itself. We showed that Nsp10 and SIRT5 are parts of separate complexes (Figure 4.1F-G), suggesting that the Nsp14/SIRT5 complex is very unlikely to have any ExoN activity either. Overall, these enzymatic assays failed to uncover a clear molecular function of the Nsp14/SIRT5 complex.

### **SIRT5 is a proviral factor**

We next wanted to examine the role of SIRT5 during SARS-CoV-2 infection. We generated a *SIRT5* knockout (*Sirt5*-KO) in A549 cells overexpressing ACE2 (A549-ACE2), using CRISPR-Cas9 editing and three commercially designed guide RNAs. The knockout was generated by transfecting cells with Cas9-gRNA ribonucleoproteins, and cells transfected with Cas9 alone and no guide RNAs were used as wild-type (WT) controls. As expected, SIRT5 was undetectable in *SIRT5*-KO cells (Figure 4.4A). WT and *SIRT5*-KO cells were infected with SARS-CoV-2 (Wuhan strain, USA/WA-1/2020 isolate) at a multiplicity of infection (MOI) of 0.1 and 1, and viral RNA was quantified by RT-qPCR after 3 days (Figure 4.4B). At both MOIs, we observed a significant 2–3-fold decrease of SARS-CoV-2 mRNA in *SIRT5*-KO cells ( $p < 0.0001$  and  $p = 0.0002$  at MOI=0.1 and 1, respectively, by ANOVA). These results were confirmed by plaque assay, and we measured a significant sixfold decrease of viral titers in *SIRT5*-KO cells (Figure 4.4C,  $p < 0.0001$ , ANOVA). These observations suggested that SIRT5 is necessary for SARS-CoV-2 replication and/or propagation.

To confirm this result, A549-ACE2 cells were infected with SARS-CoV-2 in presence of the specific inhibitor Sirt5-i. Sirt5-i caused no measurable cytotoxicity (Figure 4.4D) and significantly reduced cell-associated viral mRNA levels by almost twofold (Figure 4.4E,  $p=0.0001$  and  $p<0.0001$  at 25 and 100  $\mu\text{M}$ , respectively, ANOVA). Viral titers measured by plaque assay were also significantly reduced by fourfold in presence of Sirt5-i inhibitor (Figure 4.4F,  $p<0.0001$ , ANOVA). Human lung-cancer cells Calu-3 endogenously express ACE2 and are often considered a better model for SARS-CoV-2 infection. Calu-3 cells were infected with SARS-CoV-2 and treated with SIRT5 inhibitor Sirt5-i. Viral RNA levels were significantly reduced, with a twofold reduction in viral mRNA at 100  $\mu\text{M}$  (Figure 4.4G,  $p=0.011$ , ANOVA). Viral titers measured by plaque assay were also significantly reduced by twofold in Calu3 cells in presence of Sirt5-i inhibitor (Figure 4.4H,  $p=0.009$ ). Altogether, this showed that knocking out or inhibiting SIRT5 resulted in a decrease in SARS-CoV-2 levels.

We obtained similar results with SIRT1. SARS-CoV-2 replication was reduced in *SIRT1*-KO A549-ACE2 cells, with a significant twofold decrease in mRNA levels ( $p=0.0002$  and  $p=0.0011$  at MOI = 0.1 and 1, respectively), and a significant twofold decrease in viral titers as well (Figure 4.4A-C, I,  $p<0.0001$ ). SIRT1 inhibitor Ex-527 significantly reduced viral titers by sixfold in A549-ACE2 cells, and by twofold in Calu3 cells ( $p<0.0001$  and  $p=0.011$ , respectively, Figure 4.4E-H). This showed that SIRT1 is also necessary for efficient SARS-CoV-2 infection. Interestingly, treating A549-ACE2 or Calu3 cells with both SIRT5 and SIRT1 inhibitors did not further reduce viral levels. Titters significantly decreased by two to fourfold in cells treated with Sirt5-I and Ex-527 together, a level similar to cells treated with the inhibitors alone (Figure 4.4F, H). This

suggested that the roles of SIRT1 and SIRT5 during SARS-CoV-2 infection might be interdependent or that they act in the same pathway. In summary, our observations indicated that SIRT5 and SIRT1 are proviral factors necessary for coronaviruses replication and/or propagation. The reduction of viral levels without SIRT1 was less pronounced and consistent than without SIRT5, and we focused the rest of our investigation on SIRT5.

### **SIRT5 proviral activity is partially independent of the interaction with Nsp14**

To determine if the proviral role of SIRT5 could be explained by its interaction with Nsp14, we analyzed the role of SIRT5 during infection with human coronavirus HCoV-OC43, a distantly related beta-coronavirus. SIRT5 interacts with Nsp14 from SARS-CoV-2 and SARS-CoV, but not from MERS-CoV <sup>2</sup>. Similarly, we observed by affinity co-purification in HEK293T cells that SIRT5 was not interacting with Nsp14 from HCoV-OC43 (Figure 4.5A). This result further confirmed that SIRT5 interaction with Nsp14 is specific to SARS-like coronaviruses. Human colon adenocarcinoma cells HCT-8 were infected with HCoV-OC43 in presence of Sirt5-i inhibitor, and we observed a significant decrease in viral levels (Figure 4.5B, C). At 100  $\mu$ M, viral mRNA in the cell-culture supernatant and viral titers measured by plaque assay were both reduced 10-fold ( $p=0.0021$  and  $p < 0.0001$ , respectively, ANOVA). This observation suggested that the role of SIRT5 during infection might be partially independent of its interaction with Nsp14.

### ***SIRT5* knockout cells express a higher basal level of viral restriction factors**

To gain insight into the role of *SIRT5* during SARS-CoV-2 infection, we performed RNA-seq in A549-ACE2 cells, WT and *SIRT5*-KO, after 3 days of infection with SARS-CoV-2 (MOI=1). Sequencing was done in four biological replicates for each condition. Principal-component analysis showed that samples separated well, based on knockout and infection status (Figure S4.2A). When comparing uninfected WT and *SIRT5*-KO cells, 1139 and 869 genes were significantly up- and downregulated, respectively (q-value threshold  $q=0.05$ ). Most of these changes were modest, and only 69 genes were up- or downregulated by more than twofold (Figure 4.6A, left panel). Gene Ontology and pathway enrichment analysis showed that up-regulated genes were principally involved in metabolism and, in particular, protein catabolism processes in the lysosome, whereas down-regulated genes were involved in DNA replication and mitosis. These findings were in line with reports showing that *SIRT5* is implicated in autophagy and controls cell proliferation in cancer cells by targeting multiple metabolic enzymes<sup>31,32,38–41</sup>. In WT infected samples, around 5% of total reads mapped to the SARS-CoV-2 genome, indicating substantial and successful viral replication. Despite this high level of viral expression, we observed a muted response to infection, at least in WT cells (Figure 4.6A, middle panel). SARS-CoV-2 efficiently evades innate immune defense through multiple mechanisms, and this absence of a strong transcriptional response is characteristic of SARS-CoV-2 infection and has been documented in numerous studies<sup>42–44</sup>. For example, we could not detect induction of *IFN- $\alpha$* , *IFN- $\beta$* , *CXCL10*, interleukin *IL-6* or tumor necrosis factor (*TNF*). When comparing WT infected and WT mock-infected samples, 275 and 385 genes were significantly up- and down-regulated, respectively (threshold  $q=0.05$ ), with only

the chemokine *CXCL8* (IL-8) and the transcription factor *ATF3* being increased with a fold-change higher than 2 (Figure 4.6A, middle). Gene Ontology and pathway enrichment analysis indicated that genes involved in response to virus infections were upregulated, with the two most upregulated pathways being the NOD-like and RIG-I-like receptors signaling pathways, which are implicated in the intracellular recognition of viruses. Notably, other studies that reported a higher number of differentially expressed genes often had higher levels of viral infection, with a fraction of SARS-CoV-2 reads of 10–50%, compared to 5% in this study. This might explain why the transcriptional response that we observed is comparatively smaller<sup>42,45</sup>.

We next analyzed the effect of *SIRT5* knockout on SARS-CoV-2 infection. SARS-CoV-2 levels were almost fourfold less in *SIRT5*-KO infected cells than in WT infected cells, confirming that *SIRT5* is a proviral factor ( $q=8.4 \times 10^{-13}$ , Figure 4.6B). We focused our analysis on the 3221 genes that were differentially expressed between at least two of the four conditions (threshold  $q=0.01$ ). Hierarchical consensus clustering of the differentially expressed genes generated eight clusters, representing groups of genes that behaved similarly between the different sample conditions (Figure 4.6C, D). Enrichment analysis of biological gene sets then allowed the identification of the cellular pathways over-represented in the identified clusters (Figure 4.6E). For example, clusters 2 and 3 corresponded to genes with a lower expression in *SIRT5*-KO cells, independently of the infection status, and pathways linked to the cell cycle and cellular metabolism were significantly enriched in these clusters. In most of the clusters (clusters 2–6), pathways linked to cellular metabolism were significantly enriched, highlighting that *SIRT5* is an important metabolic enzyme. Clusters 7 and 8

were particularly interesting. They represent genes that are expressed at a higher basal level in *SIRT5*-KO cells, and whose expression is further increased during infection (Figure 4.6C, D). Strikingly, pathways linked to innate immunity, such as type I and II interferon and NF $\kappa$ B signaling, were significantly enriched in these clusters (Figure 4.6E). Genes in clusters 7 and 8 are up-regulated in *SIRT5*-KO cells, even in uninfected cells, which suggested that *SIRT5*-KO cells had a higher basal level of innate immunity markers and could mount a stronger immune response.

We thus investigated whether innate immunity pathways were up-regulated in *SIRT5*-KO cells, even without viral infection. In mock-infected cells, the Gene Ontology term “Innate Immune Response” was significantly enriched in *SIRT5*-KO samples ( $q=0.0071$ ). Type-I interferon responses are one of the most important lines of defense against viruses. We analyzed the expression of known Type-I interferon-stimulated genes, as well as of other genes broadly linked to innate immune responses and present in clusters 7 and 8 (Figure 4.7A). As could be expected, most of these genes were upregulated in infected cells. Strikingly, many of these genes, which are normally involved in the response to pathogens, were also upregulated in *SIRT5*-KO cells in absence of infection, with 39 out of the 71 selected genes being significantly upregulated in mock-infected *SIRT5*-KO cells ( $q < 0.05$ ). Many of these genes were expressed at similar levels between infected WT cells and mock-infected *SIRT5*-KO cells, and were further increased in infected *SIRT5*-KO cells (Figure 4.7A). This included cytokines (*IL33*, *CXCL5*, and *CSF1*), the transmembrane restriction factors *IFITM2* and 3, members of the complement system (*C1S*, *C1R* and *C3*), the MHC class I subunit *B2M*, and other interferon-stimulated genes or restriction factors (e.g.,



*IFIT3*, *TRIM22*, *STAT3*, *MMP7*, *LCN2*, *MUC5AC*, *SLFN5*, *NT5E*, *CAST* and *SNCA*)<sup>46–52</sup>. The upregulation between WT and *SIRT5*-KO in mock-infected cells was modest but statistically significant, ranging from 20 to 50%, and was further increased up to twofold in infected *SIRT5*-KO cells (Figure 4.7A, Figure S4.2A). These results suggest that *SIRT5*-KO cells express a higher basal level of numerous restriction factors and mount a stronger antiviral response, which could explain why SARS-CoV-2 levels are decreased in absence of SIRT5.

To confirm these observations, we validated by RT-qPCR the upregulation of several restriction factors between WT and *SIRT5*-KO cells, in absence of infection (Figure 4.7B). This confirmatory analysis was done with new samples and independently of the RNA-seq experiment, using eight biological replicates per group to increase statistical power and measure subtle effects. The cytokines *IFN-β* and *IL33* were significantly upregulated two to threefold in *SIRT5*-KO cells ( $p=0.0004$ , and  $p<0.0001$ , respectively, t-test). Other markers such as *STAT3*, *IFIT3* and *B2M* showed modest but statistically significant upregulation ranging from 20 to 70%, while *IFITM2* and *SCNA* had increased expression that did not reach statistical significance. These results confirmed that *SIRT5*-KO cells express a higher basal level of viral restriction factors.

### **SIRT5 proviral activity is independent of the MAVS signaling pathway**

SIRT5 is implicated in RIG-1/MAVS antiviral signaling, a key innate immune pathway that recognizes viral RNA in the cytosol and activates type I interferon. Specifically, SIRT5 desuccinylate MAVS and reduce MAVS aggregation on the mitochondrial

surface, resulting in lower interferon activation (Figure S4.3A) <sup>30</sup>. To explain the reduced viral replication in *SIRT5*-KO cells, we hypothesized that SIRT5 absence could lead to stronger MAVS aggregation and in turn a stronger antiviral response. To test this hypothesis, we used CRISPR-Cas9 to delete MAVS in A549 cells stably co-expressing ACE2 and TMPRSS2 (A549-A/T cells). A549-A/T cells can be infected more efficiently and represent an improvement over cells expressing ACE2 only, and were used for this experiment. Cells were transduced with a lentiviral vector expressing Cas9 and a gRNA against *MAVS*, which resulted in a 90% knockdown of MAVS by western blot (Figure 4.8A). *MAVS* knockdown (*MAVS*-KD) cells were then infected with SARS-CoV-2 in presence or absence of SIRT5 inhibitor (Figure 4.8B). *MAVS* knockdown resulted in a three to five-fold increase in viral levels in both DMSO or Sirt5-i-treated cells ( $p < 0.0001$ , ANOVA), indicating that MAVS is implicated in the antiviral response against SARS-CoV-2, independently of SIRT5. If SIRT5 was acting primarily by reducing MAVS activation, inhibiting SIRT5 in *MAVS*-KD cells would be expected to have little effect. However, we found that inhibiting SIRT5 had the same effect in WT and *SIRT5*-KO cells, with a significant reduction of titers of about twofold in both WT and *MAVS*-KD cells ( $p = 0.0052$  and  $p < 0.0001$ , respectively, ANOVA). This important result invalidated our hypothesis and suggested that SIRT5 role in innate immunity is not limited to regulating MAVS. In fact, this showed that SIRT5 function during SARS-CoV-2 infection is likely independent of the RIG-I/MAVS pathway.

Finally, we wanted to elucidate whether Nsp14 played a role in modulating SIRT5 proviral activity. A549 cells cannot be transfected efficiently, and we attempted to generate cell lines expressing Nsp14. Nsp14 is cytotoxic, and we could not build cell

lines stably expressing Nsp14 from a constitutive lentiviral vector. To circumvent this toxicity issue, we used doxycycline-inducible Nsp14 and GFP lentiviral vectors. A549-ACE2 WT and *SIRT5*-KO cells were transduced with inducible Nsp14 and GFP constructs, and cells were successfully selected with puromycin. In absence of doxycycline, cells stably transduced with inducible Nsp14 had no apparent replicative or morphological defects. As expected, doxycycline treatment induced a strong overexpression of *GFP*, with a 2000-fold induction compared to basal levels as measured by RT-qPCR (Figure 4.8C). However, we did not observe any change in *Nsp14* expression after doxycycline treatment. The continuous puromycin selection ensured that the lentivirus vector had been stably integrated, but *Nsp14* induction was nonetheless not functional. It is possible that leaky basal expression of *Nsp14* in absence of doxycycline was sufficient to negatively select against permissive integration events. Unfortunately, these results prevented us from further investigating if Nsp14 could impact SIRT5 activity in cells.

## DISCUSSION

In this study, we investigated the role of SIRT5 during SARS-CoV-2 infection. Our results show that SIRT5 interacts with the non-structural viral protein Nsp14, and that this interaction is independent of Nsp10. Interestingly, we found that the catalytic activity of SIRT5 was necessary for the interaction, as several SIRT5 catalytic mutants could not bind to Nsp14, and the interaction was blocked by specific SIRT5 inhibitors. SIRT5 is the main cellular desuccinylase, demalonylase, and deglutarylase, but we could not detect these lysine modifications on Nsp14 protein, suggesting that Nsp14 is not directly modified by SIRT5. We further showed that SIRT5 is a proviral factor and that SARS-CoV-2 levels decrease when SIRT5 is deleted or inhibited in cell-culture experiments, independently of the MAVS signaling pathway. We observed that *SIRT5*-KO cells express innate immunity markers at a higher basal level and mount a stronger antiviral response, which might explain the decrease in viral levels. Taken together, our study uncovered a novel and unexpected role for SIRT5 during SARS-CoV-2 infection.

The interaction between SIRT5 and Nsp14 is intriguing. Mutating the SIRT5 catalytic domain or treating cells with a SIRT5 inhibitor blocked the interaction (Figure 4.2B, C), and the strength of the interaction appeared to be modulated by cellular NAD levels (Figure 4.2D). NAD is necessary for SIRT5 activity, and these results highlight that SIRT5 catalytic activity or at the very least a functional catalytic domain is necessary to interact with Nsp14. SIRT5 binds to some of its targets in co-purification experiments, such as with MAVS, SHMT2, or PKM2<sup>30–32</sup>. However, in these examples, SIRT5 was also desuccinylating the target proteins. Here we found no lysine

modifications on Nsp14, either by mass spectrometry or immunoblotting. Our experiments might not have been sensitive enough to detect it, but our mass spectrometry data had very high purity, covered 94% of Nsp14 lysine residues, and our pipeline routinely detects such modifications. Besides, SIRT5 is the only known desuccinylase, demalonylase, and deglutarylase, and these experiments were performed in *SIRT5*-KD cells, which would have enriched the presence of these lysine modifications if they were present. The unusual nature of the interaction might explain why we were unable to reconstitute the complex *in vitro* with proteins purified in *E. coli*, and why our enzymatic assays failed to uncover a clear molecular function. Interestingly, an interaction of a similar nature has been described between SIRT1 and the HIV viral protein Tat<sup>53,54</sup>. Tat interacted with the SIRT1 catalytic domain and mutation of conserved residues disrupted the interaction. In this case however, Tat was deacetylated by SIRT1 and blocked SIRT1 activity. Here, we could not determine if SIRT5 activity was altered by Nsp14, and global succinylation and malonylation levels appeared unaffected as well (Figure 4.2E). Further studies will be necessary to understand the nature of the interaction and its function. They could reveal a novel interaction mechanism, in which an enzyme binds to a partner through its catalytic domain, which has rarely been observed.

The role of SIRT5 and other sirtuins in disease is unclear. SIRT5, by modulating key metabolic enzymes, could be involved in cancer<sup>31,32,38-41</sup>. *SIRT5*-KO mice display no obvious phenotype and mount strong innate immune responses against several bacterial infections<sup>55</sup>. The role of SIRT5 and other sirtuins during viral infection is understudied and likely depends on the pathogen. Knocking out SIRT5 enhances the

replication of several DNA viruses, such as herpes simplex 1, human cytomegalovirus and adenovirus type 5, and the same study reported a potential increase in influenza replication, albeit non-significantly <sup>56</sup>. By contrast, here we showed that inhibition or deletion of SIRT5 led to a decrease in viral levels with two distinct coronaviruses, SARS-CoV-2 and HCoV-OC43, indicating that SIRT5 is a proviral factor in this context (Figure 4.4, 4.5). A recent study showed that replication of vesicular stomatitis virus (VSV) and Sendai virus (SeV), two negative-strand RNA viruses, was also diminished in absence of SIRT5 <sup>30</sup>. Whether SIRT5 broadly acts as a restriction factor against DNA viruses and as a proviral factor against RNA viruses will be an interesting hypothesis to investigate in the future.

The decrease of SARS-CoV-2 levels in *SIRT5*-KO cells correlated with elevated basal levels of numerous viral restriction factors, even in mock-infected cells (Figure 4.7). This upregulation was modest but highly significant and may account for why SARS-CoV-2 propagated slower in *SIRT5*-KO cells. Several hypotheses could explain this elevation of innate defenses. SIRT5 has been directly implicated in the RIG-I/MAVS pathway, a critical component of the innate sensing of RNA virus (Figure S4.3A) <sup>30</sup>. Recognition of cytosolic RNA molecules by RIG-I-like receptors, including RIG-I and MDA5, causes recruitment of MAVS, which forms large aggregates on the surface of mitochondria, ultimately leading to type I IFN production <sup>57</sup>. MAVS is succinylated upon viral challenge with VSV and SeV, and desuccinylation of MAVS by SIRT5 diminishes MAVS aggregation, resulting in lower interferon activation. By preventing MAVS aggregation, SIRT5 therefore enhances viral replication, at least with VSV and SeV <sup>30</sup>. However, by infecting *MAVS*-KD cells in presence of SIRT5 inhibitor, here we showed

that SIRT5 likely acts independently of MAVS during SARS-CoV-2 infection (Figure 4.8B). Besides, SARS-CoV-2 efficiently counteracts MAVS activation of innate defense. The coronavirus proteins M, Orf9b and Orf3b directly antagonize MAVS aggregation or downstream signaling<sup>58–60</sup>, and MAVS knockout was reported to have no effect on SARS-CoV-2 replication<sup>43</sup>. Our results indicated otherwise, but altogether this suggests that the desuccinylation of MAVS by SIRT5 is not the main mechanism for explaining the decrease of viral levels in *SIRT5*-KO cells. Other mechanisms could be involved. For example, SIRT5 is involved in the detoxification of reactive oxygen species (ROS) and attenuates cellular ROS levels<sup>27</sup>. Elevated ROS levels activate innate immune responses, and the absence of SIRT5 could cause the activation of innate immune responses through this pathway<sup>61</sup>. Furthermore, SIRT5 regulates proteins involved in glycolysis, the TCA cycle, and fatty acid oxidation. These pathways were impaired without SIRT5, as well as mTOR signaling (Figure 4.6E). mTOR and the cellular sensing of energy and nutrient levels can directly influence immune activity<sup>62</sup>, highlighting another pathway that could lead to immune activation in absence of SIRT5.

The potential link between our two key findings, namely the Nsp14/SIRT5 interaction and the proviral role of SIRT5, will be the subject of further investigation. Several hypotheses can be considered (Figure 4.8D). First, Nsp14 might work by enhancing SIRT5 activity, which would favor viral replication by dampening innate immune responses. In this model, increased deacylation of cellular targets of SIRT5 could result in a weaker immune response and favor viral replication. Second, Nsp14 could redirect SIRT5 toward novel targets, for example other viral proteins. Nsp14 is part of

the viral replication-transcription complex, and SIRT5 could be involved in the deacylation of other members of the complex such as Nsp7, Nsp8, Nsp12 or Nsp13. Third, we observed that SIRT5 and Nsp10 were part of separate complexes, and that Nsp14 MTase activity increased slightly in presence of SIRT5 (Figure 4.3G). SIRT5 and Nsp10 could be separately involved in the two enzymatic activities of Nsp14, with the Nsp14/SIRT5 complex primarily responsible for viral mRNA Cap methylation. Absence of SIRT5 would result in a defect in cap methylation, more efficient immune recognition of viral RNA, and stronger immune response, as we observed.

To summarize, further studies will be necessary to elucidate how SIRT5 enhances SARS-CoV-2 replication, and how the interaction with Nsp14 plays in this context. Potent inhibitors of SIRT5 are in development, and SIRT5 is a potential target against cancer <sup>34,40,63</sup>. Our manuscript highlights that SIRT5 is a potential pharmaceutical target that could help against viral infections as well, and SARS-CoV-2 in particular. Currently, very few antiviral drugs are approved. Inhibiting SIRT5 will probably never represent a first line of defense, but it could be used in combination with drugs that directly target viral enzymes, leading to novel therapeutic regimens against COVID-19.



## **MATERIAL AND METHODS**

### **Mammalian cell lines and culture conditions**

All cell lines were maintained at 37 °C in a 5% CO<sub>2</sub> humidified incubator. Cells were frequently tested for mycoplasma contamination and consistently tested negative.

HEK293T cells were obtained from ATCC (Cat. CRL-11268) and maintained in high glucose Dulbecco's minimal Eagle's medium (DMEM) with 10% fetal bovine serum (FBS) (Sigma-Aldrich, USA) and 100 µm/L penicillin-streptomycin (Corning, USA).

Calu3 cells were obtained from ATCC (Cat. HTB-55) and cultured in AdvancedMEM (Gibco, USA), supplemented with 2.5% FBS (GeminiBio, USA), 1% GlutaMax, and 100 µm/L penicillin-streptomycin. Wild-type A549 cells were purchased from ATCC (Cat. CCL-185). A549 cells stably expressing ACE2 (A549-ACE2) were a gift from O. Schwartz (Pasteur Institute, Paris). A549-ACE2 cells were cultured in DMEM, supplemented with 10% FBS (GeminiBio, USA) and blasticidin (20 µg/ml) (Sigma-Aldrich, USA). Short-terminal repeat (STR) analysis by the Berkeley Cell Culture Facility on 17 July 2020 authenticated these as A549 cells with 100% probability. Vero-E6 cells were obtained from ATCC (Cat. CRL-1586) and cultured in DMEM (Corning, USA), supplemented with 10% FBS (GeminiBio, USA), 1% glutamine (Corning), and 100 µm/L penicillin-streptomycin (Corning). HCT-8 cells (ATCC Cat. CCL-244) were cultured in DMEM with 10% FBS and penicillin-streptomycin. Small-molecule inhibitors used in the study are listed in Table S4.6.

### **Plasmids**

Plasmids expressing GFP and Nsp14 proteins (from SARS-CoV-2, SARS-CoV and HCoV-OC43) with a C-terminus strep tag were a gift from Nevan Krogan<sup>1,2</sup>, and are

also available on Addgene (pLVX-EF1alpha-SARS-CoV-2-nsp14-2xStrep-IRES-Puro, Addgene #141380). Nsp10-Flag plasmid was a gift from the Ott lab. Doxycycline-inducible plasmids were also a gift from the Krogan lab. Mammalian expression plasmids for SIRT5 and SIRT5-H158Y with a myc-his tag in a pCDNA 3.1 vector were available in the Verdin lab <sup>26</sup>. Y102F, R105M, Q140A and I142A mutants were generated by Q5 site-directed mutagenesis (NEB, USA).

### **Generation of CRISPR cell lines**

Stable cell lines transduced with lentiviral vectors were generated as follow: lentiviruses expressing the constructs of interest were produced in HEK293T cells by standard protocols <sup>64</sup>. Cells were plated and transduced 24h later at low MOI when 50-80% confluent. Puromycin, hygromycin or other selection antibiotics were added 48h later and cells passaged at least three time in presence of antibiotics before being used for experiments.

The *SIRT5* knockdown (*SIRT5*-KD) cell line was generated using CRISPR interference in HEK293T cells. First, we generated a stable cell line expressing dCas9-KRAB-MeCP2. Early passage HEK293T cells were transfected with 1.5 µg of dCas9-KRAB-MeCP2 repressor plasmid (Addgene #110824) and 0.5 µg of Piggyback Transposase (gift from Maxim Greenberg), using PEI 25K transfection reagent (Polysciences Inc, Cat. 23966-1), according to the manufacturer's instructions. Cells stably expressing dCas9-KRAB-MeCP2 were selected with Blasticidin (Invivogen, USA) for 10 days before generating *SIRT5*-KD cells. Second, sequences for sgRNA against human *SIRT5* (5'- GGCGCTCCGGACCTGAGCCA-3') or non-targeting

sgRNA (5'-GCTGCATGGGGCGCGAATCA-3') were obtained from Horlbeck et al.<sup>65</sup> and cloned into Addgene #84832 by annealing and ligation using T4 ligase. Plasmids were validated by Sanger sequencing (Elim Biopharmaceuticals). HEK293T cells expressing dCas9-KRAB-MeCP2 were transduced with lentiviruses expressing the gRNAs in medium containing 1 µg/ml polybrene and 30% lentivirus-containing supernatant (v/v). Cells were then selected with Blasticidin at 5 µg/mL and Puromycin (1 µg/mL, Invivogen, USA) to select for cells stably expressing both dCas9 and the sgRNAs. Stable knockdowns were validated by western blot.

The *SIRT5* knockout (*SIRT5*-KO) cell line was generated using CRISPR-Cas9 editing in A549-ACE2 cells. sgRNAs were commercially designed by Synthego (Redwood, California, USA) and are designed to work cooperatively to generate small-fragment deletions in early exons causing knockout (Table S4.1 and S4.2). We combined 10 pmol of *Streptococcus pyogenes* NLS-Sp.Cas9-NLS (SpCas9) nuclease (Aldevron, USA, Cat. 9212) with 30 pmol of total synthetic sgRNA (10 pmol each sgRNA) to form ribonucleoproteins (RNPs) in 20 µL of total volume with SE Buffer for A549-ACE2 cells. The RNP assembly reaction was mixed by pipetting up and down and incubated at room temperature for 10 minutes. Cells were resuspended in transfection buffer, according to cell type, added to the preformed RNP solution, and gently mixed. Nucleofections were performed on a Lonza nucleofector system (Lonza, Switzerland, Cat. AAU-1001), using program CM-120 for A549-ACE2 cells. Cells were grown for several passages and genotyped by PCR and Sanger sequencing to confirm efficient editing. Absence of *SIRT5* was confirmed by western blot.

A549 cells stably co-expressing ACE2 and TMPRSS2 (A549-A/T) were generated through sequential transduction of A549 cells with TMPRSS2-encoding (generated using Addgene plasmid #170390, a gift from Nir Hacohen) and ACE2-encoding (generated using Addgene plasmid #154981, a gift from Sonja Best) lentiviruses and selection with hygromycin (250  $\mu\text{g}/\text{mL}$ ) and blasticidin (20  $\mu\text{g}/\text{mL}$ ) for 10 days, respectively. ACE2 and TMPRSS2 expression was verified by western blot. CRISPR/Cas9-mediated deletion of MAVS was accomplished using lentiviral transduction. A gRNA specific to the third exon of the *MAVS* gene was designed using Benchling.com and cloned into the lentiCRISPR v2 plasmid (Addgene #52961, gRNA sequence: 5'-GCTGGTAGCTCTGGTAGACAG-3'). A549 A/T were transduced with lentiviruses packaged with control (annotated WT) or MAVS-targeting gRNAs in the presence of polybrene (Sigma, TR-1003-G). Cells were selected with Puromycin for seven days and MAVS reduction was validated by western blot.

### **Transfection, Strep affinity purification, and Flag immunoprecipitation in HEK-293T cells**

HEK-293T cells were plated in six-well plates or 10-cm dishes. After 24 hours, cells were transfected using polyethylenimine (PEI). Nsp14 is cytotoxic, and we used 0.5  $\mu\text{g}$  of Nsp14-strep plasmid for a six-well plate and 4  $\mu\text{g}$  for a 10-cm dish. Other co-transfecting plasmids, such as pcDNA-SIRT5, were used at the same concentration except when specifically mentioned. The total amount of plasmid was normalized using empty vectors when necessary. Plasmids were complexed with PEI in Opti-MEM medium (Thermofisher) at a 1:3 ratio, and the mixture was deposited onto cells dropwise. After 48 hours, cells were washed once with PBS, scraped off the plate by

thorough pipetting, pelleted by centrifugation at 200g and 4 °C for 3 minutes, and frozen at –80 °C.

Affinity purification followed the methods of Gordon et al. 2020 <sup>1</sup>. Frozen cell pellets were thawed on ice and resuspended in 0.5 ml of lysis buffer (IP buffer: 50 mM Tris-HCl, pH 7.4, 150 mM NaCl, and 1 mM EDTA), supplemented with 0.5% Nonidet P40 substitute (NP40; Fluka Analytical) and cOmplete mini EDTA-free protease and PhosSTOP phosphatase inhibitor cocktails (Roche)). Samples were frozen on dry ice for 10–20 minutes and partially thawed at 37 °C before incubation on a tube rotator for 30 minutes at 4 °C, and centrifugation (13,000g, 4 °C, 15 minutes) to pellet debris. 30 µL of “input” was saved and frozen at –80 °C. 20 µL of MagStrep ‘type3’ beads (IBA Lifesciences) were equilibrated twice with 1 mL of wash buffer (IP buffer supplemented with 0.05% NP40) and incubated with 0.5 ml of lysate for two hours at 4 °C on a tube rotator. Tubes were placed on a magnetic rack, and beads were washed three times with 1 ml of wash buffer, and samples were shortly vortexed between washes. Bound proteins were eluted for 30 minutes using 30 µL of BXT elution buffer (IBA Lifesciences) with constant shaking at room temperature. Tubes were placed back on the magnetic rack, and the eluate was recovered and frozen at –80 °C.

Flag-immunoprecipitation was performed the same way using Anti-FLAG M2 Magnetic Beads (Sigma-Aldrich M8823) and elution was done using 3x-Flag peptide (Sigma-Aldrich F4799) at a concentration of 3 µg/50µL in IP buffer. When performing side by side Strep-affinity purification and Flag-immunoprecipitation, the same frozen cell sample was divided in two after lysis.

## **Western blot**

Western blot was performed using standard protocols. Briefly, protein lysate was mixed with 4x Laemmli sample buffer containing DTT and boiled for 5 minutes at 95 °C. Proteins were separated on a precast 4–20% gradient gel (Biorad, USA) and transferred on a nitrocellulose membrane using a semi-dry Trans-Blot Turbo Transfer System and Trans-Blot Turbo Transfer Buffer (Biorad, USA). Membranes were blocked for 1 hour with 5% milk in TBST (Tris-buffered saline and Tween 20) buffer, rinsed, and incubated overnight at 4 °C with primary antibodies in 2% BSA in TBST. Membranes were washed three times with TBST and incubated for 2 hours at room temperature with horseradish peroxidase–linked secondary antibody. The chemiluminescent signal was revealed with SuperSignal West Pico PLUS Substrate (ThermoFisher, USA) and imaged with an Azure 600 Imaging system (Azure Biosystem, USA). Antibodies are listed in Table S4.5.

## **Cellular Thermal Shift Assay (CETSA)**

CETSA was performed as described <sup>66</sup>. Shortly, HEK-293T cells in six wells were transfected with plasmids expressing Nsp14-strep and/or SIRT5. After 48 hours, cells were harvested, washed with PBS, and resuspended in PBS supplemented with EDTA-free complete protease inhibitor cocktail (Roche). Intact cells were divided into 100- $\mu$ l aliquots and heated individually at different temperatures for 3 minutes in a PCR machine (Biorad), followed by cooling for 2 minutes at room temperature. Cell suspensions were freeze-thawed three times with liquid nitrogen, and the soluble fraction was separated from the cell debris by centrifugation at 20,000 $\times$ g for

20 minutes at 4 °C. Supernatants containing soluble proteins were transferred to new microcentrifuge tubes and analyzed by western blot.

### **Immunofluorescence**

A549 cells plated in an eight-well chamber slide (Nunc Lab-Tek II, Thermo Fisher) were transfected with 500 ng of nsp14-strep plasmid encoding nsp14-strep using Lipofectamine 3000 (Thermo Fisher). The next day, cells were fixed in PBS-buffered 4 % formaldehyde at room temperature. After 15 minutes, cells were briefly rinsed with PBS once and incubated in permeabilization buffer (0.1 % Triton X-100 in PBS). After 15 additional minutes, cells were incubated in blocking buffer (permeabilization buffer supplemented with 1 % BSA), and further incubated in blocking buffer containing anti-Strep mouse antibody (1:1000 dilution), and anti-SIRT5 rabbit antibody (1:1000 dilution). The next day, the cells were washed with PBS three times and incubated in the blocking buffer containing anti-mouse IgG donkey antibody conjugated with Alexa 488 (1:500 dilution, Thermo Fisher), anti-rabbit IgG donkey antibody conjugated with Alexa 555 (1:500 dilution, Thermo Fisher), and for counter-staining, DAPI (1 µg/ml, Sigma Aldrich) and Phalloidin conjugated with Alexa 647 (1: 1000 dilution, Abcam). After 30 minutes, the cells were washed with PBS three times, and mounted in prolong gold anti-fade (Thermo Fisher), followed by curing overnight. The cells were visualized using a confocal fluorescence microscope (LSM 700, Carl Zeiss) at 63 X magnification, imaged, and analyzed using ZEN imaging software (blue edition, Ver 3.4, Carl Zeiss). Antibodies used are given in Table S4.5.

## **Protein purification and enzymatic assays**

Nsp10 and Nsp14 proteins from the Wuhan strain of SARS-CoV-2 (NC\_045512.2) were codon-optimized, ordered as Gblocks (IDT), and cloned into a pVFT1S expression vector using a HiFi DNA Assembly kit (NEB). Both nsp10 and nsp14 contained an N-terminal 6x-His tag, followed by a TEV cleavage site. *E. coli* BL21\*(DE3) cells (Invitrogen, USA) were transformed with the nsp10 and nsp14 expression vectors and grown in LB medium containing kanamycin. Cells were induced at an OD<sub>600</sub> of ~0.8 with 0.5 mM IPTG for 16 hours at 16°C. Nsp10 pellets were stored at -20°C, and nsp14 pellets were flash-frozen with liquid nitrogen and stored at -80°C until use. For nsp10/14 copurification, nsp10 pellets from 1 L of cells and nsp14 pellets from 6 L of cells were resuspended in lysis buffer (50 mM HEPES, pH 7.5, 300 mM NaCl, 5 mM MgSO<sub>4</sub>, 30 mM imidazole, and 1% NP-40) and combined. For nsp14 purification, pellets were resuspended in lysis buffer. The pellets were lysed using sonication and clarified using centrifugation at 14,500 rpm for 40 minutes at 4°C. The supernatant was loaded onto a HisTrap HP column (GE Healthcare, USA). Proteins were purified by fast protein liquid chromatography and washed using two column volumes of Ni Buffer A (50 mM HEPES, pH 7.5, 300 mM NaCl, 5 mM MgSO<sub>4</sub>, and 30 mM imidazole). For nsp10/14 copurification only, an additional wash was done over five column volumes using a buffer of 50 mM HEPES, pH 7.5, 300 mM NaCl, 5 mM MgSO<sub>4</sub>, and 60 mM imidazole. Proteins were eluted using 50 mM HEPES, pH 7.5, 300 mM NaCl, 5 mM MgSO<sub>4</sub>, and 300 mM imidazole. The elution was then concentrated and purified further using a Superdex 200 column (GE) and a buffer of 10 mM HEPES, pH 7.5, 150 mM NaCl, and 10% glycerol. The purified protein was then concentrated, flash-frozen using liquid nitrogen, and stored at -80°C.



SIRT5 purified protein was obtained commercially (BPS Bioscience, USA, Cat. 50016). In vitro desuccinylation assays were performed using Fluorogenic SIRT5 Assay Kit (BPS Bioscience, USA, Cat. 50085), following the manufacturer's instructions. Methyltransferase assays were performed using MTase-Gl Methyltransferase Assay (Promega, USA), following the manufacturer's instructions. Nsp14 and SIRT5 recombinant proteins were first incubated together in the reaction buffer, with a ratio of 1:1 corresponding to 100 nM of each protein. Desuccinylation assays were performed in a reaction buffer (25 mM Tris/HCl, pH 8.0, 137 mM NaCl, 2.7 mM KCl, 1 mM MgCl<sub>2</sub>, and 0.1 mg/ml BSA) with 0.5 mM NAD<sup>+</sup> for 30 minutes at 37°C. Methyltransferase assays were performed in reaction buffer (50 mM Hepes, pH 7.0, 6 mM KCl, 2 mM DTT, 1 mM MgCl<sub>2</sub>, and 0.1 mg/ml BSA) in presence of 0.1 mM NAD<sup>+</sup> and 10 μM SAM.

### **Sample Preparation for Proteomic Analysis**

HEK-293T *SIRT5-KD* cells were transfected with plasmids expressing Nsp14-strep in the presence or absence of SIRT5 with 3 biological replicates for each condition. Nsp14-strep and bound proteins were purified by affinity purification as described above, and eluted in 35 μL of elution buffer (100 mM Tris pH 7.4; 150 mM NaCl; 1 mM EDTA; 50 mM biotin). Each sample was subjected to a lysis buffer containing 5% SDS and 50 mM triethylammonium bicarbonate (TEAB) for proteomics sample preparation. The samples enriched for NSP14 were reduced with 20 mM dithiothreitol (DTT) in 50 mM TEAB buffer at 50 °C for 10 minutes, left to cool at room temperature for 10 minutes, and alkylated with 40 mM iodoacetamide (IAA) in 50 mM TEAB buffer in the dark at room temperature for 30 minutes. Samples were acidified with a final

concentration of 1.2% phosphoric acid. Subsequently, 90% methanol in 100 mM TEAB was added. The entire sample volume was spun through the micro S-Trap columns (Protifi) to bind the proteins to the S-Trap column. The S-Trap columns were washed again with 90% methanol in 100 mM TEAB. S-Trap columns were placed in a clean elution tube and incubated with trypsin digestion buffer (50 mM TEAB, pH ~8) at a 1:25 ratio (protease:protein, wt:wt) for 1 hour at 47 °C. The same volume of trypsin digestion buffer was added again for an overnight incubation at 37 °C. Peptides were eluted from the S-Trap column first with 50 mM TEAB spun through at 1,000 x g, then with 50 mM TEAB and 0.5% formic acid at 1,000 x g, and finally with 50% acetonitrile in 0.5% formic acid at 4,000 x g. These pooled elutions were dried in a vacuum concentrator and then re-suspended in 0.2% formic acid. The re-suspended peptide samples were desalted with stage tips generated in-house using C18 disks. They were subsequently dried again in a vacuum concentrator, and re-suspended in aqueous 0.2% formic acid containing “Hyper Reaction Monitoring” indexed retention time peptide standards (iRT, Biognosys).

### **Mass Spectrometry Analysis**

Briefly, samples were analyzed by reverse-phase HPLC-ESI-MS/MS using an Eksigent Ultra Plus nano-LC 2D HPLC system (Dublin, CA) with a cHiPLC system (Eksigent) which was directly connected to a quadrupole time-of-flight (QqTOF) TripleTOF 6600 mass spectrometer (SCIEX, Concord, CAN). After injection, peptide mixtures were loaded onto a C18 pre-column chip (200  $\mu\text{m}$  x 0.4 mm ChromXP C18-CL chip, 3  $\mu\text{m}$ , 120 Å, SCIEX) and washed at 2  $\mu\text{l}/\text{min}$  for 10 min with the loading solvent ( $\text{H}_2\text{O}/0.1\%$  formic acid) for desalting. Subsequently, peptides were transferred

to the 75  $\mu\text{m}$  x 15 cm ChromXP C18-CL chip, 3  $\mu\text{m}$ , 120 Å, (SCIEX), and eluted at a flow rate of 300 nL/min with a 3 h gradient using aqueous and acetonitrile solvent buffers.

Data-dependent acquisitions: For peptide and protein identifications the mass spectrometer was operated in data-dependent acquisition (DDA) mode, where the 30 most abundant precursor ions from the survey MS1 scan (250 msec) were isolated at 1 m/z resolution for collision-induced dissociation tandem mass spectrometry (CID-MS/MS, 100 msec per MS/MS, 'high sensitivity' product ion scan mode) using the Analyst 1.7 (build 96) software with a total cycle time of 3.3 sec as previously described<sup>67</sup>.

Data Processing: Mass spectrometric data-dependent acquisitions (DDA) were analyzed using the database search engine ProteinPilot (SCIEX 5.0 revision 4769) allowing for biological modifications and with 'emphasis' on succinylation. A fasta file was generated appending the viral NSP14 protein sequence to the human proteome fasta file. A confidence score threshold of 99 was set to filter for high quality peptide identifications. Identified protein and peptide results are provided in Supplementary Tables.

### **SARS-CoV-2 virus culture and infections**

SARS-CoV-2 isolate USA-WA1/2020 (BEI NR-52281) was used for all infection studies. All live virus experiments were performed in a Biosafety Level 3 laboratory. SARS-CoV-2 stocks were propagated in Vero-E6 cells, and their sequences were verified by next-generation sequencing. Viral stock titer was measured by plaque assays.

For infection experiments, A549-ACE2 or Calu3 cells were seeded into 12- or 24-well plates and rested for at least 24 hours prior to infection. At the time of infection, medium containing compound and/or viral inoculum (MOI 0.01 or 0.1) was added to the cells. After 3 days, the supernatant was collected and mixed with two volumes of RNA STAT-60 extraction buffer (AMSBio, UK). Cells were similarly harvested by adding RNA STAT-60 extraction buffer. Samples were stored at -80°C. Infections of HCT-8 cells with HCoV-OC43 were performed similarly.

### **Plaque assays**

Viral inoculations were harvested from experiments and serially diluted in DMEM (Corning). At the time of infection, the media on Vero-E6 cells were replaced with viral inoculation for 1 hour. After the 1-hour absorption period, 2.5% Avicel (Dupont, RC-591) was layered on the cells and incubated for 72 hours. Then, Avicel was removed and cells were fixed in 10% formalin for 1 hour, stained with crystal violet for 10 minutes, and washed multiple times with water. Plaques were counted and averaged from two technical replicates.

### **RNA extraction and RT-qPCR**

RNA in cells and supernatants resuspended in RNA STAT-60 buffer was extracted using Direct-zol RNA Miniprep kit (ZymoResearch, USA). For extraction from the supernatant, RNA was eluted in 20 µL of water, and 18 µL was directly used for reverse-transcription. RNA extracted from cells was DNase-treated, eluted in 30 µL, quantified by Nanodrop, and 2 µg of RNA was used reverse-transcription. Reverse-transcription was performed using the High-Capacity cDNA Reverse Transcription Kit

(ThermoFisher), and quantitative PCR was done using a BioRad qPCR machine and Sybr Green (ThermoFisher). RT-qPCRs were normalized using the  $\Delta\Delta C_t$  method with the reference genes *ACTIN* and *GAPDH*. qPCR primers are given in Tables S4.4. Missing data points in RT-qPCR figures represent samples where RNA extraction was of poor quality. No outliers were removed.

### **Statistics and reproducibility**

Experiments were carried out in multiple replicates. For affinity-purification and western blot data, one representative experiment out of several replicates is shown. For statistical analysis of RT-qPCR data, we used ordinary one-way ANOVA, followed by Holm–Šidák multiple comparisons test, with a single pooled variance. For RT-qPCR in figure 7, we used unpaired two-tailed t-tests. Plaque assay data do not satisfy the normality condition required for parametric tests, but are closer to a lognormal distribution <sup>68</sup>. As a consequence, statistical tests on plaque assay data were performed on log-transformed data. Analyses were run using GraphPad Prism version 9.1.2 for macOS (GraphPad Software, USA, [www.graphpad.com](http://www.graphpad.com)). Exact p-values and summaries are reported in the text and figures, respectively.

### **RNA-sequencing preparation and analysis**

Library preparation and sequencing were performed by the DNA Technologies and Expression Analysis Core at the UC Davis Genome Center (Davis, CA, USA), supported by NIH Shared Instrumentation Grant 1S10OD010786-01. Strand-specific and barcode-indexed RNA-seq libraries were generated from 500 ng of total RNA each, after poly-A enrichment, using the Kapa mRNA-seq Hyper kit (Kapa Biosystems-

Roche, Basel, Switzerland), following the instructions of the manufacturer. The fragment size distribution of the libraries was verified via micro-capillary gel electrophoresis on a LabChip GX system (PerkinElmer, Waltham, MA). The libraries were quantified by fluorometry on a Qubit instrument (Life Technologies, Carlsbad, CA) and pooled in equimolar ratios. The pool was quantified by qPCR with a Kapa Library Quant kit (Kapa Biosystems) and sequenced on an Illumina NovaSeq 6000 (Illumina, San Diego, CA) with paired-end 150-bp reads.

Paired-end sequencing reads were mapped to a composite human/SARS-CoV-2 genome using Subread Aligner v2.0.3 <sup>69</sup>. A genome index was constructed using GRCh38 genome build with Gencode v38 annotation of the transcriptome, and Genbank MT246667.1 for the sequence of SARS-CoV-2, USA/WA-1/2020 isolate. Reads mapping to annotated genes were counted using Subread featurecount v2.0.3 <sup>70</sup>. Downstream analyses were performed with R. Differential gene expression analysis was done with DEseq2, which was also used to generate normalized gene counts <sup>71</sup>. Low-expressed genes with less than three counts in at least three out of 16 samples were excluded from downstream analysis. q-Values were calculated using the q-value R package v2.24.0. For DEseq2 analysis, we used a one-factor design with four groups (WT mock, KO mock, WT infected and KO infected) and then likelihood ratio testing (LRT) to find all genes that were differentially expressed between at least two groups (q-value threshold <0.01), and with a basemean expression >15. Consensus clustering of the 3221 differentially expressed genes was performed with the degPatterns function of R DEGreport package v1.28.0, using default parameters and rlog-transformed counts. This generated eight clusters. Over-

representation of biological gene sets in the gene clusters was investigated using the R clusterProfiler package and enricher function <sup>72</sup>. Gene sets were downloaded from the MSIG data bank via the msigdb R-project package, including “Hallmark,” and “Reactome”. <sup>73</sup>. Gene sets were considered significantly enriched in a cluster if q values were < 0.05. For analysis of restriction factors in figure 6, we first selected genes in clusters 1 to 8 that belonged to the hallmark curated data set “Interferon Alpha response”. We complemented this list with additional genes from clusters 7 and 8 that belonged to the “Interferon Gamma response”, “Inflammatory response” and “TNFa signaling via NfKB” hallmark datasets, and finally added genes that we manually identified as potential restriction factors from literature searches. Average log2 fold-change compared to mock-infected WT was calculated and plotted, as well as the q-value between mock-infected WT and KO. Code developed for this study is available at [https://github.com/mariuswalter/SIRT5\\_paper](https://github.com/mariuswalter/SIRT5_paper). This analysis relied heavily on code made available by the laboratory of Denis Goldfarb ([https://github.com/GoldfarbLab/H522\\_paper\\_figures](https://github.com/GoldfarbLab/H522_paper_figures)), and described in ref <sup>45</sup>.

### **Data and code availability**

The data supporting the findings of this study are available within the paper and its Supplementary files. RNA-seq data have been deposited to the GEO repository ([GSE188382](https://www.ncbi.nlm.nih.gov/geo/query/acc.cgi?acc=GSE188382)). Code developed for RNA-seq analysis is available on Github ([github.com/mariuswalter/SIRT5\\_paper](https://github.com/mariuswalter/SIRT5_paper)). Mass spectrometric raw data have been deposited to the MassIVE repository ([MSV000088589](https://massive.ucsf.edu/MSV000088589)) and are also available at ProteomeXchange ([PXD030530](https://proteomecentral.proteomex.org/submitter/PXD030530)). Plasmids, viruses and other reagents developed in this study are available upon request and subject to standard material transfer

agreements with the Buck Institute. Any other relevant data are available upon reasonable request.



## **ACKNOWLEDGEMENTS**

We thank the QCRG Virology group at UCSF for technical and conceptual help, as well as members of the Verdin and Ott lab, in particular Rebeccah Riley, Rosalba Perrone and Anthony Covarrubias. We thank Michelle Moritz at UCSF for attempting co-purification experiments in *E. coli*. We thank David Gordon for quickly sharing the plasmid library early in the study and Max Greenberg at Paris University for sharing the Transposase plasmid.

This study was funded through institutional support from the Buck Institute for Research on Aging. IPC received support from the NIH (F31 AI164671-01). M.O. gratefully acknowledges support through gifts by Pamela and Edward Taft, and the Roddenberry Foundation. We acknowledge the support of instrumentation from the NCRN shared instrumentation grant 1S10 OD016281 (Buck Institute) for Mass Spectrometry Analysis, and the NIH Shared Instrumentation Grant 1S10OD010786-01 (UC Davis) for RNA-sequencing.

## **Author contributions**

MW and EV designed the study and analyzed the data. MW, IJK, OB, AC performed molecular biology experiments. IPC, AVG, and JMH performed SARS-CoV-2 assays and analyses. VL and JDG provided purified Nsp14 proteins. SS and BS performed mass spectrometry experiments and analysis. MW analyzed RNA-seq data. EV and OT supervised and funded the project. M.W. and E.V. wrote the manuscript with input from all authors.

## **Competing interests**

Authors declare no competing interests.

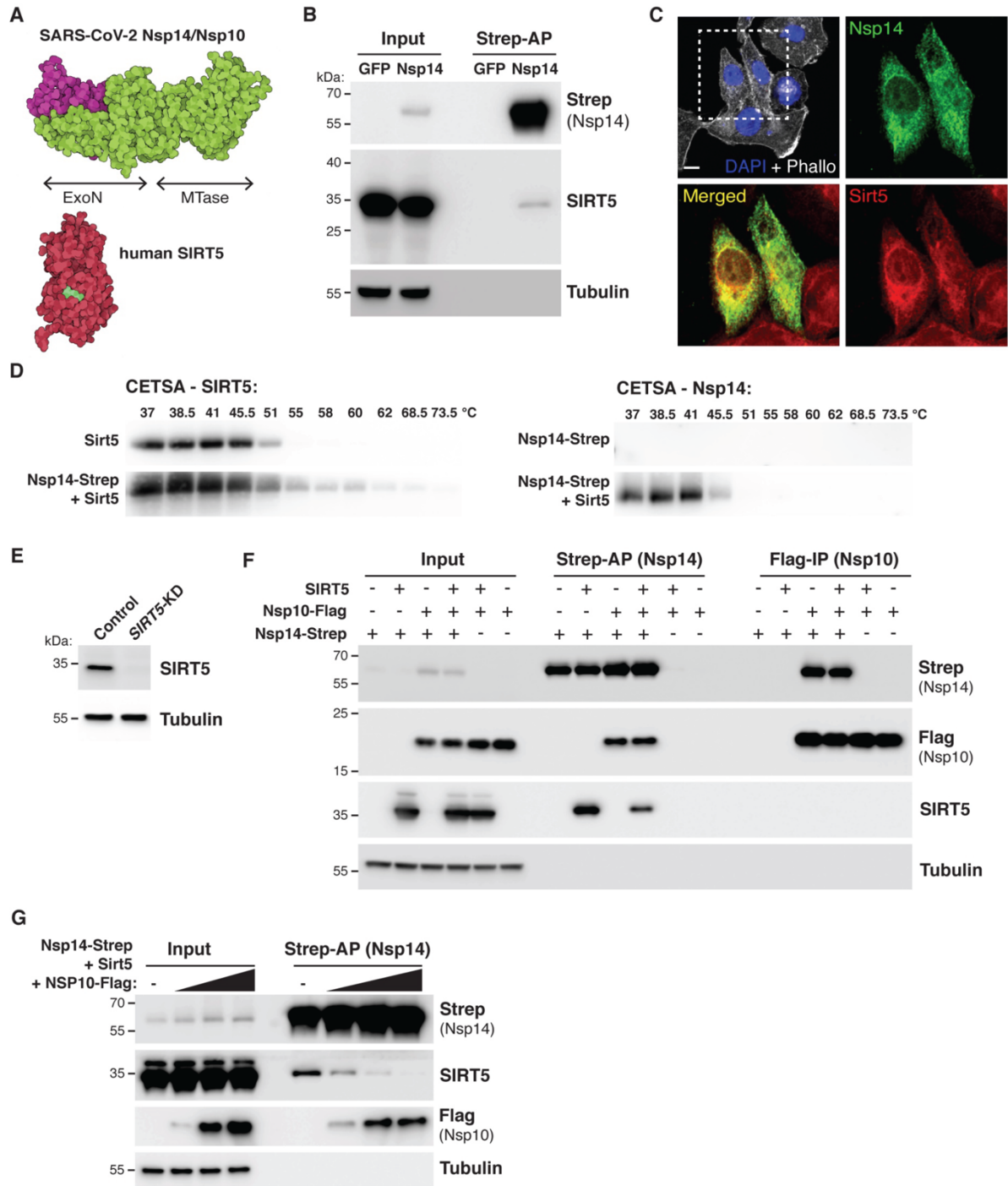


**Figure 4.1. SARS-CoV-2 Nsp14 interacts with human SIRT5.**

- A. Cartoon representation of the protein structure of Nsp14/Nsp10 (PDB 7N0B) and SIRT5 (PDB 3YIR) shows the Nsp14 N-terminal ExoN domain and C-terminal MTase domain.
- B. Affinity-purification of Nsp14-strep and co-purification of endogenous SIRT5 after transfection in HEK293T cells, as shown by western blot.
- C. Immunofluorescence of transfected Nsp14-Strep and endogenous SIRT5 in A549 cells.

- D. CETSA in HEK293T cells transfected with Nsp14-strep and/or SIRT5, showing an increase in the stability of SIRT5 and Nsp14 by western blot.
- E. Western blot showing the absence of SIRT5 in SIRT5-KD HEK293T cells.
- F. Strep-tag affinity-purification or Flag-tag immunoprecipitation, followed by western blot, after transfection with Nsp14-strep, Nsp10-flag and SIRT5 expression constructs. SIRT5 does not interact with Nsp10. 0.5  $\mu\text{g}$  of each construct or of empty control plasmids were transfected in SIRT5-KD HEK293T cells in a six-well plate.
- G. Strep-tag affinity-purification and western blot after transfection of Nsp14-strep, SIRT5 and increasing concentrations of Nsp10-tag indicate competitive binding of SIRT5 and Nsp10. 0.5  $\mu\text{g}$  of Nsp14-strep and SIRT5 plasmid were used in a 6-well plate, with 0, 0.5, 1 or 2  $\mu\text{g}$  of Nsp10-Flag.

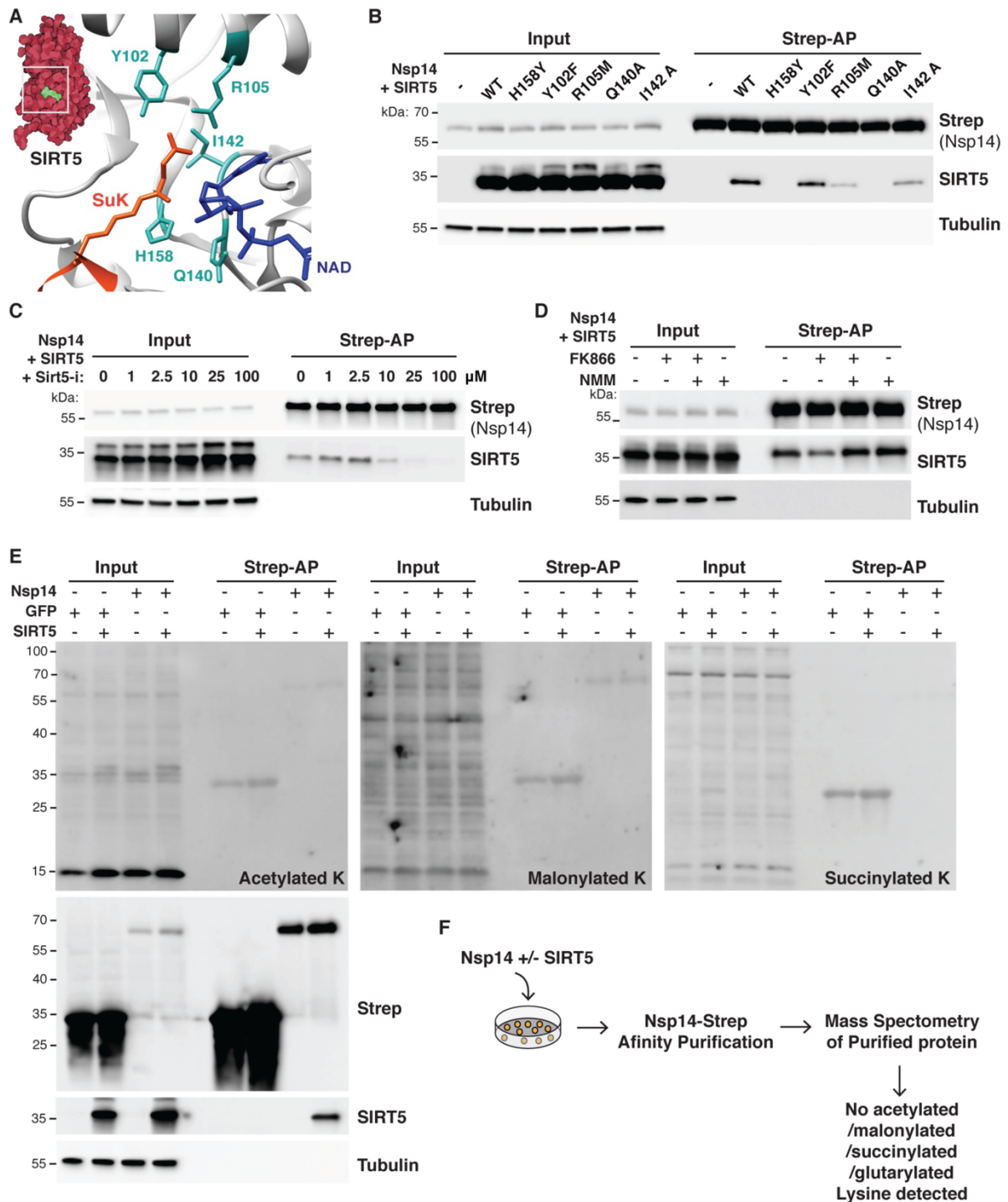


**Figure 4.2. SIRT5 catalytic activity is necessary to interact with Nsp14.**

A. Cartoon representation of the protein structure of SIRT5 catalytic site in complex with cofactor NAD and succinylated lysine substrate (SuK), showing conserved residues mutated in panel B.

B. Strep-tag affinity-purification and western blot after transfection of Sirt5-KD HEK293T cells with Nsp14-strep and SIRT5 catalytic mutants, showing that the interaction with Nsp14 is lost in several mutants.

- C. Strep-tag affinity-purification and western blot after transfection with Nsp14-strep and SIRT5, in SIRT5-KD HEK293T cells incubated with increasing concentrations of SIRT5 inhibitor Sirt5-i. High concentrations of Sirt5-i prevent the interaction.
- D. Strep-tag affinity-purification and western blot after transfection with Nsp14-strep and SIRT5, in SIRT5-KD HEK293T cells incubated with NAMPT FK866 inhibitor (low cellular NAD), FK866 and NMN, or NMN alone (high cellular NAD). SIRT5 binding strength correlated with NAD levels.
- E. Pan-acetylation, malonylation and succinylation in SIRT5-KD HEK293T total or Strep-purified proteins, after transfection with Nsp14-Strep, GFP-strep control and/or SIRT5. No specific lysine modifications could be detected.
- F. Summary of mass spectrometry experiments. Nsp14-strep proteins purified from SIRT5-KD HEK293T, with or without co-transfection with SIRT5, were analyzed by mass spectrometry. No acetylation, malonylation, succinylation or glutarylation modifications could be detected.

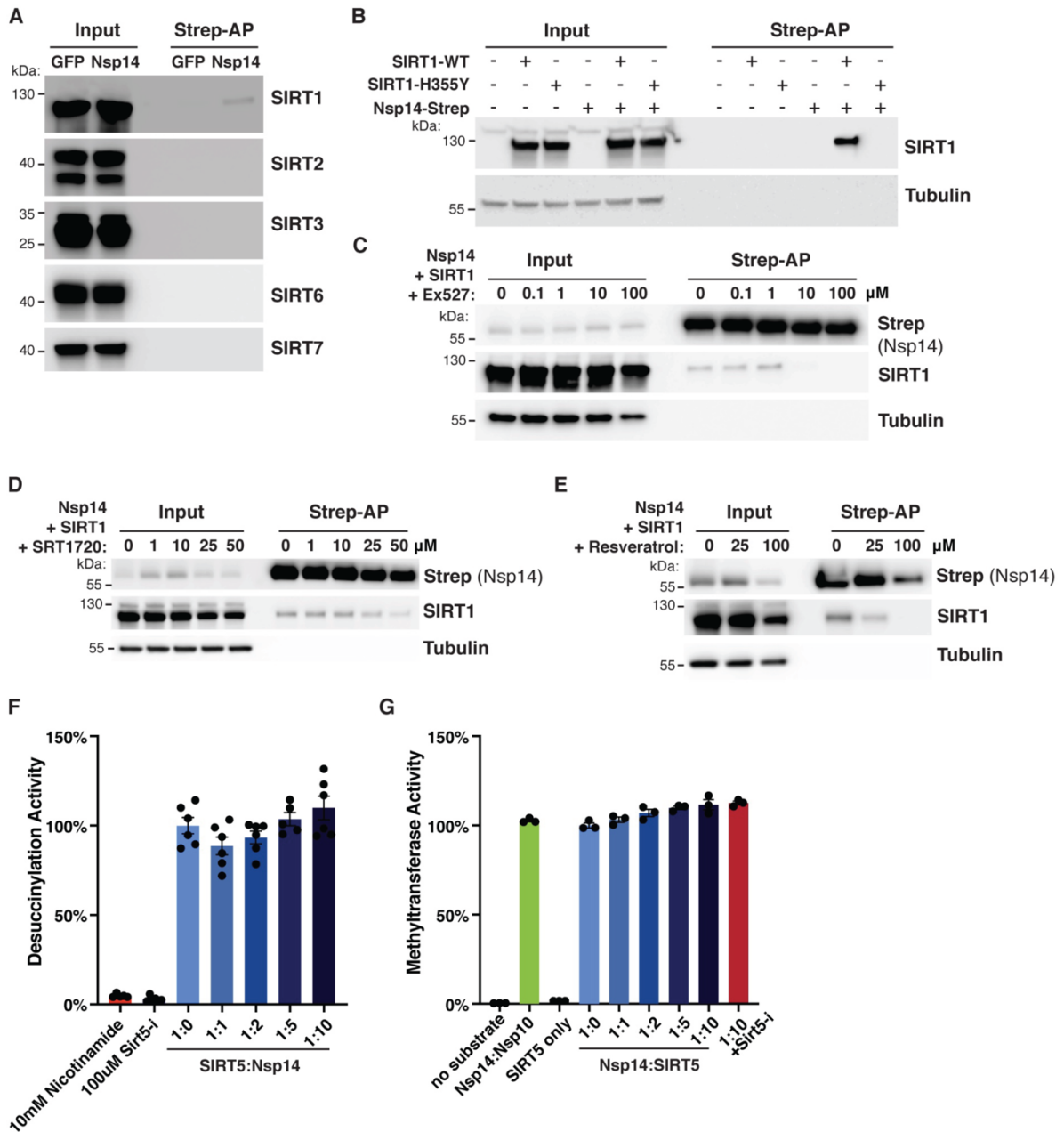


**Figure 4.3. SARS-CoV-2 Nsp14 interacts with human SIRT1.**

- Co-purification of endogenous sirtuins SIRT1, 2, 3, 6 and 7 after transfection of Nsp14-strep in HEK293T cells, as shown by western blot. Loading and purification controls are the same as in Figure 4.1B.
- Strep-tag affinity-purification and western blot after transfection of HEK293T cells with Nsp14-strep and SIRT1 WT and H355Y catalytic mutant, showing that the interaction with Nsp14 is lost in H355Y mutant.
- Strep-tag affinity-purification and western blot after transfection with Nsp14-strep and SIRT1, in HEK293T cells incubated with increasing concentrations of SIRT1 inhibitor Ex-527. High concentrations of Ex-527 prevent the interaction.

- D. Strep-tag affinity-purification and western blot after transfection with Nsp14-strep and SIRT1, in HEK293T cells incubated with increasing concentrations of SIRT1 specific activator SRT1720.
- E. Same as D with non-specific activator resveratrol. Both drugs were cytotoxic at high concentrations and the apparent decrease in SIRT1 binding correlated with a similar decrease in the input lanes.
- F. In vitro desuccinylation activity of purified SIRT5 incubated with increasing concentrations of Nsp14, showing no effect.
- G. In vitro methyltransferase activity of purified Nsp14 incubated with increasing concentrations of SIRT5, showing no specific effect. Unmethylated GpppG cap-analog was used as a substrate.



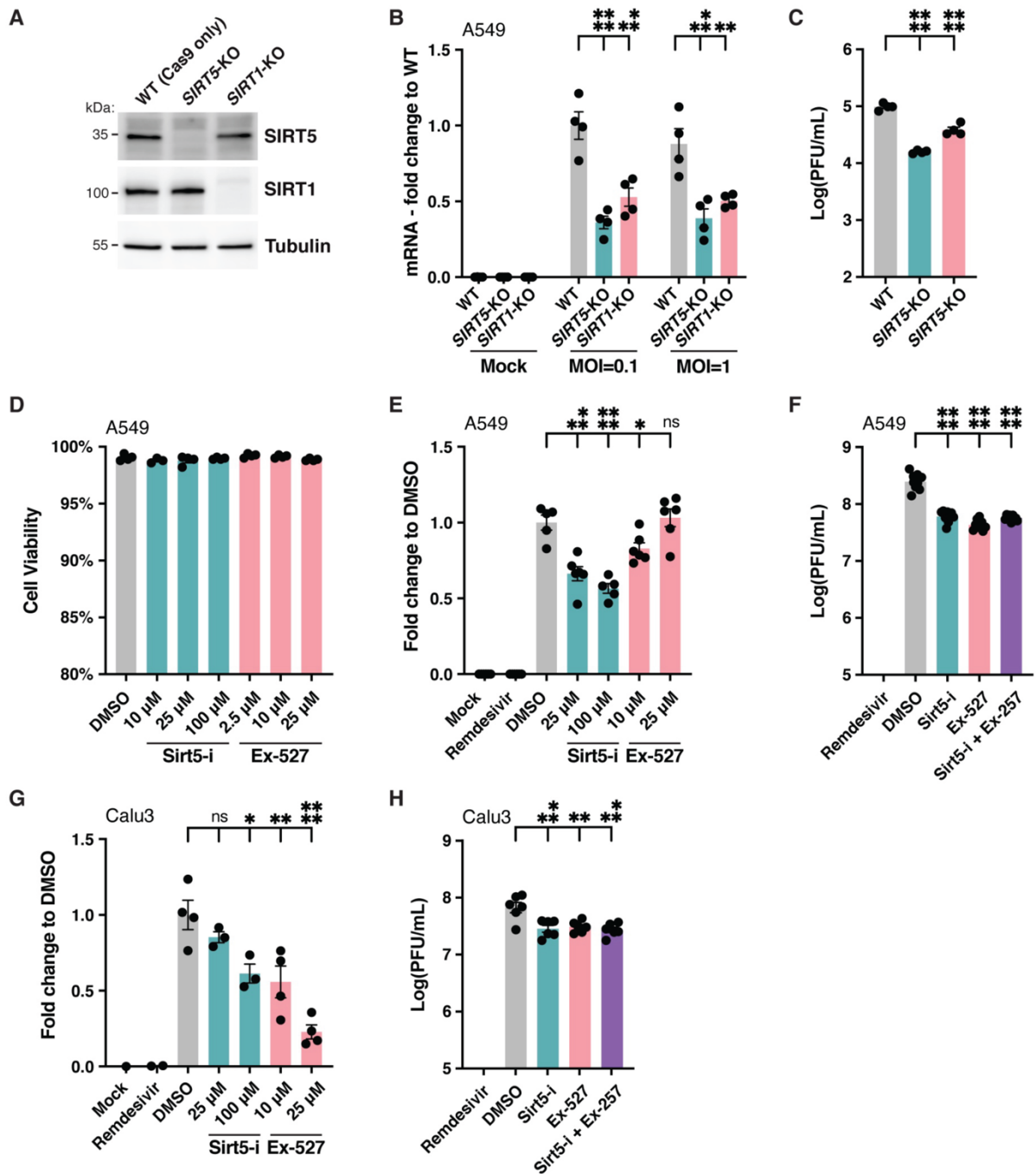


**Figure 4.4. SIRT5 is a proviral factor.**

- Western blot showing the absence of SIRT5 and SIRT1 in SIRT5- and SIRT1-KO A549-ACE2 cells, after CRISPR knockout.
- Decrease in cell-associated viral mRNA levels in SIRT5- and SIRT1-KO cells infected with SARS-Cov-2 for 3 days at MOI=0.1 or MOI=1, as shown by RT-qPCR. Data show fold-changes compared to WT levels at MOI=0.1. n=4.
- Decrease in viral titers in SIRT5- and SIRT1-KO cells infected with SARS-Cov-2 for 3 days at MOI=1, as shown by plaque assay. n=4.
- Absence of cytotoxicity in A549-ACE2 cells treated with Sirt5-i and Ex-527 inhibitor, as measured by flow cytometry. n=4.

- E. Decrease in cell-associated viral mRNA levels in A549-ACE2 cells infected with SARS-Cov-2 for 3 days at MOI=0.1, and treated with SIRT5 and SIRT1 inhibitors Sirt5-i and Ex-527, as shown by RT-qPCR. Data show fold-change compared to DMSO-treated levels. n=6.
- F. Decrease in viral titers in A549-ACE2 cells infected with SARS-Cov-2 for 3 days at MOI=0.1, and treated with SIRT5 and SIRT1 inhibitors Sirt5-i and Ex-527, as shown by plaque assay. n=9.
- G. Same as E. (with n=4) using Calu3 cells.
- H. Same as F. (n=6), using Calu3 cells. (B-H) Data show mean and standard error of the mean (SEM) between biological replicates. RT-qPCR results were internally normalized with GAPDH and ACTIN reference genes. Viral titers after plaque assay are expressed in log-transformed PFU (plaque-forming unit) per mL of supernatant. Asterisks summarize the results of one-way ANOVAs followed by Holm–Šidák multiple comparisons test (on log-transformed data for plaque assays) \*:  $p < 0.05$ , \*\*:  $p < 0.01$ , \*\*\*:  $p < 0.001$ , \*\*\*\*:  $p < 0.0001$ .

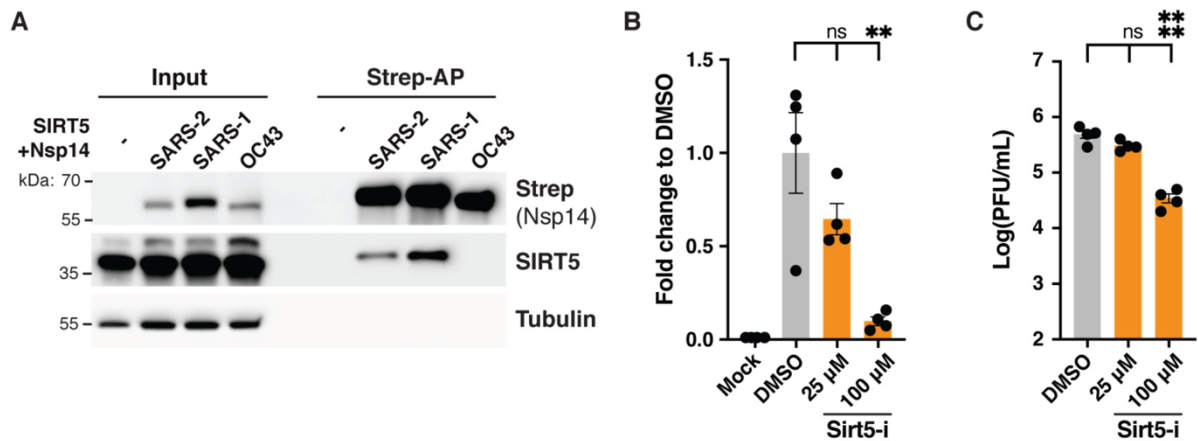


**Figure 4.5. SIRT5 proviral activity is partially independent from the interaction with Nsp14.**

- A. Strep-tag affinity-purification and western blot after transfection of SIRT5-KD HEK293T cells with SIRT5 and Nsp14-strep from different coronaviruses, showing that the interaction with SIRT5 is specific to SARS-like coronaviruses.
- B. Decrease in supernatant-associated viral mRNA levels in HCT-8 cells infected with HCoV-OC43 for 5 days at MOI=0.1, and treated with SIRT5 inhibitor Sirt5-i, as shown by RT-qPCR. Data show fold-change compared to DMSO-treated levels. n=4.
- C. Decrease in viral titers in HCT-8 cells infected with HCoV-OC43 for 5 days at MOI=0.1, and treated with SIRT5 inhibitors Sirt5-i, as shown by plaque assay. n=4.

(B-C) Data show mean and SEM between biological replicates. Asterisks summarize the results of one-way ANOVAs followed by Holm-Šidák multiple comparisons test (on log-transformed data for plaque assays) \*:  $p < 0.05$ , \*\*:  $p < 0.01$ , \*\*\*:  $p < 0.001$ , \*\*\*\*:  $p < 0.0001$ .

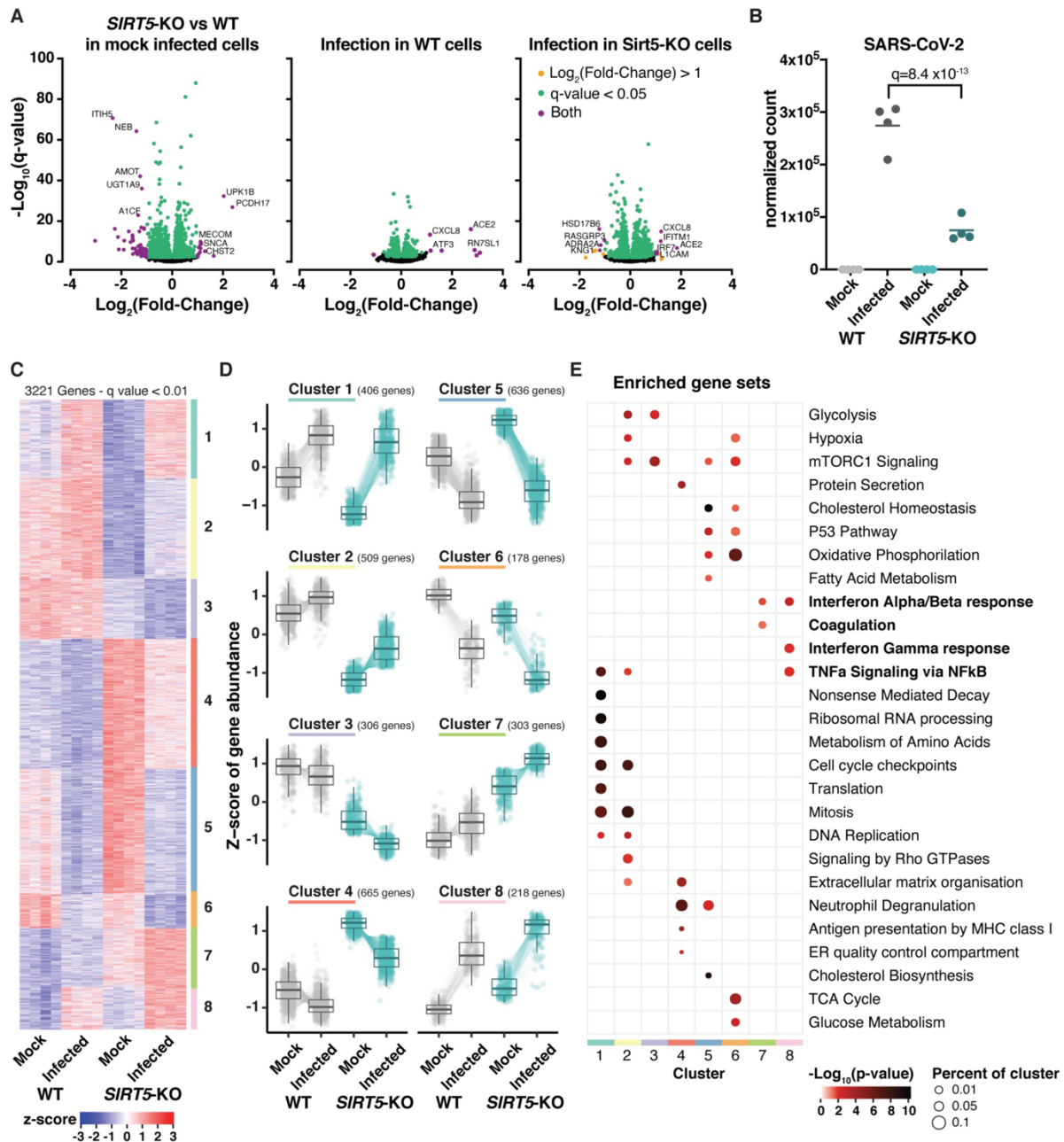


**Figure 4.6. SIRT5-KO cells mount a stronger innate immune response.**

- A. RNA-seq analysis of WT and SIRT5-KO A549-ACE2 cells infected or mock-infected for 3 days with SARS-CoV-2 at MOI=1.  $n=4$ . Volcano plots showing differentially expressed genes between the different conditions. Highlighted genes display a  $q$ -value  $q < 0.05$  (green),  $\text{log}_2$  fold-change  $> 1$  (orange), or both (purple). Left panel: SIRT5-KO vs WT in mock-infected cells. Middle: Infected vs mock-infected WT cells. Right: Infected vs mock-infected SIRT5-KO cells.
- B. Normalized gene count of SARS-CoV-2.
- C. Unsupervised clustering of the 3221 genes differentially expressed between at least two of the four conditions ( $q < 0.01$ ). Heatmap of normalized expression.

- D. Z-scores of differentially expressed genes as grouped by clustering. Colored lines represent the quantification of an individual gene whereas solid black lines show the cluster Tukey boxplot.
- E. Enrichment analysis of biological gene sets in the identified gene clusters (C and D).

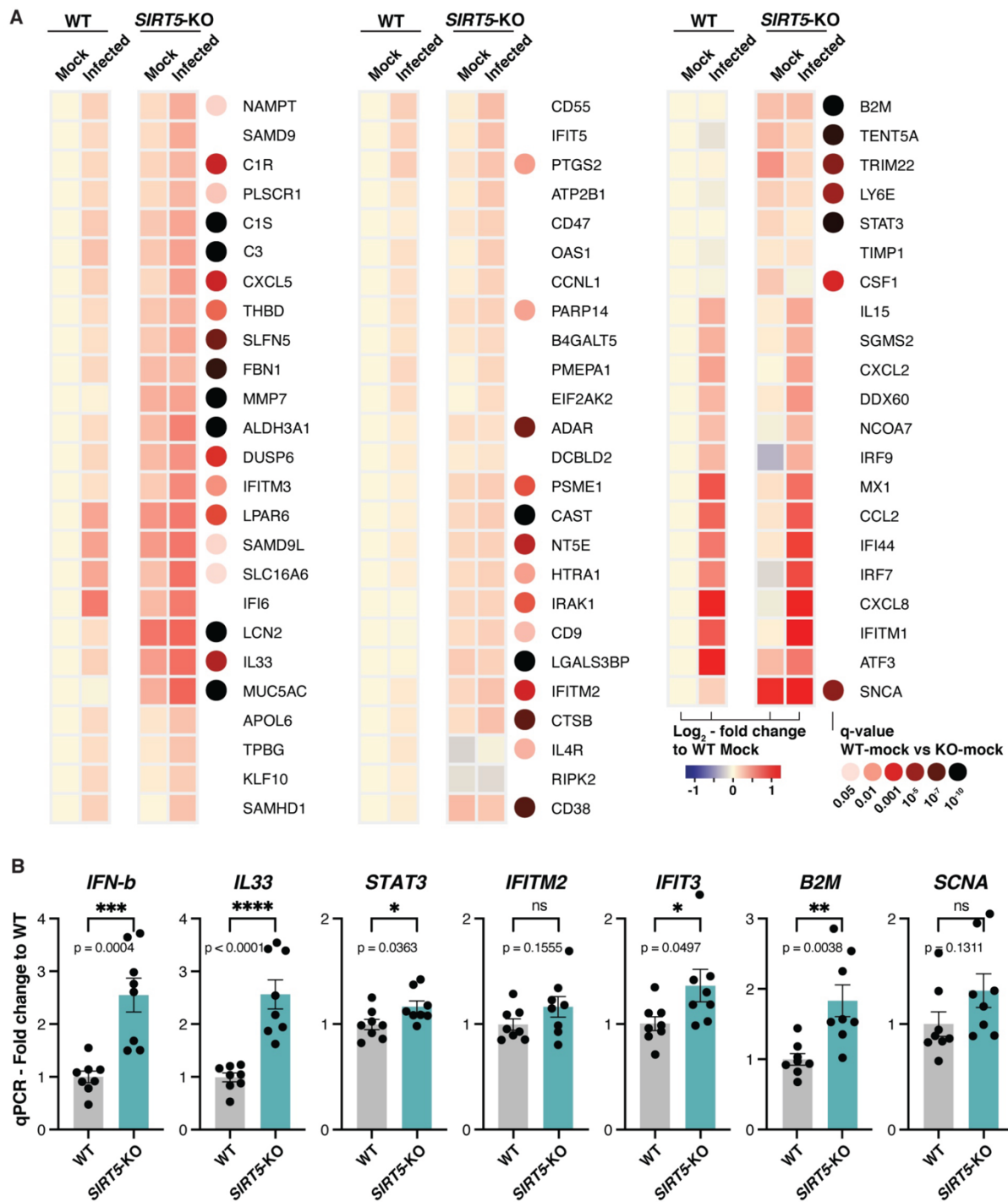


**Figure 4.7. SIRT5-KO cells express a higher basal level of viral restriction factors.**

A. Expression heatmap of interferon-stimulated genes and other restriction factors, showing that mock-infected SIRT5-KO cells express higher basal levels of restriction factors, and that antiviral responses are stronger in SIRT5-KO cells. Data show mean log<sub>2</sub> fold-change, compared to mock-infected WT, and the q-value between mock-infected WT and SIRT5-KO cells. Only genes differentially expressed between at least two conditions were included in the analysis (q<0.01).

B. RT-qPCR confirmation of restriction factors upregulated in non-infected SIRT5-KO cells (n=8). Data show fold-changes compared to WT levels after normalization with ACTIN. Data show mean and SEM between replicates. p-values after unpaired two-tailed t-test are shown and asterisks summarize the results. \*:  $p < 0.05$ , \*\*:  $p < 0.01$ , \*\*\*:  $p < 0.001$ , \*\*\*\*:  $p < 0.0001$ .

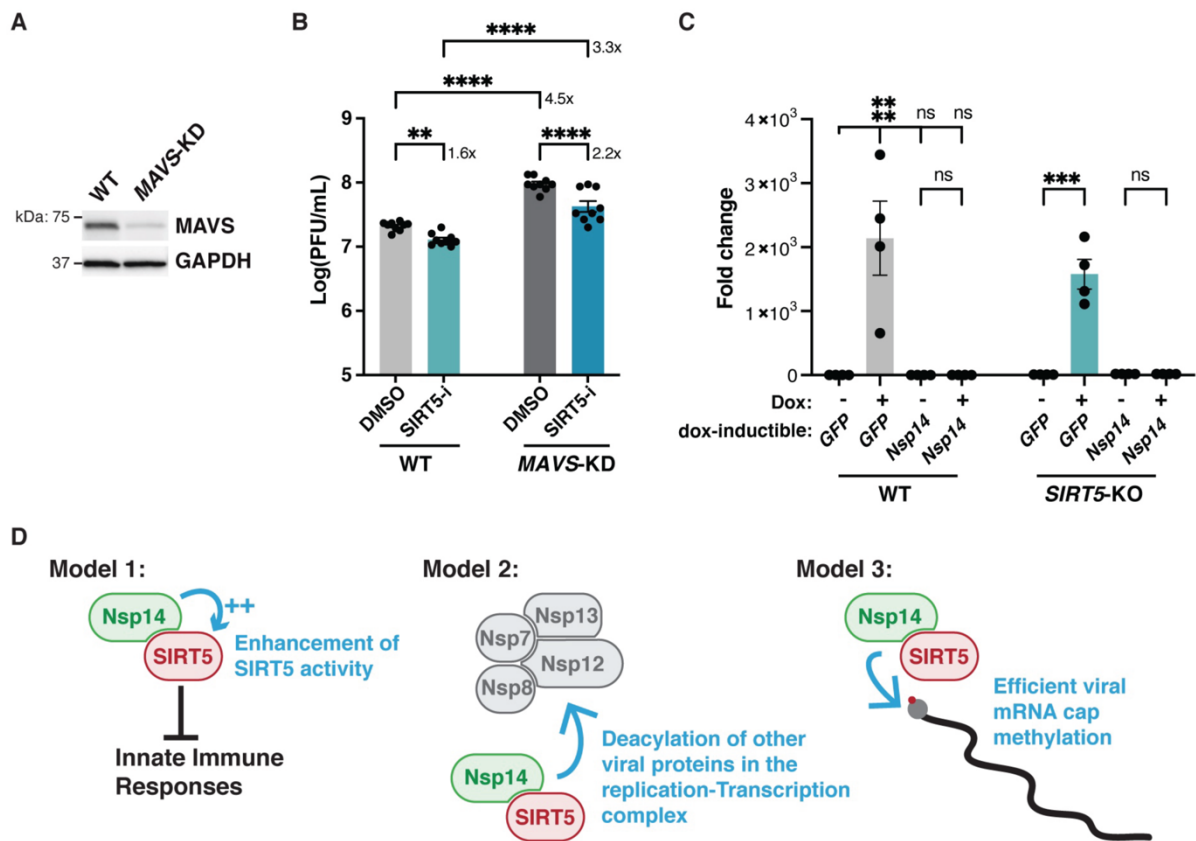


**Figure 4.8. SIRT5 proviral activity is independent of the MAVS signaling pathway.**

- A. Western blot showing 90% reduction of MAVS in A549-A/T cells transduced with a CRISPR lentivirus against MAVS. A549-A/T cells stably co-express ACE2 and TMPRSS2.
- B. Viral titers in MAVS-KD cells treated with DMSO or SIRT5 inhibitor Sirt5-i, after infection with SARS-Cov-2 for 3 days at MOI=0.1, as shown by plaque assay. Sirt5-i had a similar effect in WT and MAVS-KO, suggesting that SIRT5 function is independent of MAVS. n=9.
- C. RT-qPCR of GFP or Nsp14 after doxycycline induction. WT and SIRT5-KO A549-ACE2 cells were stably transduced with doxycycline-inducible constructs for GFP and Nsp14. After doxycycline treatment for 48 hours at 100ng/mL, GFP was strongly overexpressed, but Nsp14 failed to be expressed. Data show fold-changes compared to the first column (WT cells transduced with GFP without doxycycline), after normalization with ACTIN. n=4.
- D. Hypotheses for the role of the SIRT5/Nsp14 interaction during SARS-CoV-2 infection. In model 1, Nsp14 could enhance SIRT5 activity, which would decrease innate immune responses and favor viral replication. In model 2, Nsp14 could redirect SIRT5 to novel targets, potentially in the replication-transcription complex, where SIRT5 could deacylate other viral proteins. In model 3, the Nsp14/SIRT5 complex could be primarily involved in mRNA cap methylation. Absence or inhibition of SIRT5 would lead to incomplete cap



methylation and stronger immune recognition of viral mRNA. (B-C) Data show mean and SEM between biological replicates. Asterisks summarize the results of one-way ANOVAs followed by Holm–Šidák multiple comparisons test (on log-transformed data for plaque assays). \*:  $p < 0.05$ , \*\*:  $p < 0.01$ , \*\*\*:  $p < 0.001$ , \*\*\*\*:  $p < 0.0001$ .

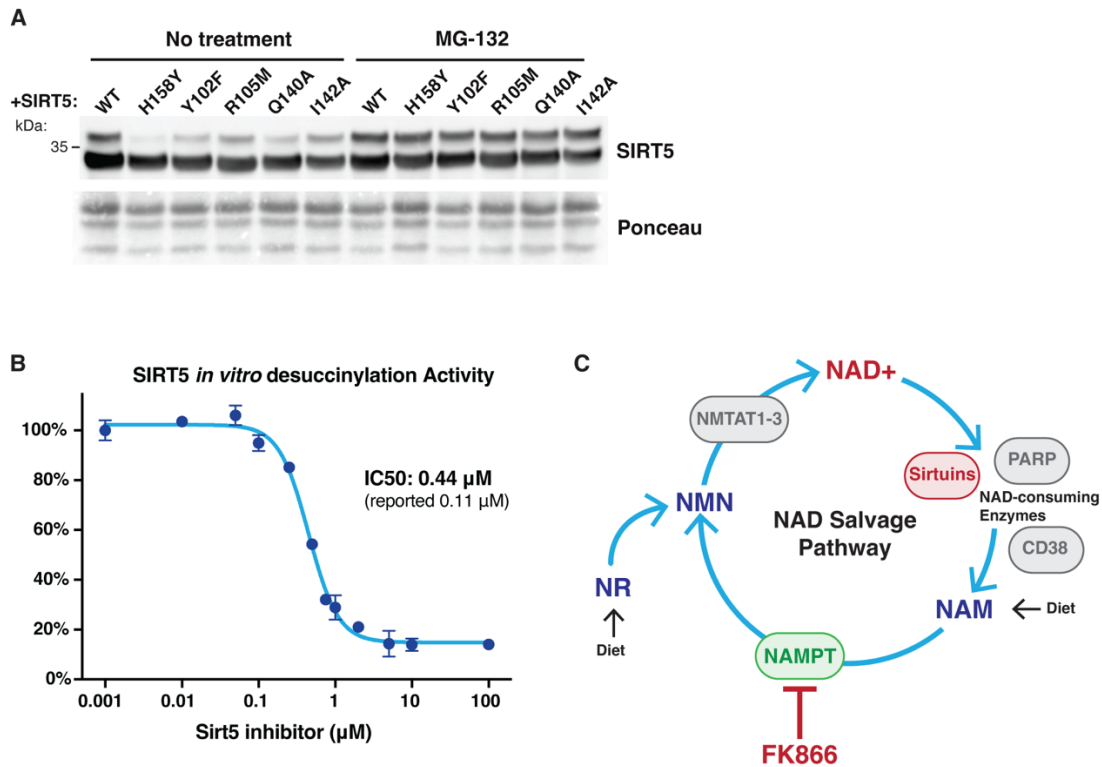
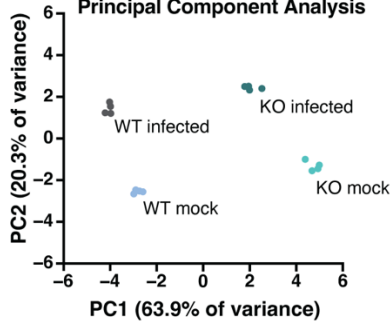


**Figure S4.1. Characterization of inhibitors.**

- A. Western Blot after transfection of HEK-293T cells SIRT5 WT and catalytic mutants, with or without treatment for 6h with the proteasome inhibitor MG-132. No major defect in protein folding could be detected.
- B. SIRT5 *in vitro* desuccinylation activity in the presence of Sirt5-i inhibitor. n=3.
- C. Diagram of the NAD salvage pathway. Inhibition of NAMPT by FK866 inhibitor depletes cellular NMN and NAD levels. Supplementation by exogenous NMN rescues NAD.

**A** Principal Component Analysis



**B**

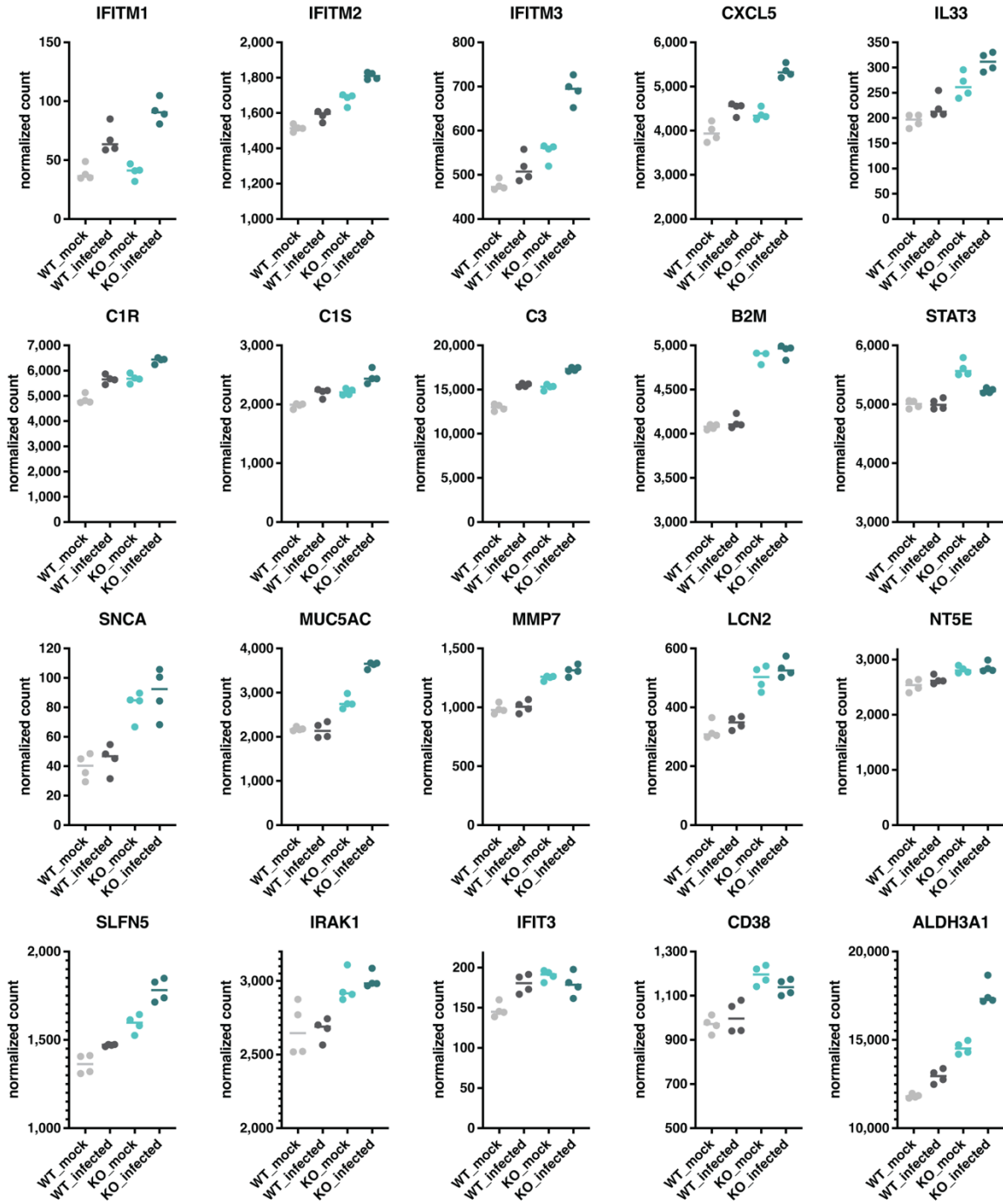


**Figure S4.2. Levels of viral restriction factors.**

- A. Principal component analysis of RNA-seq samples, showing that replicates are well separated based on knockout and infection status.
- B. Normalized gene count of interferon-stimulated genes and restriction factors, from Figure 4.7.

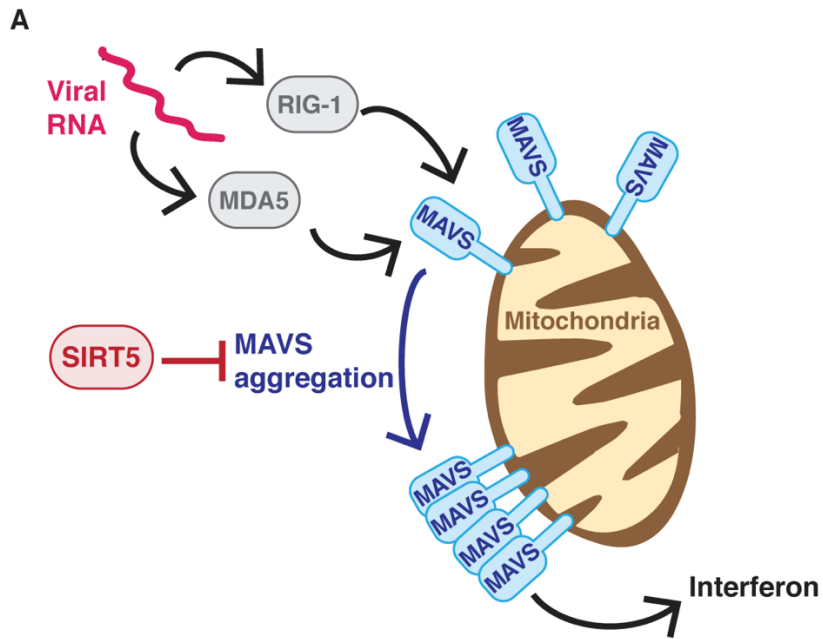


**Figure S4.3. Role of SIRT5 in the RIG-1/MAVs antiviral signaling pathway.**

A. Recognition of cytosolic viral RNA by RIG-1 or MDA5 leads to MAVS aggregation on the mitochondrial surface, which in turn causes type I interferon production. SIRT5 desuccinylation of MAVS impairs MAVS aggregation and reduces interferon production. Adapted from Liu et al. <sup>30</sup>.

**Table S4.1. CRISPR gRNAs (Knockout in A549-ACE2).**

	gRNA 1	gRNA 2	gRNA 3
<i>SIRT1</i>	CAAAGGAUAAUUCA GUGUCA	AUAGCCUUGUCAGA UAAGGA	UUGAUACAGGAAAU AUAUCC
<i>SIRT5</i>	GUGCAGCUCAUCGA UGUUCU	AGCCGAGUGUGAGA CCCGGC	CCGGGACGGGUUG UGGGCAA
<i>MAVS</i>	GCTGGTAGCTCTGG TAGACAG		

**Table S4.2. CRISPR genotyping primers (SIRT1-SIRT5 Knockout in A549-ACE2).**

	Forward	Reverse	Sequencing
<i>SIRT1</i>	GCATATGACAGCAA CCGTCC	GCTTTATCTCCACTT CTCGATG G	GTGTCGCATCCATCT AGATAC TTTAAAAT
<i>SIRT5</i>	GCATCTGCCATGTT GTTTGA	CTGAAACAGCAGGA CAGGTG	CATCTGCCATGTTGT TTGAAC ATAGT

**Table S4.3. CRISPRi gRNAs (knockdown in HEK293T).**

	gRNA
<i>SIRT5</i>	GGCGCTCCGGACCTGAGCCA
Non-targeting control	GCTGCATGGGGCGCGAATCA



**Table S4.4. qPCR Primers.**

	Forward	Reverse
SARS-CoV-2 N	CACATTGGCACCCGCAATC	GAGGAACGAGAAGAGGCTTG
OC43 N	CCGACTAGGTTTCCGCCTGG	TCTGCTGGATGTGCGCGAAG
GAPDH	TTCTACAATGAGCTGCGTGTG	GGGGTGTTGAAGGTCTCAA
ACTIN	CTGTTGCTGTAGCCAAATTCG T	ACCCACTCCTCCACCTTTGAC
GFP/Nsp1 4	AGCTAAGCTGGACAGCCAAT	ACCCGTCTTTGGATTAGGCA
STAT3	CTTTGAGACCGAGGTGTATCA CC	GGTCAGCATGTTGTACCACAG G
IL33	GTGACGGTGTTGATGGTAAGA T	AGCTCCACAGAGTGTTCCCTTG
IFNB	ATGACCAACAAGTGTCTCCTC C	GGAATCCAAGCAAGTTGTAGC TC
IFITM2	ATGAACCACATTGTGCAAACC T	CCCAGCATAGCCACTTCCT
B2M	TGTCTTTCAGCAAGGACTGGT	CTGCTTACATGTCTCGATCCC A
SNCA	AAGAGGGTGTTCTCTATGTAG GC	GCTCCTCCAACATTTGTCACTT
IFIT3	AAAAGCCCAACAACCCAGAAT	CGTATTGGTTATCAGGACTCA GC

**Table S4.5. Antibodies.**

Strep-tag mouse	Qiagen #34850
Flag-tag rabbit	Cell Signaling #14793S
Beta-tubulin rabbit	Cell Signaling #2128S
SIRT1 rabbit	Cell Signaling #9475
SIRT2 rabbit	Cell Signaling #12650
SIRT3 rabbit	Cell Signaling #5490
SIRT4 rabbit	Cell Signaling 8779S
SIRT5 rabbit	Cell Signaling #12486
SIRT6 rabbit	Cell Signaling #5360
SIRT7 rabbit	Bethyl #A300-782A
Acetyllysine rabbit	PTM Biolab # PTM-105
Succinyllysine rabbit	PTM Biolab # PTM-401
Malonyllysine rabbit	PTM Biolab # PTM-901
Anti-mouse IgG, HRP-linked	Cell Signaling #7076
Anti-rabbit IgG, HRP-linked	Cell Signaling #7074

**Table S4.6. Small molecule inhibitors and activators.**

SIRT5 inhibitor 1	Medchemexpress HY-112634
SIRT1 inhibitor Ex-527	Sigma-Aldrich E7034-5MG
NAMPT inhibitor FK866	Sigma-Aldrich F8557
Resveratrol	Sigma-Aldrich R5010-100MG
SRT1720	Selleckchem S1129
MG-132	Selleckchem S2619
Doxycycline	Sigma-Aldrich F9891

## REFERENCES

1. Gordon, D.E., Jang, G.M., Bouhaddou, M., Xu, J., Obernier, K., White, K.M., O'Meara, M.J., Rezelj, V.V., Guo, J.Z., Swaney, D.L., et al. (2020). A SARS-CoV-2 protein interaction map reveals targets for drug repurposing. *Nature* 583, 459–468.
2. Gordon, D.E., Hiatt, J., Bouhaddou, M., Rezelj, V.V., Ulferts, S., Braberg, H., Jureka, A.S., Obernier, K., Guo, J.Z., Batra, J., et al. (2020). Comparative host-coronavirus protein interaction networks reveal pan-viral disease mechanisms. *Science* 370. 10.1126/science.abe9403.
3. Li, J., Guo, M., Tian, X., Wang, X., Yang, X., Wu, P., Liu, C., Xiao, Z., Qu, Y., Yin, Y., et al. (2021). Virus-Host Interactome and Proteomic Survey Reveal Potential Virulence Factors Influencing SARS-CoV-2 Pathogenesis. *Med (N Y)* 2, 99–112.e7.
4. Laurent, E.M.N., Sofianatos, Y., Komarova, A., and Gimeno, J.P. (2020). Global BioID-based SARS-CoV-2 proteins proximal interactome unveils novel ties between viral polypeptides and host factors involved in multiple COVID19 .... *BioRxiv*.
5. Minskaia, E., Hertzog, T., Gorbalenya, A.E., Campanacci, V., Cambillau, C., Canard, B., and Ziebuhr, J. (2006). Discovery of an RNA virus 3'->5' exoribonuclease that is critically involved in coronavirus RNA synthesis. *Proc. Natl. Acad. Sci. U. S. A.* 103, 5108–5113.
6. Chen, Y., Cai, H., Pan, J., 'an, Xiang, N., Tien, P., Ahola, T., and Guo, D. (2009). Functional screen reveals SARS coronavirus nonstructural protein nsp14 as a novel cap N7 methyltransferase. *Proc. Natl. Acad. Sci. U. S. A.* 106, 3484–3489.

7. Ma, Y., Wu, L., Shaw, N., Gao, Y., Wang, J., Sun, Y., Lou, Z., Yan, L., Zhang, R., and Rao, Z. (2015). Structural basis and functional analysis of the SARS coronavirus nsp14-nsp10 complex. *Proc. Natl. Acad. Sci. U. S. A.* *112*, 9436–9441.
8. Yan, L., Yang, Y., Li, M., Zhang, Y., Zheng, L., Ge, J., Huang, Y.C., Liu, Z., Wang, T., Gao, S., et al. (2021). Coupling of N7-methyltransferase and 3'-5' exoribonuclease with SARS-CoV-2 polymerase reveals mechanisms for capping and proofreading. *Cell* *184*, 3474–3485.e11.
9. Ferron, F., Subissi, L., Silveira De Moraes, A.T., Le, N.T.T., Sevajol, M., Gluais, L., Decroly, E., Vonrhein, C., Bricogne, G., Canard, B., et al. (2018). Structural and molecular basis of mismatch correction and ribavirin excision from coronavirus RNA. *Proc. Natl. Acad. Sci. U. S. A.* *115*, E162–E171.
10. Bouvet, M., Imbert, I., Subissi, L., Gluais, L., Canard, B., and Decroly, E. (2012). RNA 3'-end mismatch excision by the severe acute respiratory syndrome coronavirus nonstructural protein nsp10/nsp14 exoribonuclease complex. *Proc. Natl. Acad. Sci. U. S. A.* *109*, 9372–9377.
11. Liu, C., Shi, W., Becker, S.T., Schatz, D.G., Liu, B., and Yang, Y. (2021). Structural basis of mismatch recognition by a SARS-CoV-2 proofreading enzyme. *Science*. [10.1126/science.abi9310](https://doi.org/10.1126/science.abi9310).
12. Eckerle, L.D., Lu, X., Sperry, S.M., Choi, L., and Denison, M.R. (2007). High fidelity of murine hepatitis virus replication is decreased in nsp14 exoribonuclease mutants. *J. Virol.* *81*, 12135–12144.
13. Eckerle, L.D., Becker, M.M., Halpin, R.A., Li, K., Venter, E., Lu, X., Scherbakova, S., Graham, R.L., Baric, R.S., Stockwell, T.B., et al. (2010). Infidelity of SARS-CoV

- Nsp14-exonuclease mutant virus replication is revealed by complete genome sequencing. *PLoS Pathog.* *6*, e1000896.
14. Gorbalenya, A.E., Enjuanes, L., Ziebuhr, J., and Snijder, E.J. (2006). Nidovirales: evolving the largest RNA virus genome. *Virus Res.* *117*, 17–37.
  15. Lauber, C., Goeman, J.J., Parquet, M. del C., Nga, P.T., Snijder, E.J., Morita, K., and Gorbalenya, A.E. (2013). The footprint of genome architecture in the largest genome expansion in RNA viruses. *PLoS Pathog.* *9*, e1003500.
  16. Ogando, N.S., Zevenhoven-Dobbe, J.C., van der Meer, Y., Bredenbeek, P.J., Posthuma, C.C., and Snijder, E.J. (2020). The Enzymatic Activity of the nsp14 Exoribonuclease Is Critical for Replication of MERS-CoV and SARS-CoV-2. *J. Virol.* *94*. 10.1128/JVI.01246-20.
  17. Hsu, J.C.-C., Laurent-Rolle, M., Pawlak, J.B., Wilen, C.B., and Cresswell, P. (2021). Translational shutdown and evasion of the innate immune response by SARS-CoV-2 NSP14 protein. *Proc. Natl. Acad. Sci. U. S. A.* *118*. 10.1073/pnas.2101161118.
  18. Hayn, M., Hirschenberger, M., Koepke, L., Nchioua, R., Straub, J.H., Klute, S., Hunszinger, V., Zech, F., Prelli Bozzo, C., Aftab, W., et al. (2021). Systematic functional analysis of SARS-CoV-2 proteins uncovers viral innate immune antagonists and remaining vulnerabilities. *Cell Rep.* *35*, 109126.
  19. Li, T., Kenney, A.D., Liu, H., Fiches, G.N., Zhou, D., Biswas, A., Que, J., Santoso, N., Yount, J.S., and Zhu, J. (2021). SARS-CoV-2 Nsp14 activates NF- $\kappa$ B signaling and induces IL-8 upregulation. *bioRxiv.* 10.1101/2021.05.26.445787.
  20. Gribble, J., Stevens, L.J., Agostini, M.L., Anderson-Daniels, J., Chappell, J.D., Lu, X., Pruijssers, A.J., Routh, A.L., and Denison, M.R. (2021). The coronavirus

- proofreading exoribonuclease mediates extensive viral recombination. *PLoS Pathog.* *17*, e1009226.
21. Houtkooper, R.H., Pirinen, E., and Auwerx, J. (2012). Sirtuins as regulators of metabolism and healthspan. *Nat. Rev. Mol. Cell Biol.* *13*, 225–238.
  22. Imai, S.-I., and Guarente, L. (2016). It takes two to tango: NAD<sup>+</sup> and sirtuins in aging/longevity control. *NPJ Aging Mech Dis* *2*, 16017.
  23. Du, J., Zhou, Y., Su, X., Yu, J.J., Khan, S., Jiang, H., Kim, J., Woo, J., Kim, J.H., Choi, B.H., et al. (2011). Sirt5 is a NAD-dependent protein lysine demalonylase and desuccinylase. *Science* *334*, 806–809.
  24. Tan, M., Peng, C., Anderson, K.A., Chhoy, P., Xie, Z., Dai, L., Park, J., Chen, Y., Huang, H., Zhang, Y., et al. (2014). Lysine glutarylation is a protein posttranslational modification regulated by SIRT5. *Cell Metab.* *19*, 605–617.
  25. Rardin, M.J., He, W., Nishida, Y., Newman, J.C., Carrico, C., Danielson, S.R., Guo, A., Gut, P., Sahu, A.K., Li, B., et al. (2013). SIRT5 regulates the mitochondrial lysine succinylome and metabolic networks. *Cell Metab.* *18*, 920–933.
  26. Nishida, Y., Rardin, M.J., Carrico, C., He, W., Sahu, A.K., Gut, P., Najjar, R., Fitch, M., Hellerstein, M., Gibson, B.W., et al. (2015). SIRT5 Regulates both Cytosolic and Mitochondrial Protein Malonylation with Glycolysis as a Major Target. *Mol. Cell* *59*, 321–332.
  27. Kumar, S., and Lombard, D.B. (2018). Functions of the sirtuin deacylase SIRT5 in normal physiology and pathobiology. *Crit. Rev. Biochem. Mol. Biol.* *53*, 311–334.
  28. Yu, J., Sadhukhan, S., Noriega, L.G., Moullan, N., He, B., Weiss, R.S., Lin, H., Schoonjans, K., and Auwerx, J. (2013). Metabolic characterization of a Sirt5 deficient mouse model. *Sci. Rep.* *3*, 2806.

29. Yeo, N.C., Chavez, A., Lance-Byrne, A., Chan, Y., Menn, D., Milanova, D., Kuo, C.-C., Guo, X., Sharma, S., Tung, A., et al. (2018). An enhanced CRISPR repressor for targeted mammalian gene regulation. *Nat. Methods* *15*, 611–616.
30. Liu, X., Zhu, C., Zha, H., Tang, J., Rong, F., Chen, X., Fan, S., Xu, C., Du, J., Zhu, J., et al. (2020). SIRT5 impairs aggregation and activation of the signaling adaptor MAVS through catalyzing lysine desuccinylation. *EMBO J.* *39*, e103285.
31. Yang, X., Wang, Z., Li, X., Liu, B., Liu, M., Liu, L., Chen, S., Ren, M., Wang, Y., Yu, M., et al. (2018). SHMT2 Desuccinylation by SIRT5 Drives Cancer Cell Proliferation. *Cancer Res.* *78*, 372–386.
32. Xiangyun, Y., Xiaomin, N., Linping, G., Yunhua, X., Ziming, L., Yongfeng, Y., Zhiwei, C., and Shun, L. (2017). Desuccinylation of pyruvate kinase M2 by SIRT5 contributes to antioxidant response and tumor growth. *Oncotarget* *8*, 6984–6993.
33. Davenport, A.M., Huber, F.M., and Hoelz, A. (2014). Structural and functional analysis of human SIRT1. *J. Mol. Biol.* *426*, 526–541.
34. Rajabi, N., Auth, M., Troelsen, K.R., Pannek, M., Bhatt, D.P., Fontenas, M., Hirschey, M.D., Steegborn, C., Madsen, A.S., and Olsen, C.A. (2017). Mechanism-Based Inhibitors of the Human Sirtuin 5 Deacylase: Structure-Activity Relationship, Biostructural, and Kinetic Insight. *Angew. Chem. Int. Ed Engl.* *56*, 14836–14841.
35. Verdin, E. (2015). NAD<sup>+</sup> in aging, metabolism, and neurodegeneration. *Science* *350*, 1208–1213.
36. Covarrubias, A.J., Kale, A., Perrone, R., Lopez-Dominguez, J.A., Pisco, A.O., Kasler, H.G., Schmidt, M.S., Heckenbach, I., Kwok, R., Wiley, C.D., et al. (2020). Senescent cells promote tissue NAD<sup>+</sup> decline during ageing via the activation of CD38<sup>+</sup> macrophages. *Nat Metab* *2*, 1265–1283.



37. Bouhaddou, M., Memon, D., Meyer, B., White, K.M., Rezelj, V.V., Correa Marrero, M., Polacco, B.J., Melnyk, J.E., Ulferts, S., Kaake, R.M., et al. (2020). The Global Phosphorylation Landscape of SARS-CoV-2 Infection. *Cell* *182*, 685–712.e19.
38. Polletta, L., Vernucci, E., Carnevale, I., Arcangeli, T., Rotili, D., Palmerio, S., Steegborn, C., Nowak, T., Schutkowski, M., Pellegrini, L., et al. (2015). SIRT5 regulation of ammonia-induced autophagy and mitophagy. *Autophagy* *11*, 253–270.
39. Wang, Y.-Q., Wang, H.-L., Xu, J., Tan, J., Fu, L.-N., Wang, J.-L., Zou, T.-H., Sun, D.-F., Gao, Q.-Y., Chen, Y.-X., et al. (2018). Sirtuin5 contributes to colorectal carcinogenesis by enhancing glutaminolysis in a deglutarylation-dependent manner. *Nat. Commun.* *9*, 545.
40. Abril, Y.L.N., Fernandez, I.R., Hong, J.Y., Chiang, Y.-L., Kutateladze, D.A., Zhao, Q., Yang, M., Hu, J., Sadhukhan, S., Li, B., et al. (2021). Pharmacological and genetic perturbation establish SIRT5 as a promising target in breast cancer. *Oncogene* *40*, 1644–1658.
41. Chang, L., Xi, L., Liu, Y., Liu, R., Wu, Z., and Jian, Z. (2018). SIRT5 promotes cell proliferation and invasion in hepatocellular carcinoma by targeting E2F1. *Mol. Med. Rep.* *17*, 342–349.
42. Blanco-Melo, D., Nilsson-Payant, B.E., Liu, W.-C., Uhl, S., Hoagland, D., Møller, R., Jordan, T.X., Oishi, K., Panis, M., Sachs, D., et al. (2020). Imbalanced Host Response to SARS-CoV-2 Drives Development of COVID-19. *Cell* *181*, 1036–1045.e9.
43. Yamada, T., Sato, S., Sotoyama, Y., Orba, Y., Sawa, H., Yamauchi, H., Sasaki, M., and Takaoka, A. (2021). RIG-I triggers a signaling-abortive anti-SARS-CoV-2

- defense in human lung cells. *Nat. Immunol.* *22*, 820–828.
44. Kasuga, Y., Zhu, B., Jang, K.-J., and Yoo, J.-S. (2021). Innate immune sensing of coronavirus and viral evasion strategies. *Exp. Mol. Med.* *53*, 723–736.
45. Puray-Chavez, M., LaPak, K.M., Schrank, T.P., Elliott, J.L., Bhatt, D.P., Agajanian, M.J., Jasuja, R., Lawson, D.Q., Davis, K., Rothlauf, P.W., et al. (2021). Systematic analysis of SARS-CoV-2 infection of an ACE2-negative human airway cell. *Cell Rep.* *36*, 109364.
46. Sanders, C., and Thomas, P. (2014). MMP-7 promotes host recovery and lung function to influenza virus infection (VIR2P.1016). *The Journal of Immunology* *192*, 75.5–75.5.
47. Flo, T.H., Smith, K.D., Sato, S., Rodriguez, D.J., Holmes, M.A., Strong, R.K., Akira, S., and Aderem, A. (2004). Lipocalin 2 mediates an innate immune response to bacterial infection by sequestering iron. *Nature* *432*, 917–921.
48. Ehre, C., Worthington, E.N., Liesman, R.M., Grubb, B.R., Barbier, D., O’Neal, W.K., Sallenave, J.-M., Pickles, R.J., and Boucher, R.C. (2012). Overexpressing mouse model demonstrates the protective role of Muc5ac in the lungs. *Proc. Natl. Acad. Sci. U. S. A.* *109*, 16528–16533.
49. Arslan, A.D., Sassano, A., Saleiro, D., Lisowski, P., Kosciuczuk, E.M., Fischietti, M., Eckerdt, F., Fish, E.N., and Plataniias, L.C. (2017). Human SLFN5 is a transcriptional co-repressor of STAT1-mediated interferon responses and promotes the malignant phenotype in glioblastoma. *Oncogene* *36*, 6006–6019.
50. Niemelä, J., Henttinen, T., Yegutkin, G.G., Airas, L., Kujari, A.-M., Rajala, P., and Jalkanen, S. (2004). IFN-alpha induced adenosine production on the endothelium: a mechanism mediated by CD73 (ecto-5'-nucleotidase) up-regulation. *J. Immunol.*

172, 1646–1653.

51. Blanc, F., Furio, L., Moisy, D., Yen, H.-L., Chignard, M., Letavernier, E., Naffakh, N., Mok, C.K.P., and Si-Tahar, M. (2016). Targeting host calpain proteases decreases influenza A virus infection. *Am. J. Physiol. Lung Cell. Mol. Physiol.* *310*, L689–L699.
52. Massey, A.R., and Beckham, J.D. (2016). Alpha-Synuclein, a Novel Viral Restriction Factor Hiding in Plain Sight. *DNA Cell Biol.* *35*, 643–645.
53. Kwon, H.-S., Brent, M.M., Getachew, R., Jayakumar, P., Chen, L.-F., Schnolzer, M., McBurney, M.W., Marmorstein, R., Greene, W.C., and Ott, M. (2008). Human immunodeficiency virus type 1 Tat protein inhibits the SIRT1 deacetylase and induces T cell hyperactivation. *Cell Host Microbe* *3*, 158–167.
54. Pagans, S., Pedal, A., North, B.J., Kaehlcke, K., Marshall, B.L., Dorr, A., Hetzer-Egger, C., Henklein, P., Frye, R., McBurney, M.W., et al. (2005). SIRT1 regulates HIV transcription via Tat deacetylation. *PLoS Biol.* *3*, e41.
55. Heinonen, T., Ciarlo, E., Th roude, C., Pelekanou, A., Herderschee, J., Le Roy, D., and Roger, T. (2018). Sirtuin 5 Deficiency Does Not Compromise Innate Immune Responses to Bacterial Infections. *Front. Immunol.* *9*, 2675.
56. Koyuncu, E., Budayeva, H.G., Miteva, Y.V., Ricci, D.P., Silhavy, T.J., Shenk, T., and Cristea, I.M. (2014). Sirtuins are evolutionarily conserved viral restriction factors. *MBio* *5*. 10.1128/mBio.02249-14.
57. Hou, F., Sun, L., Zheng, H., Skaug, B., Jiang, Q.-X., and Chen, Z.J. (2011). MAVS forms functional prion-like aggregates to activate and propagate antiviral innate immune response. *Cell* *146*, 448–461.
58. Fu, Y.-Z., Wang, S.-Y., Zheng, Z.-Q., Yi Huang, Li, W.-W., Xu, Z.-S., and Wang,

- Y.-Y. (2021). SARS-CoV-2 membrane glycoprotein M antagonizes the MAVS-mediated innate antiviral response. *Cell. Mol. Immunol.* *18*, 613–620.
59. Shi, C.-S., Qi, H.-Y., Boullaran, C., Huang, N.-N., Abu-Asab, M., Shelhamer, J.H., and Kehrl, J.H. (2014). SARS-coronavirus open reading frame-9b suppresses innate immunity by targeting mitochondria and the MAVS/TRAF3/TRAF6 signalosome. *J. Immunol.* *193*, 3080–3089.
60. Freundt, E.C., Yu, L., Park, E., Lenardo, M.J., and Xu, X.-N. (2009). Molecular determinants for subcellular localization of the severe acute respiratory syndrome coronavirus open reading frame 3b protein. *J. Virol.* *83*, 6631–6640.
61. Chen, Y., Zhou, Z., and Min, W. (2018). Mitochondria, Oxidative Stress and Innate Immunity. *Front. Physiol.* *9*, 1487.
62. Weichhart, T., Hengstschläger, M., and Linke, M. (2015). Regulation of innate immune cell function by mTOR. *Nat. Rev. Immunol.* *15*, 599–614.
63. Guan, J., Jiang, X., Gai, J., Sun, X., Zhao, J., Li, J., Li, Y., Cheng, M., Du, T., Fu, L., et al. (2020). Sirtuin 5 regulates the proliferation, invasion and migration of prostate cancer cells through acetyl-CoA acetyltransferase 1. *J. Cell. Mol. Med.* *24*, 14039–14049.
64. Vallejo-Gracia, A., Chen, I.P., Perrone, R., Besnard, E., Boehm, D., Battivelli, E., Tezil, T., Krey, K., Raymond, K.A., Hull, P.A., et al. (2020). FOXO1 promotes HIV latency by suppressing ER stress in T cells. *Nat Microbiol* *5*, 1144–1157.
65. Horlbeck, M.A., Gilbert, L.A., Villalta, J.E., Adamson, B., Pak, R.A., Chen, Y., Fields, A.P., Park, C.Y., Corn, J.E., Kampmann, M., et al. (2016). Compact and highly active next-generation libraries for CRISPR-mediated gene repression and activation. *Elife* *5*, e19760.

66. Tezil, T., Chamoli, M., Ng, C.-P., Simon, R.P., Butler, V.J., Jung, M., Andersen, J., Kao, A.W., and Verdin, E. (2019). Lifespan-increasing drug nordihydroguaiaretic acid inhibits p300 and activates autophagy. *NPJ Aging Mech Dis* 5, 7.
67. Christensen, D.G., Meyer, J.G., Baumgartner, J.T., D'Souza, A.K., Nelson, W.C., Payne, S.H., Kuhn, M.L., Schilling, B., and Wolfe, A.J. (2018). Identification of Novel Protein Lysine Acetyltransferases in *Escherichia coli*. *MBio* 9. 10.1128/mBio.01905-18.
68. Walter, M., and Verdin, E. (2020). Viral gene drive in herpesviruses. *Nat. Commun.* 11, 4884.
69. Liao, Y., Smyth, G.K., and Shi, W. (2013). The Subread aligner: fast, accurate and scalable read mapping by seed-and-vote. *Nucleic Acids Res.* 41, e108.
70. Liao, Y., Smyth, G.K., and Shi, W. (2014). featureCounts: an efficient general purpose program for assigning sequence reads to genomic features. *Bioinformatics* 30, 923–930.
71. Love, M.I., Huber, W., and Anders, S. (2014). Moderated estimation of fold change and dispersion for RNA-seq data with DESeq2. *Genome Biol.* 15, 550.
72. Yu, G., Wang, L.G., Han, Y., and He, Q.Y. (2012). clusterProfiler: an R package for comparing biological themes among gene clusters. *OMICS*.
73. Liberzon, A., Subramanian, A., Pinchback, R., Thorvaldsdóttir, H., Tamayo, P., and Mesirov, J.P. (2011). Molecular signatures database (MSigDB) 3.0. *Bioinformatics* 27, 1739–1740.

## Chapter 5

### Conclusions and Outlook

As I complete my dissertation and thesis work, four vaccines and three antiviral treatments have been approved by the US Food and Drug Administration for COVID-19 disease. The speed at which vaccine and antiviral candidates have advanced in research, testing, and production has been unprecedented and could have only been made possible by the scientists who dedicated their work to developing different vaccine modalities and understanding host-pathogen interactions long before the emergence of SARS-CoV-2. However, the need for varied and effective COVID-19 therapeutics remain as SARS-CoV-2 continues to evolve. This was painfully evident when existing (pre-November 2021) vaccines and monoclonal antibodies were no longer protective against the first Omicron variant, BA.1, and this continues to be an issue with the current emerging variants<sup>1-12</sup>. By continuing viral therapeutic and vaccine research, new infections can be prevented and severe COVID-19 disease can be mitigated.

Furthermore, the COVID-19 pandemic will certainly not be the last viral pandemic humanity endures. More zoonotic diseases will emerge as humans experience globalization and encroach on land previously inhabited by wildlife. Without steady and significant investment in infectious disease research, therapeutics will continue to lag behind the speed of viral evolution. By understanding how viruses attack and hijack host processes, we can identify common pathways targeted by multiple viruses and design pan-antivirals and vaccines against them. At the same time, designing therapeutics against the host can have unintended effects, such as the BET inhibitors

presented here. This dissertation serves as a reminder that therapeutics can be both anti- and proviral in different contexts and each new target and therapeutic needs to be thoroughly investigated. Nevertheless, research on host-pathogen interactions add to the collective knowledge of the cellular functions and pathways that are important for fending off viral infection.

## REFERENCES

1. Cele, S., Jackson, L., Khoury, D.S., Khan, K., Moyo-Gwete, T., Tegally, H., San, J.E., Cromer, D., Scheepers, C., Amoako, D.G., et al. (2022). Omicron extensively but incompletely escapes Pfizer BNT162b2 neutralization. *Nature* *602*, 654–656.
2. Lu, L., Mok, B.W.Y., Chen, L.L., Chan, J.M.C., Tsang, O.T.Y., Lam, B.H.S., Chuang, V.W.M., Chu, A.W.H., Chan, W.M., Ip, J.D., et al. (2021). Neutralization of Severe Acute Respiratory Syndrome Coronavirus 2 Omicron Variant by Sera From BNT162b2 or CoronaVac Vaccine Recipients. *Clin. Infect. Dis.* *75*, e822–e826.
3. Miller, J., Hachmann, N.P., Collier, A.-R.Y., Lasrado, N., Mazurek, C.R., Patio, R.C., Powers, O., Surve, N., Theiler, J., Korber, B., et al. (2022). Substantial Neutralization Escape by the SARS-CoV-2 Omicron Variant BQ.1.1. *bioRxiv*, 2022.11.01.514722. 10.1101/2022.11.01.514722.
4. Dejnirattisai, W., Huo, J., Zhou, D., Zahradník, J., Supasa, P., Liu, C., Duyvesteyn, H.M.E., Ginn, H.M., Mentzer, A.J., Tuekprakhon, A., et al. (2022). SARS-CoV-2 Omicron-B.1.1.529 leads to widespread escape from neutralizing antibody responses. *Cell*. 10.1016/j.cell.2021.12.046.
5. Syed, A.M., Ciling, A., Taha, T.Y., Chen, I.P., Khalid, M.M., Sreekumar, B., Chen, P.-Y., Kumar, G.R., Suryawanshi, R., Silva, I., et al. (2022). Omicron mutations enhance infectivity and reduce antibody neutralization of SARS-CoV-2 virus-like particles. *Proc. Natl. Acad. Sci. U. S. A.* *119*, e2200592119.



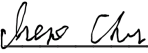
6. Mannar, D., Saville, J.W., Zhu, X., Srivastava, S.S., Berezuk, A.M., Tuttle, K.S., Marquez, A.C., Sekirov, I., and Subramaniam, S. (2022). SARS-CoV-2 Omicron variant: Antibody evasion and cryo-EM structure of spike protein-ACE2 complex. *Science* 375, 760–764.
7. Cao, Y., Wang, J., Jian, F., Xiao, T., Song, W., Yisimayi, A., Huang, W., Li, Q., Wang, P., An, R., et al. (2021). Omicron escapes the majority of existing SARS-CoV-2 neutralizing antibodies. *Nature*. 10.1038/s41586-021-04385-3.
8. VanBlargan, L.A., Errico, J.M., Halfmann, P.J., Zost, S.J., Crowe, J.E., Jr, Purcell, L.A., Kawaoka, Y., Corti, D., Fremont, D.H., and Diamond, M.S. (2022). An infectious SARS-CoV-2 B.1.1.529 Omicron virus escapes neutralization by therapeutic monoclonal antibodies. *Nat. Med.* 10.1038/s41591-021-01678-y.
9. Hoffmann, M., Krüger, N., Schulz, S., Cossmann, A., Rocha, C., Kempf, A., Nehlmeier, I., Graichen, L., Moldenhauer, A.-S., Winkler, M.S., et al. (2022). The Omicron variant is highly resistant against antibody-mediated neutralization: Implications for control of the COVID-19 pandemic. *Cell* 185, 447–456.e11.
10. Planas, D., Saunders, N., Maes, P., Guivel-Benhassine, F., Planchais, C., Buchrieser, J., Bolland, W.-H., Porrot, F., Staropoli, I., Lemoine, F., et al. (2022). Considerable escape of SARS-CoV-2 Omicron to antibody neutralization. *Nature* 602, 671–675.
11. Yue, C., Song, W., Wang, L., Jian, F., Chen, X., Gao, F., Shen, Z., Wang, Y., Wang, X., and Cao, Y. (2023). ACE2 binding and antibody evasion in enhanced transmissibility of XBB.1.5. *Lancet Infect. Dis.* 23, 278–280.

12. Uriu, K., Ito, J., Zahradnik, J., Fujita, S., Kosugi, Y., Schreiber, G., Genotype to Phenotype Japan (G2P-Japan) Consortium, and Sato, K. (2023). Enhanced transmissibility, infectivity, and immune resistance of the SARS-CoV-2 omicron XBB.1.5 variant. *Lancet Infect. Dis.* 23, 280–281.

## Publishing Agreement

It is the policy of the University to encourage open access and broad distribution of all theses, dissertations, and manuscripts. The Graduate Division will facilitate the distribution of UCSF theses, dissertations, and manuscripts to the UCSF Library for open access and distribution. UCSF will make such theses, dissertations, and manuscripts accessible to the public and will take reasonable steps to preserve these works in perpetuity.

I hereby grant the non-exclusive, perpetual right to The Regents of the University of California to reproduce, publicly display, distribute, preserve, and publish copies of my thesis, dissertation, or manuscript in any form or media, now existing or later derived, including access online for teaching, research, and public service purposes.

DocuSigned by:  
  
5359629679E349B... Author Signature

3/17/2023  
Date